Old Dominion University Research Foundation

DEPARTMENT OF MECHANICAL ENGINEERING AND MECHANICS
COLLEGE OF ENGINEERING AND TECHNOLOGY
OLD DOMINION UNIVERSITY
NORFOLK, VIRGINIA 23529

DEVELOPMENT OF A PERTURBATION GENERATOR
FOR VORTEX STABILITY STUDIES

By

J.E. Riester

and

Robert L. Ash, Principal Investigator

Progress Report
For the period ended 12/31/90

March 1991

DEPARTMENT OF MECHANICAL ENGINEERING AND MECHANICS
COLLEGE OF ENGINEERING AND TECHNOLOGY
OLD DOMINION UNIVERSITY
NORFOLK, VIRGINIA 23529

DEVELOPMENT OF A PERTURBATION GENERATOR
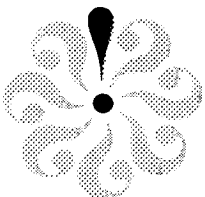*FOR VORTEX STABILITY STUDIES*

By

J.E. Riester

and

Robert L. Ash, Principal Investigator

Progress Report
For the period ended 12/31/90

ABSTRACT

Theory predicts vortex instability when subjected to certain types of disturbances. It was desired to build a device which could introduce controlled velocity perturbations into a trailing line vortex in order to study the effects on stability. A perturbation generator has been designed and manufactured which can be attached to the centerbody of an airfoil type vortex generator. Details of design tests and manufacturing of the perturbation generator are presented. The device produced controlled perturbations with frequencies in excess of 250 Hz. Preliminary testing and evaluation of the perturbation generator performance was conducted in a 4 inch cylindrical pipe. Observations of vortex shedding frequencies from a centerbody were measured. Further evaluation with the perturbation generator attached to the vortex generator in a 2'x3' Wind Tunnel have also been conducted. Hot-wire anemometry was used to confirm the perturbation generator's ability to introduce controlled frequency fluctuations. Comparison of the energy levels of the disturbances in the vortex core was made between locations 42 chord lengths and 15 chord lengths downstream.

NOMENCLATURE

a	drum thickness
a_0	average drum thickness
ACU	Axis Control Unit
c	complex phase velocity
c_r	real portion of complex phase velocity
c_i	imaginary part of complex phase velocity
D	diameter
E	voltage
E_f	integrated frequency voltage
E_t	total integrated voltage
E_m	maximum voltage
f_{peak}	frequency of spectral peak
h_l	head loss (across orifice plate)
I.D.	inside diameter
K	orifice constant
l	equivalent viscous length
M_f	perturbation generator frequency in hertz
m/s	meters per second
n	azimuthal wavenumber
O.D.	outside diameter
P	pressure
$\triangle P$	differential pressure
q	swirl parameter
Q	volumetric flow rate
r	radius
Re	Reynolds number
St	Strouhal number based on diameter
T_∞	free stream temperature
u	axial component of velocity

U_m	mean pipe velocity
U_∞	free stream velocity
V_m	mean velocity
α	axial wavenumber
δ	gap width
μ	dynamic viscosity
ω	temporal frequency
ϕ	azimuthal co-ordinate
ρ	density
θ	angular position

1. INTRODUCTION:

Vortex stability has been the subject of considerable controversy, due partly to a lack of experimental verification. Since vortex modification can impact practical problems ranging from improved combustor design through lift augmentation for high performance aircraft, stability implications are important. Before vortex modification strategies can be developed, the stability of various types of vortices must be understood. However, not all vortices are alike. Vortical flows are found in turbulence at sub-millimeter scales, bathtub vortices, tornadoes, hurricanes, and even star patterns in galaxies. Axial vortices are one characteristic type of vortex which need to be studied. Axial vortex breakdown has been described for a variety of flow conditions, but since the axial vortex reforms typically behind the breakdown, it is not clear whether vortex breakdown is a true instability. Many fundamental questions remain concerning the meaning of stability in vortex flows.

1.1 Historical Overview

In 1916, Raleigh[1] examined the stability of constant density swirling flows in an effort to better understand meteorology. Using concentric cylinders, he determined that, in the absence of an axial flow component, swirling flows were unconditionally stable when the circulation increased monotonically with radius. Hence, a necessary and sufficient condition

for stability is that the square of the circulation , $(rV)^2$ should not decrease as r increases. He stated further that if there were regions where the circulation was constant, equilibrium would be neutral. Howard and Gupta[2] also used concentric cylinders in an effort to develop a stability criteria for non-dissipative swirling flows. They extended their study to more complex vortices including the influences of variable density, axial flow, and non-axisymmetric perturbations. They were able to determine different stability criteria for each flow case studied; however, they were unable to develop a set of general necessary and sufficient conditions for vortex stability.

In an attempt to describe the phenomena which causes a vortex to breakdown, many prominent theories have been developed. H. B. Squire[3] studied the growth of line vortices and trailing vortices behind a wing tip (assuming that it was not influenced by the trailing vortex from the other tip). He suggested a wave theory wherein the axisymmetric breakdown was connected with the possible appearance of infinitesimal standing waves in the flow. If standing waves could exist, some disturbances far downstream could propagate upstream along the vortex axis and disrupt the flow upstream. He also developed a swirl ratio parameter which could be used to determine when a steady disturbance solution could exist. He assumed that a steady solution which yielded standing waves represented vortex breakdown.

T. B. Benjamin[4] arrived at the same criticality condition as Squire, but his analysis was based upon defining the conditions under which a vortex flow could no longer support standing (disturbance) waves. Benjamin noted that experiments have shown that the

breakdown phenomenon moves upstream, but pointed out that the group velocity of Squire's standing waves was directed downstream. This meant that the waves could not spread upstream (i.e. the perturbation velocity is less than the axial velocity). He constructed a complete analogy of axisymmetric finite transitions between conjugate (subcritical and supercritical) flow states in rotating fluids, and hydraulic jumps in open channel flow. His analytical criteria for breakdown was the same as Squire's, but his interpretation of the phenomena responsible for breakdown was quite different.

Leibovich[5] stated that in many flows, fluid particles execute helical motions on cylindrical, or nearly cylindrical surfaces. These flows were called "quasi-cylindrical", and when the ratio of the axial velocity to the greatest azimuthal velocity fell below a certain value (which depends upon the details of both velocity profiles, but is typically near unity) the quasi-cylindrical flow "breaks down" and is no longer likely to occur. He also noted that this breakdown involves a marked deceleration of the through flow, and is usually accompanied by the development of a stagnation point on the rotation axis, followed by axial backflows. For both internal (pipe) flows and external (wing) flows, breakdown seemed to occur in two distinct modes; one in which the disturbed flow appeared to be axially symmetric (bubble), and the other in which the disturbances assumed a spiral form.[6]

Sarpkaya[7,8] has reported on experiments in swirling flows in a diverging cylindrical tube which produced various types of vortex breakdowns. Using dye and turning vanes, he found that there were three basic types of stationary vortex breakdown. Stationary, in this context, meant that the flow rate was maintained constant while adjusting turning vanes to

desired values, or the vane settings were maintained constant while varying the flow rate. The mean breakdown location was obtained qualitatively for these cases. The three basic types of breakdown; double helix, spiral, and axisymmetric, were studied for various flow situations. The type and shape of breakdown depended upon the Reynolds and circulation numbers. He also conducted a set of experiments using small changes (oscillating one of the vanes, releasing a small air bubble, changing flow rates, changing dye injection rates) imposed on the upstream swirling flow. These disturbances affected the location of the breakdown. Another set imposed small changes on the downstream flow conditions. When the flow was decelerated (constricting an exit hole) the breakdown moved upstream. When the downstream flow was accelerated, the breakdown moved downstream. This effect of local adverse pressure gradients has the same effect on breakdown position as a change in circulation or mean flow and appears to be consistent with the subcritical-supercritical states discussed by Benjamin[4].

Leibovich[6] also contended that vortex stability and vortex breakdown were not necessarily the same effects, because flow criticality (e.g. hydraulic jump) and flow instability (e.g. boundary layer transition) are not the same phenomena. He pointed out that a vortex can be unstable without breakdown, and that it appears that axial flow reversals can be created in swirling flows without any sign of hydrodynamic instability. He noted that flows downstream of a breakdown contain fluctuations that are not axially symmetric regardless of the upstream axial symmetry. Leibovich contended that the expansion of the vortex core in the wake of a breakdown was due to the mixing associated with the instabilities and

turbulence. Supporting the importance of instabilities with respect to vortex flow, he concluded that even if instabilities were not responsible for the breakdown, they play an essential role in shaping the global structure of the flow and in determining the aerodynamic effects of breakdown. This points out the difficulty in determining the actual effects of an experimental perturbation on the flow.

Batchelor[9] studied the axial flow in laminar trailing line vortices (developed from one side of a wing) and other types of line vortices. He noted that strong axial currents occur near the axis of symmetry. Looking at flow fields in which axial gradients were small compared with radial gradients, he found that the pressure in the vortex core increased if the core diameter increased with distance downstream. Similarly, if the core diameter decreased as the core moved downstream, there was a decrease in pressure associated with axial acceleration. This is in contrast to the boundary layer situation in which the pressure variation across the layer is negligible and has no effect on the boundary layer. Analyzing the vortex roll-up process and treating the trailing vortex far downstream as axisymmetric, he developed a similarity solution for the flow in a trailing vortex far downstream. Far downstream the difference between the axial velocity of the vortex and the free stream velocity is small. The azimuthal motion is also slowed due to viscosity, which leads to a positive axial pressure gradient and consequently to a loss of axial momentum.

Lessen, Singh, and Paillet[10] studied the inviscid stability of swirling flows, with mean velocity profiles similar to those developed by Batchelor, to model a trailing vortex behind an aircraft. This was accomplished by superimposing a swirling flow on an axisymmetric wake.

They only studied non-axisymmetric disturbances since Howard and Gupta[2] found that axisymmetric disturbances were purely stabilizing when introduced into a stable swirl. The asymmetric disturbances were velocity and pressure perturbations in the form of $\exp(i(\alpha x + n\phi - \alpha c t))$, where α and n are axial and azimuthal wavenumbers, $c = c_r + ic_i$ is the complex phase velocity, and ϕ is the azimuthal coordinate. The interesting point is that these disturbances are completely stable for a non-swirling wake. However, when a swirling flow is superimposed on the axisymmetric wake, vortex destabilization was found to exist. They defined a swirl parameter, q, as the ratio of the magnitude of the maximum swirl velocity to the maximum axial velocity. When the inviscid swirling flows and mean velocity profiles were perturbed by these infinitesimal non-axisymmetric disturbances they found distinctions between the positive and negative azimuthal wavenumbers. They found that as the swirl increased continuously from zero, the disturbances decay quickly for small values of q, if $n = +1$. However, for negative modes $(-n)$ the disturbance amplification rate increases initially as q was increased, up to $q = 0.83$ and then decreased with additional swirl. Even greater instability was found for the $n \leq -2$ modes, which were known to be completely stable in the absence of swirl. They found that the maximum growth rate for each negative azimuthal mode appears to increase continuously with n as q approached 0.83. They also noted that all modes exhibited complete stabilization when the swirl was increased to give values of q greater than 1.5.

Khorrami, Malik, and Ash[11] examined the laminar stability of several types of vortex flows, identifying various types of perturbation waves which should grow exponentially on

certain types of axial vortices. Based upon the conclusions of Howard and Gupta[2] that there are no general necessary and sufficient conditions for the stability of vortex flows, they approached the problem considering a separate stability analysis for each type of vortex flow. They developed an algorithm for spatial and temporal stability calculations. Using a quasi-parallel flow they input disturbances of the form used by Lessen, Singh, and Paillet[10] $\exp(i(\alpha z + n\theta - \omega t))$, where $\omega = \alpha c$. It should be noted that if n is zero, axisymmetric disturbances exist. When n is positive or negative, asymmetric disturbances occur in the direction given by the sign of n/ω. If the temporal frequency, ω, is real, then spatial stability only is considered. If the wavenumber, α, is real, then a temporal stability solution is considered. The sign of the imaginary part determines whether the disturbance is growing or decaying. They studied various flow situations including the temporal stability of a trailing line (Bachelor) vortex. They found trends similar to those found by Lessen, Singh, and Paillet,[10] but they found an instability mode not observed previously. The disturbance growth rates also were shifted to lower values of the swirl parameter, q, with larger maximum growth rates over a smaller range of q.

Khorrami[12] has found subsequently that axisymmetric, viscous instabilities can exist in a trailing line vortex which have wavelengths that scale well with features observed in certain types of aircraft condensation trails. However, the dominant majority of instabilities predicted for unconfined trailing line vortices are helical wave instabilities which depend upon the direction of the helix[2,8,10]. It is apparent that theory predicts vortex instabilities or amplification of certain disturbances for a variety of flow conditions. If appropriate

disturbances can be introduced into a steady, vortex flow field, they should be amplified. If these disturbances do in fact cause vortex breakdown or other types of instabilities, a vortex modification technique exists which requires minimal amounts of energy.

1.2 Experimental Challenges

A major challenge for the experimentalist is to try and introduce controlled perturbations into a flow field and determine subsequently their effects on vortex stability and/or breakdown. Experiments on vortex stability are difficult to perform because of the absence of an attached surface and due to the inviscid character of the outer part of the vortex flow. It is difficult either to produce a controlled disturbance or to probe the resulting flow. Hence, few experiments have been conducted which address the stability of trailing line vortices. Thus the type of helical disturbances which destabilize a vortex have not been identified experimentally.

One particular type of disturbance is that of sinusoidal fluctuations. Mathematical models have been developed to study the amplification of small sinusoidal velocity oscillations away from a steady, laminar flow and are used in the development of linear vortex stability theories. By analogy, the Orr-Sommerfeld equations were developed for boundary layer stability theory and predicted that certain types of sinusoidal fluctuations would grow. However, even though the theory was developed in the early 1900's, no experimental evidence supported those predictions for over thirty years. In 1943, Schubauer and Skramstad[13] were able to use a very low turbulence level wind tunnel, developed by H. L. Dryden, to study

the phenomenon of transition from laminar to turbulent boundary layer flow. Their measurements showed that sinusoidal velocity fluctuations were amplified. They showed also that amplified, damped and neutral oscillations occurred simultaneously. Hence the frequency of the oscillations played a role in the life of the oscillation. It was determined that previous experiments to support velocity fluctuation amplification had been unsuccessful due primarily to high background turbulence levels which saturated the linear instability growth region. The turbulent saturation masked the initial amplification process. Schubauer and Skramstad produced artificially controlled, two-dimensional, sinusoidal velocity oscillations using a thin vibrating metal ribbon stretched across a laminar, flat-plate boundary layer. The vibrating metal ribbon was driven by a magnetic field to produce the oscillations. Their experiments confirmed the evolution and growth of two-dimensional Tollmien-Schlichting waves[14,15] which had been predicted more than a decade earlier.

Singh and Uberoi[16] conducted an experimental wind tunnel study of laminar instabilities in an isolated trailing vortex. They used background wind tunnel turbulence as the perturbation source to generate laminar instability modes. Those instabilities were not controlled, but were random in nature. Measurements of the instabilities showed them to have both symmetric and helical modes with wavelengths on the order of the core diameter. They showed that near the wing tip the vortex core velocity profile had an axial jet. Downstream of the wing the axial jet dissipated rapidly and a velocity-defect wake developed subsequently in the core, while the intensity of turbulent velocity fluctuations decreased. From 13 to 40 chord lengths behind the airfoil vortex generator, periodic oscillations

dominated the velocity fluctuations, with little accompanying background turbulence. They found that in the 13 to 40 chord range of distances along the vortex core the maximum axial, swirl, and fluctuating vortex core velocities varied slowly. Then at 40 chord lengths behind the wing there was a rapid change in the vortex velocities, accompanied by changes in the velocity fluctuations from periodic to turbulent. The core showed spatial excursions. These effects suggest that a vortex breakdown or instability was occurring, but they did not observe violent vortex breakdown directly. However, their perturbations were not controlled and they did not pursue the details of the flow structure near 40 chords. The fact that the instabilities are not controlled points out a need for a device to generate controlled instabilities for vortex stability studies.

1.3 Airfoil Vortex Generator

A trailing line vortex generator has been designed by D. J. Stead[17] which produces a single vortex along the nominal axis of a closed circuit, low-speed wind tunnel. The generator was used in a study of the influence of free-stream turbulence on the generated vortex. A companion effort was initiated during those experiments with the goal of building a device which could inject helical perturbations into the core region of a trailing line vortex. The advantage of this device was the ability to introduce controlled perturbations into the vortex. If the type of perturbation (frequency, direction, and magnitude) are known, stability analysis could be attempted to determine the types of helical disturbances required to cause the vortex to become unstable or breakdown. The development of a device to introduce velocity

perturbations into a vortex flow field and the evaluation of the perturbation signals in the flow is the subject of this thesis.

Since a trailing line vortex only emanates from solid boundaries, it is formed from a complex set of vortical flows emanating from the generating surface(s). This formation occurs at some distance behind the solid boundaries and can include vortex sheet roll-up as well as the amalgamation of more than one axial vortex. In the present case, using a matched pair of airfoils with equal but opposite angles of attack, attached to a centerbody in a wind tunnel, the trailing vortex results primarily from two pairs of inboard juncture vortices and their respective airfoil vorticity sheets which are wrapped around the centerbody wake. From that perspective, the ability to introduce a controlled perturbation from the centerbody which can survive the vortex formation process is an entirely different challenge than introducing two-dimensional sinusoidal oscillations into a laminar boundary layer. The perturbation generator was built to introduce velocity perturbations aft of the vortex generator airfoils; hence into the roll-up region of the evolving axial vortex.

The experiments which are reported here have been directed toward documenting the conditions under which a sinusoidal, helical velocity perturbation can be introduced into a wake and the resulting axial vortex stability studies. The preliminary study was necessary to characterize the possible disturbances which can be introduced by a centerbody perturbation generator, in order to enable controlled vortex stability experiments to proceed. The perturbation generator design and experimental facilities will be discussed along with associated hot wire measurements. The goal of these studies was to determine the range of

perturbation frequencies, fluctuation velocity strengths, and helicity or pitch which could be introduced into the vortex. Subsequently, hot-wire measurements at various locations downstream of the vortex were taken to determine if any perturbation effects could be detected. Evidence that the perturbation signal was still present in the vortex at large downstream distances was needed before detailed studies could proceed. When the signal was detected, an attempt to determine its quality and whether there was evidence of amplification or decay of the signal was conducted. The design and evaluation of the perturbation generator, prior to its intended use, has produced some interesting results which may be useful in other studies. Since most of the theoretical stability analyses assume parallel flow (no axial variation) and determine the temporal stability of the vortex, the measurements required to corroborate the theory are complex. The purpose of the measurements reported in this study are to establish the potential of the vortex-perturbation generator system for making research quality stability measurements.

2. PERTURBATION GENERATOR DESIGN :

It was desired to design a model which could introduce a sinusoidal velocity perturbation into a trailing line vortex core. Measurements of the effects of the perturbation generator were to be taken in a wind tunnel. A vortex generator was designed previously by D.J.Stead[17] for use in the NASA 2'x3' Low Speed Boundary Layer Channel Wind Tunnel as part of this research project. Stead was to investigate the influence of free stream turbulence on the mean behavior of a trailing line vortex, and he employed two NACA 0012 airfoils with 10.2 cm chords, each with 43 cm span, which were separated by a 2.54 cm diameter centerbody (Figure 1). Different centerbodies were employed by interchanging nose and tail elements (of different length). The vortex generator model spanned the width of the wind tunnel test section. Thus, each wing generated juncture vortices, which, along with the centerbody wake and airfoil vorticity sheets, rolled up into an axial vortex which trailed behind the centerbody. The two airfoils could be adjusted independently and set at different angles of attack. The vortex generator airfoils and centerbody were supported with a hollow, 7.94 mm (5/16 inch) stainless steel tube. The tube ran from outside one side of the wind tunnel, through the wall, the airfoils, the centerbody, and the opposite wind tunnel wall. The tubing carried electrical leads and the air supply line to the centerbody.

RIGHT AIRFOIL

LEFT AIRFOIL
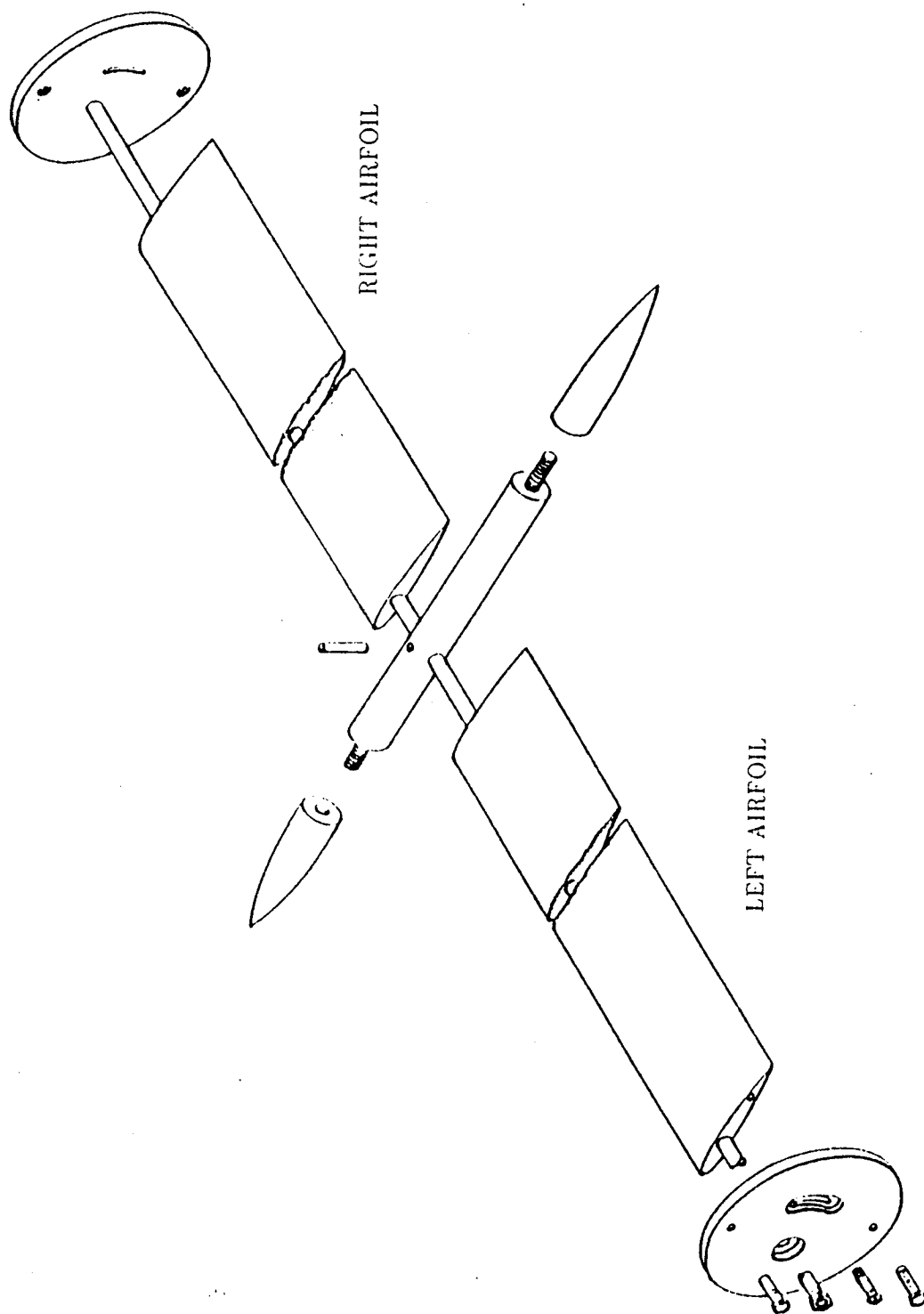
Figure 1. Schematic Breakout of Vortex Generator

The vortex generator model was configured with the right wing (facing upstream) set up 8° ($\alpha = 8°$) from horizontal and the left wing set down 8° ($\alpha = -8°$). Eight degree angles of attack were used to provide strong vortices, but still avoided significant flow separation along the airfoils, which would alter the axial vortex structure. A thin line of grit along the upper forward surface of each airfoil was used to trip the airfoil boundary layers and thus employ turbulence to further reduce airfoil separation. With Stead's vortex generator capability of interchangeable tail sections, it was desired to design a perturbation generator which could attach to the aft end of the existing centerbody model. Since the existing vortex generator diameter was 25.4 mm, it was desirable for the new model to be 25.4 mm in diameter. It was also desired to limit the new model length to approximately 125 mm, ending with a pointed rear tip. The perturbation frequency requirements were unknown initially because of limited data on the vortex swirl velocity field which would be produced by Stead's design, since it had not been operated in the wind tunnel. Estimates of expected swirl velocities suggested that a maximum perturbation frequency requirement of 300 Hz could occur.

A variety of designs were considered. The challenge was to build a cylindrical, 25.4 mm (1 inch) diameter unit which could generate fluctuations at up to 300 Hz. It was decided to develop a model which utilized an internal spinning drum, to open and close air ports. For example, if the drum face had eight openings, then the model would generate eight velocity injection pulses or cycles per drum revolution. The rotating drum concept required an internally mounted motor which could drive the drum at about 50 Hz (3000 RPM) to give 400 velocity injection pulses per second. This design concept was capable of producing an

on/off pulsing velocity fluctuation signal (square wave). Further discussion determined that instead of a pulsating signal at various frequencies, a sinusoidal velocity perturbation was desired. This could be accomplished using a drum with a sloped face (not perpendicular to the axis of rotation, Figure 2a). If the drum or disk face was located beneath a circumferential slot in such a way that the drum face varied from blocking a portion of the slot completely through not blocking the slot at all, a sinusoidal perturbation (Figure 2b.) could be produced when the drum was rotated. Furthermore, by using compound slopes on the drum face, more than one sine wave per revolution could be produced.

The miniature motor requirement for 300 Hz perturbations (18,000 RPM) was not trivial. Furthermore, the circumferential slot width could not be specified arbitrarily. If a large slot were used, the system would act like a dynamic orifice plate, producing a velocity which was controlled only by pressure differences between the air supply and the external stream (a mass flow perturbation, rather than a velocity perturbation). On the other hand, very small gaps can control the injected velocity via viscous forces, causing variations in velocity which are more or less linearly proportional to the slot width, but the strength of the perturbations is diminished significantly. Furthermore, small tolerances in bearings and motor shafts could result in loss of control of the gap width during operation, for very fine gaps.

The first question to be addressed was the slot width. Since orifice plates are not normally circumferential slots, the range of gap widths where flow is controlled only by pressure differences was uncertain. It is noted that for two-dimensional slot flow, the governing relation for an orifice plate is:

VARIABLE GAP

25.4 mm O.D. PIPE

AIR

MOTOR

VARIABLE THICKNESS
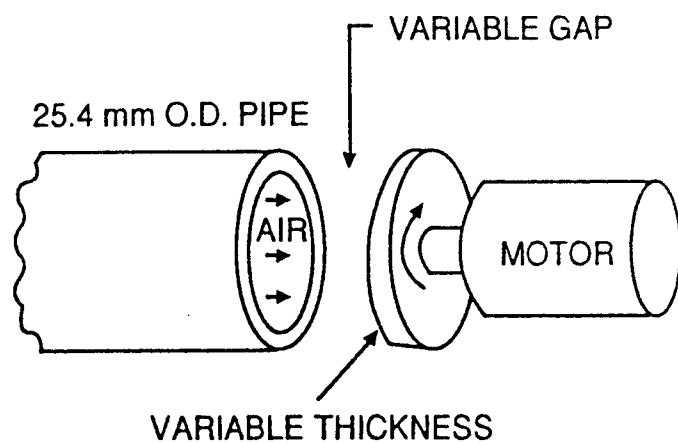
Figure 2a. Rotating drum with a sloped face.

V_{JET}

FULLY
OPEN

FULLY
CLOSED

TIME
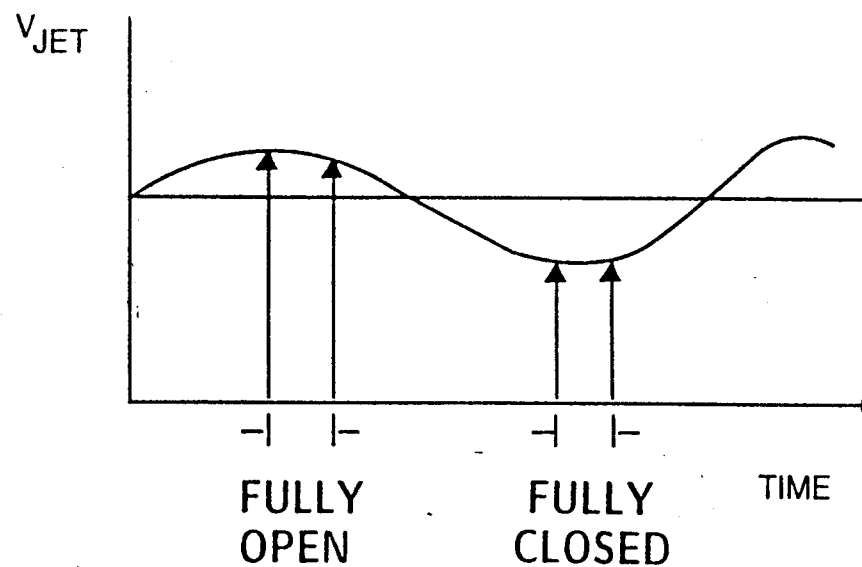
Figure 2b. Sinusoidal velocity perturbation signal.

Figure 2.   Schematic of rotating drum with a sloped face and the resulting sinusoidal velocity perturbation signal

$$h_l = K\frac{V^2}{2} = \frac{\Delta P}{\rho} \tag{1}$$

It can be seen that if K and ρ are constant, the velocity out of the slot depends only on the differential pressure across the slot (ΔP) and the width of the slot has no direct control on the velocity out of the slot. The slot width does have an effect on the volume flow rate (Q) through the slot by the following relationship:

$$Q = (C_d)(\text{Width})(\text{length})(V) \tag{2}$$

where C_d is a coefficient of discharge. There is a minimum slot width for which the orifice plate correlation applies. That (minimum) slot width is the maximum width for which viscous effects are still controlling the injection velocity. In the desired design, the instantaneous slot width must be less than this maximum slot width if instantaneous local perturbation velocity is to be controlled.

It was determined that maximum required pressure differences only on the order of one torr were required. For example, if the differential pressure, ΔP, is 1 torr the velocity of air through an orifice plate is approximately 12.5 meters per second. Since perturbation velocities no higher than 10% of free stream velocity were desired, the maximum perturbation velocities produced by the model should be less than 4 meters per second for a 40 m/s free stream velocity. This assessment made model design significantly easier since the problem of routing a large mass flow of air through the vortex generator airfoils, and then through the inside of the centerbody was eliminated. Because of the small perturbation flowrate, injecting helium through the model for flow visualization purposes also became a possibility.

Testing to determine the useful range of slot widths was required. Initially, a box-shaped, plenum chamber was built which used movable metal strips to produce different slots. That design was not very successful because of difficulties in controlling two-dimensionality of the slot. Furthermore, the question of how a circular slot behaved was not addressed. A "slot width" test rig was built which consisted of a 25.4 mm OD (22.2 mm ID) brass pipe, 102 mm in length, one end of which was connected to an air line. The pipe was fitted with a pressure tap, which was located near its open end. The pipe unit was mounted to a plexiglass base plate. A sliding vernier (Figure 3) was also mounted to the base plate. The vernier was fitted with a block assembly which supported a protruding washer (25.4 mm diameter) aligned with the pipe axis. Using the vernier, the washer could be moved against the open end of the pipe to establish a reference position (zero slot width). It could then be adjusted in controlled increments to open a circular slot. Slot width was measurable to a resolution of one micron ($\pm$ 0.5 μm). A hyperdermic needle sized pitot tube was mounted perpendicular to the slot to measure the velocity distribution of the air coming out of the slot. The pitot tube could survey across the width of the slot to determine the maximum velocity. During these tests the pressure inside the pipe was kept constant as the slot width was varied. The variation of velocity with slot width at constant pressure could then be plotted to determine the limits of viscous velocity control. That is, since the measured maximum velocity approaches the pressure controlled, orifice plate limit with increasing width, the velocity-slot width curve asymptotes to the orifice plate limit. The results of the pipe tests are presented in Appendix A. It was determined that over the expected pressure range, the maximum allowable slot

PIPE SUPPORT →

PIPE PRESSURE TAP

MOUNTING PLATE TO MOUNT
FIXED DISK OR MOTOR WITH
ROTATING DISK

25.4 mm O.D. PIPE

BASE
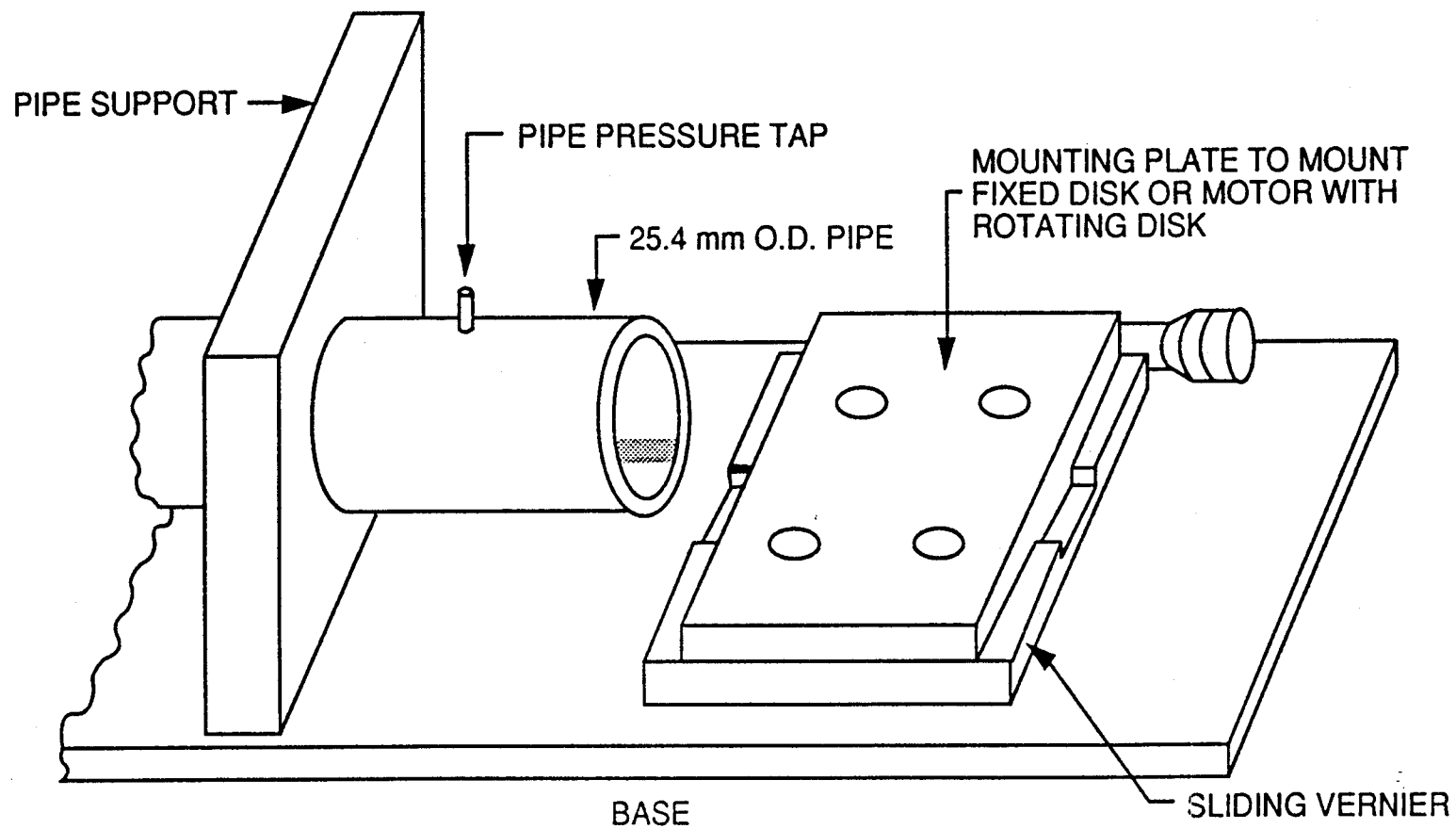
SLIDING VERNIER

Figure 3. Schematic of the Variable Gap Test Rig with sliding vernier for mounting test assemblies.

width for the model was 0.2 mm. Although the anticipated pressures were small, the tolerances for the slot width were obviously very small.

The pipe tests also verified the contention that the velocity varied approximately linearly with gap width over a range of gaps. A disk with a slanted face, cut on an angle with respect to the disk axis, and with a thickness change of 0.2 mm across the disk face was thus selected for the subsequent dynamic tests (Figure 4). Since 0.2 mm was the upper limit on gap width, the drum thickness, a, varied with drum orientation according to:

$$a = a_o + \frac{\Delta a}{2} \cos \theta \qquad (3)$$

where a_o is the average drum thickness (5.18 mm), (Δa) is the total variation in drum thickness, and θ is the shaft angular position, with $\theta = 0$ at the location of maximum drum thickness.

The next design problem was selection of an appropriate electric motor to power the rotating drum. Internally and externally mounted motors were considered. A motor could be mounted on the outside of the wind tunnel to drive the drum shaft via a gearbox in the middle of the model. The gearbox output could drive the drum shaft, connected to the aft end of the model. An advantage of this design was its ability to use any size motor as well as the ability to monitor the shaft speed of the motor outside of the tunnel. The disadvantage of this design was finding a gearbox and drive train which could fit inside a one-inch diameter model. No gearbox could be found which met the design requirements.

Definition of a small motor which could be mounted inside the model was developed in consultation with Dr. Leonard Weinstein of NASA Langley Research Center. A small DC

5.08 mm

TAPERED FACE

25.4 mm

5.28 mm

SIDE VIEW

SCALE: 2 TO 1

3.2 mm DIA

FRONT VIEW
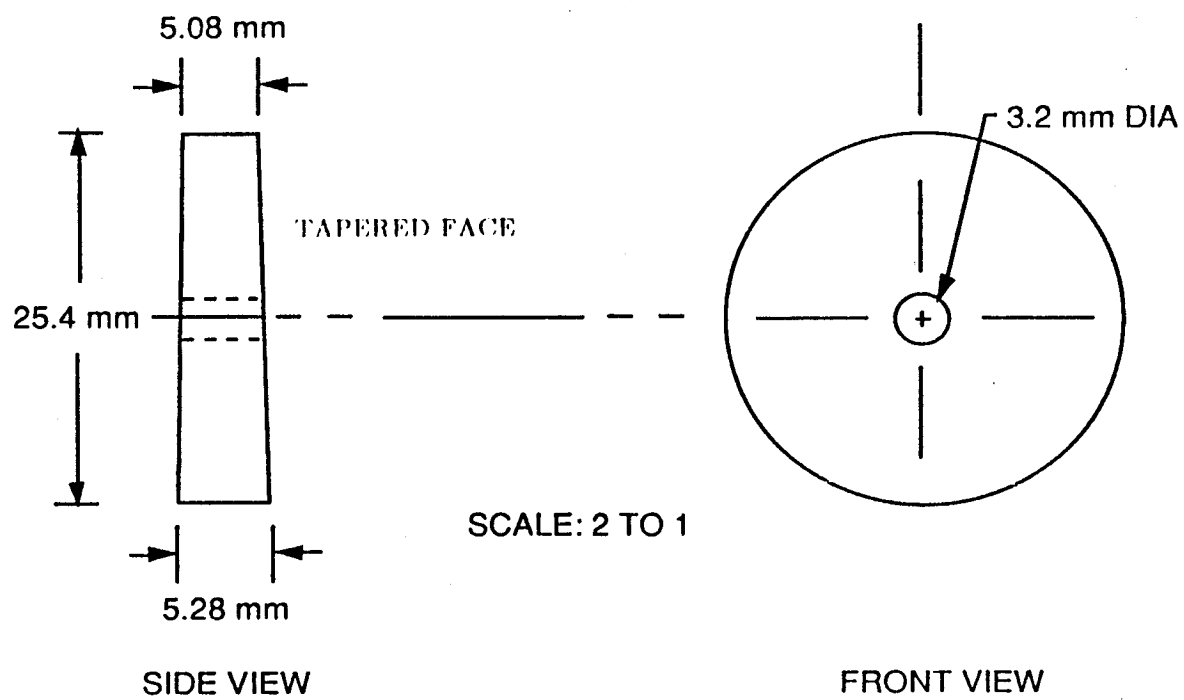
Figure 4. Diagram of the disk with a 0.2 mm change across the face.

motor, manufactured by Micro Mo Electronics Inc. (Series 2338) was identified as meeting the design requirements most closely. The motor could operate at shaft speeds up to 18,000 RPM (300 Hz) and was capable of both clockwise and counterclockwise operation.

The outside diameter of the motor was 22.0 mm. Because of the need to mount the rotating shaft behind the motor, air passages were required to traverse from the air supply tubing, around the motor, and to the rotating disk. The flow of air over the motor was considered to be desirable for motor cooling. Since a 7.938 mm ($\frac{5}{16}$ inch) diameter tube was selected to port air into the model, it was desired to maintain a similar flow cross-sectional area around the motor to facilitate smooth air flow. The area of the inside tube opening was determined to be 49.5 mm^2. A plenum chamber was required ahead of the rotating disk to allow the air to be metered through the slot and enable uniform flow around the slot circumference. Hence the internal geometry of the model had to allow passages for air to flow uniformly around the motor and then recombine in a plenum chamber prior to escaping through the slot--with minimum pressure drop. Adding the air passage requirement to the motor cross section resulted in an estimated inside bore diameter of 23.4 mm. The remaining metal thickness (1 mm) in a 25.4 mm diameter tube was considered insufficient for either manufacturing tolerances or for the model structural integrity. Hence, it was deemed necessary to relax the constraint on the outside model diameter. An outside model diameter of 30.5 mm was selected as a good compromise between structural requirements and minimum vortex core modifications. The minimum housing thickness was thus increased to 3.5 mm and an adapter ramp between 12.7 and 15.2 mm radii, over a 25.4 mm length (slope

of 0.1) was incorporated into the forward portion of the perturbation generator design. The ramp provided a smooth transition from the rear end of Stead's vortex generator centerbody (25.4 mm) to the motor housing (30.5 mm).

The problem of determining the motor speed and hence the rotational speed of the disk during operation inside the highly confined metal chamber presented a challenge. A novel method for measuring motor speed utilized a spectrum analyzer and 1 Ω resistors which were added to each motor lead, between the motor and the regulated DC power source. Speed was measured externally, prior to final installation, by driving a teflon disk, with the DC motor. The disk had identification marks on it to facilitate the use of a strobelight for measuring motor speed. Simultaneously an oscilloscope was connected to the motor leads between the resistors and the motor. It was determined that the motor brush contacts produced a voltage spike each time their connections with the armature were interrupted. The spikes were observed on the oscilloscope for each brush interruption. A sample voltage history for the motor turning at 5280 RPM (97 Hz) is shown in Figure 5. Using the known motor speed, the number of brush spikes were counted during each rotation cycle. It was determined that there were ten voltage spikes per motor rotation. Hence, the voltage spikes associated with brush contact could be counted to determine the motor speed. Disk rotational speed was measured finally using a Data Precision, Data 6000 Waveform Analyzer to measure the frequency spectrum of the motor voltage signal. Due to the number of voltage spikes per revolution the spectral frequency peak measured with the Data 6000 is exactly ten times higher than the disk (motor) speed, and is thus a very accurate (0.1 Hz) measurement of the
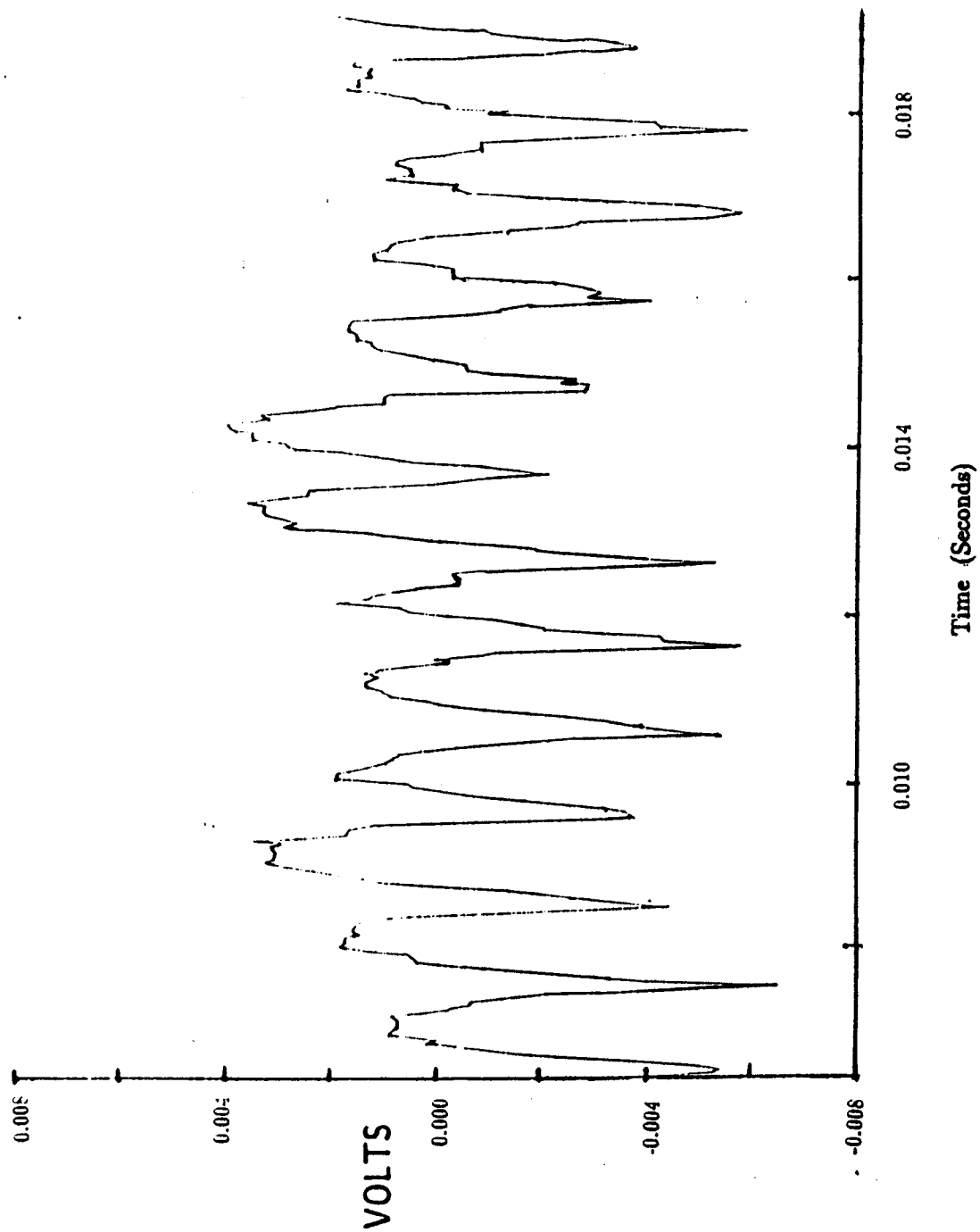
Figure 5. Typical voltage signal on the motor leads.

motor speed. All motor speed measurements using the Data 6000 Waveform Analyzer were converted to actual motor frequency and reported as such. Examples of frequency spectra for 78.1 Hz (4680 RPM) and 50.3 Hz (3018 RPM) are shown in Figures 6 and 7.

Concerns were raised concerning the ability of the motor to tolerate the dynamic imbalance of the disk as well as overcome the loads produced by the air flow and pressure forces. Tests were run outside of the model using the one-inch pipe apparatus (25.4 mm) and an external rotating disk mounted to the test platform in Figure 3 to verify the dynamic flow characteristics. The preliminary tests could thus ensure that the motor had the power to spin the aluminum disk while the expected pressure forces were exerted on it, prior to construction of the final unit. It was noted that another benefit of the minimal 0.2 mm, required variation in disk (drum) thickness, coupled with the use of aluminum resulted in a unit that did not require dynamic balancing of the disk. The motor ran well under all conditions tested. Results from these preliminary tests and the subsequent design decisions were used as the basis for the final model body design.

The model design is shown in Figure 8 with details in Figures 9 through 12. For the sake of explaining model design, the figures have omitted machining details. The model consists of four parts. The motor housing is the first piece (Figure 9). It is 73.6 mm long and has internal threading (12 UNF and 13 UNC) at each end. The forward end adapts to the aft end of the pre-existing vortex generator model and is bored out to accommodate air, electrical leads, and pressure sensing lines. The aft portion houses the motor, which is held in place with six set screws, and forms the air plenum chamber, when assembled with the housing.
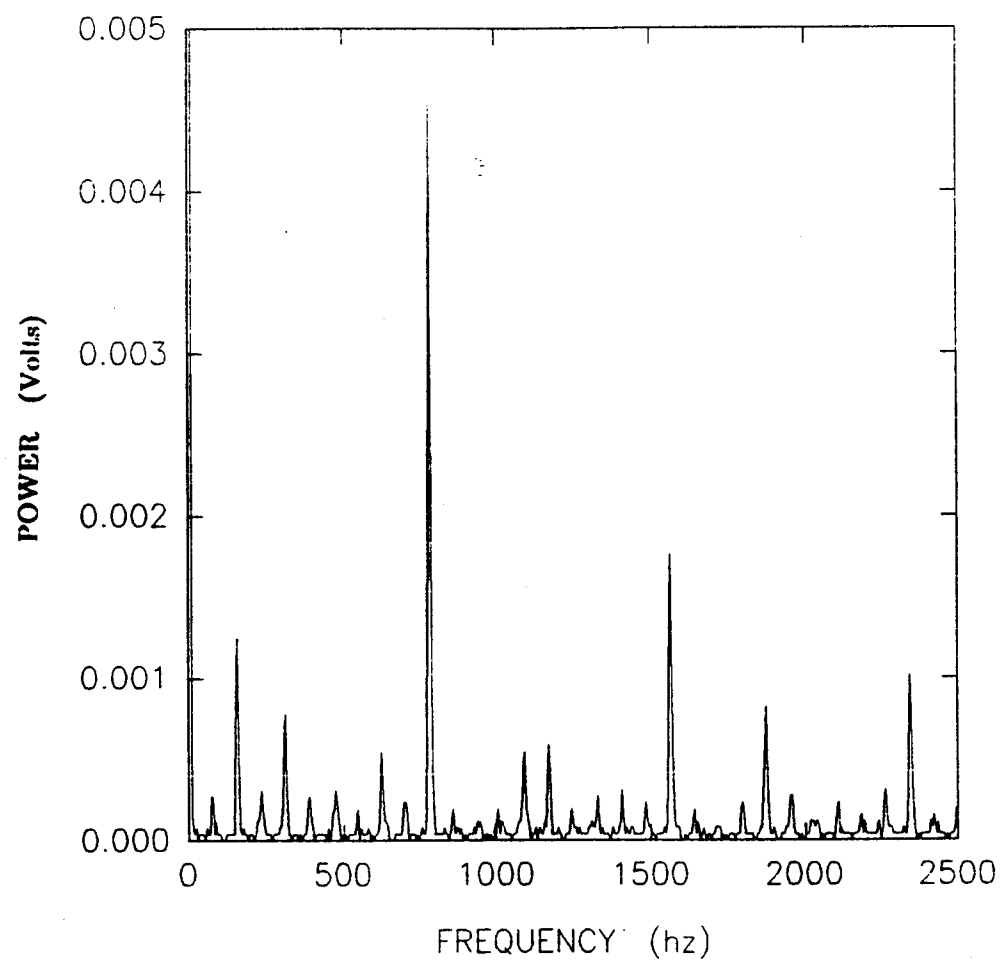
Figure 6. Frequency spectrum of motor voltage, showing peak at 781 Hz. Motor frequency = 78.1 Hz (4680 RPM).
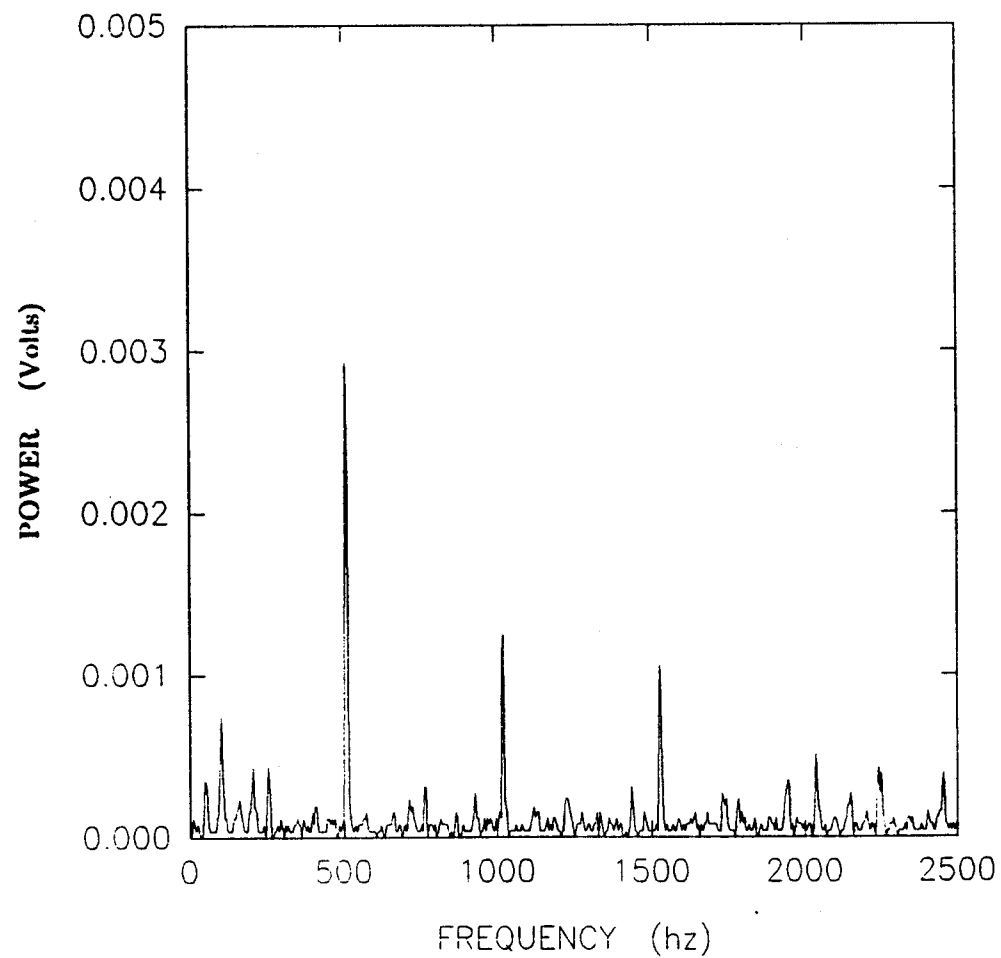
Figure 7. Frequency spectrum of motor voltage, showing peak at 503 Hz. Motor frequency = 50.3 Hz (3018 RPM).

ROTATING DISK WITH CONTOUR FACE

MOTOR
SET SCREWS

MOTOR HOUSING   FORWARD   AFTER
                      BEARING   BEARING
                      ASSEMBLY ASSEMBLY

PERTURBATION ASSEMBLY
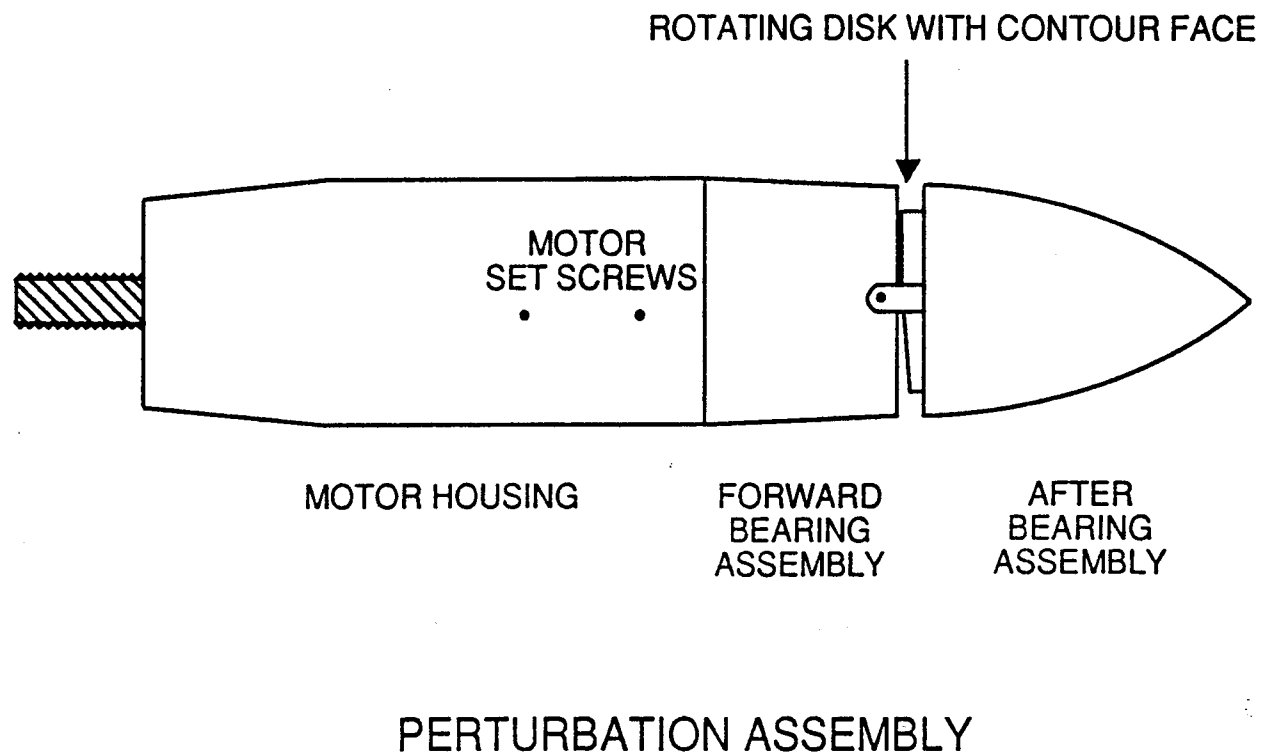
Figure 8. Schematic of the Perturbation Generator Assembly.
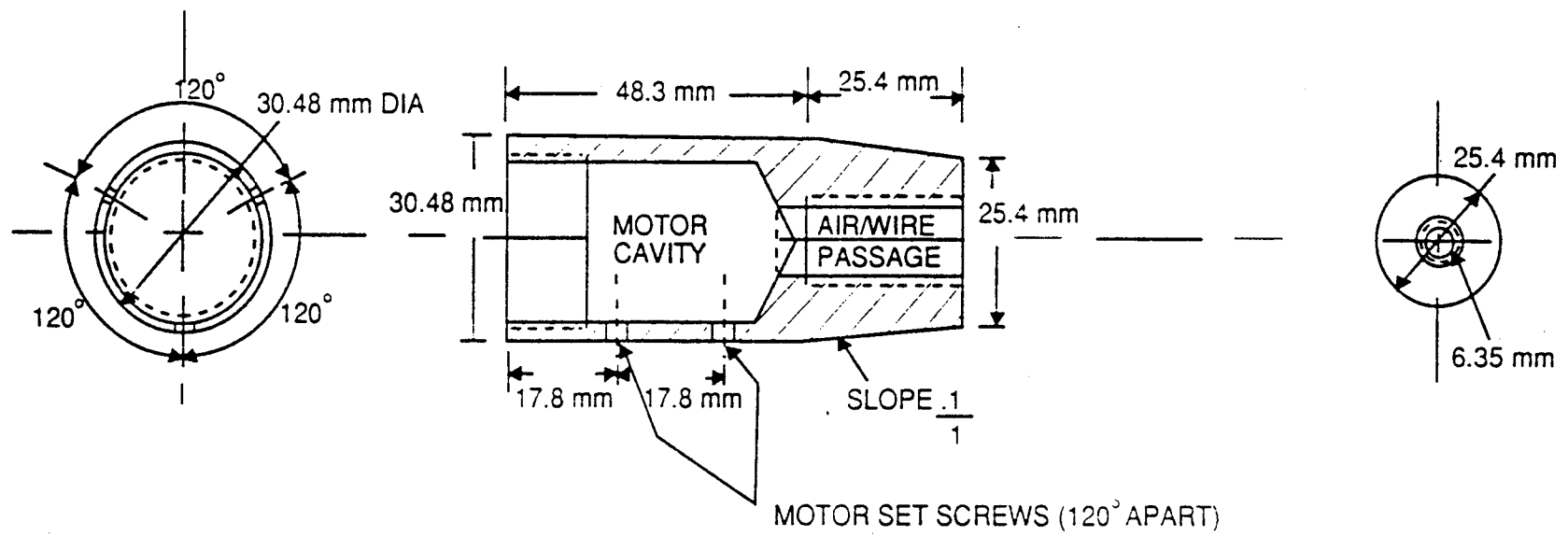
MOTOR HOUSING

Figure 9. Schematic of the Motor Housing Assembly.

The motor was modified slightly. The integrated drive reduction gear assembly was removed and the plastic collar used to attach the drive gear to the motor was filed down. The reduction gear was not needed and filing allowed air to flow around the motor and into the air plenum chamber. As mentioned previously, the air flow around the motor prevented electrical heating problems.

The third element is the forward bearing housing (Figure 10). It has external threads which screw into the motor housing. The internals are bored out to complete the formation of the air plenum chamber (with the forward disk bearing fitted into the back of the unit). Eight 3.2 mm (1/8 inch) diameter holes were drilled around the bearing fitting to allow air to pass over the bearing to the disk. The flat surface on the end of the housing acts as one surface of the circumferential slot. By design, the clearance between this aft surface and the rotating disk varies continuously between approximately 0.0 and 0.2 mm during each revolution, thereby providing the valving for the sinusoidal velocity perturbation. There are three keyways cut in the external skin of the forward bearing housing. The after bearing housing is attached to the forward bearing housing via these keyways.

The final element is the after bearing housing. It attaches to the forward bearing housing with three keyway support ribs (Figure 11). The velocity perturbations developed between the rotating disk face and the aft surface of the forward bearing housing exit the open slot around the model circumference into the flowfield. The after bearing is also housed inside. The bearings keep the disk positioned accurately inside the model, which was extremely important considering the clearances involved.

10.2 mm

30.5 mm

BEARING

EIGHT 3.2 mm HOLES
FOR AIR PASSAGE
AROUND BEARING

28.6 mm

AIR PRESSURE
PLENUM

3 KEYWAYS TO
ATTACH AFTER
BEARING ASSEMBLY
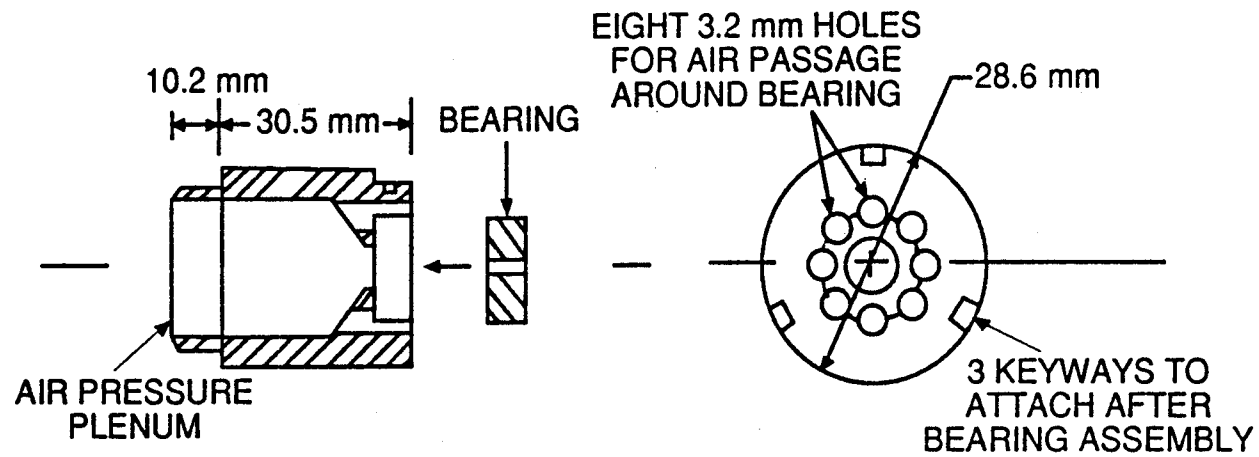
FORWARD BEARING ASSEMBLY

Figure 10. Schematic of the Forward Bearing Assembly.

25.8 mm

|◄— 43.2 mm —►|

DISK CAVITY

14.3 mm DIA.
BEARING CAVITY

AFTER BEARING

KEYWAY SUPPORTS TO
ATTACH AFTER BEARING
ASSEMBLY TO FORWARD
BEARING ASSEMBLY
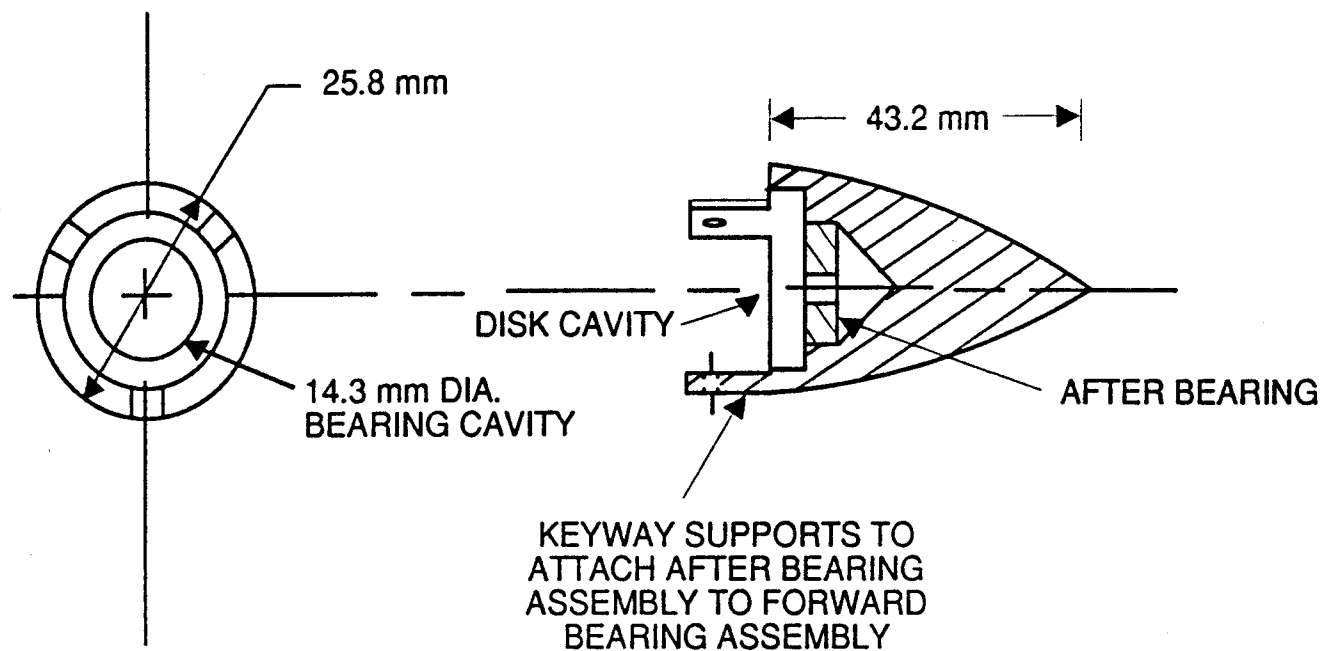
SCALE 1:1

AFTER BEARING ASSEMBLY

Figure 11. Schematic of the After Bearing Assembly.

The rotating disk valve incorporates a forward and aft axis. The disk face was cut on a slant, varying by 0.2 mm over the face (Figure 12). The forward axle mates with the motor using a small piece of tygon tube as a flexible coupling. There is a small machining hole on the end of the axle which accomodates a nipple on the end of the motor shaft for positioning. The forward axle fits through the forward bearing. The aft axle fits into the aft bearing. A small washer is used between the aft bearing and the aft face of the disk to maintain the disk position, controlling the maximum gap width at 0.2 mm. A small washer was fit between the forward disk face and the forward bearing to keep the disk from contacting the surface of the forward bearing housing. Contact between the disk and housing would restrict rotation speeds and reduce control, as well as accelerate wear.

After manufacturing, the perturbation generator model was subjected to bench tests to evaluate the quality of the resulting sinusoidal signal. Improvements were made in the model assembly, which included installing a plenum pressure sensor, ataching the air supply, and integrating the electrical leads during the evaluation testing. Initial velocity fluctuation testing was accomplished using an IFA 100 hot-wire anemometer system, with output sent to a Data Precision Data 6000 Waveform Analyzer and an HP 4328 Plotter. Preliminary tests showed that a cyclic velocity signal was produced by the model (Figure 13) over a range of frequencies and supply pressures. The initial signal, measured on an oscilloscope, was much better defined than the one shown in Figure 13, but a permanent record was not obtained. It is believed that signal degradation was due to longitudinal slippage of the rotating disk inside the perturbation generator. This slippage caused the gap width formed by the disk and the

LINEAR CONTOURED FACE SLOPE $\dfrac{.02}{.8}$

20.6 mm

FORWARD

3.175 mm

5.08 mm

6.5 mm

FLAT

30.5 mm

5.28 mm

6.35 mm

SCALE 1:1
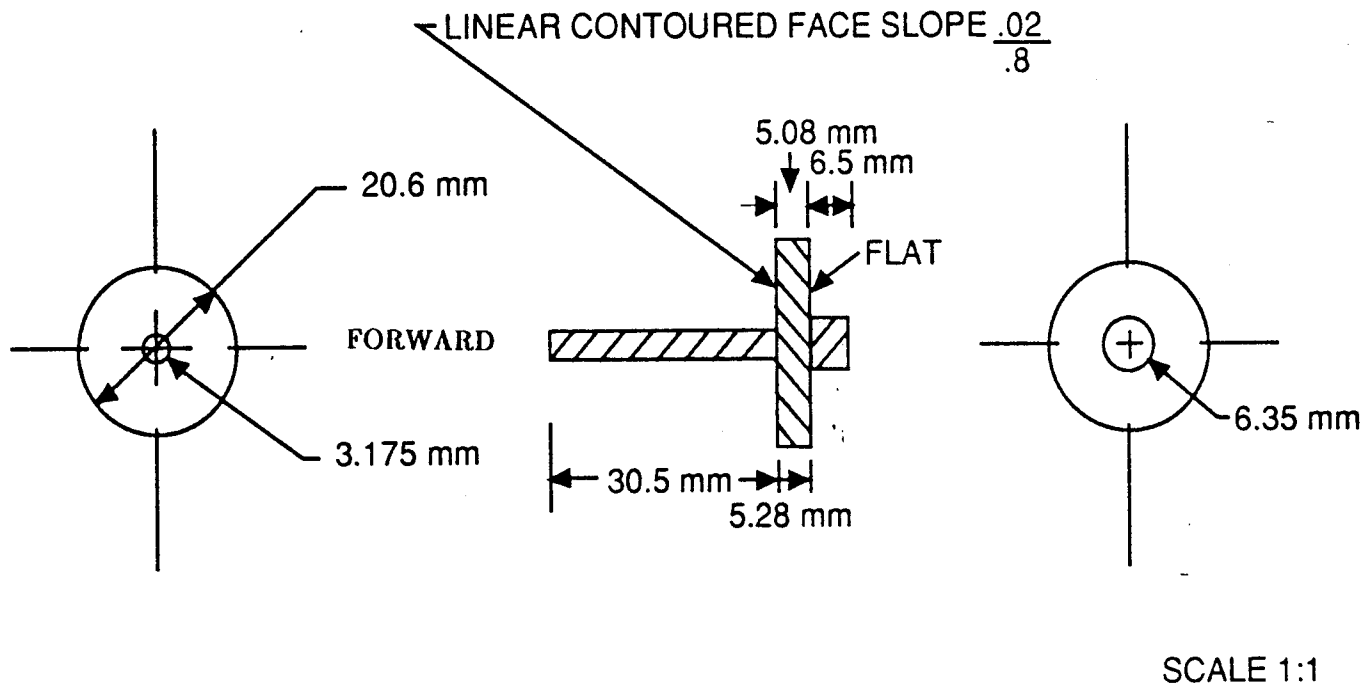
ROTATING DISK VALVE

Figure 12. Schematic of the Rotating Disk Valve.

and motor frequency of 100 Hz.

Figure 13. Typical preliminary time varying component of hot-wire velocity history with no cross flow

13b. Frequency spectrum corresponding to the outlet velocity trace.

Frequency

13a. Voltage trace corresponding to varying outlet velocity.

Time (Seconds)

forward bearing housing to increase. It was determined that washers had to be inserted on the shaft of the rotating disk in order to prevent longitudinal slippage. Figure 14 shows the velocity trace after the washers were added to the shaft.
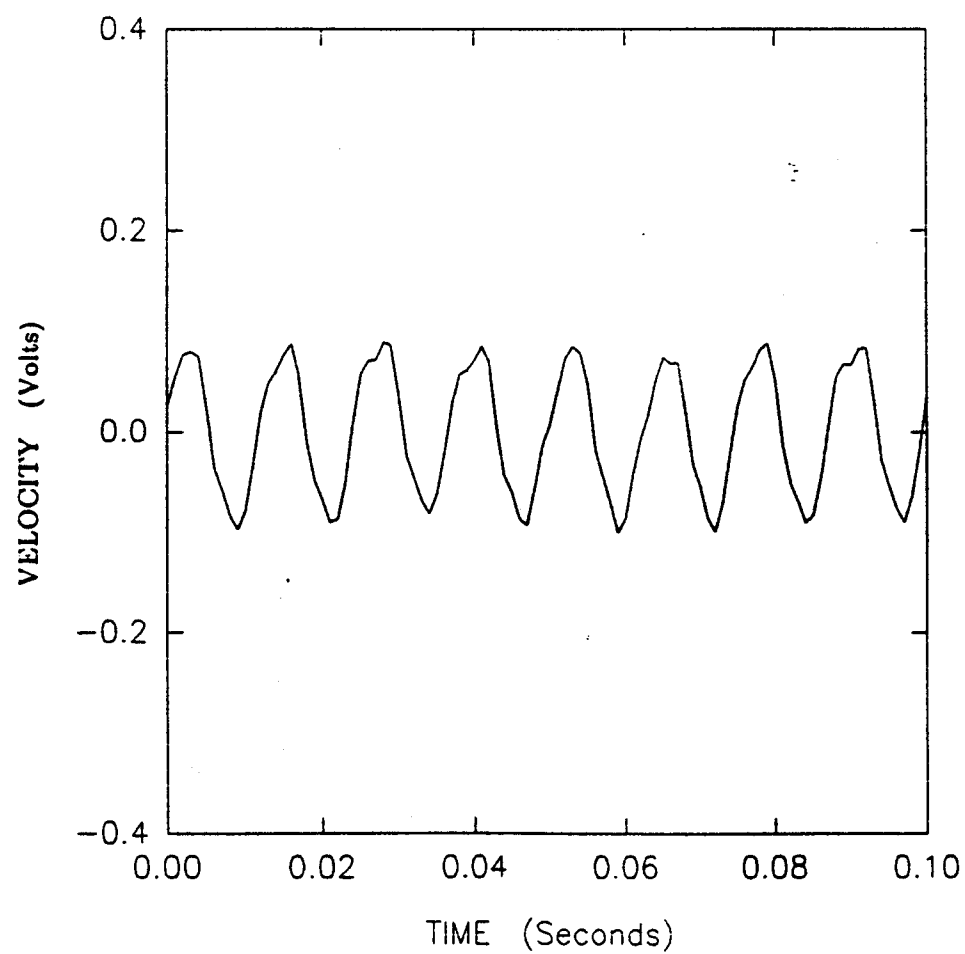
Figure 14. Time varying component of linearized hot-wire velocity history after adjustments to the Perturbation Generator. Motor frequency = 79 Hz, Δ P = 14.8 Pa.

3.   4-INCH PIPE FACILITY

3.1 4-Inch Pipe Experimental Setup:

Organized vortex shedding could influence the character of the controlled perturbations behind the centerbody. By analogy, the essentially two-dimensional Karman vortex street is a form of vortex shedding which influences the design of such diverse elements as smoke stacks, telephone lines, and suspension bridges. From a basic fluid mechanical standpoint, it is important to know when organized flow structures occur in natural flows because they often influence other fluid flow phenomena profoundly. Vortex shedding from an axisymmetric body has not been studied extensively due to difficulties in designing experiments and to what has been assumed to be their minor impact on axisymmetric wakes. However, in order to validate the perturbation generator developed in this study, it has been necessary to look more closely at wake flow characteristics to isolate perturbation generated periodic structures from possible natural fluctuation sources.

Since both torroidal and helical periodic structures may be possible and since a variety of scales or combinations of scales exist in the natural flow, it was necessary to study the frequency spectrum of the velocity field behind the axisymmetric body over a range of flow conditions. In order to study the velocity field behind the model and develop proficiency in hot wire-anemometry and data gathering techniques, the perturbation generator was tested in

a 4-inch diameter pipe tunnel.[18] The pipe tunnel was available on a regular basis, unlike the 2'x3' Boundary Layer Tunnel. While it was not possible to produce an axial vortex in the 4-inch pipe, the ability to make hands on adjustments to the perturbation generator, while developing hot-wire measurement and flow visualization techniques, was an important attribute.

The 4-inch (10.16 cm) ID pipe was constructed from five ft. (1.524 meters) sections of plexiglass connected together as described by Bandyopadhyay and Weinstein[18]. Four sections were assembled into a pipe unit with an overall length of 20 feet (6.1 meters). A screen was mounted over the entrance to the pipe for turbulence reduction. A traverse whose position control was accomplished by a digitally controlled Probe Positioning System (PPS), was used to control the vertical position of the hot-wire probe. One external PPS control unit controlled probe movements in the vertical direction inside the pipe. That control unit could be controlled manually or from inputs from an Intelligent Data Systems (IDS) PC-286T. The PPS consisted of the Axis Control Unit (ACU), a lead screw assembly, a DC servo motor, and an optical encoder. Using signals from the ACU, the DC motor was used to drive the lead screw, moving the traverse in the desired direction. As the lead screw turned, the encoder (which was coupled mechanically to the lead screw shaft) rotated and sent a digital counting signal back to the ACU. The encoder generated 500 pulses per revolution of the lead screw. Each revolution of the lead screw corresponded to 1 mm of movement, with a resolution of ± 0.025 mm. Once a position was selected and entered as a command, the PPS determined the number of turns (counts) needed to get to the new position.

The hot-wire probe was mounted to the traverse and moved in the vertical direction inside the pipe. The hot-wire signal was fed into a TSI Model 1050 Constant Temperature Anemometer. The signal was then linearized with a TSI Model 1052 Signal Linearizer. The linearized analog signal was input to a Data Precision Data 6000 for waveform analysis. Subsequently, the Data 6000 digitized (and stored temporarily) the analog input signals. The Data 6000 provided an extensive library of pre-programmed analysis functions for manipulation of the stored data, and it could then display those results or other information. The processed data were sent to the IDS PC microcomputer for final storage via a GPIB interface.

The free stream velocity, U_{∞}, of the pipe tunnel was measured using a standard pitot-static tube. The pitot-tube was mounted in the annular region above the model. The pitot probe differential pressure lines were connected across a Datametrics Type 570 Barocel Pressure Sensor with a maximum differential pressure range of 10 Torr. Those pressure transducers were used throughout the present experiments.

A 20 horsepower, 440 volt, 3 phase, 60 cycle Reliance AC motor was used to drive the fan controlling the pipe tunnel air flow. A variable voltage controller was used which was capable of producing pipe velocities of up to 32 meters per second, when the model was installed. A small DC motor powered fan was used as an alternate low-speed drive. That unit was installed by removing one of the pipe sections and substituting the DC fan system. The DC unit was capable of producing velocities of up to 1.3 meters per second.

A new forward centerbody and support were designed to mount the perturbation generator in the 4-inch pipe (Figure 15). The new design was 30.48 mm in diameter with provisions for an aluminum airfoil mounting unit. The airfoil was a single element which passed through a custom-built forward centerbody. The centerbody was threaded to mate with the perturbation generator. The airfoil was attached to both sides of the pipe, thus suspending the model on the axis of the pipe. Air lines, electrical leads, and the pressure sensing line were accommodated through holes cut in the airfoil. The forward nose of the model was elliptical in shape. The new fixture also served as the motor housing, eliminating the need for the forward housing on the perturbation generator. Furthermore, no transition from a 25.4 mm diameter to a 30.5 mm OD was required since the custom-built unit was already 30.5 mm in diameter. A schematic of the centerbody mounted in the 4-inch pipe facility is shown in Figure 16.

The hot-wire probe was positioned 35 mm behind the model for measurements during the pipe flow tests. A Data 6000 Waveform Analyzer was set up to record the velocity trace measured by the hot-wire as well as measure the fluctuating perturbation motor lead voltage. Velocity histories (buffer A) were stored as 1024 sampling points taken with fixed sampling intervals, varying between 2 and 5 milliseconds. Hence the velocity record lentghs varied between 2 and 5 seconds. Perturbation motor speeds (buffer B) were taken by sampling 2048 voltages with a fixed sampling interval, varying between 0.4 and 0.2 milliseconds, depending on nominal motor speed (which could be estimated through the DC power supply voltage). This configuration allowed the Data 6000 to record the motor frequency trace at the same
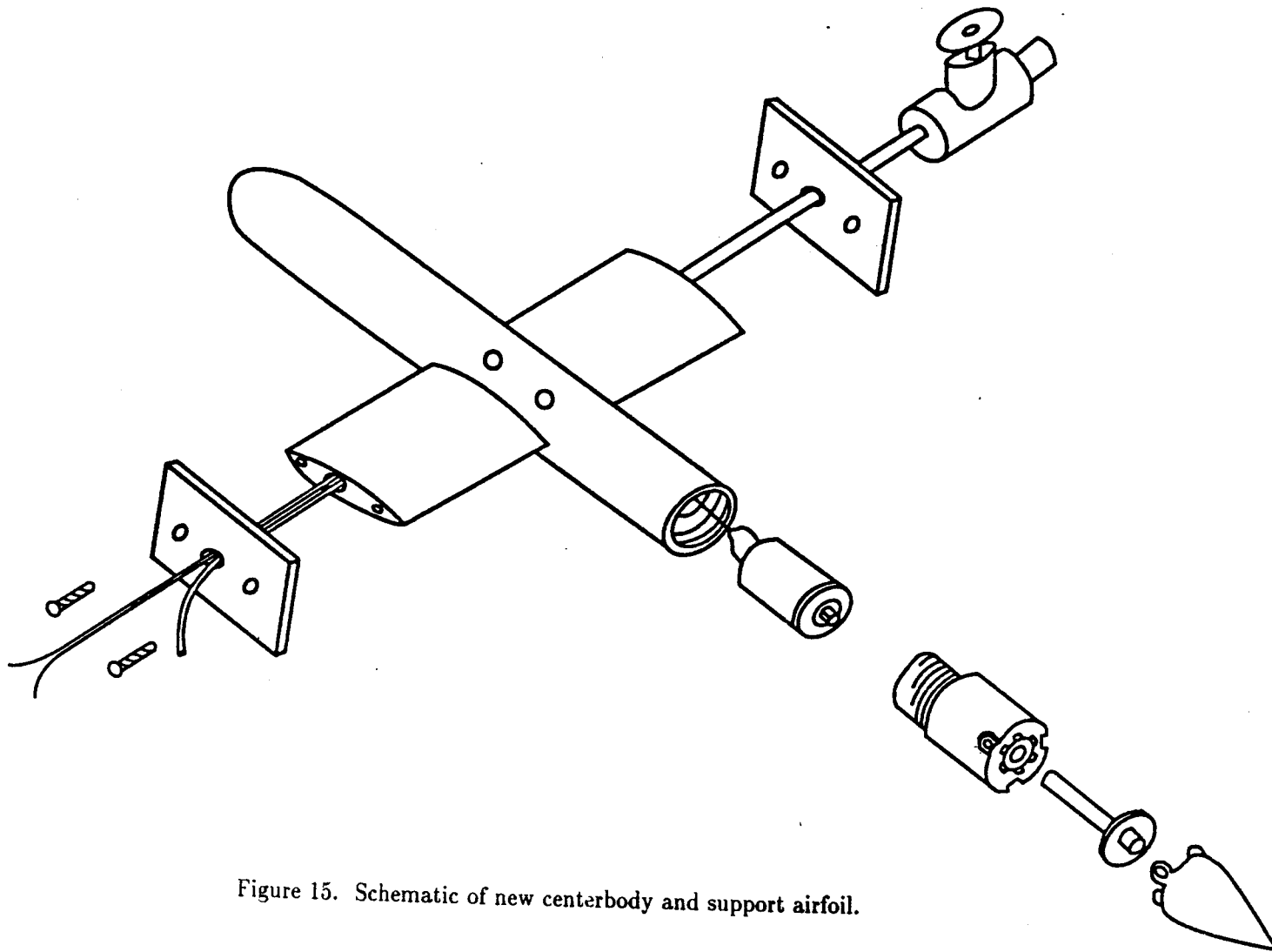
Figure 15. Schematic of new centerbody and support airfoil.
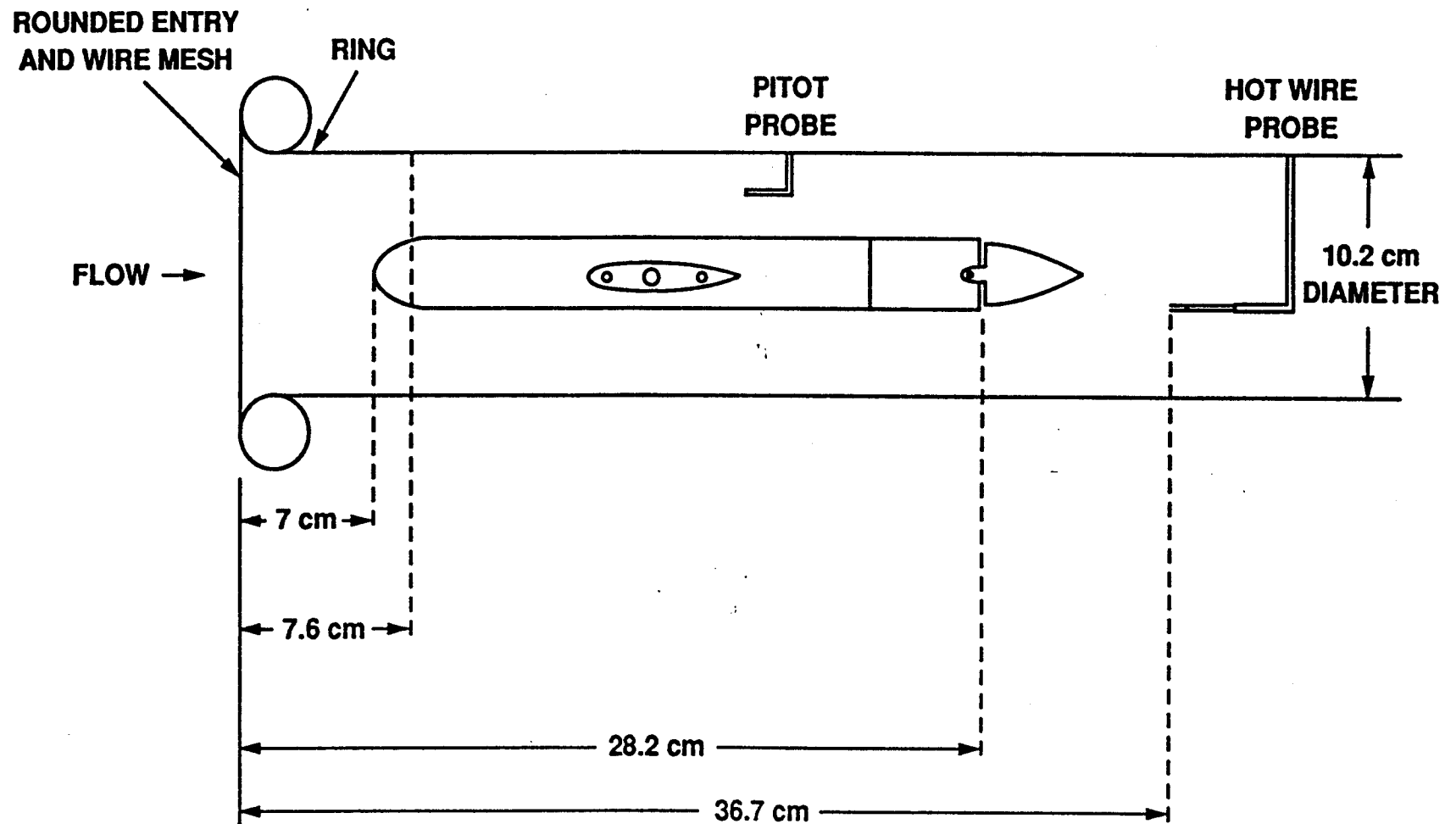
Figure 16. Schematic for centerbody mounted in the 4 inch pipe.

-44-

time it recorded the hot-wire trace. Thus, when in the Data 6000 was triggered manually, the hot-wire trace and corresponding motor frequency trace could be processed simultaneously. Processing of the velocity trace was accomplished using the Fast Fourier Transform (FFT) function on the Data 6000. The resulting velocity FFT spectrum was transferred to an IDS PC for storage. The motor frequency, M_f, read from the FFT spectrum of buffer B was displayed on the Data 6000. This set up of the Data 6000 was maintained for the 4-inch pipe tests.

Flow out of the perturbation generator was governed by the difference between the plenum pressure and the local static pressure outside the rotating disk. Plenum pressure was sensed through a pressure tube inserted into the plenum chamber inside the model. The pressure tube was attached to tygon tubing, which passed outside the wind tunnel via the mounting airfoils (along with the motor electrical leads). Pressure taps in the 4-inch pipe wall allowed the differential pressure between the plenum pressure and local static pressure to be measured. This pressure is denoted ΔP for all 4-inch pipe measurements.

During the initial hot-wire surveys taken after mounting the perturbation generator in the 4-inch pipe, a large voltage spike at 95 Hz was observed in frequency spectra. The spike (Figure 17) was observed under all flow conditions tested. Furthermore, hot-wire measurements taken with the model out of the pipe showed the same spectral peak. The spike was not present when the flow was secured as shown in Figure 18. Several modifications to the tunnel (screens, and honeycomb) were employed in an attempt to get rid of the signal, but no satisfactory solution was found. It was determined subsequently that the

17d. U_∞ = 21 m/s, no model in the pipe.

17c. U_∞ = 21 m/s, perturbation generator secured.

17b. U_∞ = 21 m/s, perturbation generator operating at 115 hz.

17a. U_∞ = 6 m/s, perturbation generator operating at 105 hz.
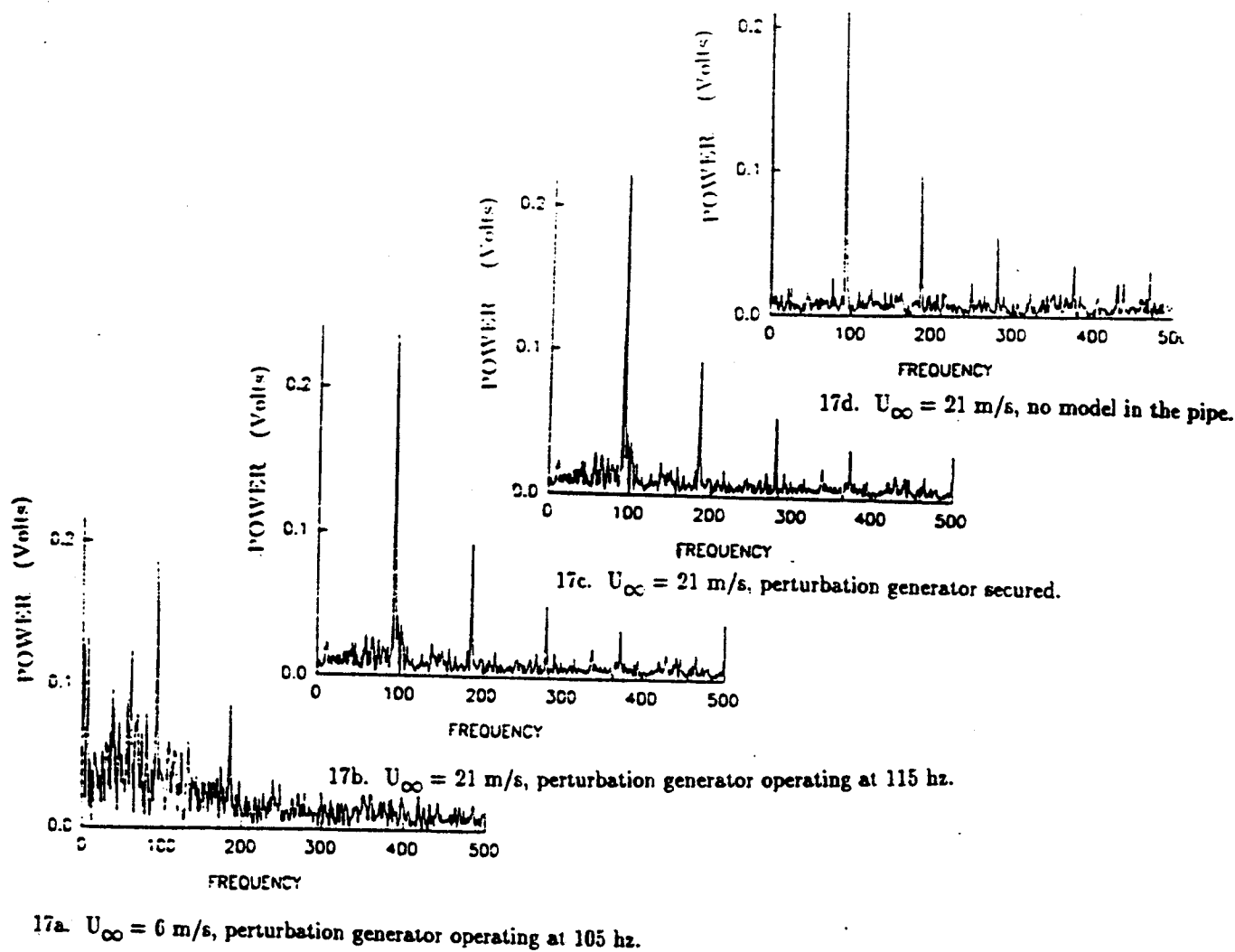
Figure 17. Sample of frequency spectra demonstrating the 95 hz spectral spike for various flow conditions in the 4 inch pipe facility.
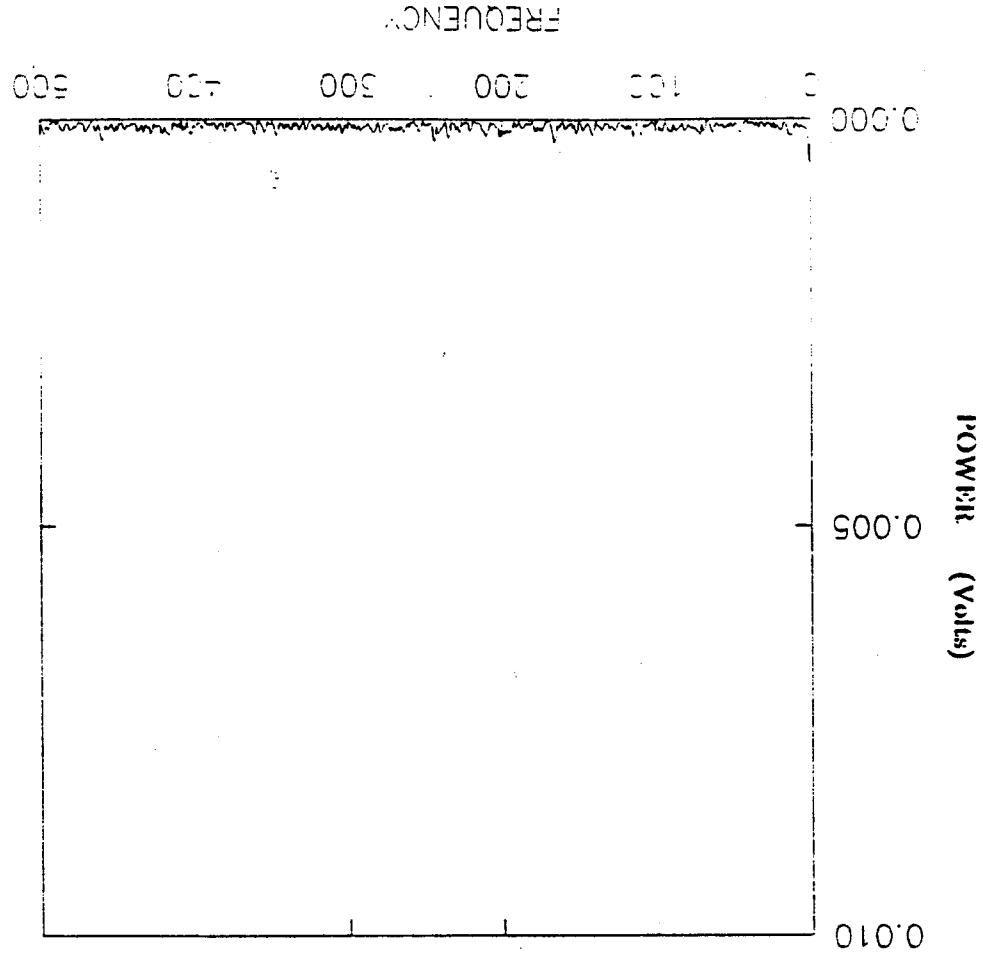
Figure 18. Frequency spectrum with no pipe flow (expanded voltage scale).

large fan unit was producing the signal. When the small DC fan unit was substituted, the 95 Hz signal was not present (Figure 19). Finally, it was determined that voltage peaks between 95 and 100 Hz should be ignored in processing spectral data taken in the plexiglass pipe with the 20 HP fan unit in operation due to the presence of the motor-based spike.

A variety of model geometry effects were tested concurrently in the pipe tunnel experiments. During those experiments, when the hot-wire probe was located 35 mm (1.375 inches) behind the model, wake velocity fluctuations were surveyed. A vertical survey was taken with the hot-wire along the tunnel centerplane while the perturbation motor and its air supply were secured. Mean velocities and frequency spectra were taken at (radial) increments of 1.0 mm.

Significant differences in the voltage amplitude spectral peaks were noted between spectra obtained above the model centerline and spectra obtained below the model centerline (Figure 20). Specifically, larger voltage amplitudes were measured when the hot-wire probe was positioned above the pipe centerline. Figure 21 shows the location of the three keyway support ribs used to hold the aft end of the model to the mainbody. They are located 120 degrees apart around the model circumference. Depending on the orientation of the model, one keyway support rib was aligned along the vertical centerline of the model with an open slot centered on the opposite side. Larger voltage amplitudes were measured when the hot-wire probe was aligned with the keyway support rib, when compared with measurements aligned with the open slot. That effect was verified when the model tail configuration was rotated 180 degrees so that the keyway support rib was on the bottom of the model and the
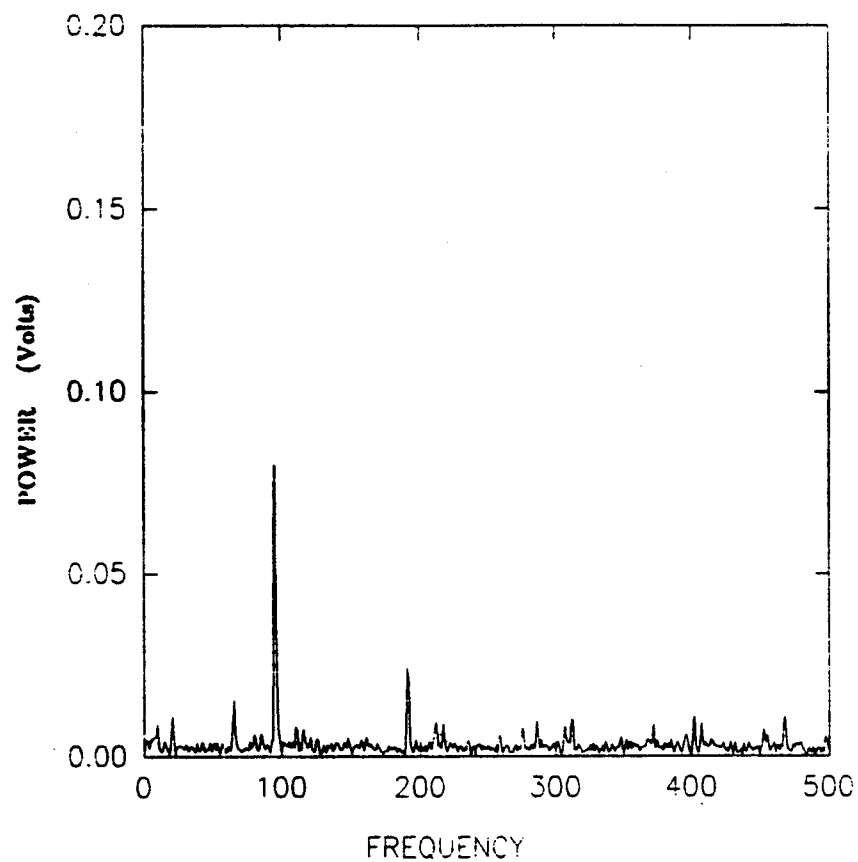
19a. Large Fan, $U_\infty = 1.5$ m/s.
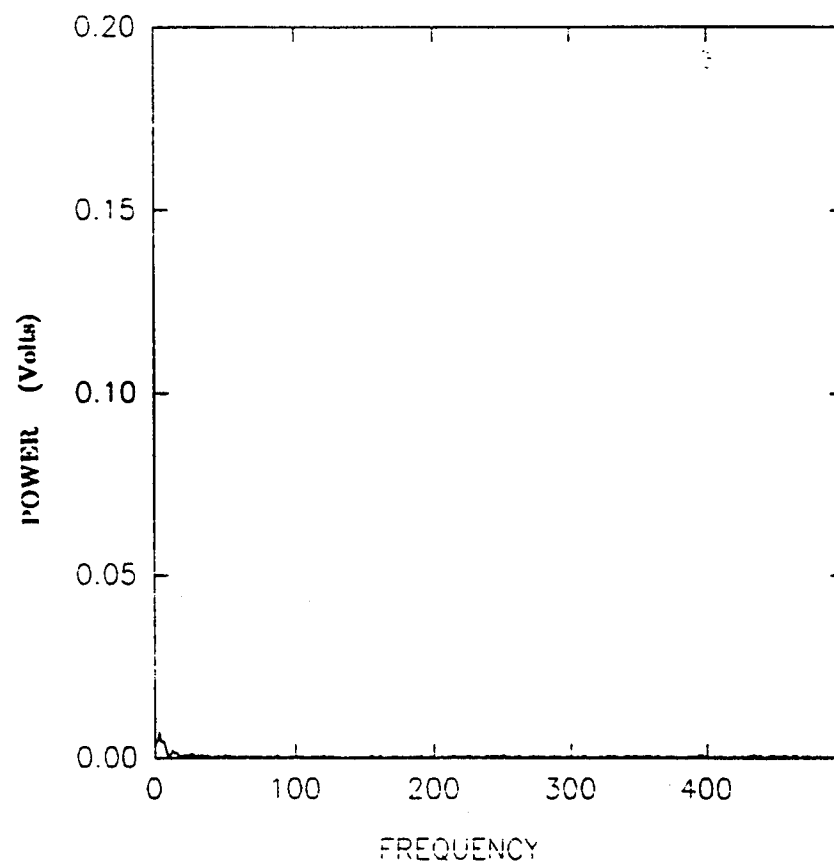
19b. Small Fan. $U_\infty = 1.9$ m/s.

Figure 19. Frequency spectra comparison between large and small fan.
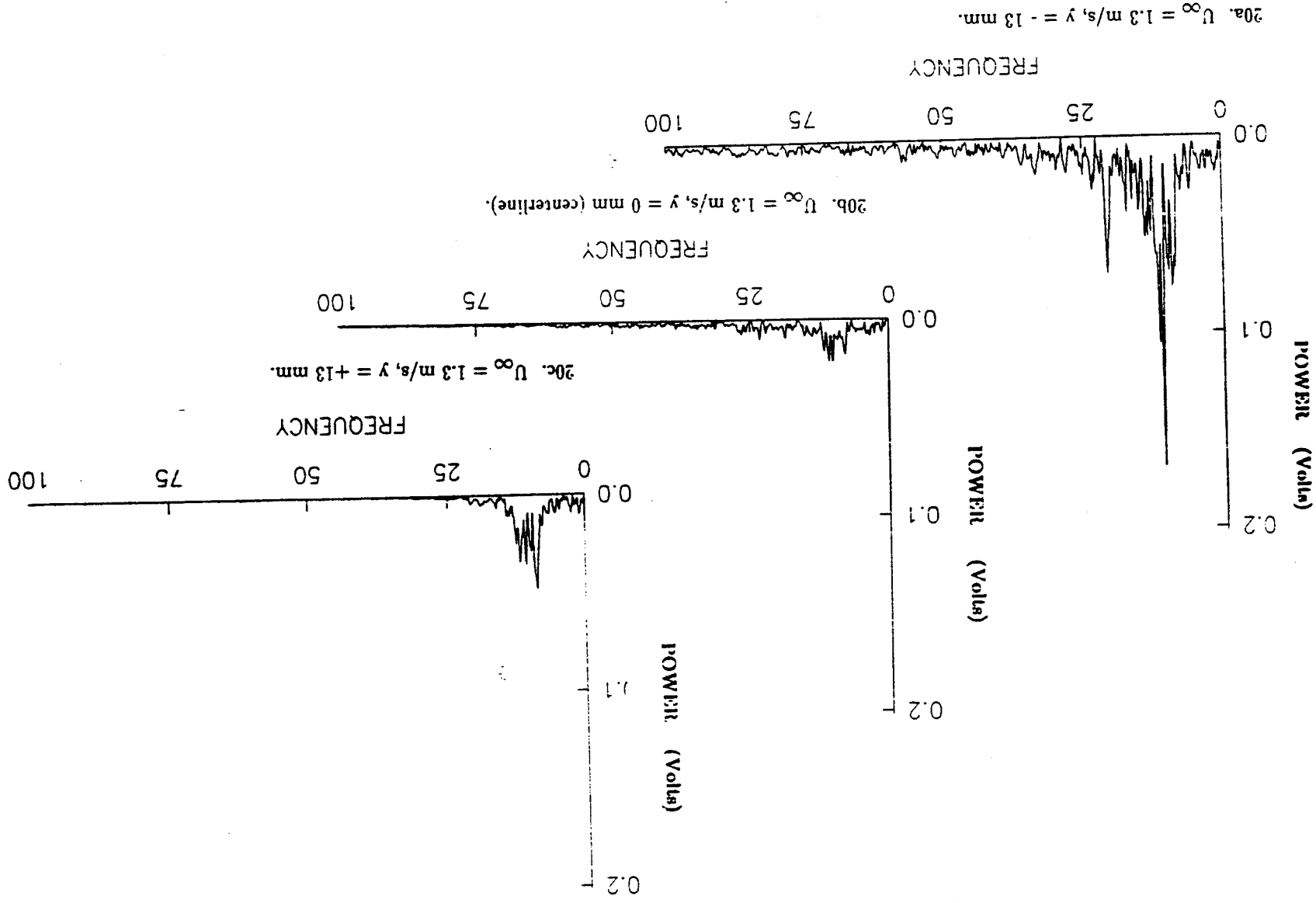
KEYWAY SUPPORT RIBS

KEYWAY SUPPORT RIB POSITIONED
ALONG THE MODEL BOTTOM CENTERLINE

KEYWAY SUPPORT RIB POSITIONED
ALONG THE MODEL TOP CENTERLINE
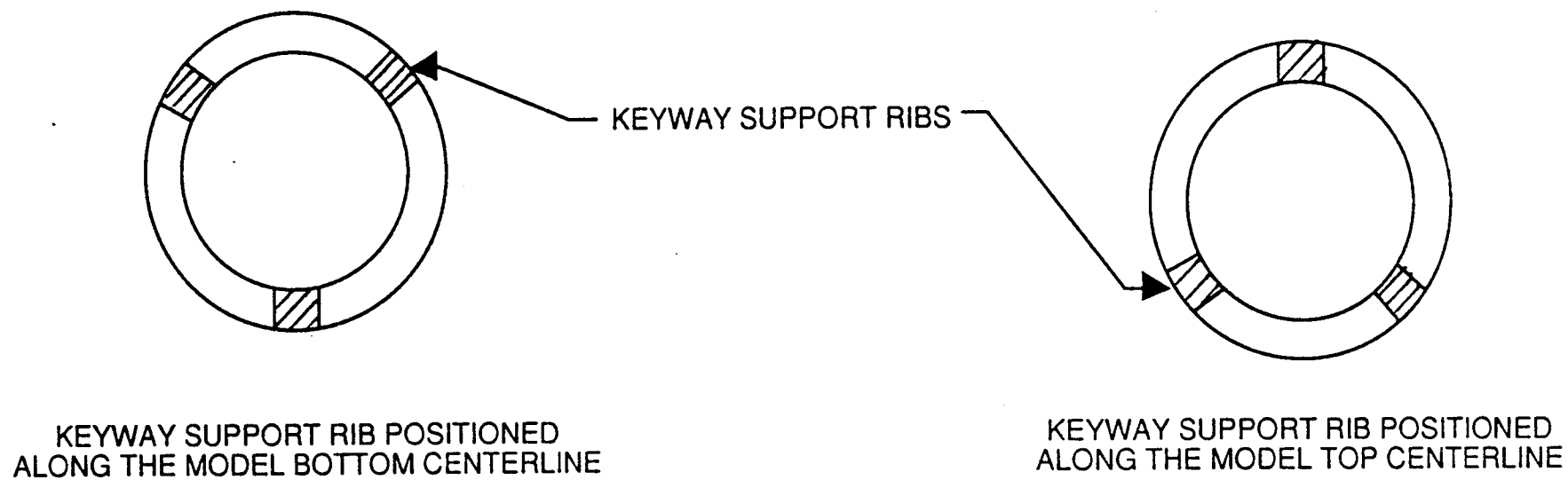
Figure 21. Schematic of the keyway support rib orientation.

corresponding open slot was on top of the model. The large amplitude peaks in spectra were then observed below the model (Figure 22). Hence the orientation of the model's keyway support ribs in the tube had an effect on the frequency spectra downstream. It was noted that the peak amplitude decreased rapidly as the hot-wire was moved to radial positions more than 15 mm from the centerline, which corresponded to the nominal radius of the model.

Adhesive tape was placed over the slot openings on the model to eliminate perturbations produced by the slot geometry. Frequency spectra were obtained subsequently and were found to be essentially symmetrical with respect to the model centerline (Figure 23) unlike the open slot data. Furthermore, the peak voltage amplitudes obtained with tape covering the slots were found to be on the same order of magnitude as the "untaped" peak amplitudes obtained when the keyway support rib was aligned with the vertical plane, and in the same model quadrant as the hot-wire (Figure 22).

Initial model flow spectral data were taken with the tape remaining over the perturbation slots. Those tests were intended to identify any boundary layer or geometrically controlled periodic flow structures. The hot-wire probe was positioned 13 mm below the model centerline. That location was selected after the vertical survey showed the strongest spectral peaks at the 13 mm position below the model centerline. A similar frequency spectrum was obtained at 13 mm above the model centerline (when the keyway slot was rotated), but a pitot probe was mounted above the model during these tests in order to determine the free stream velocity. Hence, the hot-wire position below the centerline was selected to avoid spectral contamination from the pitot probe.
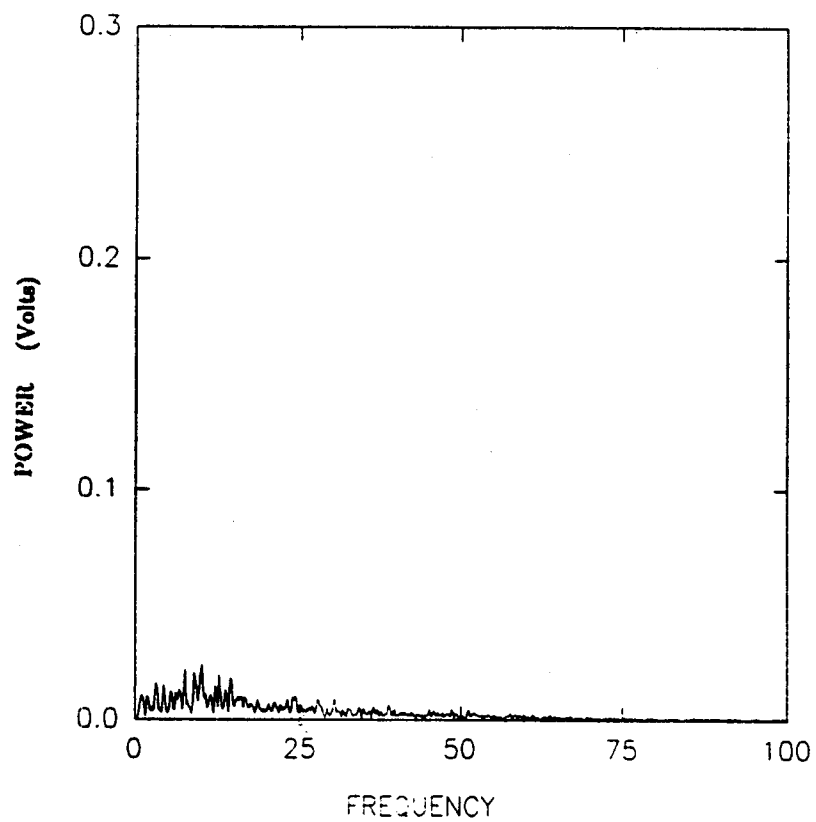
22a. $U_\infty = 1.3$ m/s, y $= -13$ mm.
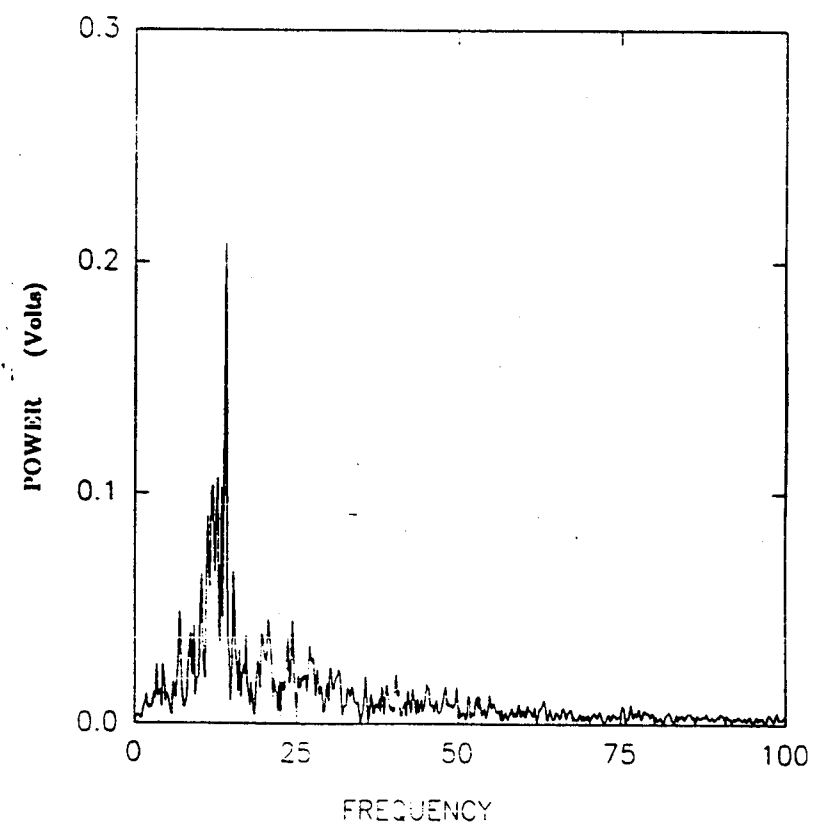
22b. $U_\infty = 1.3$ m/s. y $= -13$ mm.

Figure 22. Frequency spectra displaying larger voltage amplitudes below the model centerline.
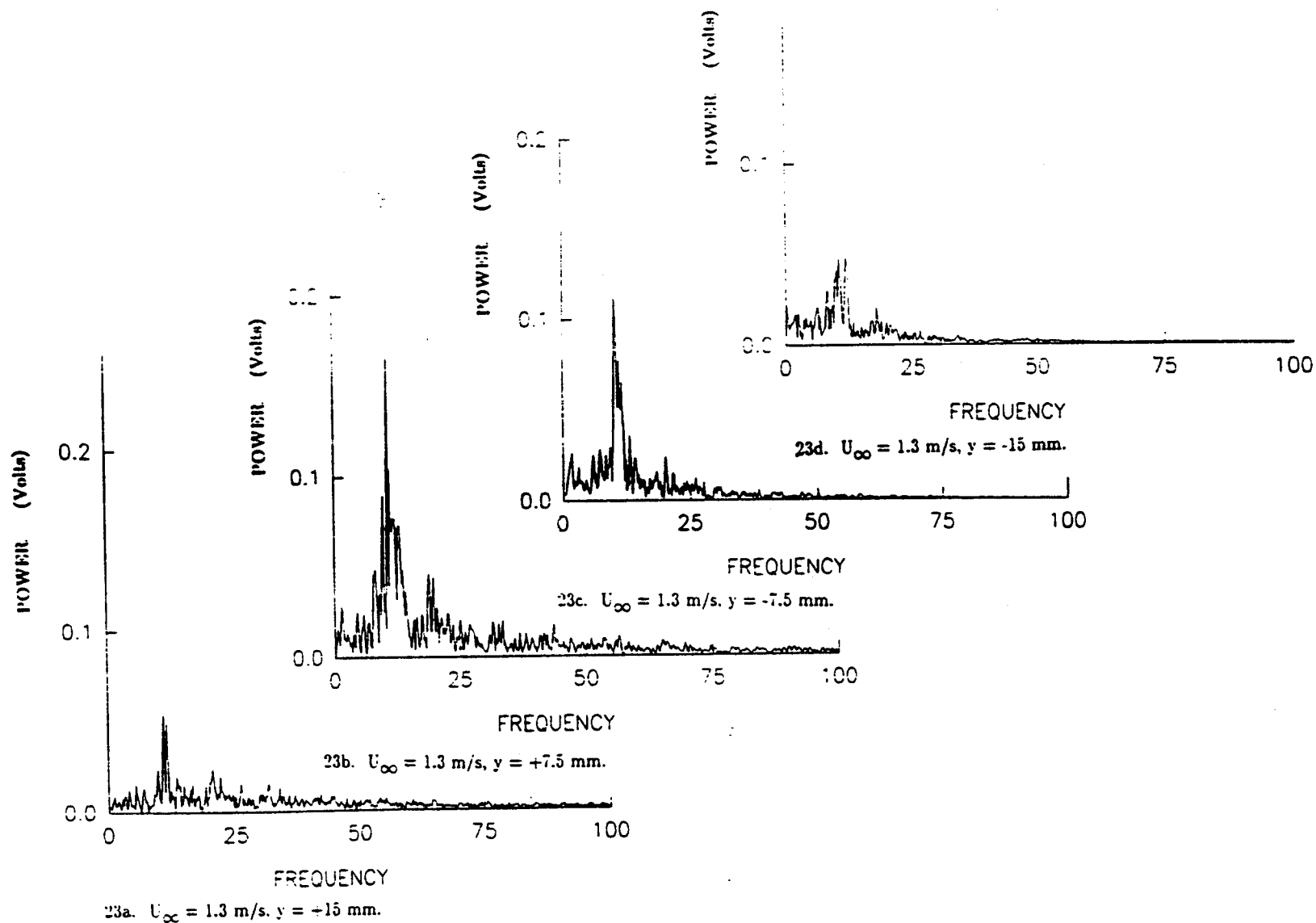
Figure 23. Frequency spectra with tape applied over the slot openings.

23a. $U_\infty = 1.3$ m/s, y = +15 mm.

23b. $U_\infty = 1.3$ m/s, y = +7.5 mm.

23c. $U_\infty = 1.3$ m/s, y = -7.5 mm.

23d. $U_\infty = 1.3$ m/s, y = -15 mm.

The influence of natural transition was investigated by installing a circular-ring, trip-wire on the axisymmetric nose. The wire was employed in order to fix the forward transition point and assure an axisymmetric boundary layer flow over the body. This allowed testing to be made to compare the resulting spectra with those produced under similar conditions while the trip wire was removed. There were no differences noted when the trip wire was removed as discussed in the results and discussion section.

Frequency spectra were measured for several different combinations of free stream velocity, perturbation generator motor speeds, plenum pressures, and disk rotation directions. The first test in this series was conducted to study the influence of the perturbation injection slots on the flow without power to the model motor, and with the line supplying air to the model plenum chamber secured. Tape also covered the perturbation slots. The large fan (maximum velocity 32 meters per second) and the small fan (maximum velocity 1.3 meters per second) were utilized to supply the primary flow through the 4-inch pipe.

In order to investigate the effects of the perturbation generator slots, the adhesive tape was removed and frequency spectra were measured at several different free stream velocities while the model motor was unpowered and the perturbation supply pressure secured. This test series was intended to verify that no change occurred in the energy spectra between the tape covered slots and the open slots. The large-motor fan was used exclusively for these measurements, recognizing that there were fan inherent frequency spikes between 95 and 100 Hz. The trip wire was retained on the front of the axisymmetric body to assure axisymmetric boundary layer flow development over the body.

Tests were also conducted with the perturbation generator in operation, but with no cross-flow in the pipe. Hot-wire measurements at the perturbation generator outlet were taken to establish the sharpness of the perturbation waveform, prior to combining the perturbation flow with the pipe flow. These results were intended to establish an operating envelope of motor frequencies and plenum pressures which produced controlled perturbations during pipe flow tests. Perturbation velocity tests were accomplished by positioning the hot-wire at the outlet slot and running the motor at selected speeds, while controlling the supplied air. Measurements were taken for motor frequencies, M_f, up to 121 Hz and differential pressures, ΔP, between .07 and 4.7 torr (9 to 625 Pa).

With the hot-wire probe positioned 35 mm behind the model and 13 mm below the centerline, measurements were taken for different free stream velocities, motor speeds, and plenum pressures. These tests were run with the perturbation generator motor operating in both directions. The tests were repeated after removing the circular ring trip wire, mounted on the nose of the axisymmetric body, for a comparision of the resulting spectra with those produced under similar conditions while the trip wire was attached.

The hot-wire remained 35 mm behind the model and was traversed vertically through the wake to study the variation of the perturbation generator signal with respect to the location in the wake. The free stream velocity of the pipe was set at approximately 6.2 m/s, the model motor frequency set at 66 Hz, and the plenum pressure set at 0.5 torr. The probe traversed from 20 mm below the centerline to 20 mm above the centerline.

Measurements of the mean and RMS velocity levels over the flow field were taken by traversing the hot-wire probe vertically through the wake. Surveys were taken for free stream velocities of 6 m/s, 14 m/s, and 21 m/s, with the perturbation generator operating at a constant speed of 75 Hz, and with the plenum pressure maintained at 0.65 torr (86 Pa). These measurements were compared to the mean velocity and RMS levels obtained when the perturbation generator was secured, to determine any influences of the perturbation generator flow on the wake.

It is important to determine the magnitude of the mass injection perturbation to understand how it affects any vorticular flow. The volume flow rate of injected air can be estimated by assuming the slot flow is quasi-steady and laminar. Then, since the gap varies with motor shaft angle, θ, the injection gap, $\delta(\theta)$, is given by:

$$\delta(\theta) = \delta_0(1 + \cos \theta), \qquad (4)$$

and the velocity profile leaving the gap at any instant is given by:

$$V(\eta) = \frac{3}{2} V_m (\theta) [1 - \eta^2/\delta^2(\theta)], \qquad (5)$$

where η is a coordinate which is referenced to the mid-plane in the gap, $-\delta_o \leq \eta \leq \delta_o$, and $V_m(\theta)$ is the mean velocity leaving, at shaft location θ, given by:

$$V_m(\theta) = \frac{\Delta P\, \delta^2 (\theta)}{3\mu l} \qquad (6)$$

where ΔP is the pressure difference between the plenum and the surroundings, μ is the dynamic viscosity, and l is the equivalent viscous length traversed by the air through the gap.

Then, the estimated air injection rate, Q, is given by:

$$Q = \frac{D_o}{2} \int_0^{2\pi} \delta(\theta) \; V_m(\theta) \; d\theta = \frac{5\pi D_o}{6} \frac{\Delta P}{\mu l} \delta_o^3 \qquad (7)$$

Alternatively, if Q is in liters/sec and D_o and δ_o are in millimeters

$$Q = K_1 \Delta P \quad \text{and} \quad V_{MAX} = \frac{764}{D_o \delta_o} K_1 \Delta P \qquad (8)$$

where K_1 can be determined experimentally and V_{MAX} is the maximum velocity at the centerplane of the gap (at $\theta=0$) in m/s.

The last set of tests in the 4-inch pipe were to determine whether the perturbation signal was convected downstream in the pipe. The hot-wire probe was moved downstream to a location 2.5 meters behind the perturbation generator. Measurements were taken with various combinations of pipe free stream velocity, motor frequency, and plenum pressure. The perturbation signal was not detecetd at those locations.

3.2 4-Inch Pipe Results And Discussion:

Spectra were measured for several different free stream velocities using the small and large fans. The perturbation generator was secured and tape was over the holes during those tests. Figure 24 shows typical voltage spectra across the wake using the small motor-driven fan ($U_\infty = .96$ m/s). Figure 25 shows similar spectra over a range of free stream velocities.
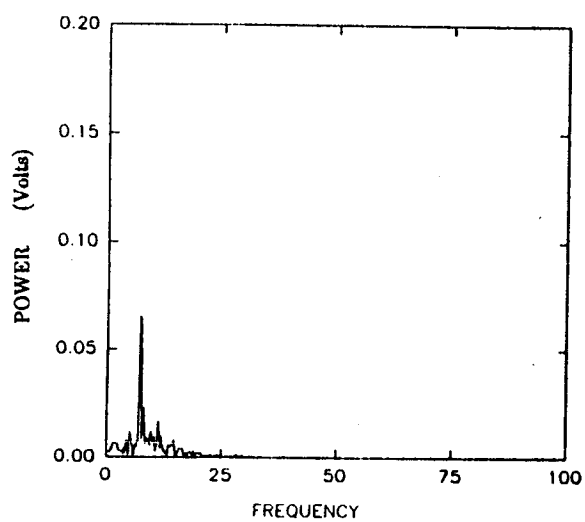
24a. Y = + 15 mm.
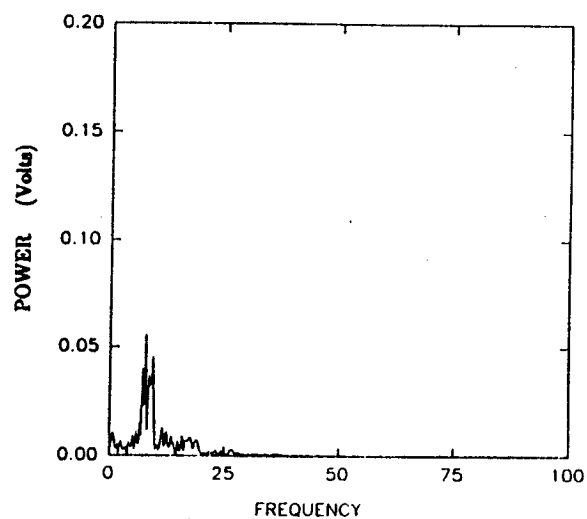
24b. Y = +13 mm.
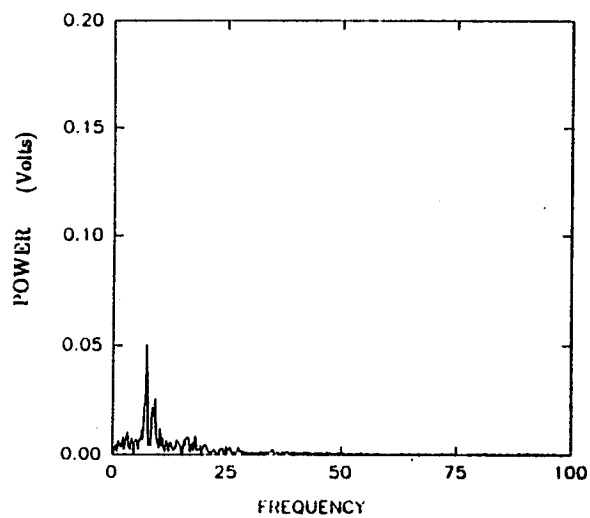
24c. Y = +10 mm.
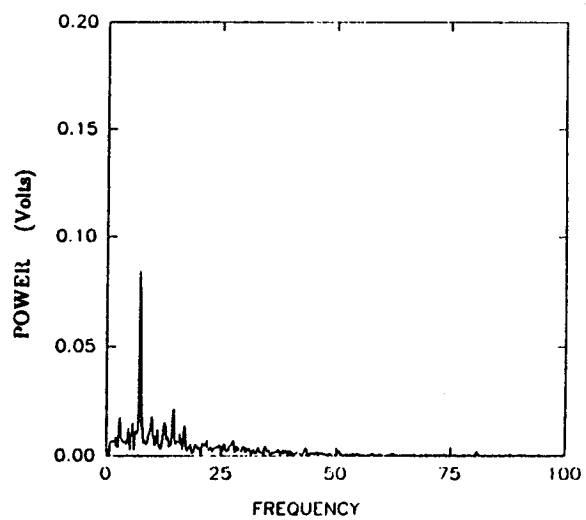
24d. Y = + 6 mm.

Figure 24. Voltage spectra as probe is moved through the wake, $U_\infty = .96$ m/s, small fan.
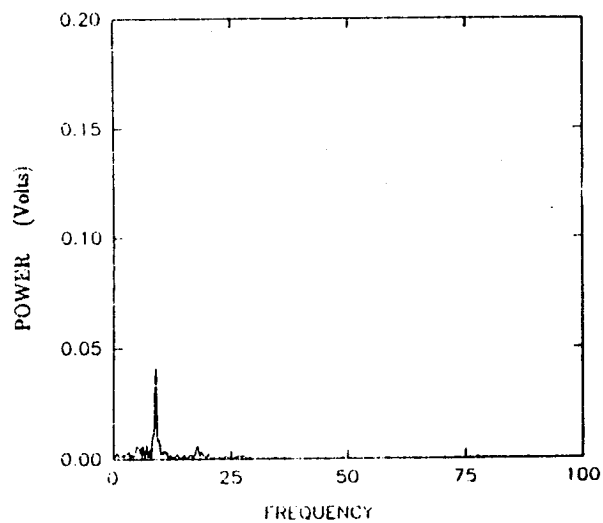
24e. Y = -6 mm.
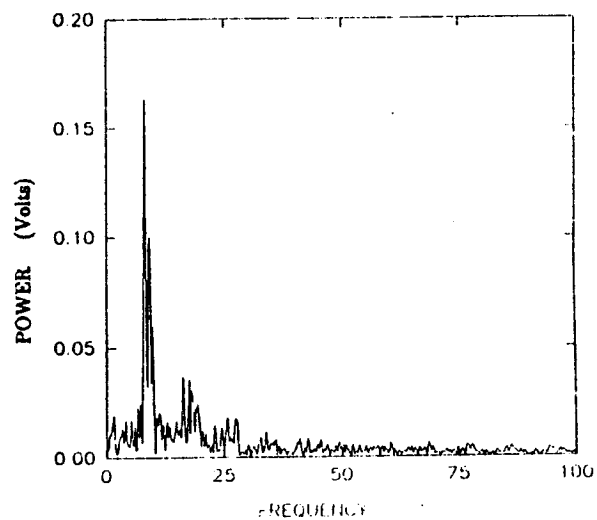
24f. Y = -10 mm.
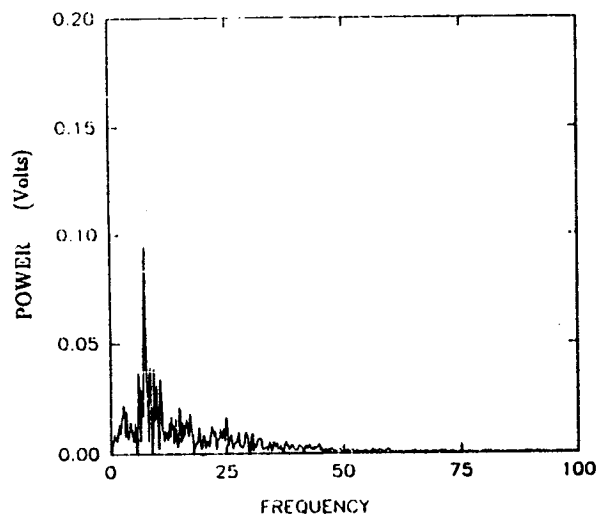
24g. Y = -13 mm.
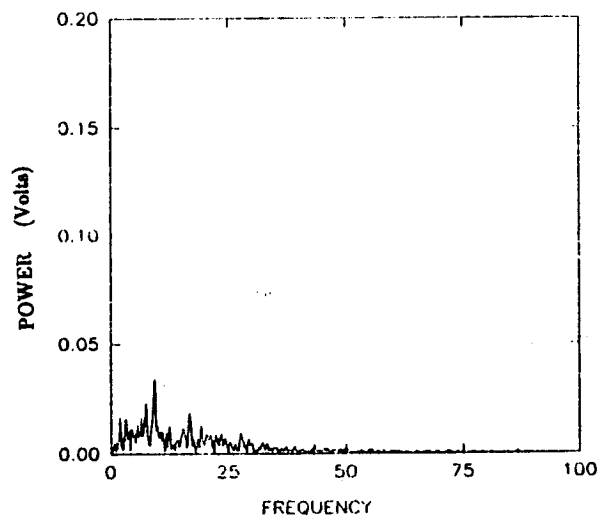
24h. Y = -15 mm.

Figure 24 (continued)

25a. $U_\infty = 0.96$ m/s.

25b. $U_\infty = 1.33$ m/s.

25c. $U_\infty = 1.6$ m/s.

25d. $U_\infty = 1.83$ m/s.
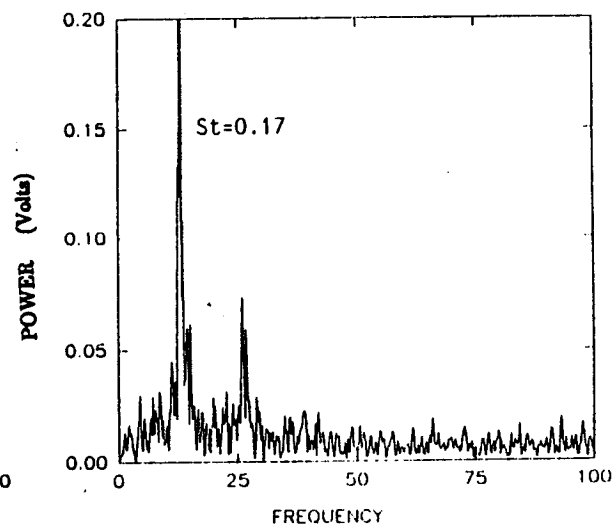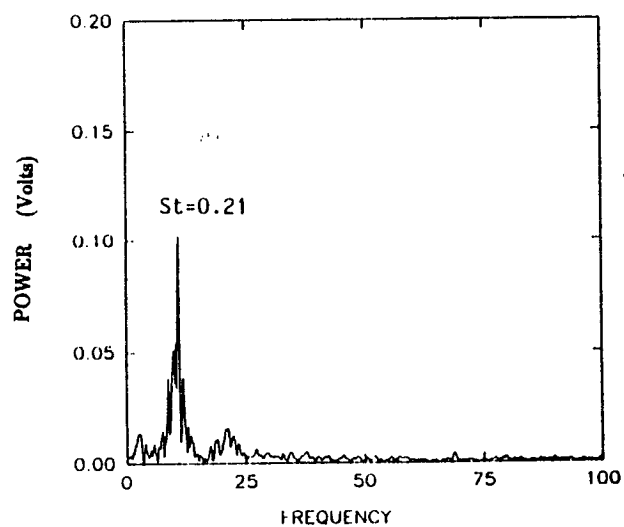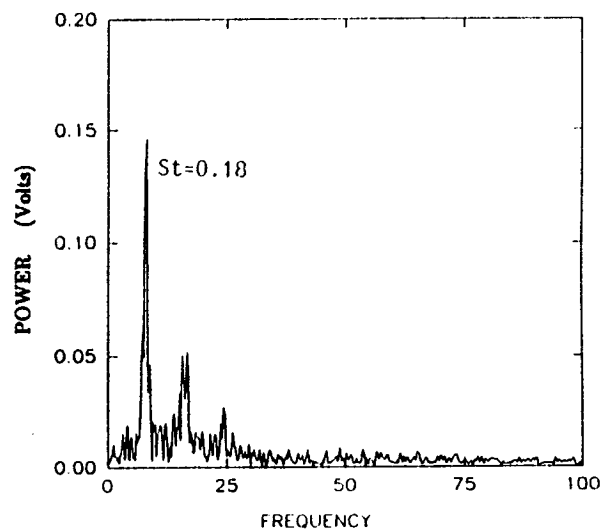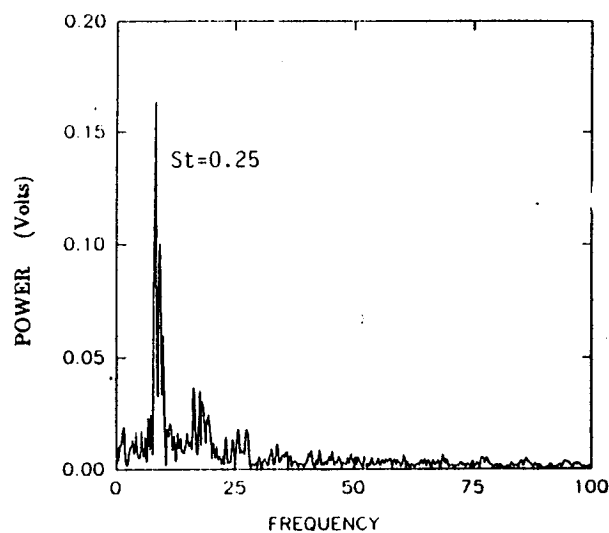
Figure 25. Frequency spectra for various small fan freestream velocities, $y = -13$ mm.

Figure 26 presents representative spectra using the large motor-driven fan. Large differences in voltage amplitudes were observed for similar velocities between the two motor-driven fans which was due at least partially to a new hot-wire calibration which was required to accommodate the higher velocities produced by the large-motor fan. While the energy spectra are quite noisy, in all cases peaks were observed at similar frequencies, controlled by the free stream velocity. These peaks corresponded to a mean Strouhal number, S_t, of 0.2, with

$$S_t = \frac{f_{peak}D}{U_m} \qquad (9)$$

where D is the model diameter (30.5 mm), f_{peak} is the largest frequency peak (Hz) and U_m is the free stream velocity in the pipe, ranging from 1.3 m/s to 32 m/s. The spectral peak corresponding to S_t = 0.2 was observed during all of the test runs. It was also observed when the hot-wire probe was moved vertically; but the largest peak amplitudes were measured at the 13 mm position below (with corresponding measurements above) the centerline. The hot-wire location was also where the largest wake effects occurred, as seen from a typical plot of the mean flow versus height taken 38 mm behind the perturbation generator tip.

The peak Strouhal number result was consistent with earlier experiments on turbulent boundary layers reported by Bandyopadhyay.[19] He observed that Tollmien-Schlichting waves, whose origins were in the transitional phase of the boundary layer, were amplified and persisted for low Reynolds number turbulent flows, even after passage over embedded

26a. $U_\infty = 1.11$ m/s.

26b. $U_\infty = 1.8$ m/s.

26c. $U_\infty = 11.4$ m/s.

26d. $U_\infty = 31.2$ m/s.
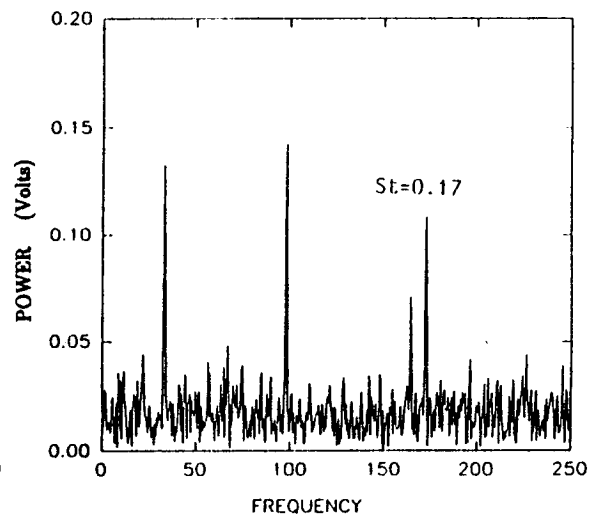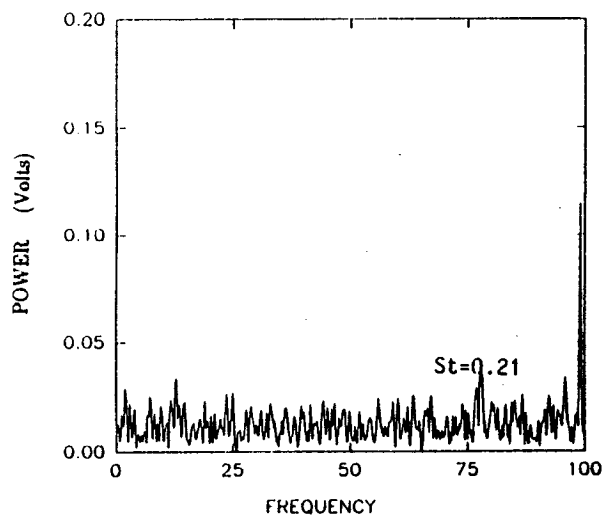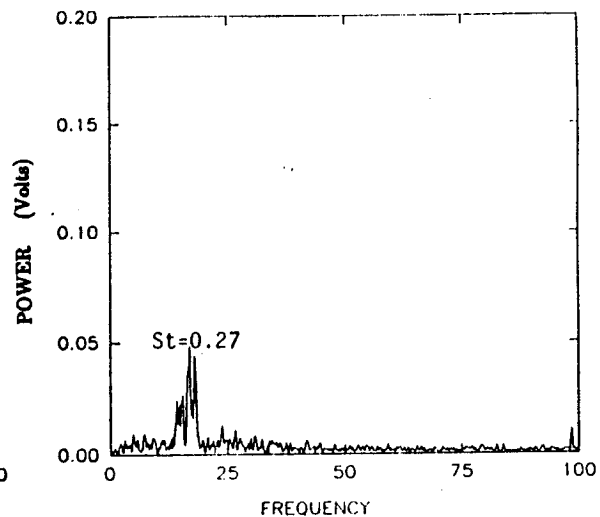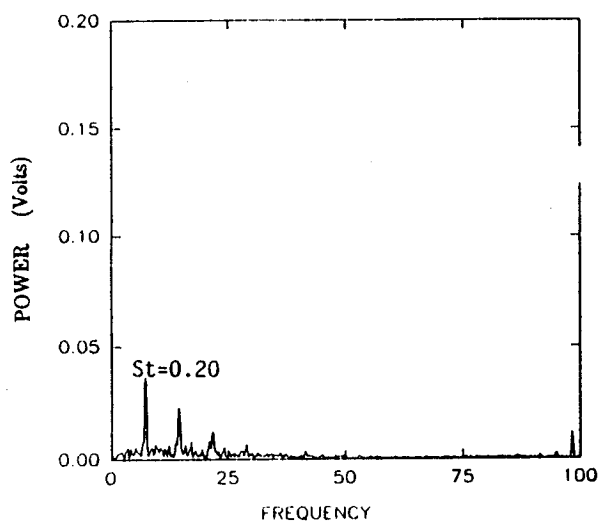
Figure 26. Frequency spectra for various large fan freestream velocities, y = -13 mm.

cavities. Here the data suggest that the Tollmien-Schlichting waves, which are evolving over the axisymmetric model, may form ring-mode fluctuations which can be identified in the wake flow velocity spectrum. The variation of Strouhal number with Reynolds number is only slight, as shown in Figure 27, which shows a slight drop in Strouhal number (Slope: $\simeq$ - 1.4×10^{-6}, Re) with increasing Reynolds number. It is noted that each spectrum had a peak corresponding approximately to $S_t = 0.2$, but the amplitude of the peak was not always the largest peak measured for the spectrum, as shown in Figure 28. The background effects due to Strouhal number controlled fluctuation waves were an important consideration for all subsequent tests.

When the adhesive tape was removed, frequency spectra were measured at several different free stream velocities while the perturbation generator was secured to investigate the effects of the open slots. Similar to the previous results, the frequency peaks corresponding to a Strouhal number of approximately 0.2 were observed for these tests. Plots of Strouhal number versus Reynolds number for the maximum amplitude peaks are shown in Figure 29. Again, the slope decreases slightly with increasing Reynolds number (slope: $\simeq$ -2.9 x 10^{-6}, Re). It is interesting to note that high Strouhal number data ($S_t > .3$) which occurred at low Reynolds numbers with the tape over the slots, vanish when the tape was removed from the slots.

Results of tests conducted with the perturbation generator in operation and with the hot-wire positioned at the perturbation generator slot were obtained. There was no cross-flow in the pipe for these measurements. Plots of representative outlet velocity traces and their
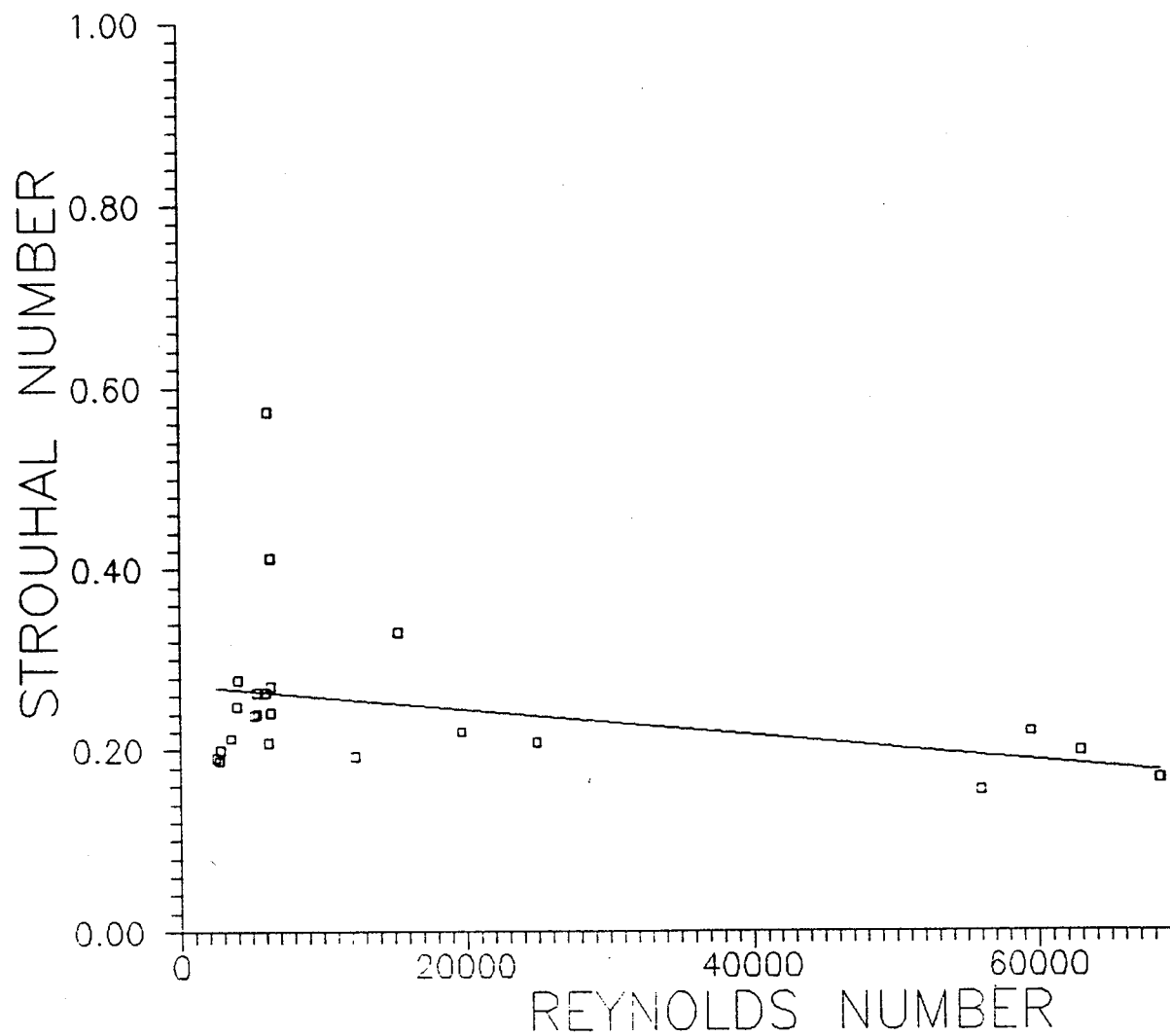
Figure 27. Strouhal number for peak wake frequency vs pipe Reynolds number, tape over the slots, large fan, and trip ring on the centerbody nose.
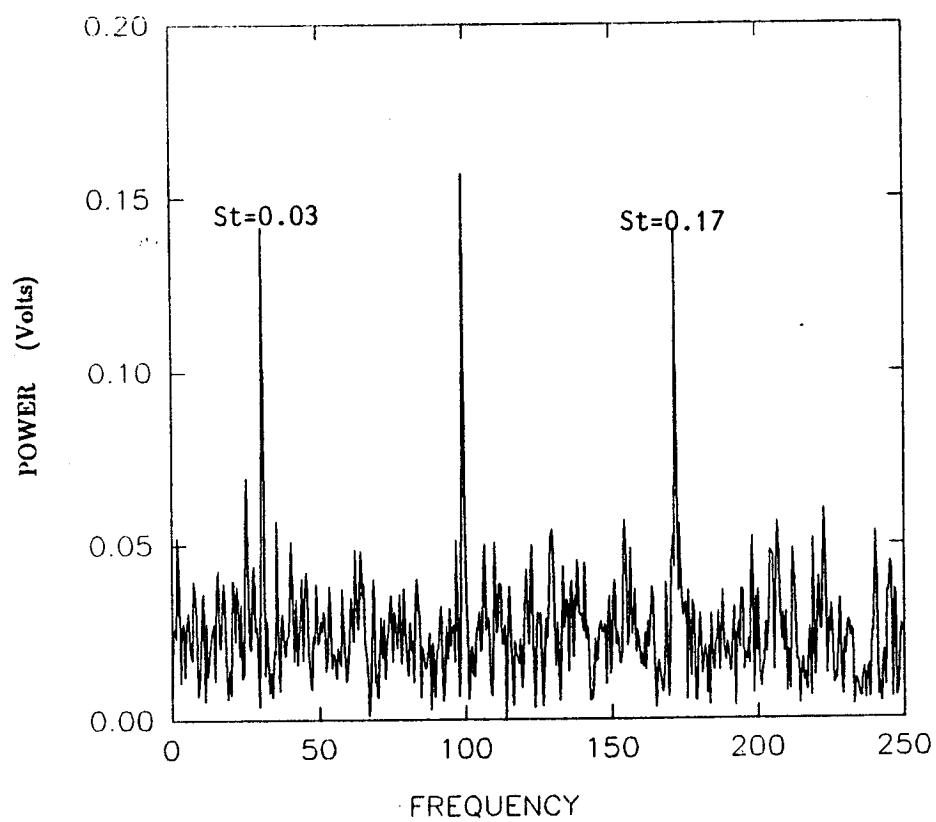
Figure 28. Frequency spectrum showing spectral peaks other than St = 0.2. Model holes taped, U_∞ = 31.1m/s.
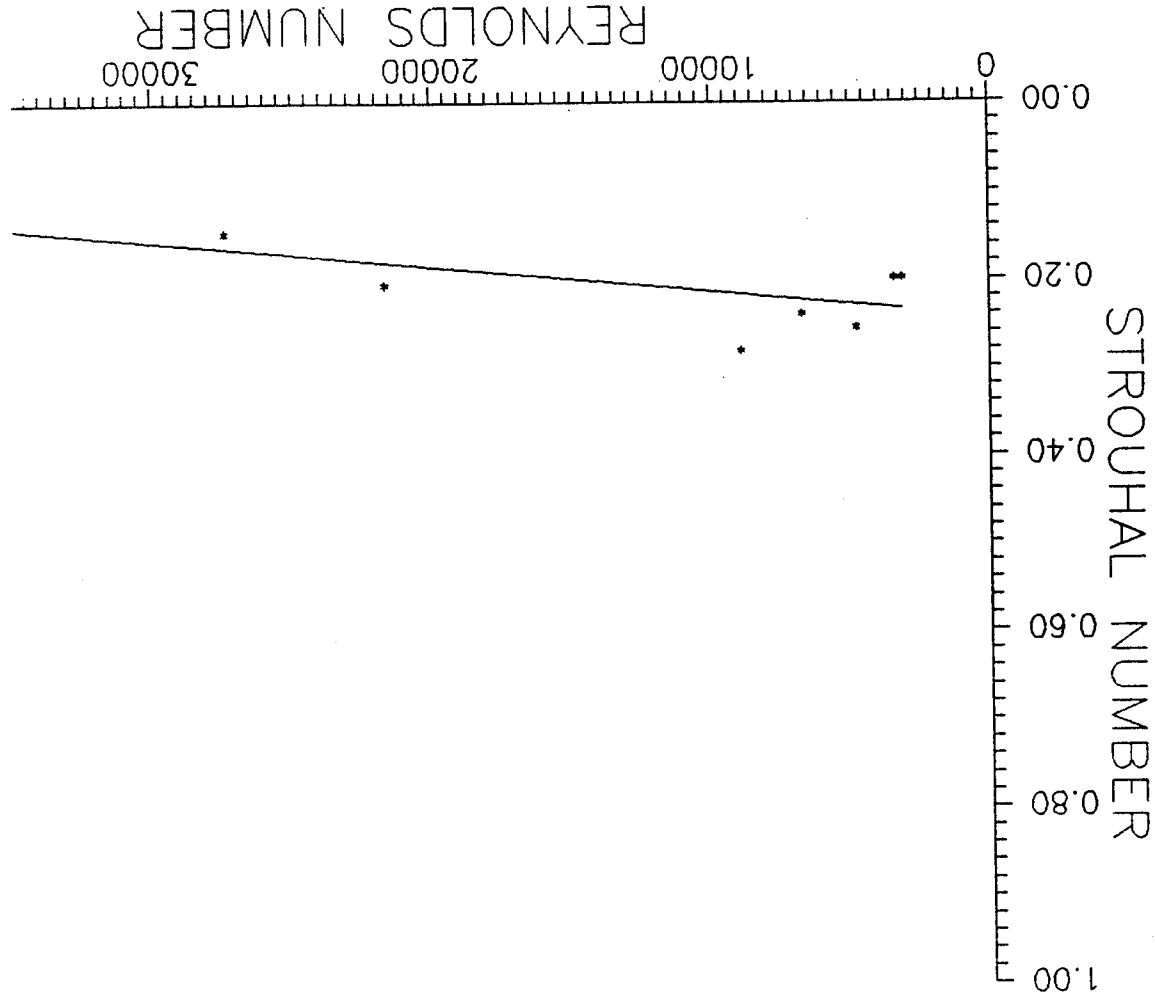
Figure 29. Strouhal number for peak wake frequency vs pipe Reynolds number; open slots, large fan, and trip ring.

corresponding frequency spectra are shown in Figure 30. The power spectra showed sharp peaks at the driven motor frequencies; and the emergence of detectable higher harmonics was noted as the supply pressure was increased.

The hot-wire probe was positioned 35 mm behind the model and 13 mm below the centerline in conjunction with different free stream velocities, motor speeds, and plenum pressures. Inspection of the velocity traces, taken when the perturbation generator was operating, showed little difference from the velocity traces taken in the unperturbed wake region. However, the frequency spectra taken from the perturbed velocity traces showed that the fundamental frequency, introduced by the perturbation generator, was the dominant frequency over the range of test conditions. Numerous frequency spectra were recorded to observe the effects of pipe free stream velocity, plenum pressure, and motor frequency. Examples of the frequency spectra for various flow conditions are shown in Figure 31. Figure 32 shows similar measurements when the direction of the perturbation generator spin was reversed.

The Strouhal number associated with frequency peaks, not associated with the perturbation signal, was also examined for the wake flow while the perturbation generator was running. The peaks corresponding to a Strouhal number of approximately 0.2 were not the same relative order of magnitude as those of the perturbation generator; however, they were significant compared with other peaks as shown in Figure 33. Again, the Strouhal number was plotted against the Reynolds number (Figure 34) and it showed a slight decrease as the Reynolds number increased (slope: $\simeq -1.2 \times 10^{-6}$, Re).
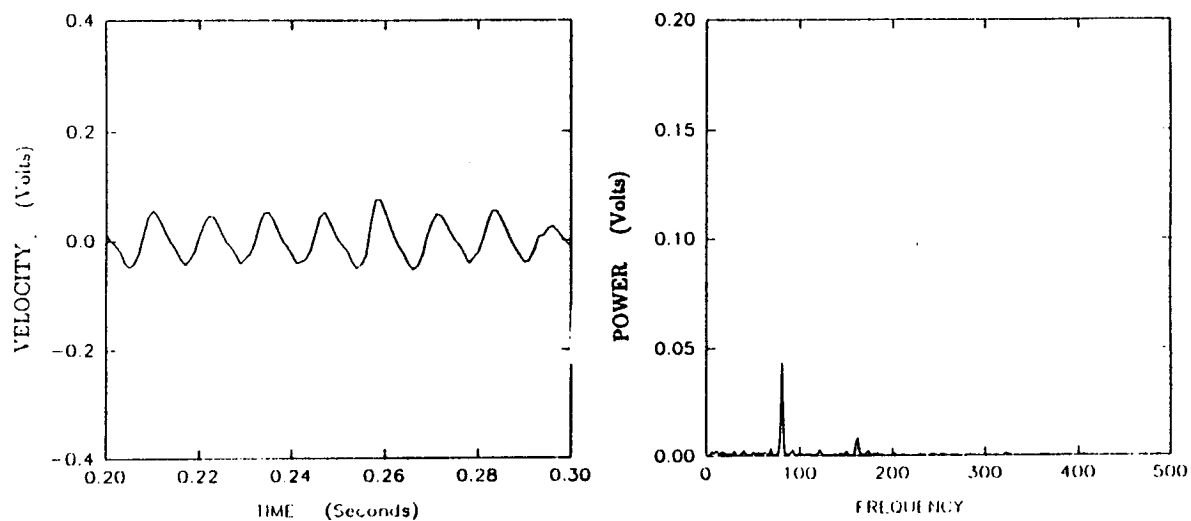
30a. $M_f = 80$ Hz, $\Delta P = 0.073$ torr (9.6 Pa.)
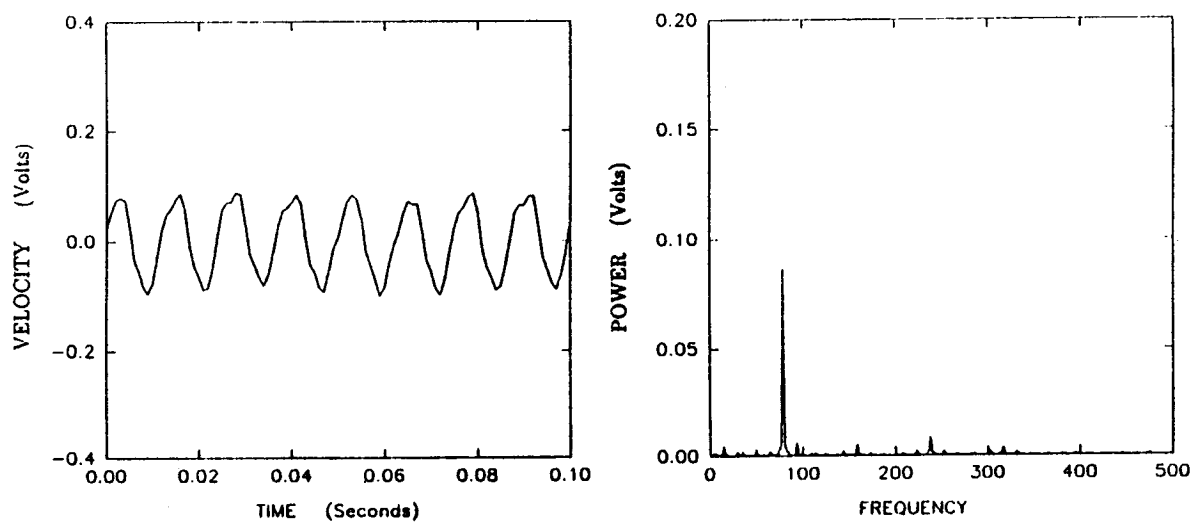
30b. $M_f = 79.1$ Hz, $\Delta P = 0.112$ torr (14.8 Pa.)

Figure 30... Time varying component of linearized hot-wire voltage (velocity) histories above perturbation slot and the corresponding voltage spectra. No cross flow.
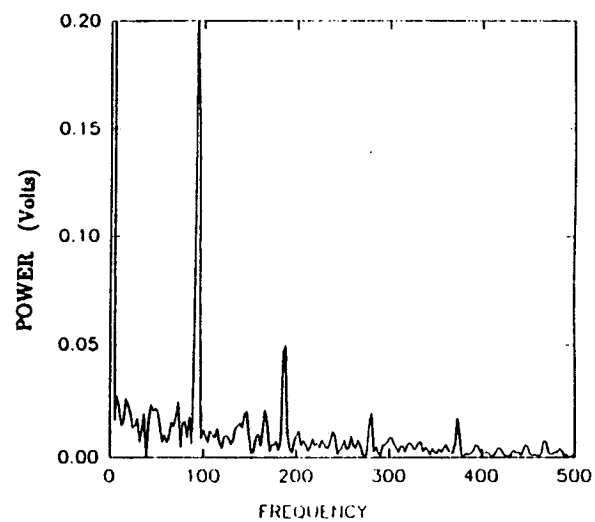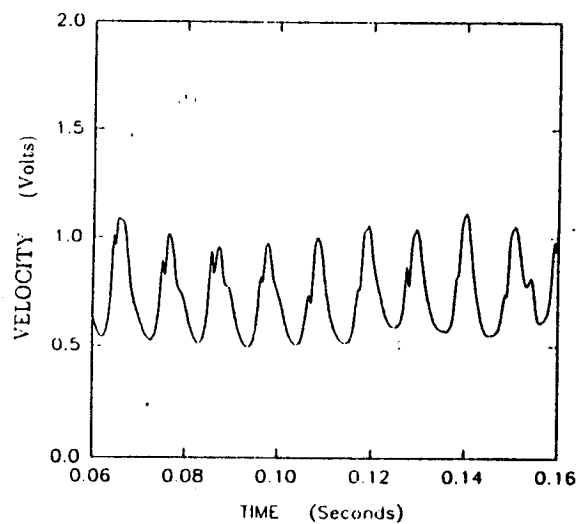
30c. $M_f = 95$ Hz, $\Delta P = 0.2$ torr (26 Pa.)
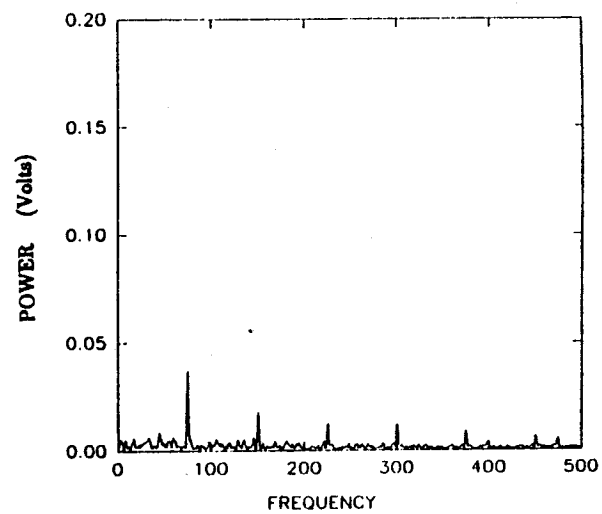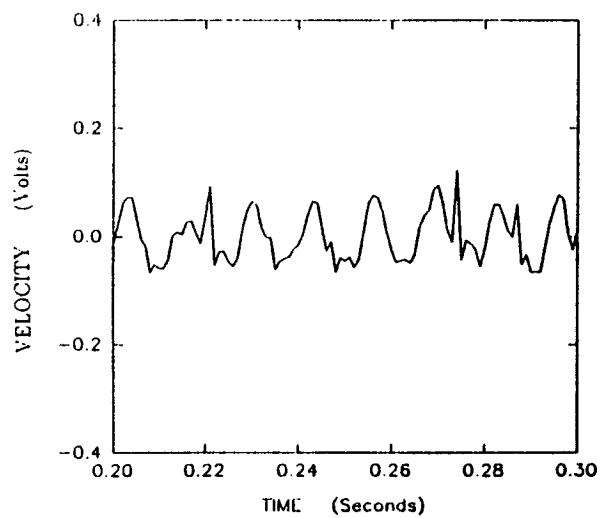
30d. $M_f = 75$ Hz, $\Delta P = 0.198$ torr (26 Pa.)

Figure 30 (continued)
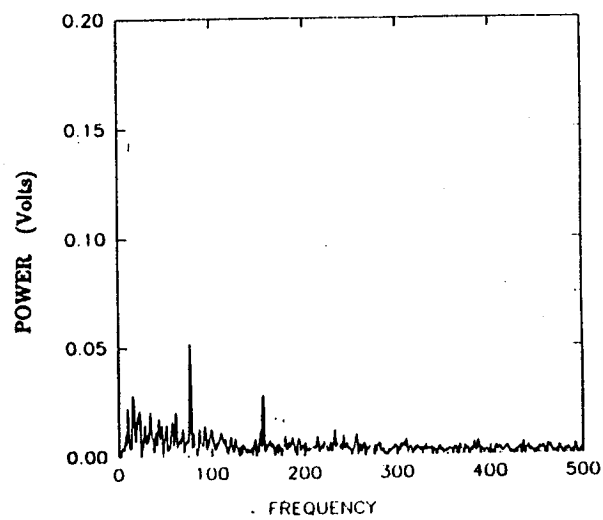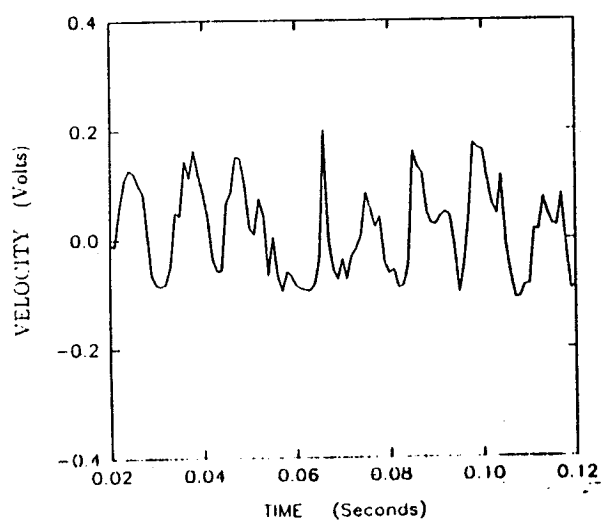
30e. $M_f = 77$ Hz, $\Delta P = .35$ torr (46 Pa.)
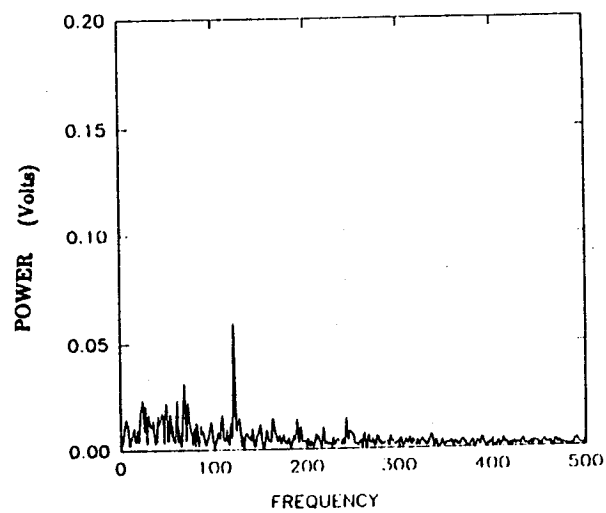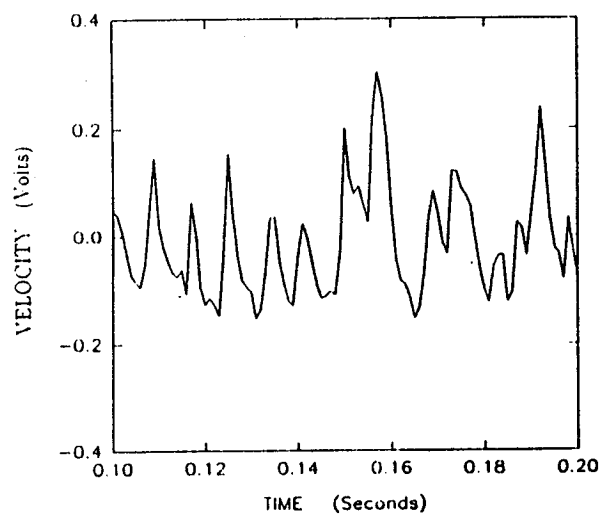
30f. $M_f = 121$ Hz, $\Delta P = 0.11$ torr (15 Pa.)

Figure 30 (continued)
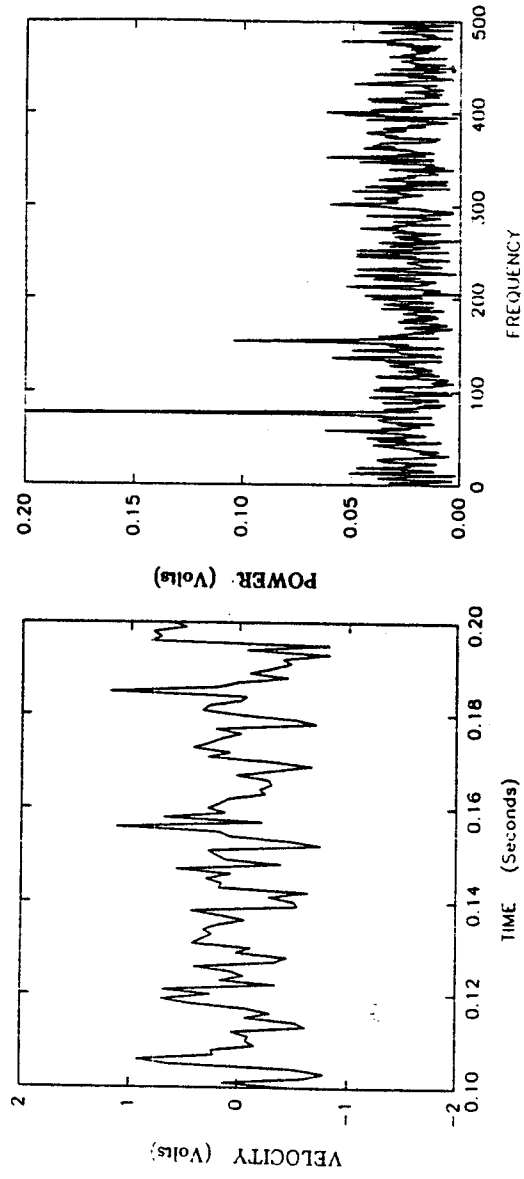
30g. $M_f = 77.1$ Hz, $\Delta P = 2.09$ torr (276 Pa.)
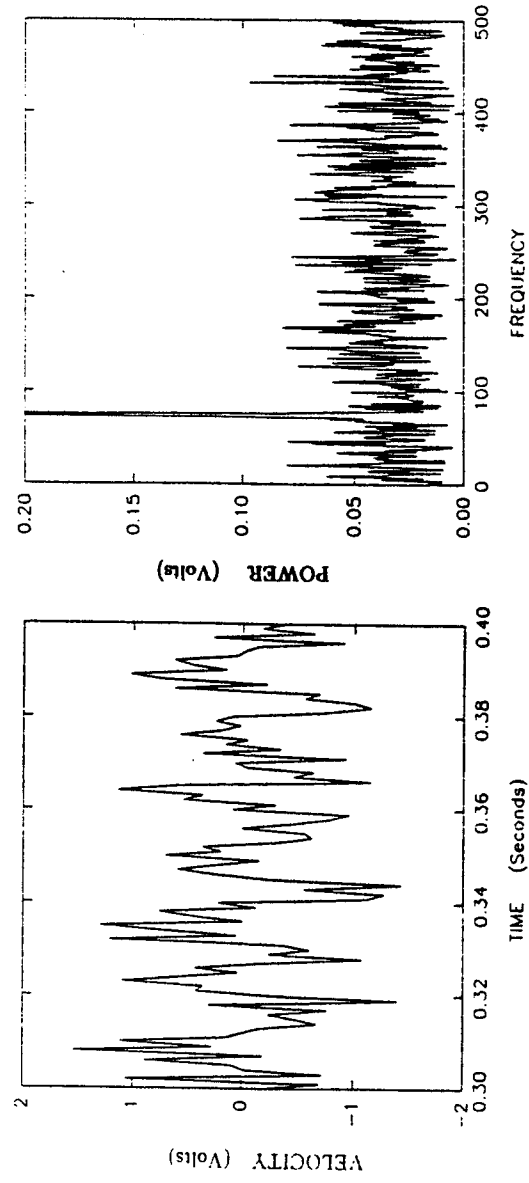
30h. $M_f = 74$ Hz, $\Delta P = 4.7$ torr (620 Pa.)

Figure 30 (continued)

-72-
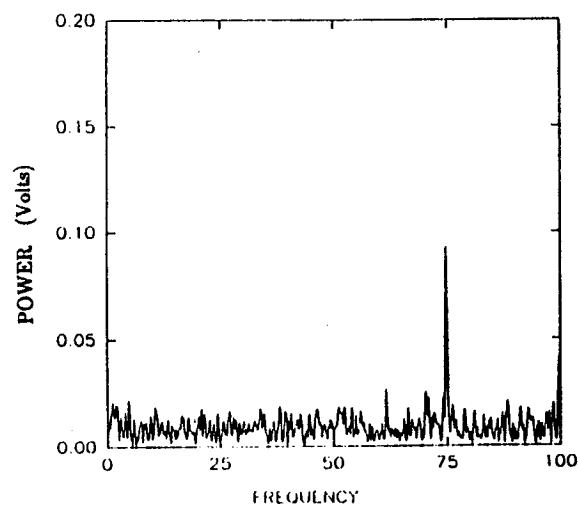
$U_\infty = 5.0$ m/s, $M_f = 75$ Hz, $\Delta P = 0.48$ torr (64 Pa)
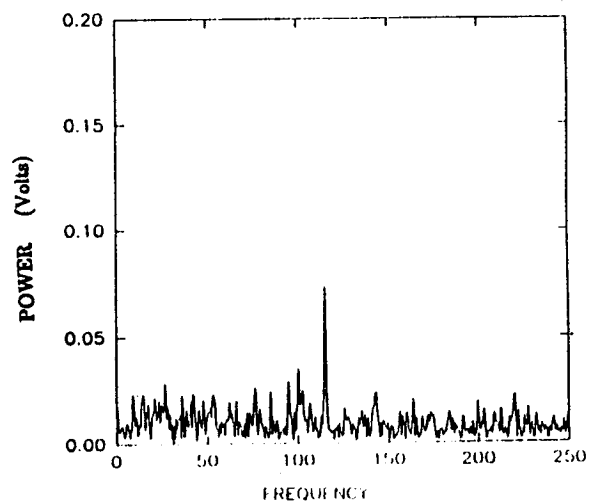
$U_\infty = 5.1$m/s, $M_f = 116$ Hz, $\Delta P = 0.43$ torr (57 Pa)
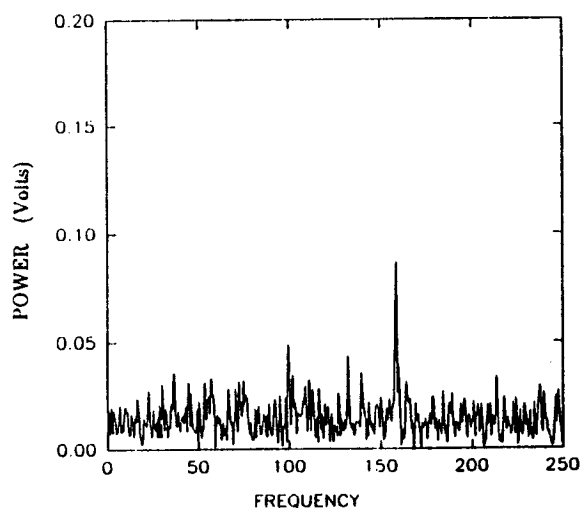
$U_\infty = 8.3$ m/s, $M_f = 158$ Hz, $\Delta P = 0.51$ torr (68 Pa)
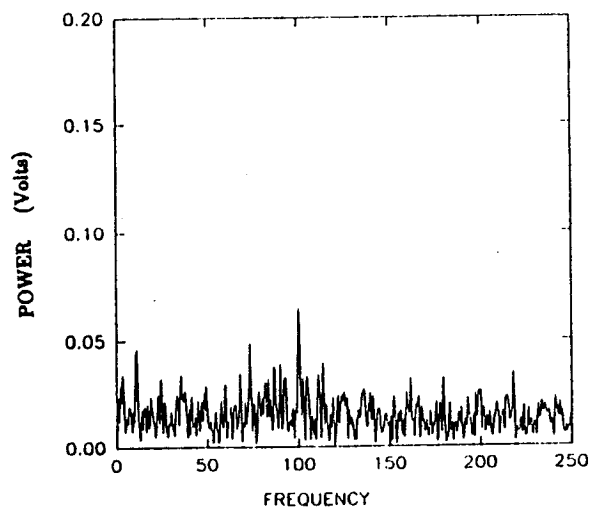
$U_\infty = 8.3$ m/s, $M_f = 221$ Hz, $\Delta P = 0.51$ torr (68 Pa)

31a Influence of Frequency.

Figure 31. Influence of perturbation frequency, plenum pressure and free stream velocity on frequency spectra.

-73-
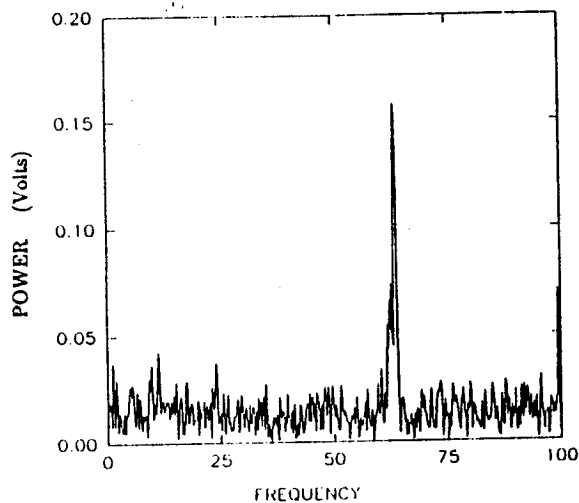
$U_\infty = 7.8 \text{ m/s}, \ M_f = 64 \text{ Hz}, \ \Delta P = 0.76 \text{ torr (101 Pa)}$
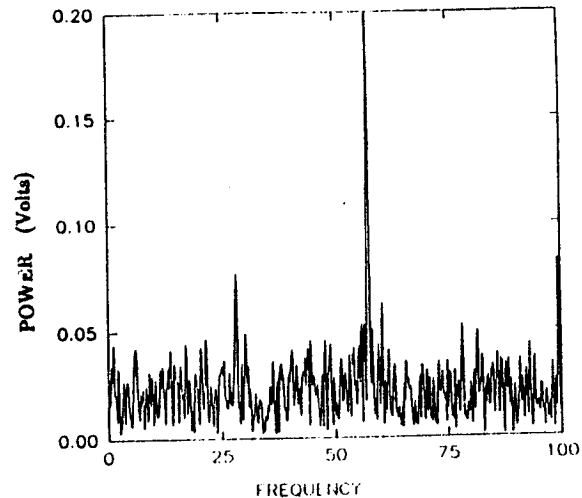
$U_\infty = 11.8 \text{ m/s}, \ M_f = 57 \text{ Hz}, \ \Delta P = 1.39 \text{ torr (185 Pa)}$
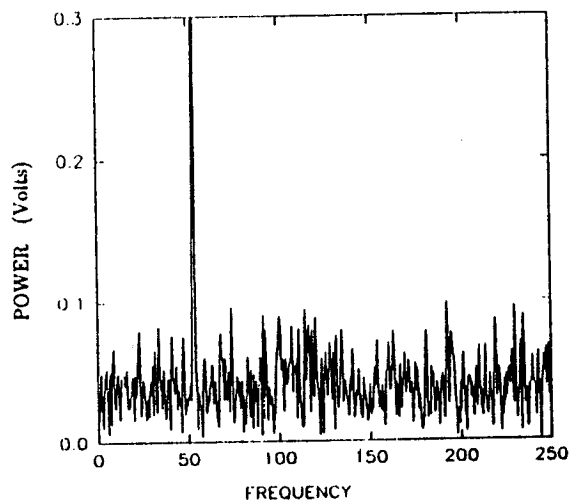
$U_\infty = 25.5 \text{ m/s}, \ M_f = 55 \text{ Hz}, \ \Delta P = 5.67 \text{ torr (755 Pa)}$
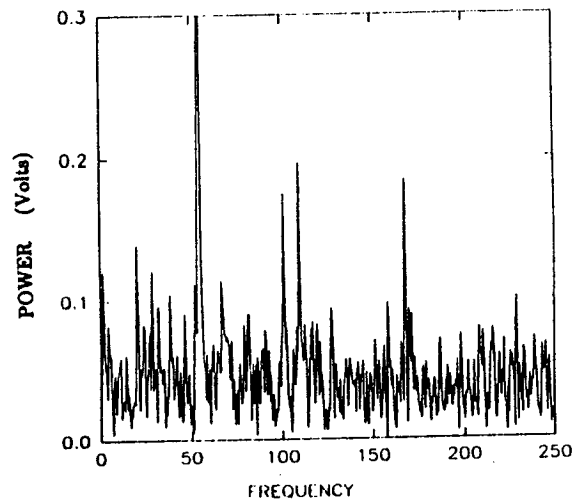
$U_\infty = 32.0 \text{ m/s}, \ M_f = 54 \text{ Hz}, \ \Delta P = 7.94 \text{ torr (1058 Pa)}$

31b. Influence of Free Stream Velocity.
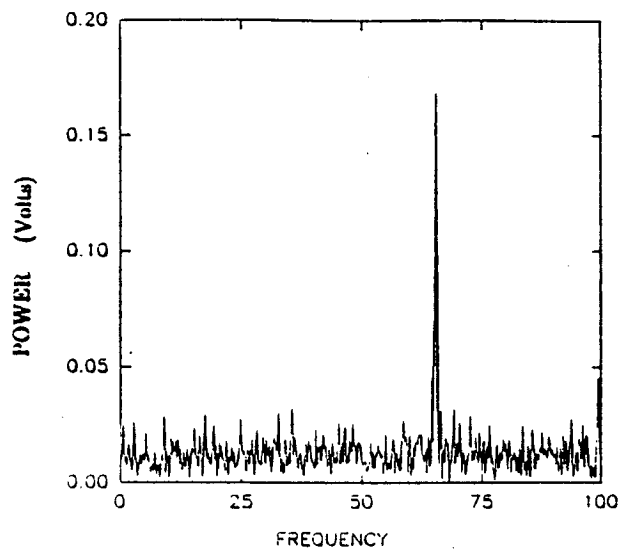
$U_\infty = 6.7$ m/s, $M_f = 66$ Hz,
$\triangle P = 0.52$ torr (69 Pa)
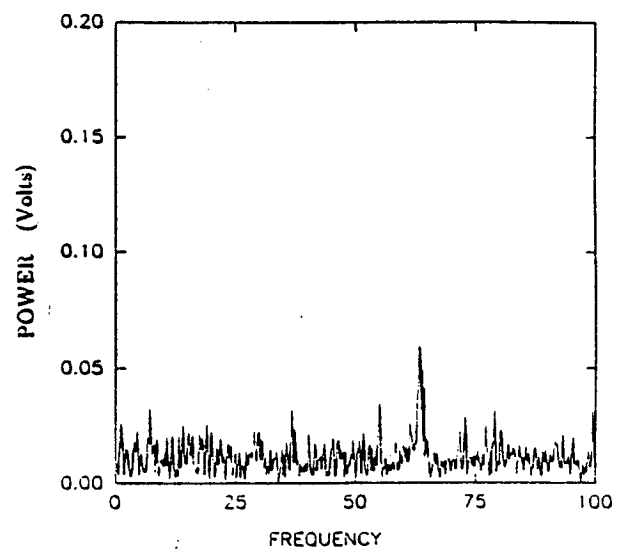
$U_\infty = 6.7$ m/s, $M_f = 64$ Hz,
$\triangle P = 0.97$ torr (129 Pa)

31c. Influence of Plenum Pressure
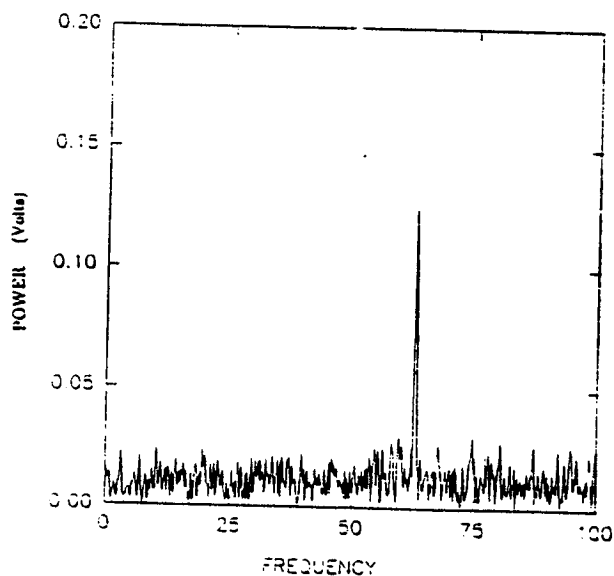
32a. $U_\infty = 6.7$ m/s, $M_f = 66$ Hz,
$\triangle P = 0.52$ torr (69 Pa)
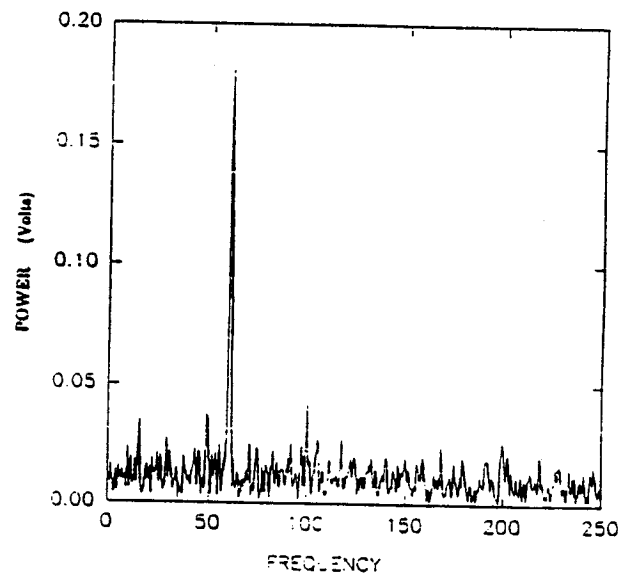
32b. $U_\infty = 6.7$ m/s, $M_f = 66$ Hz,
$\triangle P = 0.52$ torr (69 Pa)

Figure 32. Influence of direction of rotation on Frequency Spectra.
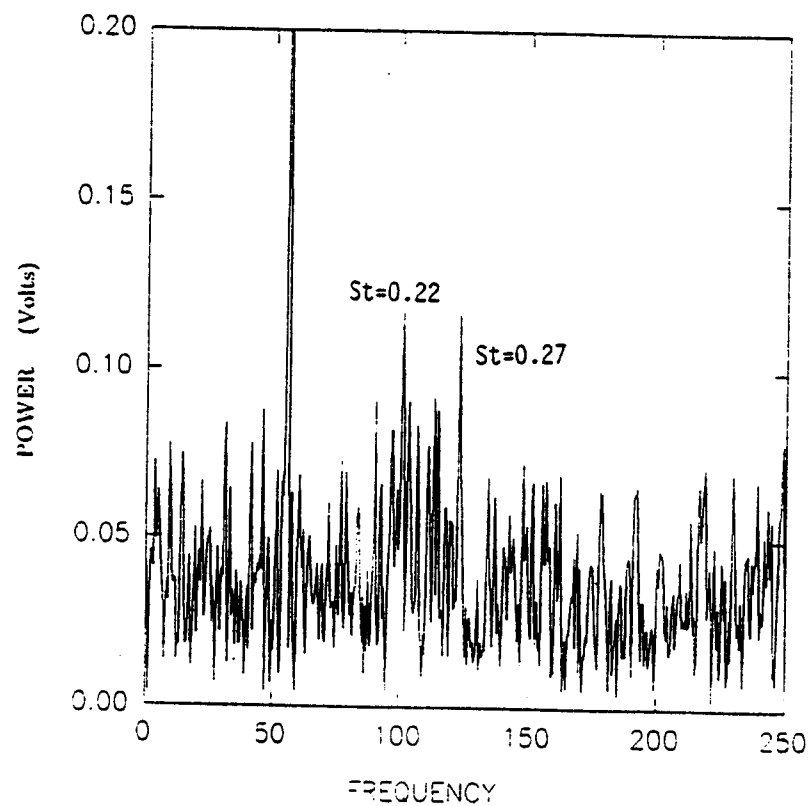
33a. $U_\infty = 13.7$ m/s. $M_f = 57$ Hz. $\Delta P = 1.9$ torr (253 Pa), perturbation generator peak larger.
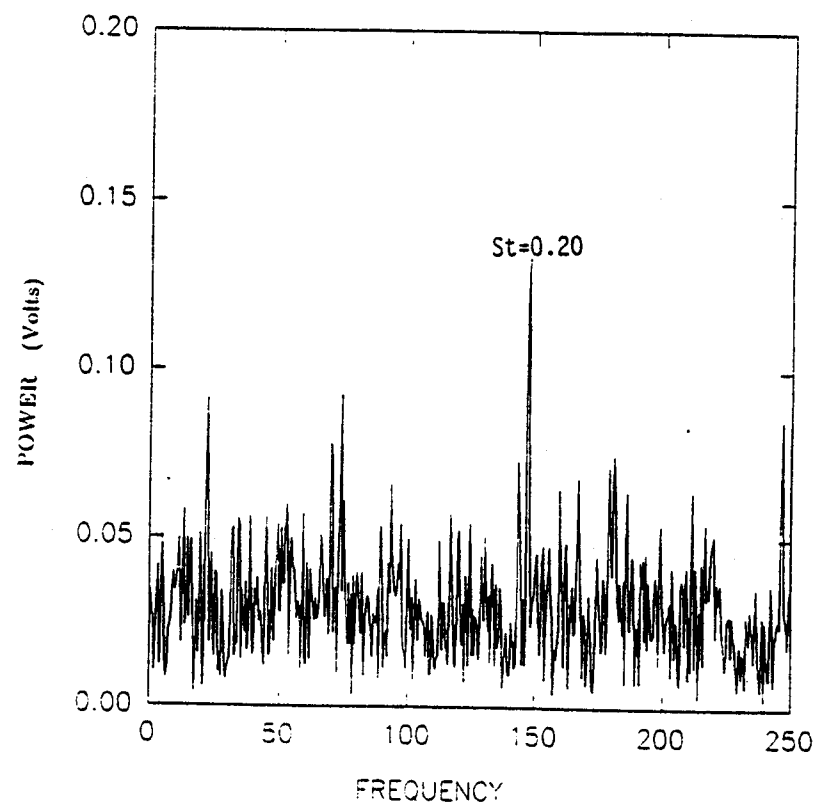
33b. $U_\infty = 22.7$ m/s, $M_f = 74$ Hz. $\Delta P = 3.8$ torr (506 Pa.), Strouhal number peak larger.

Figure 33. Comparison of peaks with Strouhal numbers $\simeq 0.2$ to those generated by the perturbation generator.

REYNOLDS NUMBER

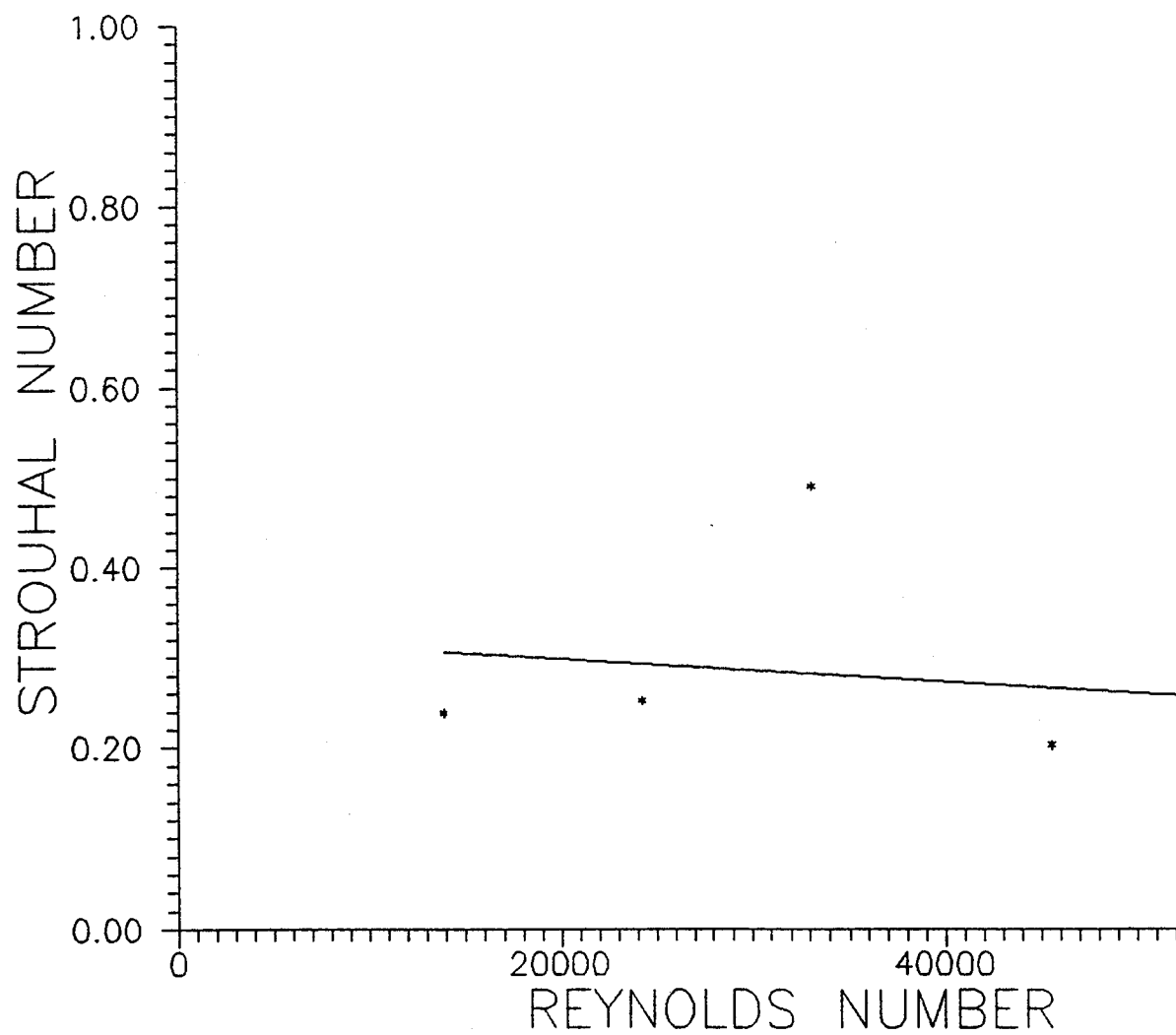| 0 | 20000 | 40000 | 60000 |

STROUHAL NUMBER
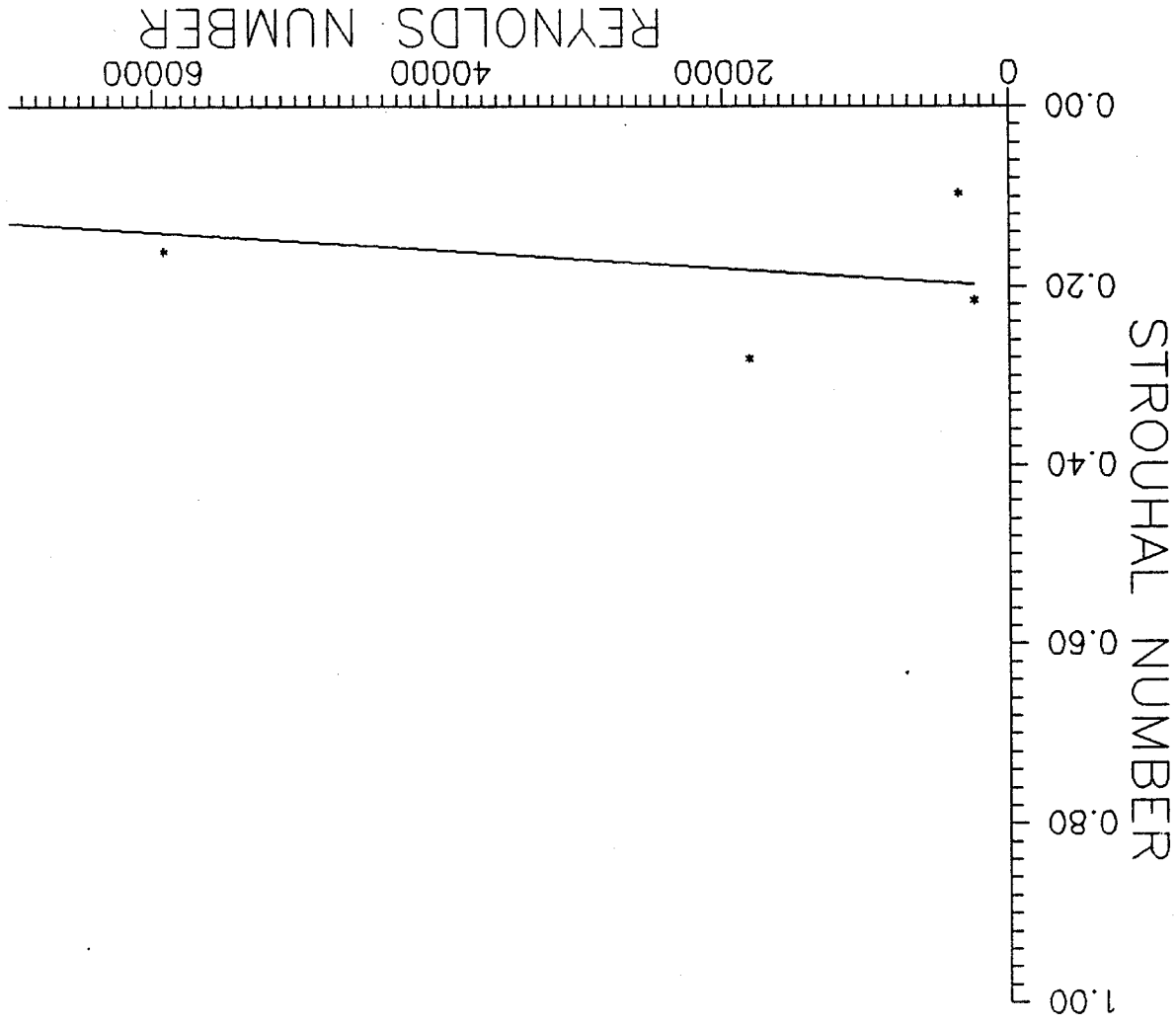
0.00 0.20 0.40 0.60 0.80 1.00

Figure 34. Strouhal number for peak wake frequency vs pipe Reynolds number with the perturbation generator operating, large fan, and trip ring.
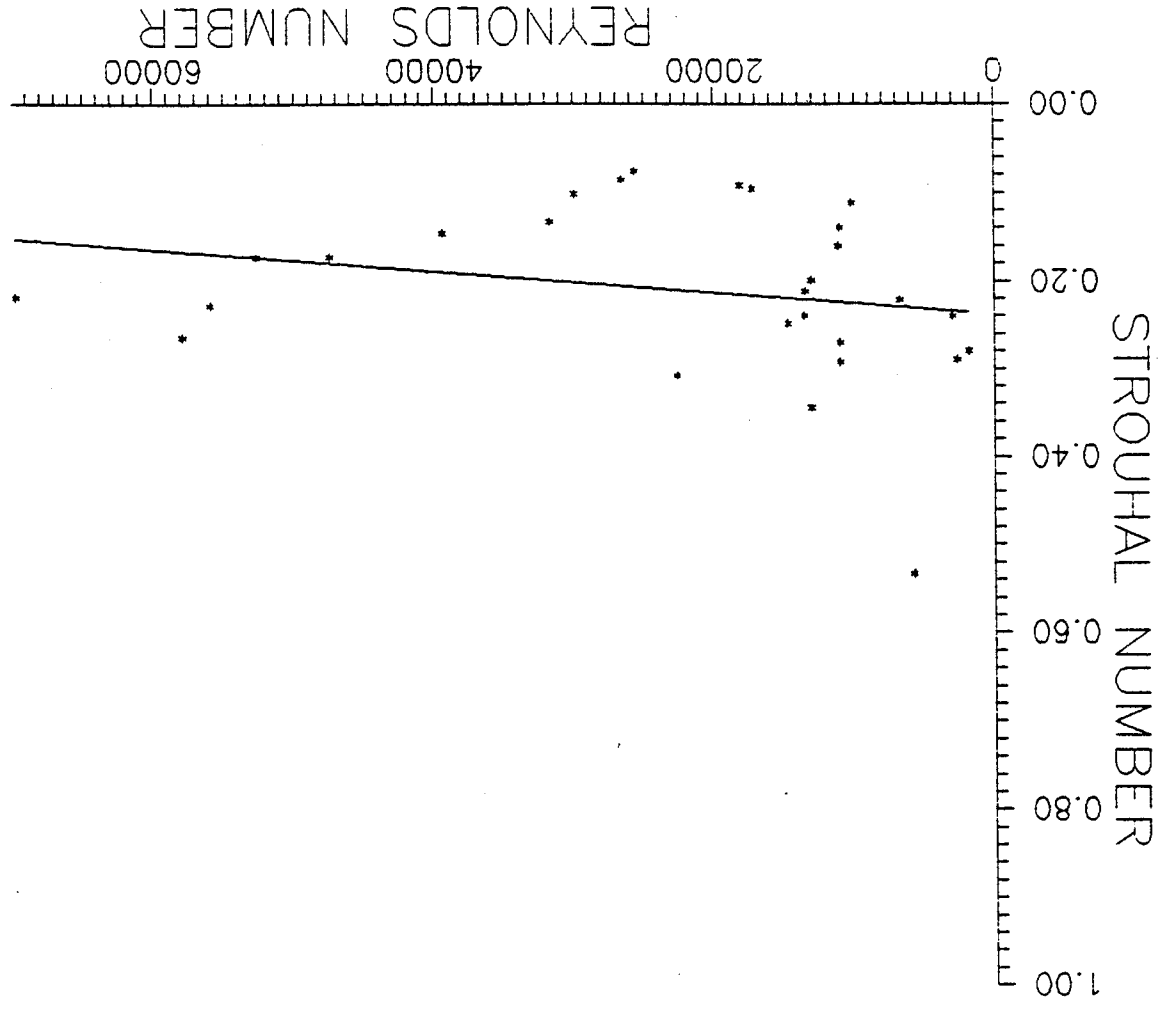
When the influence of natural transition was investigated by removing the circular ring trip wire, mounted on the nose of the axisymmetric body measurements were made with the perturbation generator in operation. Figure 35 shows that there were no noticeable differences between spectra taken with and without the circular ring trip wire. The only noticeable differences due to the trip wire can be seen in the plots of the Strouhal number versus the Reynolds number. When the trip wire was attached to the axisymmetric body, data occurred occasionally at higher Strouhal numbers (up to .55) for the low Reynolds number cases (5000 to 10,000) for both perturbed and unperturbed tests (Figure 36). When the circular trip wire was removed, there were no extraordinary Strouhal number peaks at the lower Reynolds numbers, as shown in Figures 37. The slopes of the best fit lines were about the same (slope: $\simeq -1.3 \times 10^{-6}$, Re) for the perturbation generator running and when the perturbation generator was secured (slope: $\simeq -1.0 \times 10^{-6}$, Re).

Resulting spectra obtained when traversing the hot-wire probe vertically through the wake to study the variation of the perturbation generator signal with respect to the location in the wake are shown in Figure 38. The spectra show that the amplitude of the peak corresponding to the perturbation signal increased to a maximum when the hot-wire was located 12 mm below the centerline. The peak amplitude became a minimum at the centerline, and then increased up to a position 12 mm above the centerline. Above 12 mm, the peak amplitude began to decrease again as the hot wire probe was moved further away from the wake center.
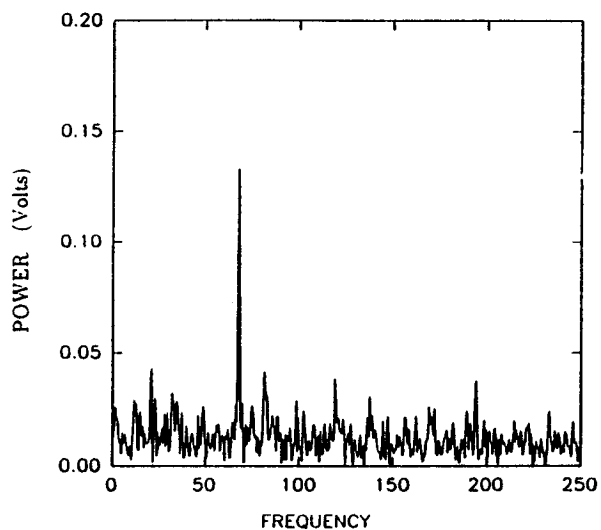
35a. Trip ring attached, U_∞ = 6.2 m/s,
M_f = 68 Hz, ΔP = 0.24 torr (32 Pa)
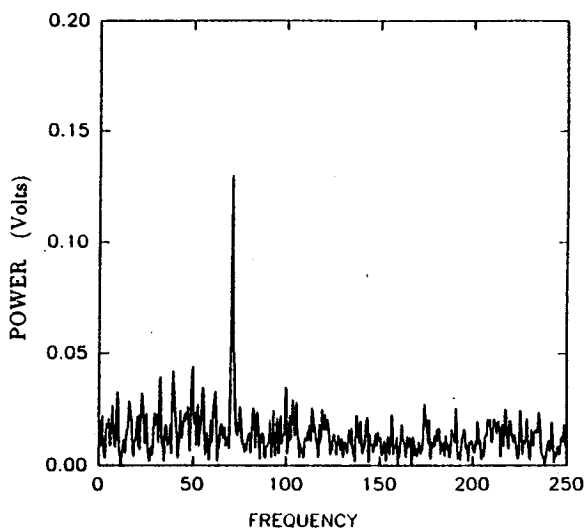
35b. Trip ring removed, U_∞ = 6.4 m/s,
M_f = 70 Hz, ΔP = 0.36 torr (48 Pa)
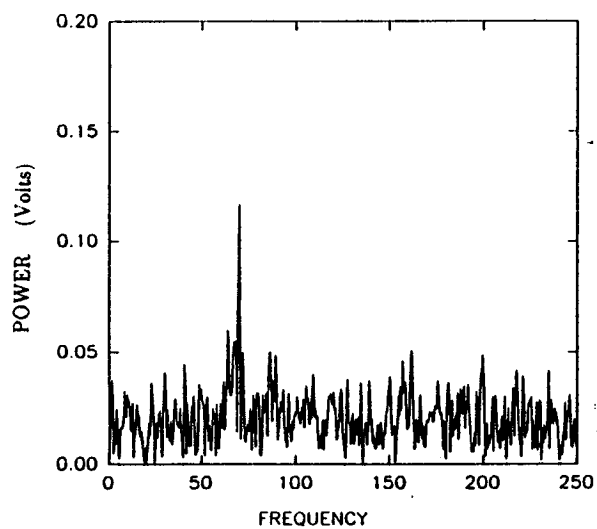
35c. Trip ring attached, U_∞ = 10.3 m/s,
M_f = 70 Hz, ΔP = 0.46 torr (61 Pa)
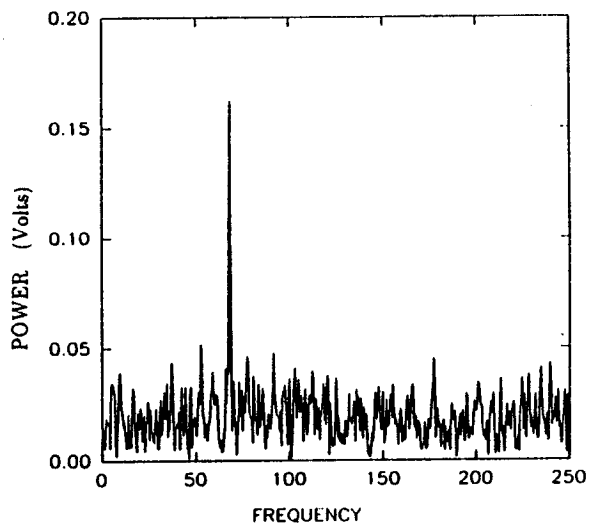
35d. Trip ring removed, U_∞ = 11.0 m/s,
M_f = 67 Hz, ΔP = 0.67 torr (89 Pa)

Figure 35. Comparison between spectra with the circular trip ring attached and when the ring was removed.
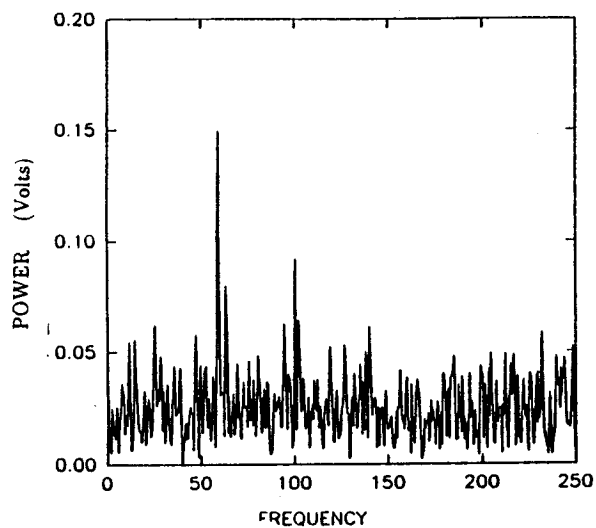
35e. Trip ring attached, $U_\infty = 14.5$ m/s,
$M_f = 59$ Hz, $\Delta P = 0.85$ torr (113 Pa)
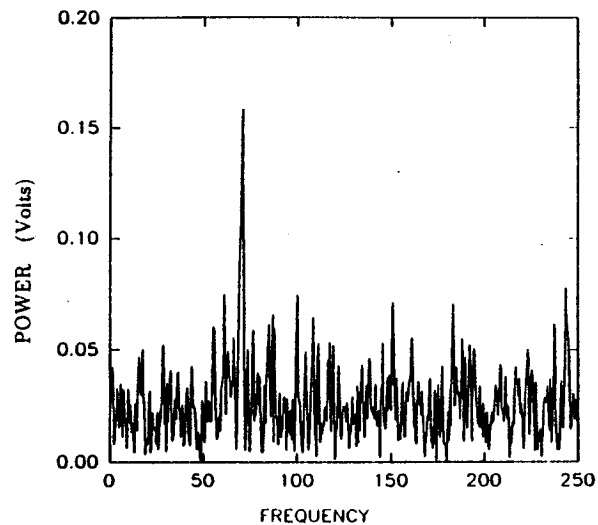
35f. Trip ring removed, $U_\infty = 15.1$ m/s,
$M_f = 70$ Hz, $\Delta P = 0.9$ torr (120 Pa)
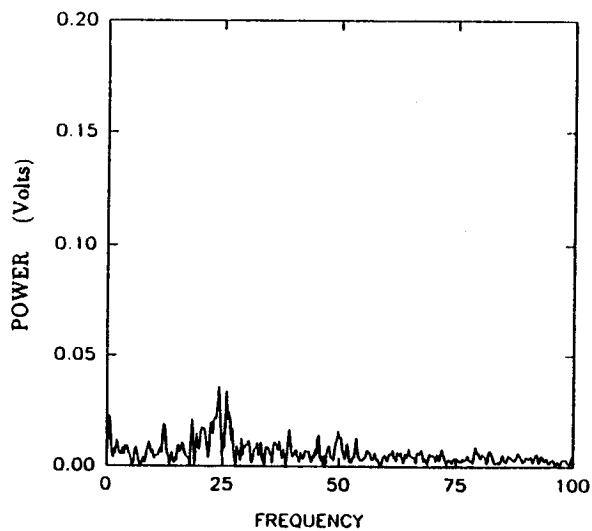
35g. Trip ring attached, $U_\infty = 3.1$ m/s,
Perturbation generator secured.
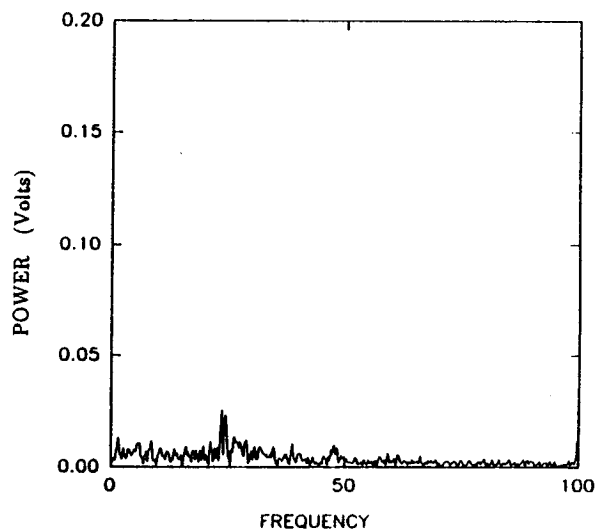
35h. Trip ring removed, $U_\infty = 2.4$ m/s,
Perturbation generator secured.

Figure 35 continued

Figure 36. Strouhal number for peak wake frequency vs pipe Reynolds number with the perturbation generator operating, large fan, and no trip ring.
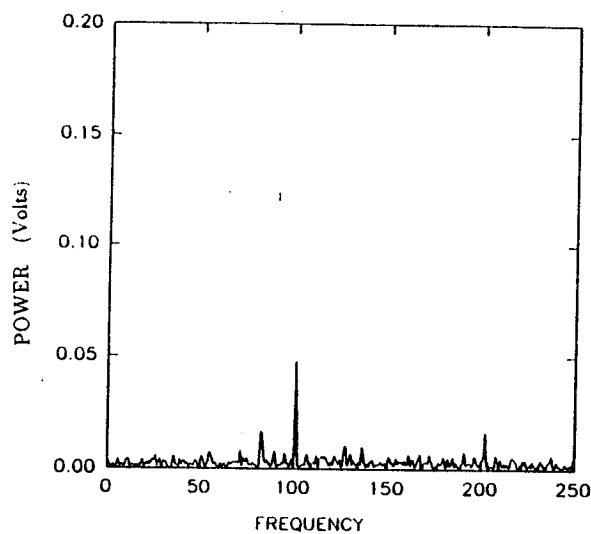
38a. $U_\infty = 6.2$ m/s, $M_f = 84$ Hz,
$\Delta P = .5$ torr (66 Pa), $y = +20$ mm.
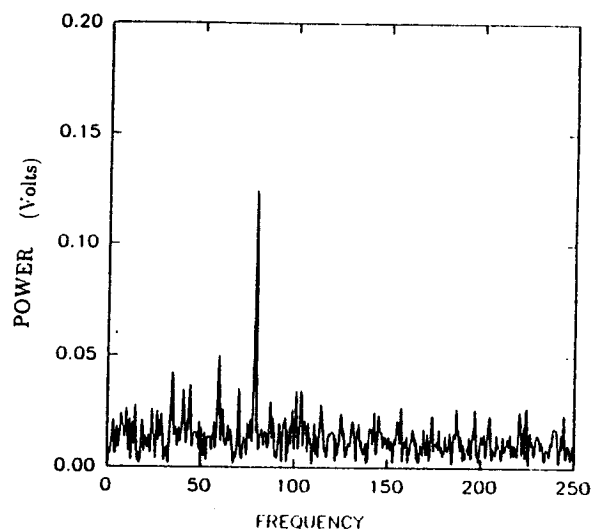
38b. $U_\infty = 6.2$ m/s, $M_f = 78$ Hz,
$\Delta P = .45$ torr (59 Pa), $y = +10$ mm.
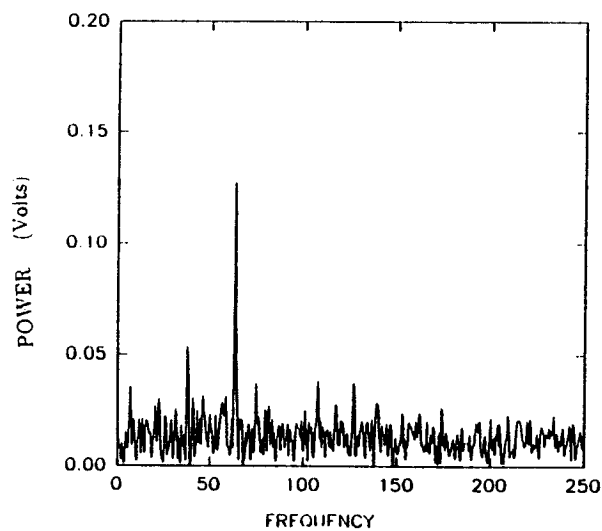
38c. $U_\infty = 6.2$ m/s, $M_f = 64$ Hz,
$\Delta P = .45$ torr (59 Pa), $y = +5$ mm.
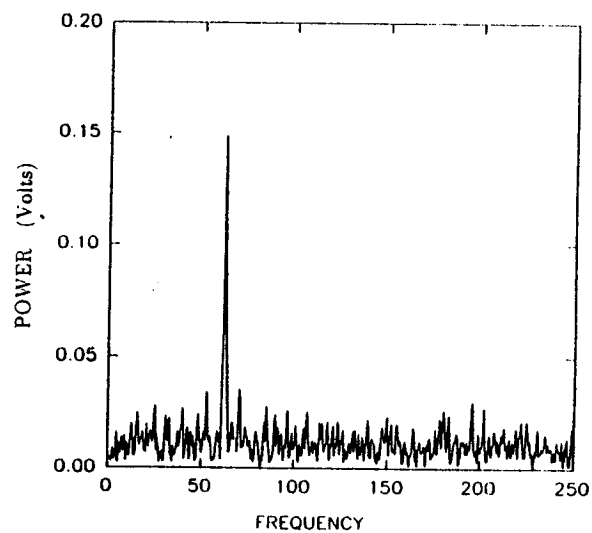
38d. $U_\infty = 6.2$ m/s, $M_f = 61.5$ Hz,
$\Delta P = .45$ torr (59 Pa.), $y = 0$

Figure 38. Influence of hot-wire vertical position on perturbation signal ($x = 38$ mm).

-83-
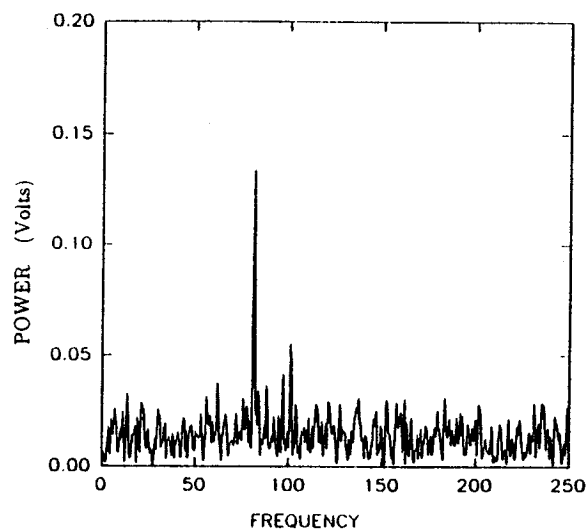
38e. $U_\infty = 6.2$ m/s, $M_f = 81$ Hz,
$\Delta P = .45$ torr (59 Pa), y = -5 mm.
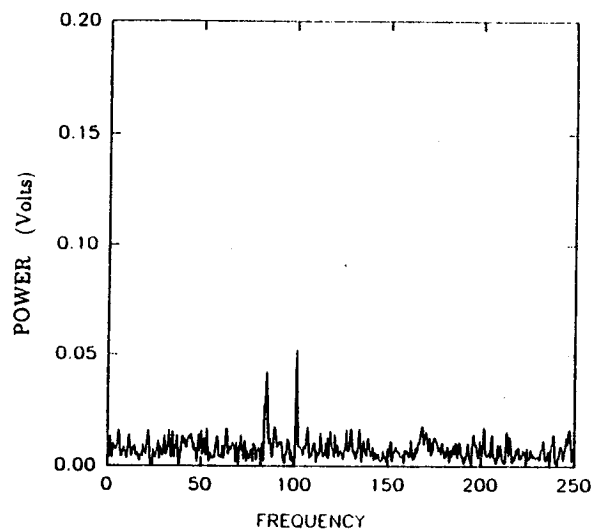
38f. $U_\infty = 6.2$ m/s, $M_f = 86$ Hz,
$\Delta P = .45$ torr (59 Pa), y = -10 mm.
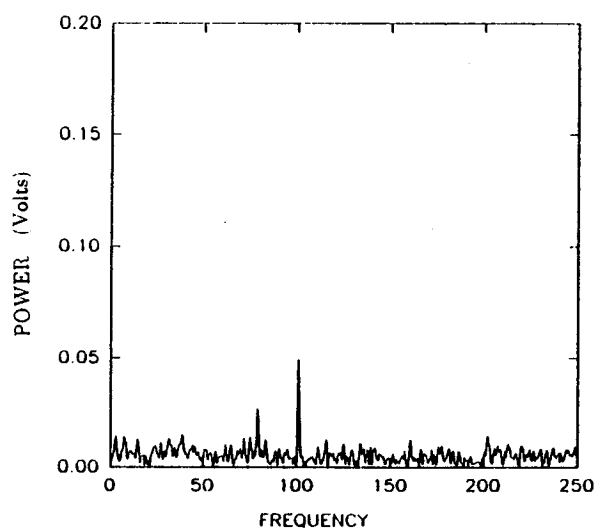
38g. $U_\infty = 6.2$ m/s, $M_f = 81$ Hz,
$\Delta P = .45$ torr (59 Pa), y = -17 mm.
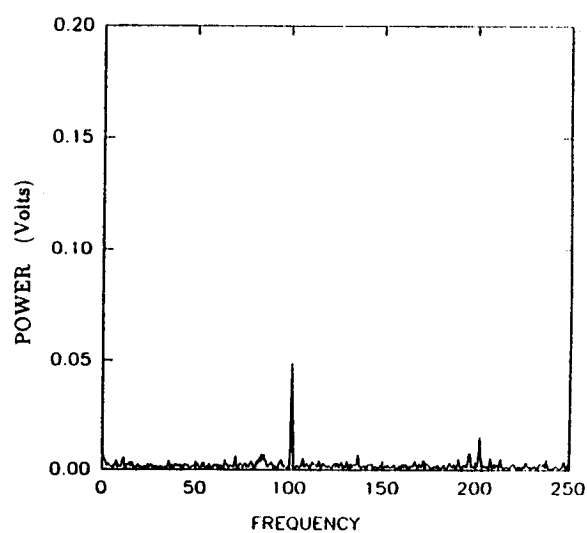
38h. $U_\infty = 6.2$ m/s, $M_f = 83$ Hz,
$\Delta P = .45$ torr (59 Pa), y = -20 mm.

Figure 38 continued

-84-

Measurements of the mean velocity and RMS levels of the flow field were taken as the hot-wire probe was traversed vertically through the wake. Maximum differential pressures were less than 100 Pa in virtually all of these tests and it was determined from the mass flow rate analysis developed in Section 3.1, that the injected volume flow rate was less than 0.01 percent of the unmodified pipe flow rates in all cases tested. Figure 39 shows that the wake velocity distribution is modified slightly by the perturbation generator at low speeds (6 m/s). At higher speeds (14 m/s) the injected air may have altered the separation region as indicated by the velocity profile measurements shown in Figure 40. However, the variations in velocity profiles in both figures could be due partially to changes in pipe flow mean velocities and drift in hot-wire signals due to temperature changes.

The mean flow profile using the small fan is shown in Figure 41, which indicates a slight jet in the center of the wake when the perturbation generator is being operated. This is not seen when the perturbation generator is secured and the jet is possibly due to the air injection at the low pipe free stream velocities. Neglecting measurement errors, the ratio of momentum flow to the square of the corresponding volume flowrate can be used to assess the influence of the perturbation generator operation on the overall flow conditions in the pipe. Those ratios were calculated using velocity surveys taken at nominal pipe flow speeds of 6 m/s and 14 m/s with the perturbation generator operating at 75 Hz. The data show changes in the momentum ratios of less than 0.1 percent between the perturbed and unperturbed cases. Since alteration of the flow separation zone is considered to be the most significant effect, the impact of the perturbation generator on the anticipated vortex experiments was
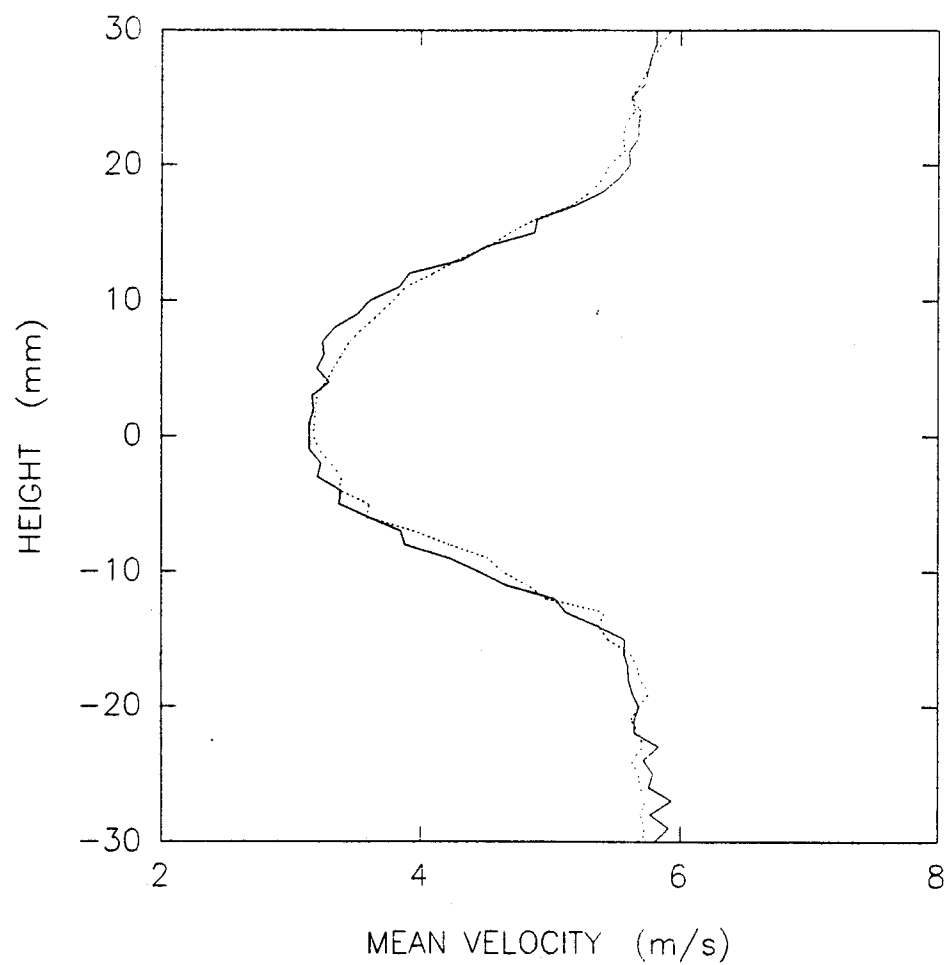
Figure 39. Mean velocity profiles, 38 mm behind the perturbation generator, $U_\infty = 6$ m/s. The dashed line is for $M_f = 77$ Hz, $\triangle P = .234$ torr (31 Pa), and the solid line is without perturbation.
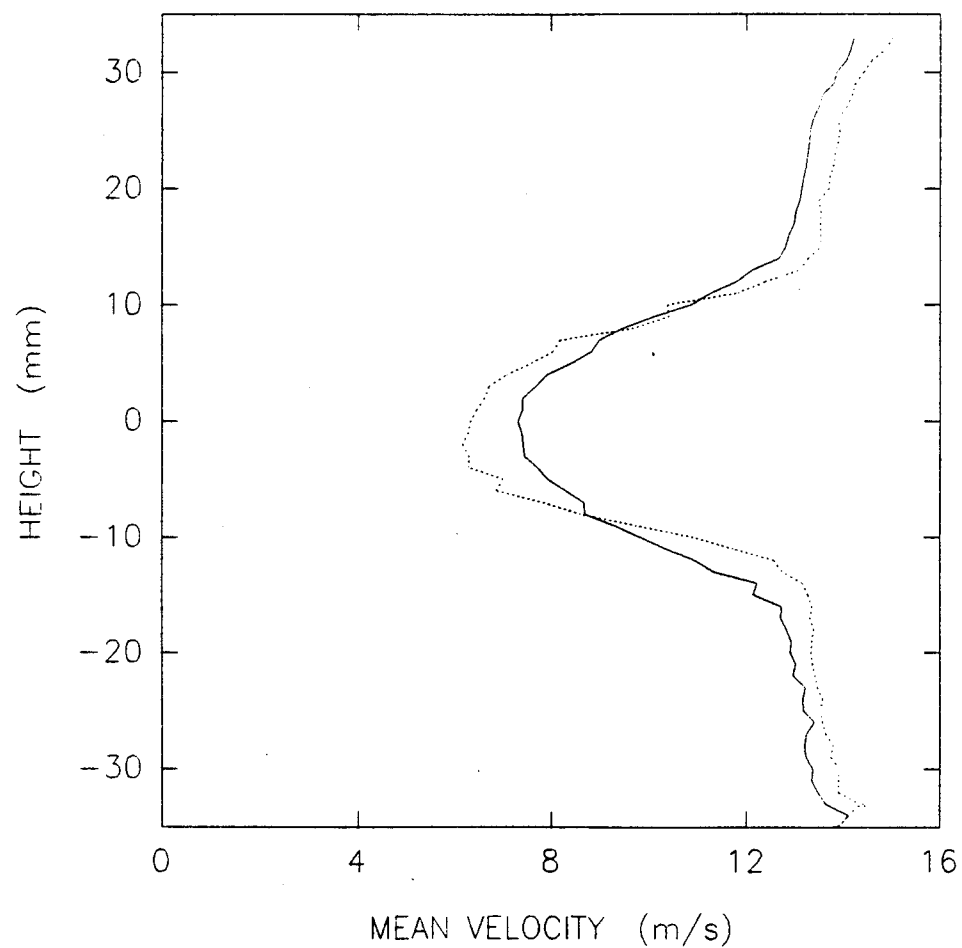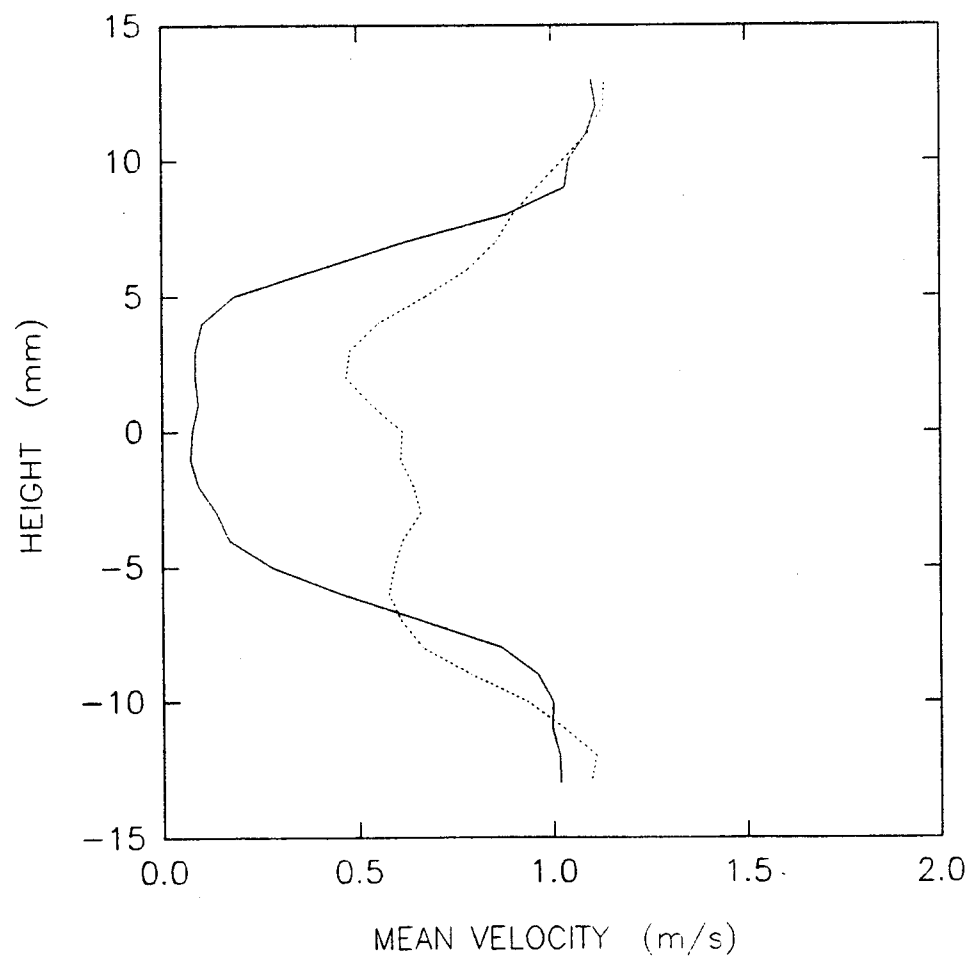
Figure 40. Mean velocity profiles, 38 mm behind the perturbation generator, $U_\infty = 14$ m/s. The dashed line is for $M_f = 72$ Hz, $\triangle P = 2.82$ torr (375 Pa), and the solid line is without perturbation.

Figure 41.   Mean velocity profiles, 38 mm behind the perturbation generator, $U_\infty = 1$ m/s. The dashed line is for $M_f = 74$ Hz, $\triangle P = .33$ torr (50 Pa), and the solid line is without perturbation.

considered to be minimal because flow separation was inhibited by the swirling flow around the centerbody[16].

Comparisons of the RMS levels between the perturbation generator at the nominal setting of 75 Hz were made in conjunction with the mean velocity profile measurements and are shown in Figure 42. There are only small differences between the two curves and the differences may be attributed to differences in pipe free stream velocity or drift in hot-wire signals due to temperature changes. There is also some asymmetry in the curves seen between the upper portion (above the centerline) and the portion from below the centerline. This is possibly due to the hot-wire probe being off center as it traversed the wake.

The hot-wire probe was moved downstream in the pipe to a location 2.5 meters behind the perturbation generator. Measurements were taken with various combinations of pipe free stream velocity, motor frequency, and plenum pressure. Spectra from the velocity traces did not show any evidence of amplitude peaks at the fundamental frequency of the perturbation generator output. Some samples of the spectra are shown in Figure 43. Those data imply that the perturbation signal was damped out as it was convected down the pipe. This was expected and it was not considered important to determine how far downstream the perturbed signal was convected before it was lost in the background noise.
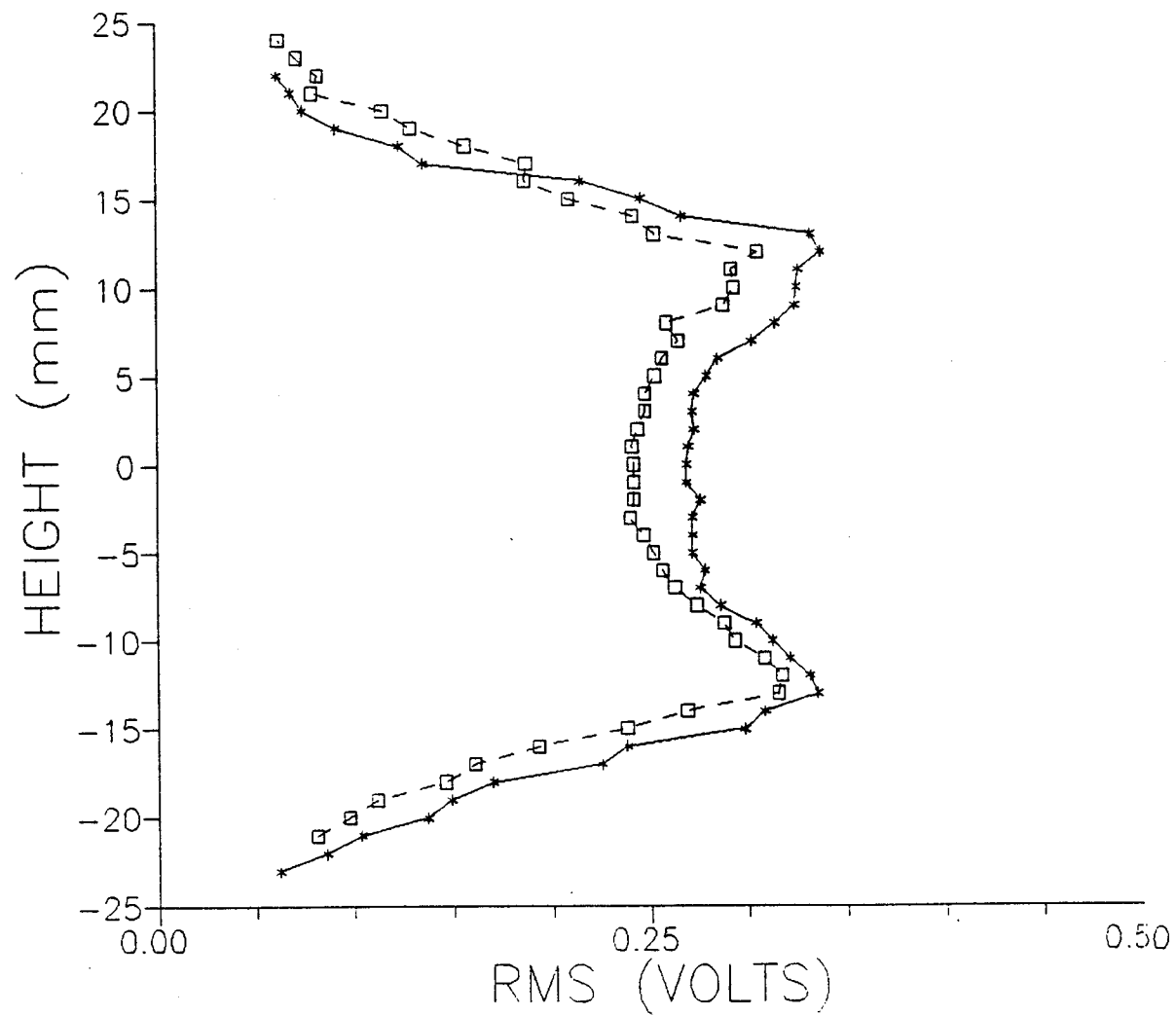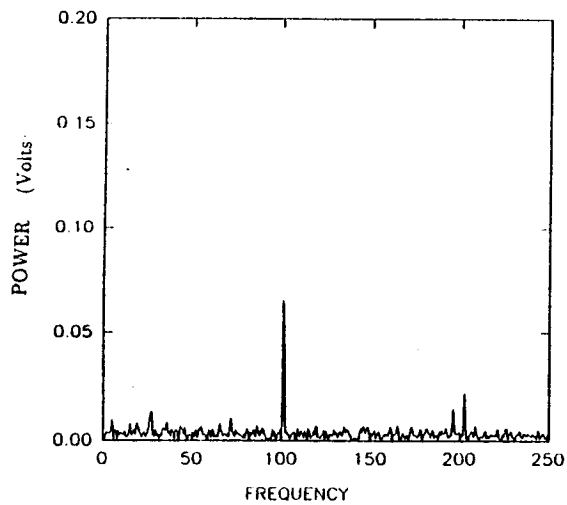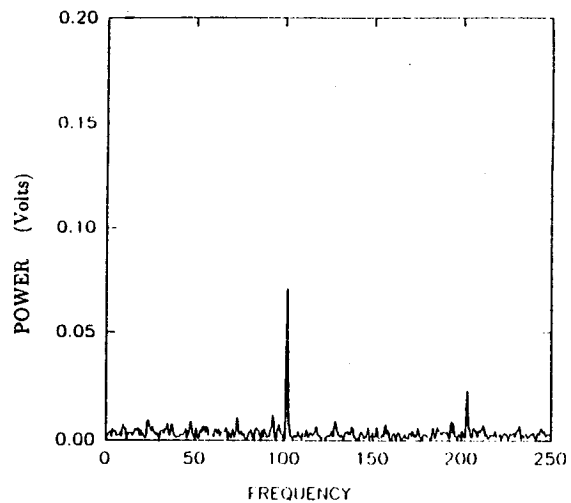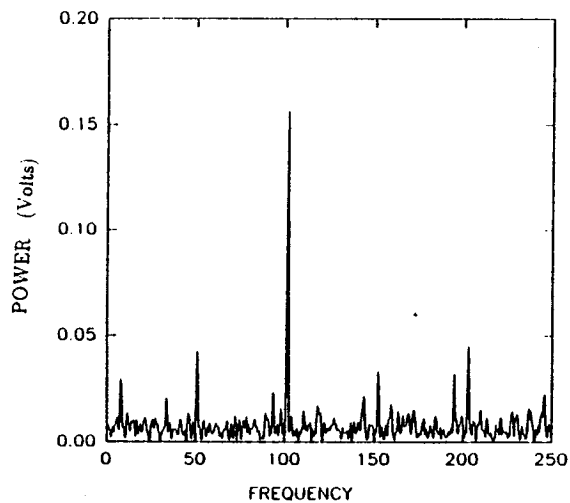
Figure 42. RMS profile of the wake, 38 mm behind the perturbation generator. $U_\infty = 6$ m/s. The dashed line is for $M_f = 67.4$ Hz, $\Delta P = .316$ torr (42 Pa), and the solid line is without perturbation.
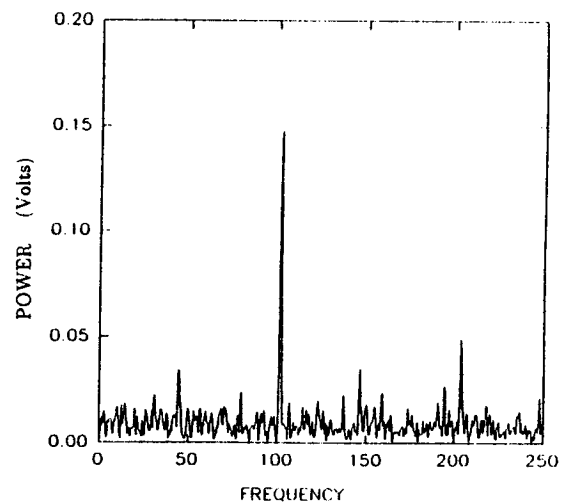
43a. Perturbation generator secured, $U_\infty = 6.8$ m/s.

43b. $U_\infty = 6.3$ m/s, $M_f = 77$ Hz, $\Delta P = .38$ torr (50 Pa.)

43c. Perturbation generator secured, $U_\infty = 17.7$ m/s.

43d. $U_\infty = 18.3$ m/s, $M_f = 65.4$ Hz, $\Delta P = 2.2$ torr (290 Pa.)

Figure 43. Spectra taken 2.5 meters downstream of the perturbation generator.

4.1 EQUIPMENT AND TEST PROCEDURE IN THE 2' X 3' TUNNEL

After completion of model bench testing in the 4-inch pipe facility, the perturbation generator was installed in the NASA Langley 2' x 3' Low Speed Boundary Layer Channel Wind Tunnel (Fig 44). The closed loop wind tunnel test section has a cross section which is 0.91 m wide by 0.61 m high with a usable length of 6.1 m. A 35 horsepower motor drives a fan which produces a maximum free stream velocity of 50 m/s in the test section. Low turbulence levels are maintained using a honeycomb, followed by four screens which are located ahead of the contraction. The test section had adjustable upper and lower walls to minimize pressure gradients and maintain nearly constant free stream conditions. Maximum static pressure variations in the test section were controlled to less than 1 percent of the dynamic pressure.[20] Manual control of flow speed was accomplished using a rheostat system which controls the motor voltage. The controller was operated "locally" outside the wind tunnel or "remotely" from inside the control room. Data runs were made at nominal free stream velocities of 7, 14, 21, and 42 m/s.

The wind tunnel free stream velocity was measured using a standard, 5 mm diameter pitot-static tube with a stagnation port and four peripheral static pressure ports. The pitot-tube extended into the test section from the ceiling and was positioned approximately 0.7 meters downstream from the beginning of the test section. The pitot probe differential pressure lines were connected (at external ports) across a Datametrics, Type 570 Barocel
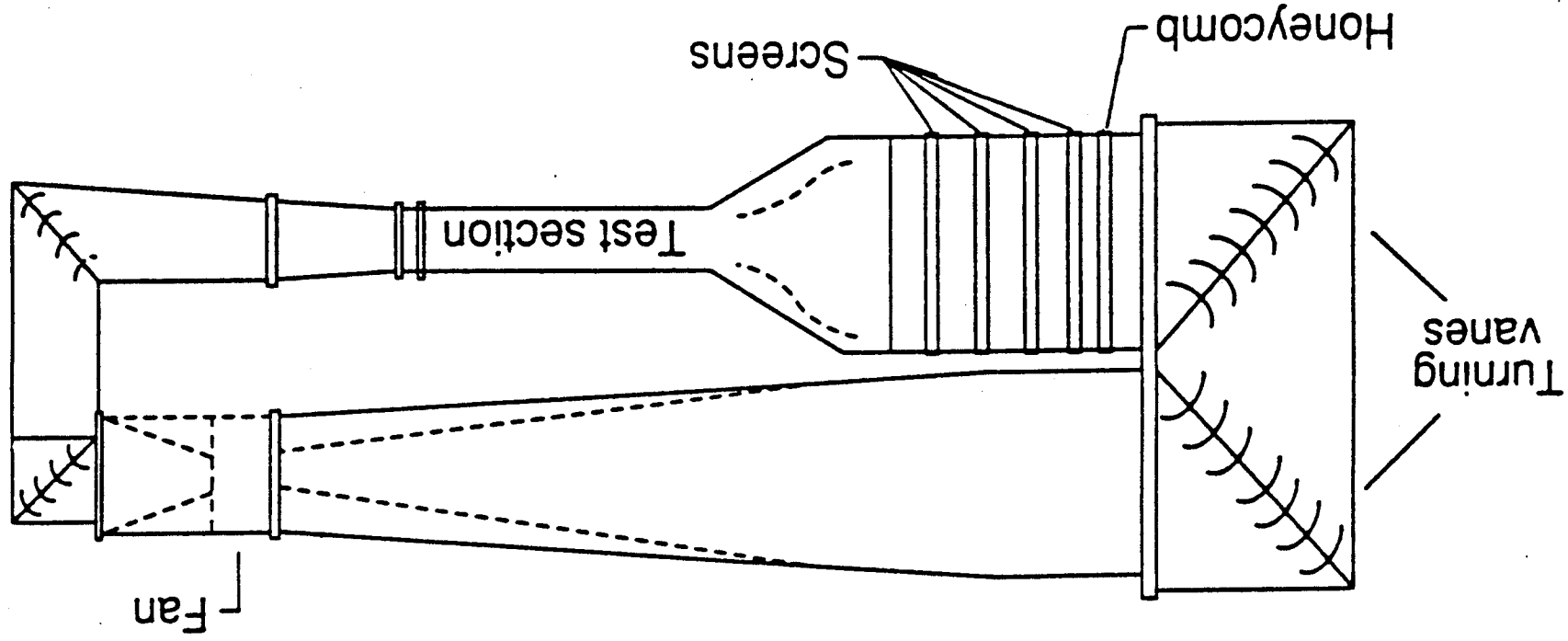
Figure 44. Schematic of 2' X 3' Wind Tunnel[21]

Pressure Sensor. The free stream temperature, T_∞, was measured using an iron-constantan thermocouple, located in the inlet portion of the test section.

The vortex flow field behind the 1-inch diameter centerbody was measured using a seven-hole probe and hot-wire anemometry, as reported by Stead.[20] Vortex flow field measurements taken after the perturbation generator was installed were taken using hot-wire anemometry. The same instrumentation used in the 4-inch pipe was used in the 2' X 3' wind tunnel experiments, except the data from the Data 6000 Waveform Analyzer were sent to an HP1000 computer instead of the IDS PC microcomputer. The HP1000 computer was used to collect and store the following data: hot-wire frequency spectra information; hot-wire mean and RMS velocities; wind tunnel velocities; perturbation generator plenum pressures; and hot wire probe position information. The HP1000 computer was programmed for data collection in either an automatic or a manual mode.

Similar to the pipe experiments, the Data 6000 Waveform Analyzer was set up utilizing two buffers, but with three data channels and it was triggered from the HP1000. Buffer A was set up to sample 1024 points with a sample rate of 2 ms. The hot-wire velocity trace was decomposed into DC and fluctuation (AC) parts and the separate elements were input to two channels. The DC part was used to determine the mean velocity of the trace. An FFT and RMS function were performed on the AC component of the velocity trace. These were sent to the HP1000 for storage. The only time the sampling rate was changed was during the high speed wind tunnel tests which required higher frequency resolution.

The second Data 6000 buffer (B) was set up to sample 2048 samples points with a sampling rate of 0.4 ms. The shorter sampling interval was required for determination of the perturbation generator motor speed. As explained before, the motor rotation produced a characteristic frequency which was equal to ten times the actual motor frequency. The hot-wire was calibrated for a maximum velocity of 25 m/s, which corresponded to the maximum velocity obtained in the majority of the 4-inch pipe tests.

Position control of the hot-wire probe was accomplished automatically using a digitally controlled Probe Positioning System (PPS), similar to the single-axis system used in the 4-inch pipe facility. The PPS consisted of three identical control units--each controlling movements along one orthogonal axis of motion inside the test section. The control units could be controlled locally at the unit (using switches), remotely from a control box mounted on the wind tunnel (for probe alignment purposes), or using inputs generated by an HP 9825 computer. The computer controlled data acquisition via an IIPIB interface bus and managed the probe position concurrently. The vertical, or y-axis control unit was the only one used in the automatic mode while the spanwise (z) and streamwise (x) movements of the hot-wire were controlled manually. Limit switches were not installed on the traverse system; hence operation of the system had to be monitored closely to avoid probe and model damage.

At the completion of wind tunnel testing by Stead, the vortex generator described previously was kept in the same wind tunnel test position (airfoils at + 8° and - 8°). The motor housing unit (which was not used in the 4-inch pipe facility) was used to attach and transition the perturbation generator to the 25.4 mm diameter centerbody. The motor leads

and perturbation generator plenum air supply and pressure sensing lines were fed through the 7.95 mm (5/16 inch) stainless steel tubing which supported the vortex generator unit. A hole was cut in the tubing, at the centerbody location, to allow the wires and perturbation air supply to traverse through the centerbody. It should be noted that air was supplied to the perturbation generator through the stainless steel tube from the opposite side of the wind tunnel as the electrical leads.

After the perturbation generator was installed on the model centerbody, tests were conducted operating the device without an imposed free stream velocity to ensure that the perturbation generator was still producing a sinusoidal velocity signal. These tests were accomplished with a hot-wire anemometer probe located at the outlet of the perturbation generator slot and the cyclic velocity signal (without crossflow) was measured. The perturbation generator was found to produce a velocity perturbation signal, similar to Figure 30, enabling the follow-on wind tunnel tests.

The perturbation generator plenum pressure could not be used directly to control perturbation velocity because the external local static pressure was influenced by the wind tunnel free stream velocity (Figure 45). It was noted that as the free stream velocity was increased, the plenum pressure, referenced to the tunnel static pressure at the walls, also increased. The local static pressure was measured for various wind tunnel free stream velocities by using the model plenum pressure sensor while the air supply to the model was secured. The difference, ΔP, between the perturbation plenum pressure, and local static pressure could then be determined during wind tunnel testing.
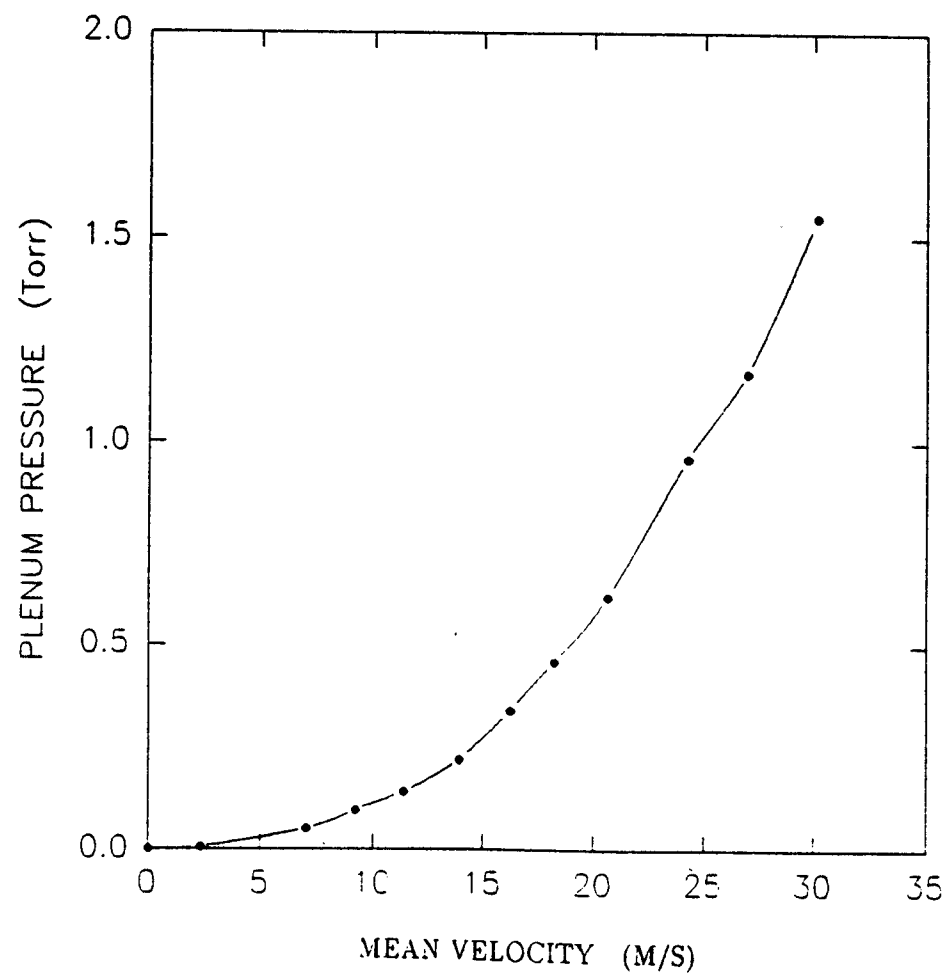
Figure 45. Variation of slot static pressure with freestream velocity.

The hot-wire probe was placed initially at the aft end of the test section. This "downstream" location was at an x-location of 48' 1" (14.66 m). The tail of the perturbation generator was located at a reference x-location of 34' 1" (10.39 m), which meant that the distance between the perturbation generator and the hot-wire probe was 14' (4.27 meters). This distance corresponded to 42 generator airfoil chord lengths. The center of the vortex was estimated from Stead's measurements in the wind tunnel. Vortex location was established accurately via velocity surveys. Specifically, vertical velocity surveys of the mean and RMS levels in the downstream x-plane to establish the vertical vortex center. The wake (decrease in mean velocity) and corresponding increase in RMS levels, which accompany the vortex enabled estimation of the vertical center of the vortex (Figure 46). Subsequently, the probe was positioned on the estimated vertical vortex axis, (the 276 mm position for the case shown in Figure 46) and a horizontal survey of mean and RMS levels was conducted (Figure 47).

The horizontal center of the vortex was established in the same manner as the vertical survey (e.g. -3 mm for Figure 47). Since these two surveys were not taken concurrently, the probe was positioned in the nominal lateral center and then a second set of vertical and horizontal surveys were taken to refine the vortex center location. After that procedure was completed, the probe was positioned in the center of the vortex for data collection. This centering procedure was performed each time the longitudinal (x) position in the wind tunnel was changed. A vertical survey was conducted to verify the position of the vortex center after each wind tunnel velocity change, and at the start of each testing period. The vertical
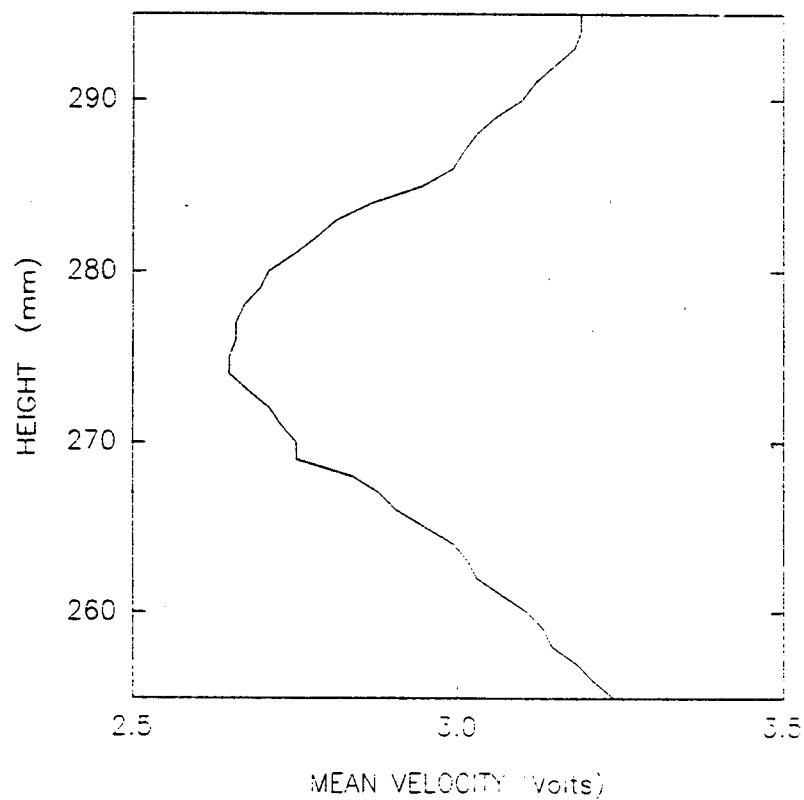
46a. Mean Velocity Survey
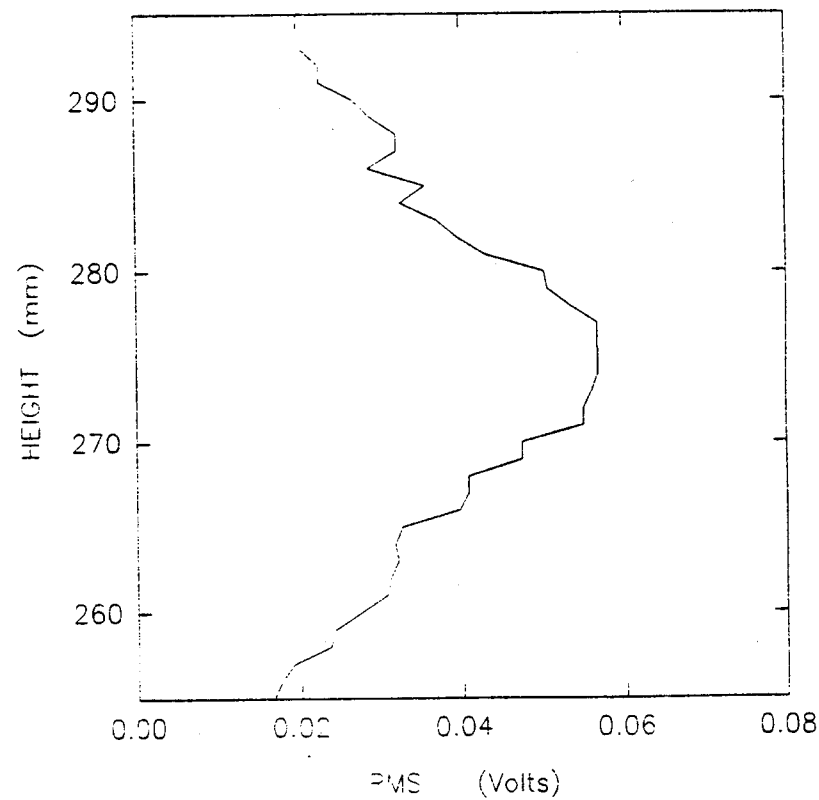
46b. RMS Survey

Figure 46. Typical Vertical Mean and RMS velocity surveys used to locate vortex center. $U_\infty = 13.7$ m/s (Velocity = 2.56 x Voltage).
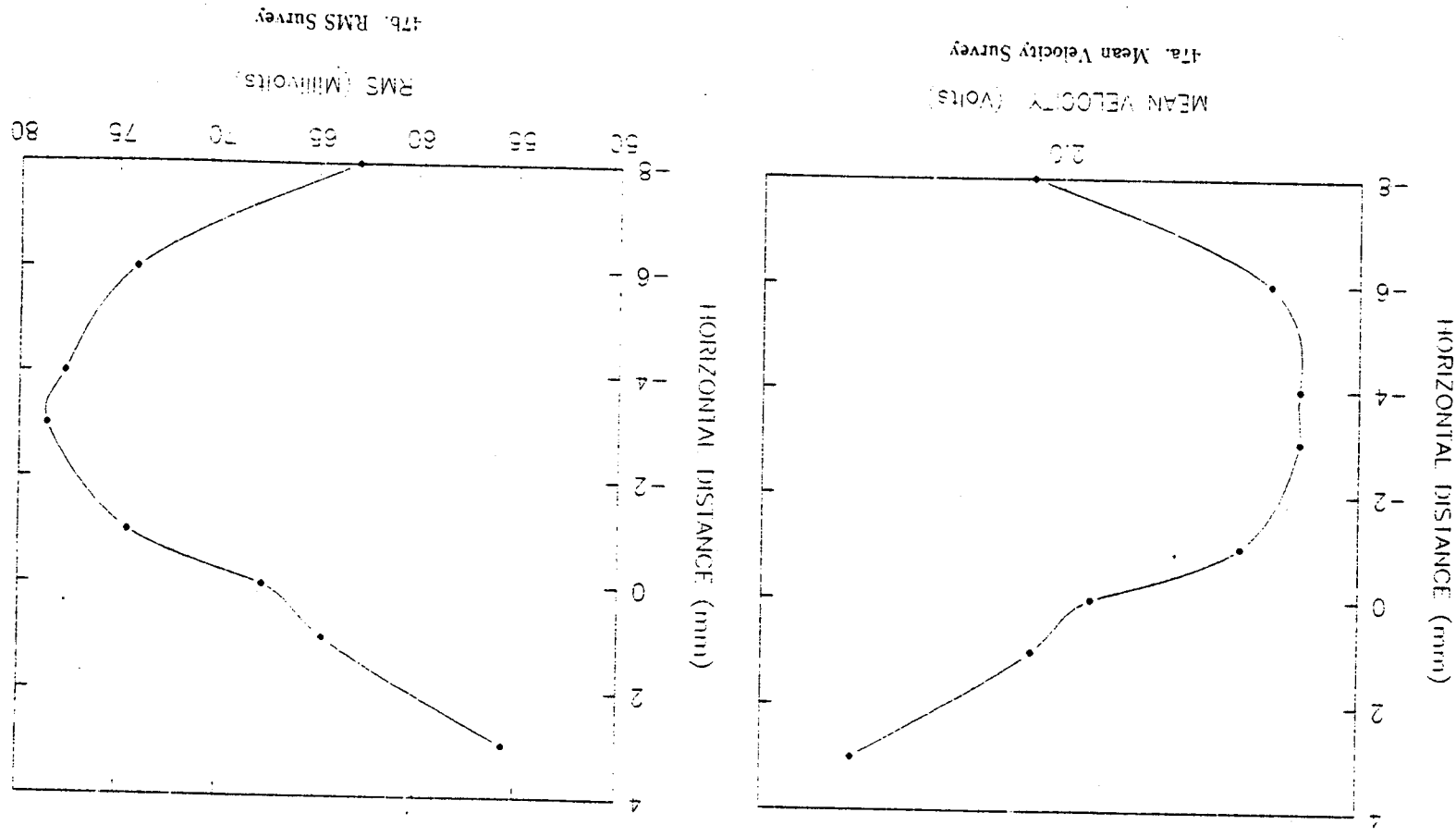
Figure 47. Typical horizontal mean and RMS velocity surveys used to determine vortex center, U_∞ = 134 m/s.

47a. Mean Velocity Survey

47b. RMS Survey

position was more likely to change than the horizontal position, since there were only second order sources for the horizontal position change.

Several baseline surveys were taken with a nominal free stream velocity of 14 m/s, while the perturbation generator was secured, to obtain: mean, RMS, and spectral data of the undisturbed vortex. Representative results for $U_\infty = 14$ m/s are shown in Figure 48. It is observed that as the free stream velocity increases slightly, a corresponding increase in RMS velocity occurs.

The perturbation generator was operated subsequently with the wind tunnel free stream velocity maintained at 14 m/s. For reference purposes, the direction of spin of the perturbation generator was called "co-rotational" when it coincided with the direction of the vortex swirl. A "counter-rotational" direction meant the perturbation generator spin opposed the direction of the vortex rotation. Spectra, with the hot-wire probe centered in the middle of the vortex, were obtained at the downstream vortex location for various conditions of plenum pressure (23 to 253 Pa), perturbation generator disk spin frequency (50 to 220 Hz), and for both directions of disk rotation.

The tunnel free stream velocity was reduced to 7 m/s in an attempt to make measurements at a low speed. No indication of strong perturbation signals was obtained for tests conducted and data collection at that speed was terminated. Hence, the results of the data collected at 7 m/s are not reported.

The extent of the perturbation signal in the vortex core was investigated next. The hot-wire probe was traversed on the vertical axis through the vortex at a free stream velocity of
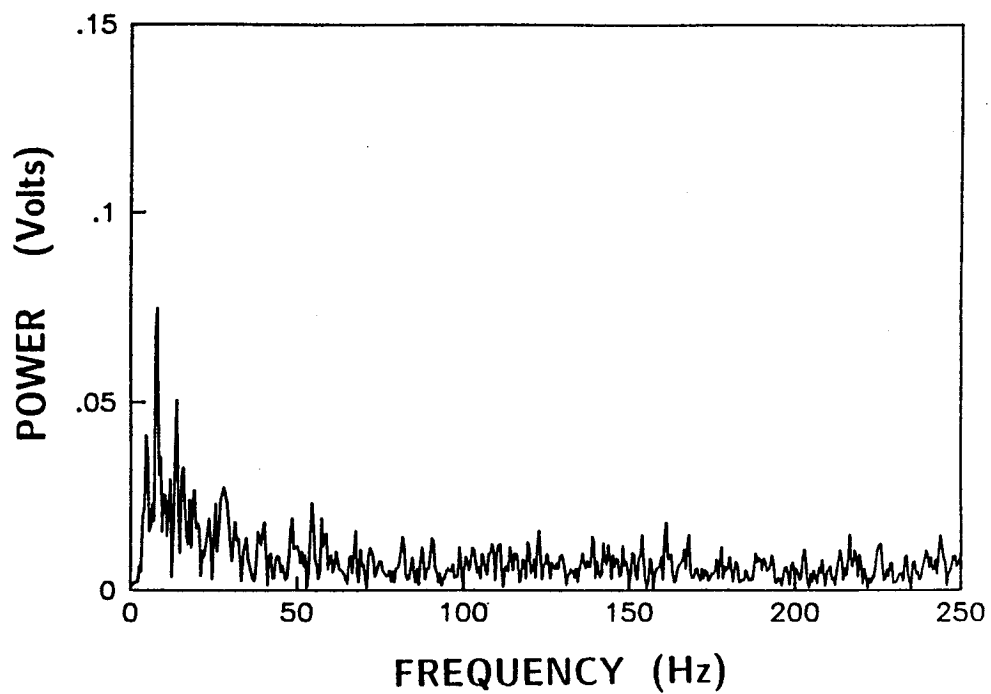
48a. $U_\infty = 13.5$, RMS $= .141$ volts
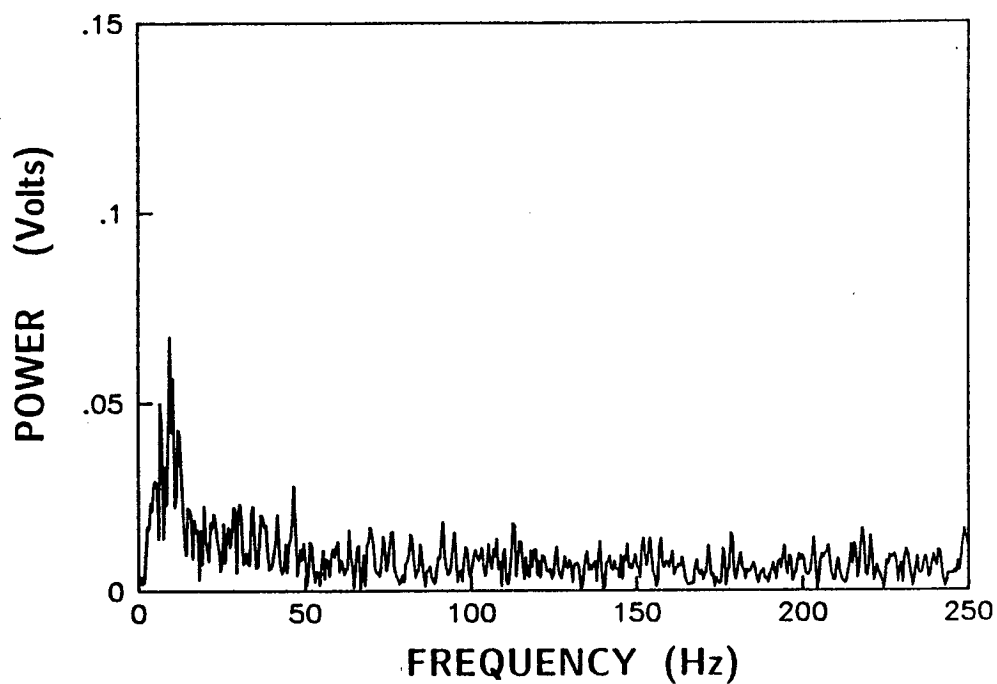
48b. $U_\infty = 13.7$, RMS $= .157$ volts

Figure 48. Vortex frequency spectra with perturbation generator secured, hot-wire in vortex center, x $= 4.27$ m.

approximately 14 m/s while velocity spectra were collected. The model motor frequency (85 Hz) and plenum pressure ($\Delta P = 176$ Pa) were held constant so that hot-wire position was the only variable. The hot-wire probe was returned to the center of the vortex core and the tunnel free stream velocity was increased to approximately 21 m/s for data measurements. Motor frequencies were varied from 77 to 122 Hz and plenum pressures, ΔP, were varied between 116 Pa and 368 Pa. The vortex core was also traversed to compare spectral amplitudes as a function of position in the core while motor frequency (90 Hz) and plenum pressure (160 Pa) were held constant.

It was decided to look at Strouhal values and perturbation operation at the highest Reynolds number possible in the wind tunnel. The hot-wire was recalibrated[1] for the maximum velocity of the wind tunnel (approximately 42 meters/second) and positioned in the center of the vortex core to run tests at a wind tunnel free stream velocity of 42 m/s.

The sampling interval was changed to 1.5 ms in order to investigate frequencies up to 333 Hz. This was done to observe spectral data in the higher frequency range associated with the increase in free stream velocity. Spectra were obtained with the perturbation generator secured and with it operating in order to evaluate the effects of the perturbation generator frequency and amplitude on the hot-wire spectral peaks. These data were all taken while the model was turning with a counter-rotational spin. Differential plenum pressures used for 42 m/s were varied between 236 and 660 Pa while motor speeds were varied from 79 to 144 Hz.

It was desired to take spectral measurements at upstream and downstream axial locations

1. This decision would void any absolute comparison between new data collected with the new hot-wire calibration and the data obtained previously from the 25 m/s hot-wire calibration. This was not realized at the time. A full set of data were repeated for 14 and 21 m/s free stream velocities.

along the vortex centerline to determine evidence of amplification or decay. Ideally, the two measurements should be taken simultaneously to give a true determination of amplification. However, instrumentation was lacking and simultaneous measurements were deferred. It was decided to use a representative set of measurements at the downstream location and repeat the operating conditions when the probe was moved upstream. Data sets were produced for free stream velocities of 14 and 21 m/s with the hot-wire probe located at the downstream position, x = 48'1" (14.66 m). This was done since the previous measurements used the hot-wire while it was calibrated for a maximum velocity of 25 m/s.

The hot-wire probe was moved forward to an intermediate position which is referenced as the 39' 9" (12.12 m) longitudinal position in the wind tunnel. The new hot-wire position corresponded to a position 5' 8" (1.73 m) behind the perturbation generator. That distance was equivalent to 17 chord lengths. The same tunnel free stream velocity, plenum pressure, disk rotation speed, and rotation direction were employed for the two measurement sets with the hot-wire centered in the vortex. Although the measurements were not taken simultaneously, it was desired to obtain some indication of perturbation amplification or decay during these preliminary studies.

Lastly, the effect of spin direction was investigated. Similar to upstream versus downstream, the flow conditions and plenum pressures were matched, and only the direction of spin was changed. This was done at the intermediate and downstream locations with various combinations of motor frequency, plenum pressure, and free stream velocity.

4.2 2' X 3' Wind Tunnel Results and Discussion:

Data measurements obtained with the perturbation generator operating (counter-rotating) at a nominal wind tunnel velocity of 14 m/s are shown in Figure 49. The hot-wire, which was centered in the vortex for these measurements, was 4.27 m (42 airfoil chord lengths) downstream from the vortex generator. Examples of co-rotating perturbation data are shown in Figure 50. It was noted that the co-rotating perturbations appeared to produce larger spectral amplitudes than their counter-rotating counterparts. It was also determined that the fundamental frequency of the perturbation generator was observable downstream while the hot-wire probe was in the center of the vortex. This is significant in that a signal input into the vortex during roll-up has convected downstream in the vortex core.

Figure 51 shows the effects when the hot-wire probe was traversed on the vertical axis through the vortex. The free stream velocity was a nominal 14 m/s (model motor frequency and plenum pressure held constant). The amplitudes of the peak signals drop off quickly as the hot-wire probe is moved out of the vortex core. A spectrum was taken outside the core at a radius of 20 mm above the centerline to determine whether the disturbance was wrapping around the core. There was no evidence of the perturbed frequency outside the vortex core (Figure 52).

Representative samples of frequency spectra for various parameters at 21 m/s are shown in Figure 53. It is noted that there is a large spectral peak for a co-rotating case (Figure
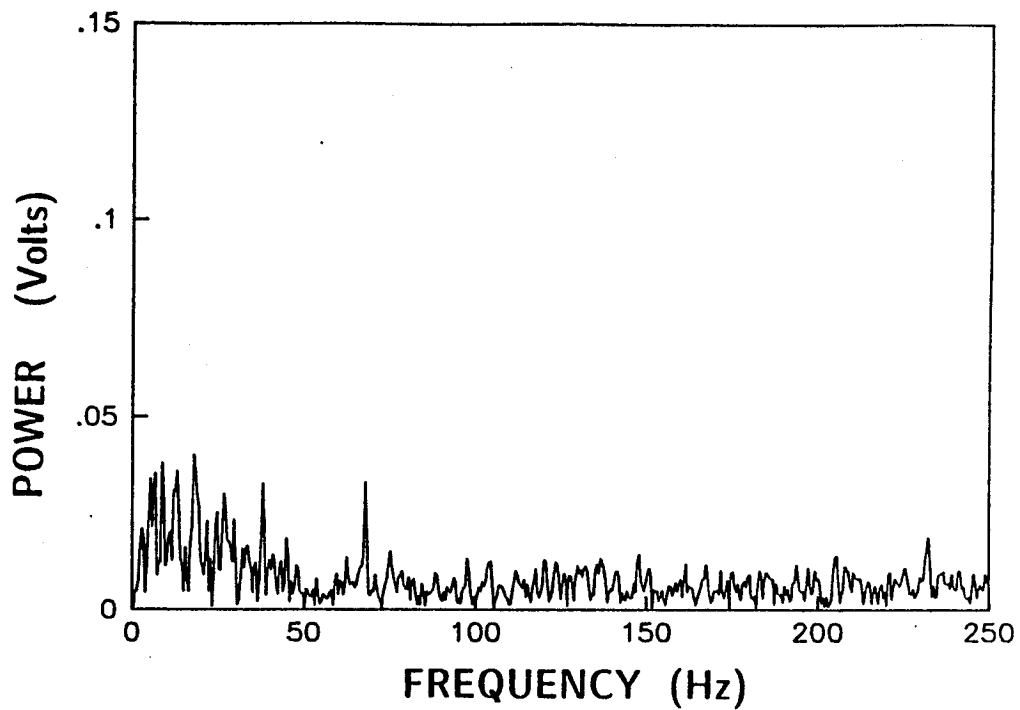
-105-
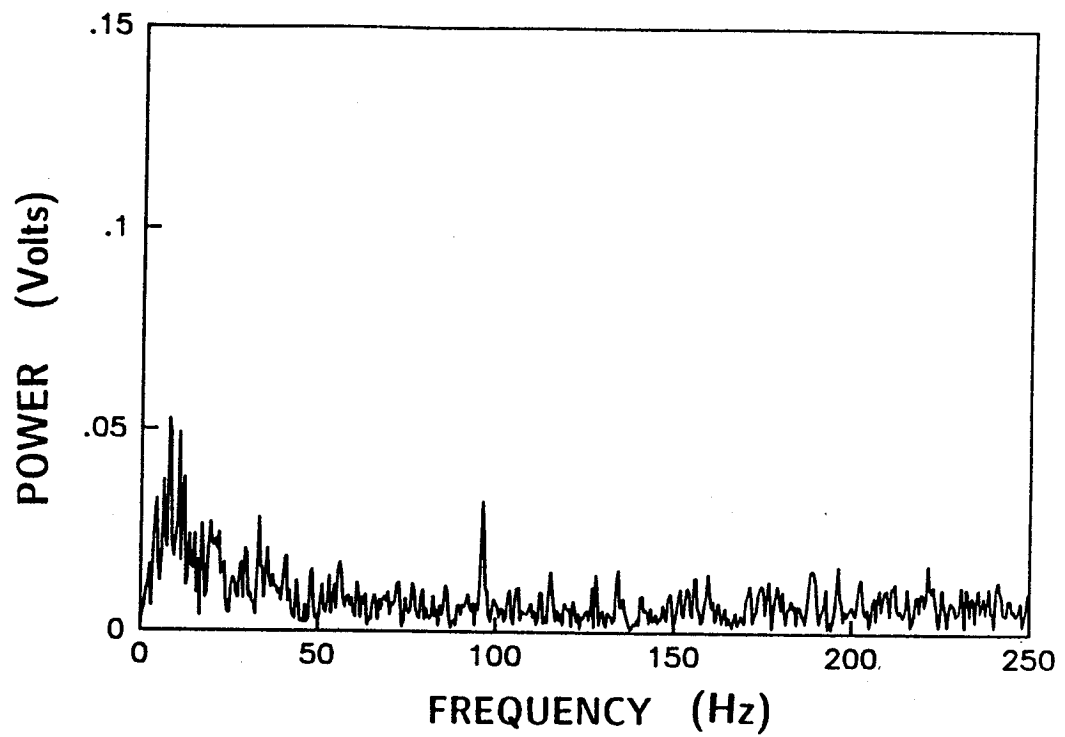
49a. $U_\infty = 13.7$ m/s, $M_f = 97$ Hz, $\Delta P = 1.31$ torr (174 Pa.)
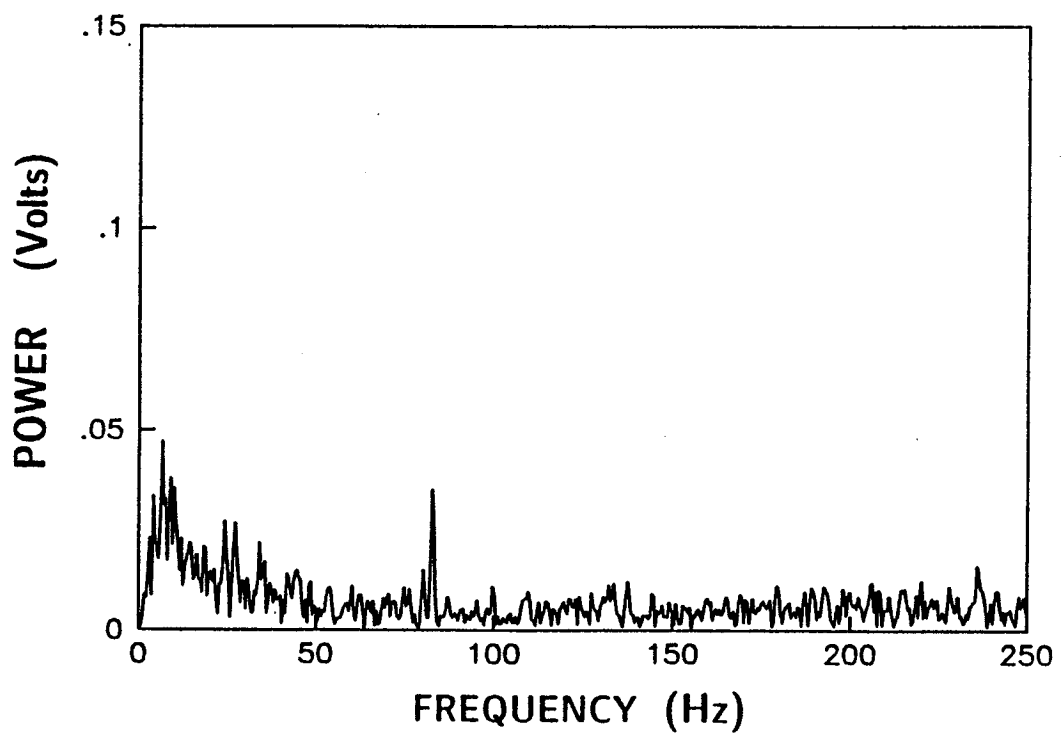
49b. $U_\infty = 13.7$ m/s, $M_f = 84$ Hz, $\Delta P = 1.69$ torr (223 Pa.)

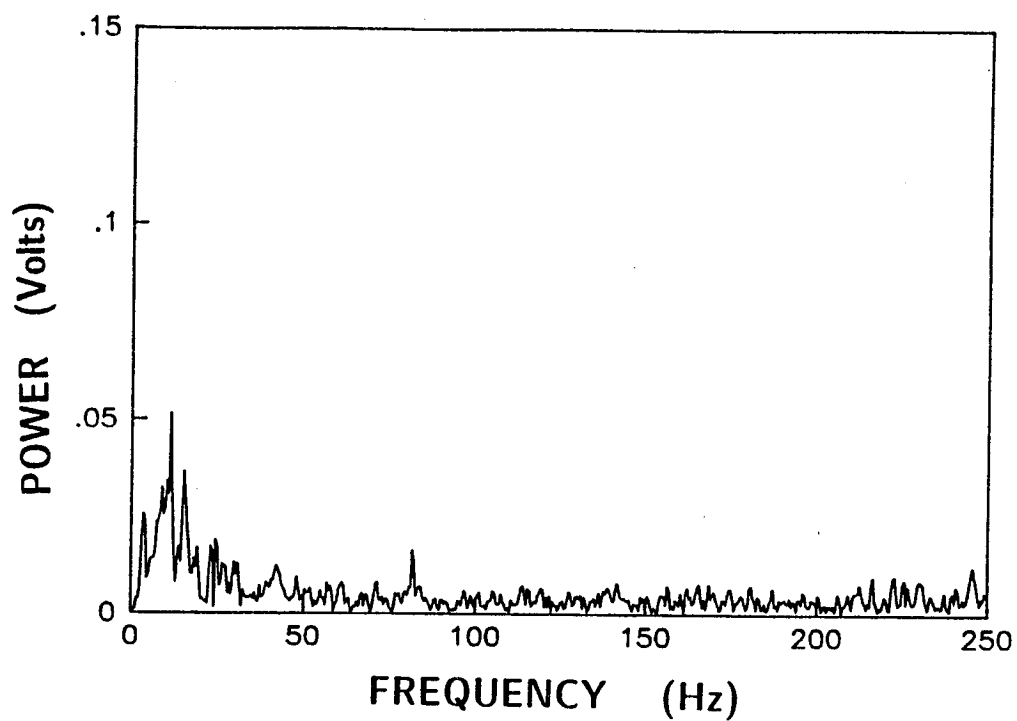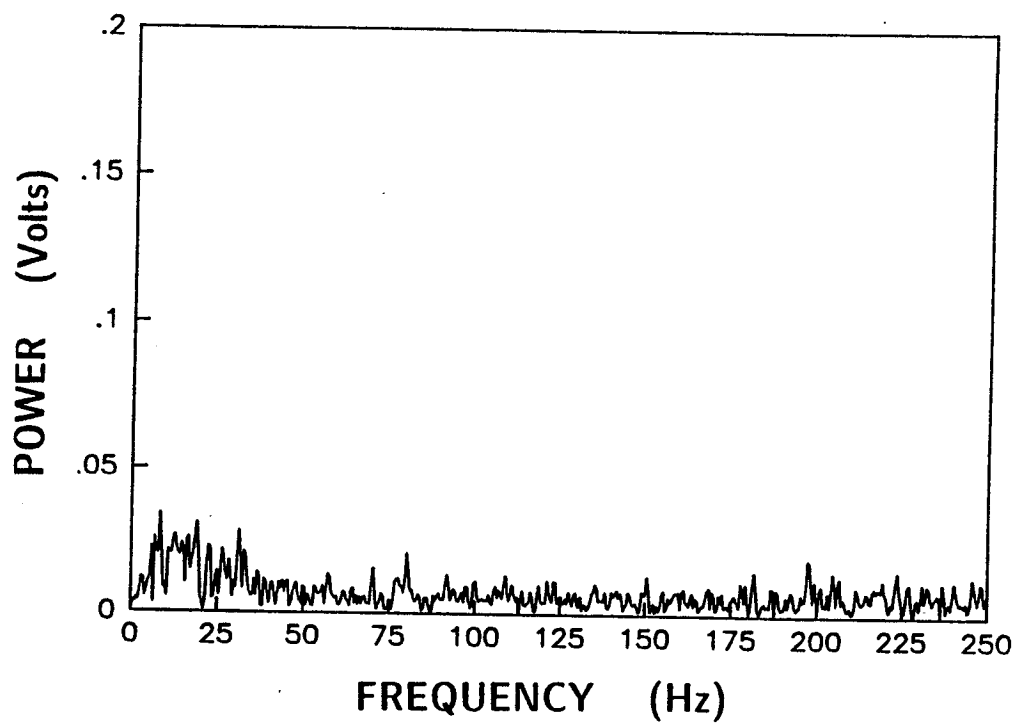Figure 49.   Frequency spectra, counter-rotating perturbations.

-106-
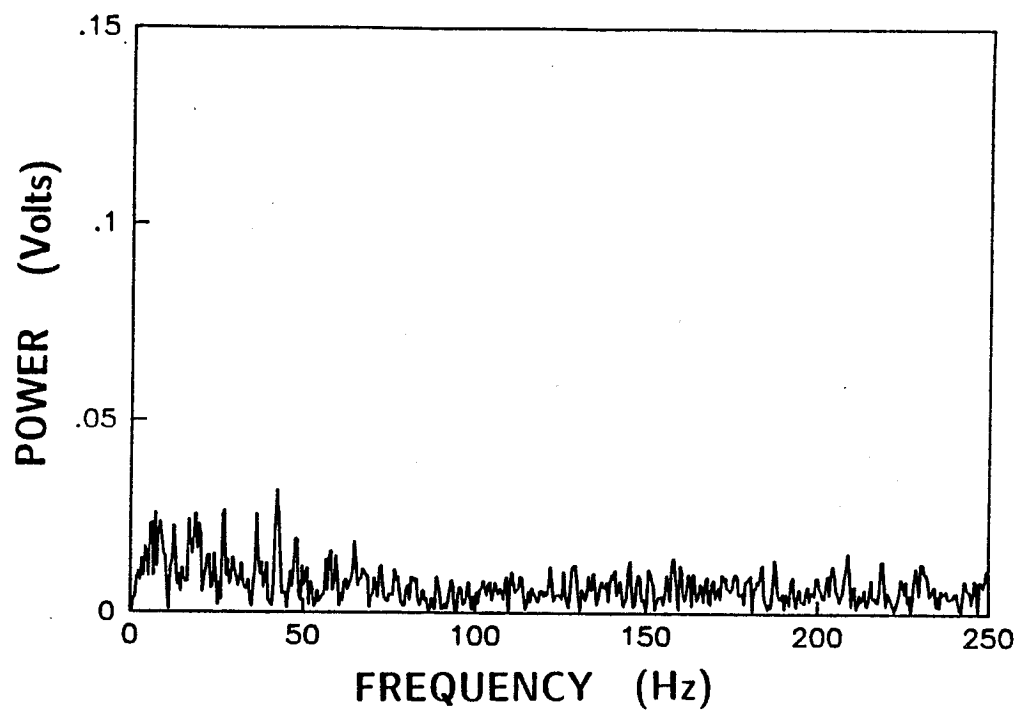
49c. $U_\infty = 13.7$ m/s, $M_f = 211$ Hz, $\triangle P = 1.32$ torr (175 Pa.)
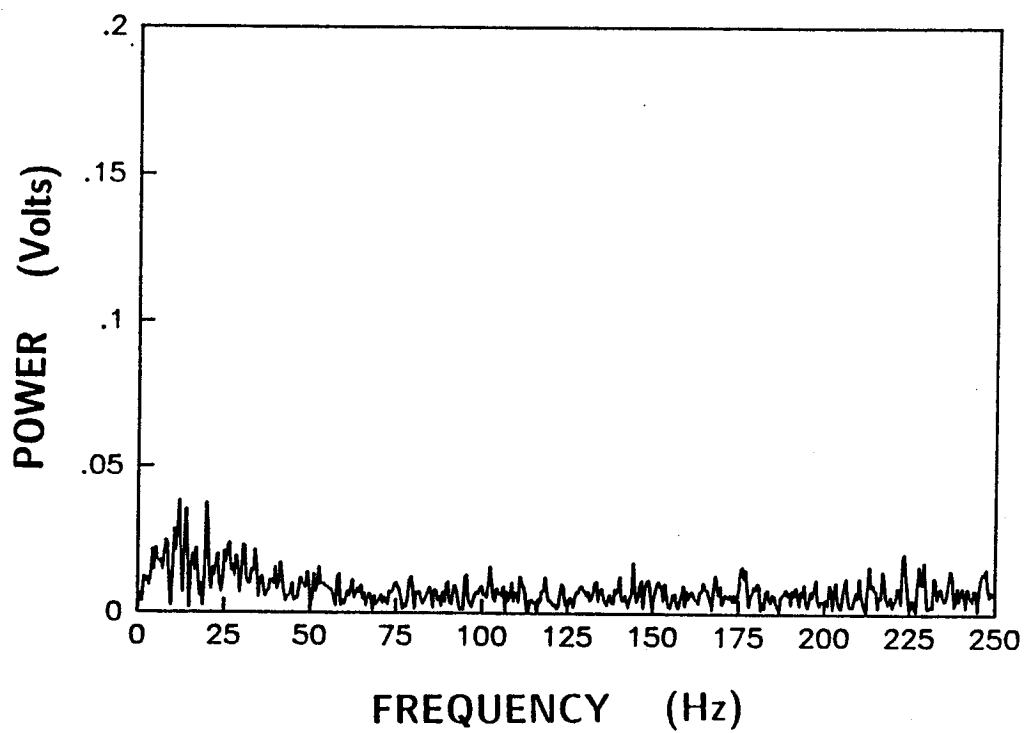
49d. $U_\infty = 13.7$ m/s, $M_f = 144$ Hz, $\triangle P = 2.16$ torr (256 Pa.)

Figure 49 continued
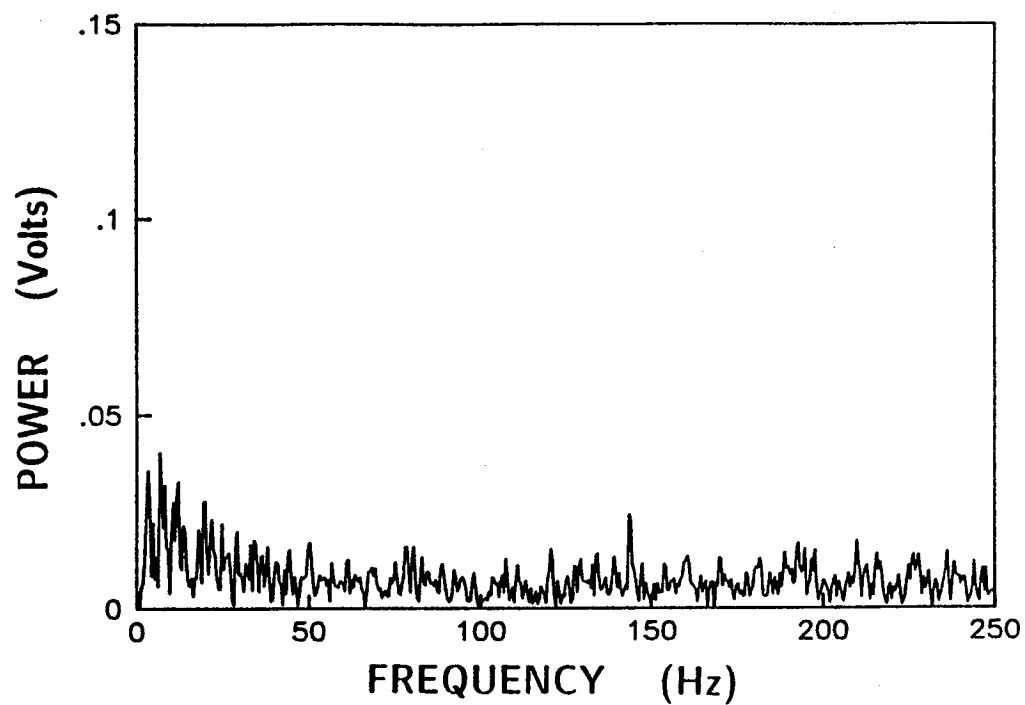
49e. $U_\infty = 13.7$ m/s, $M_f = 143$ Hz, $\triangle P = 1.3$ torr (169 Pa.)
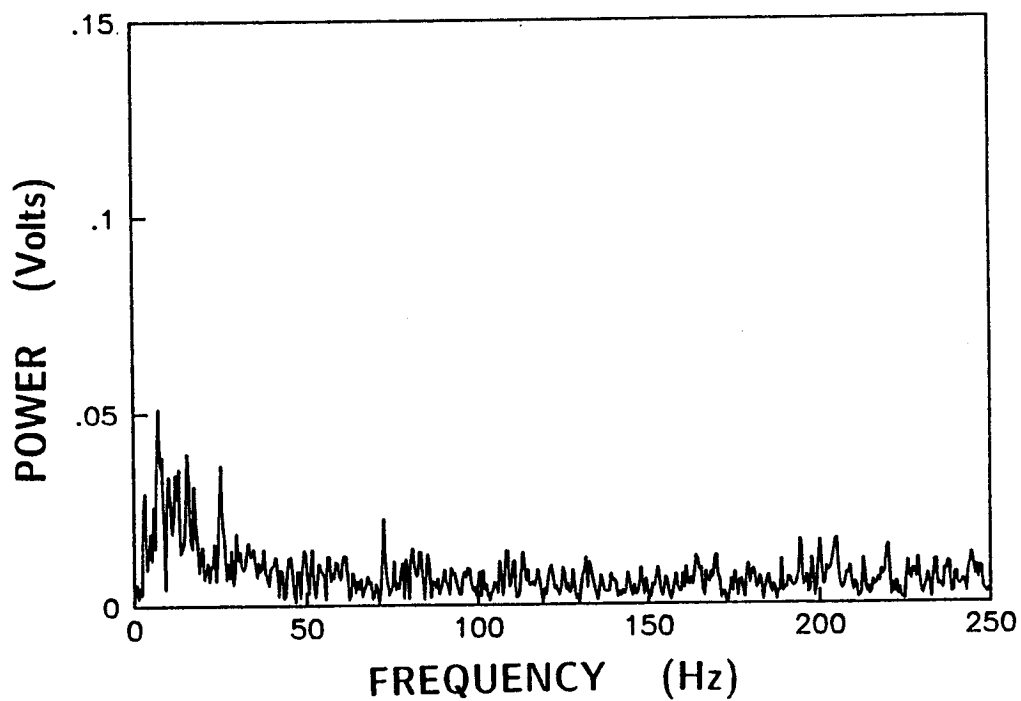
49f. $U_\infty = 13.7$ m/s, $M_f = 72$ Hz, $\triangle P = 1.4$ torr (182 Pa.)

Figure 49 continued

50a. $U_\infty = 13.7$ m/s, $M_f = -67$ Hz, $\triangle P = 1.6$ torr (208 Pa.)
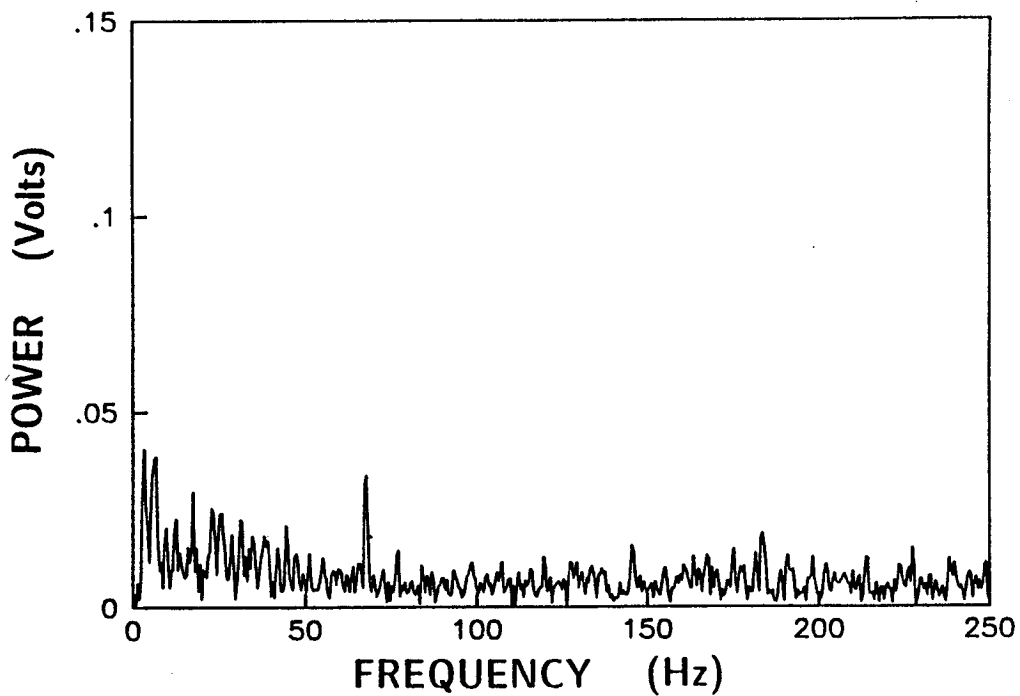
50b. $U_\infty = 13.7$ m/s, $M_f = -68$ Hz, $\triangle P = 1.63$ torr (215 Pa.)

Figure 50. Frequency spectra, co-rotating perturbations.
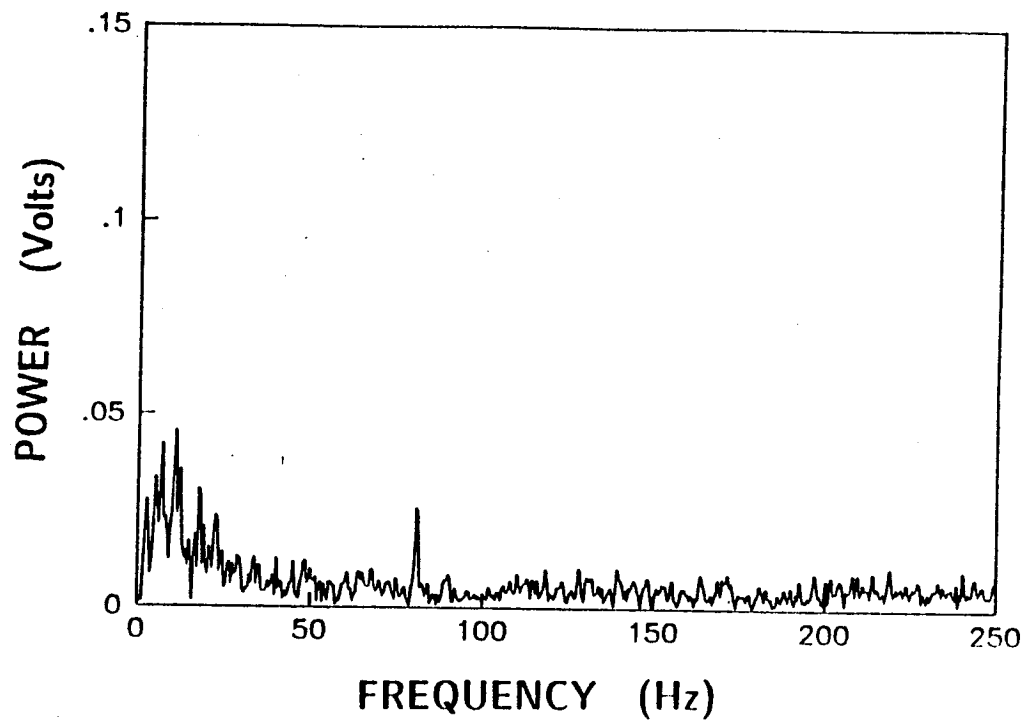
51a. Y = +3mm
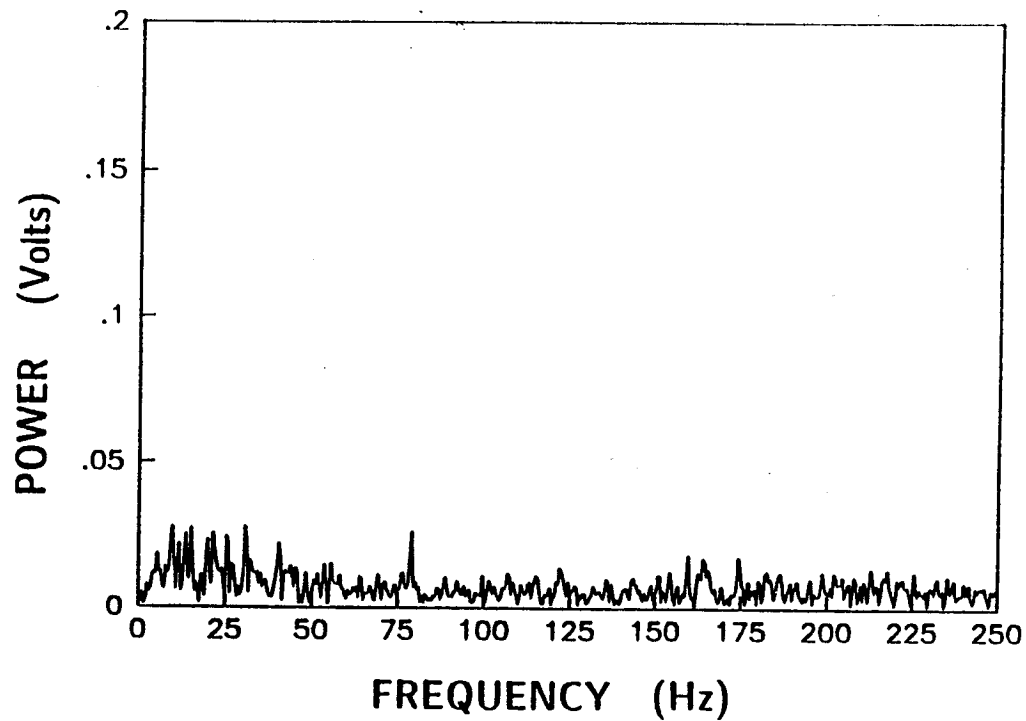
51b. Y = -3 mm.

Figure 51. Comparison of frequency spectra as the probe is traversed through the vortex, $U_\infty = 13.7$ m/s, $M_f = 84$ Hz, $\Delta P = 1.3$ torr (176 Pa.), x = 4.27 m.

51c. Y = +5 mm.

51d. Y = -5 mm.

Figure 51 continued

-111-

POWER (Volts)

.15 .1 .05 0

FREQUENCY (Hz)

0 50 100 150 200 250

51e. Y = +9 mm.

POWER (Volts)

.15 .1 .05 0

FREQUENCY (Hz)

0 50 100 150 200 250
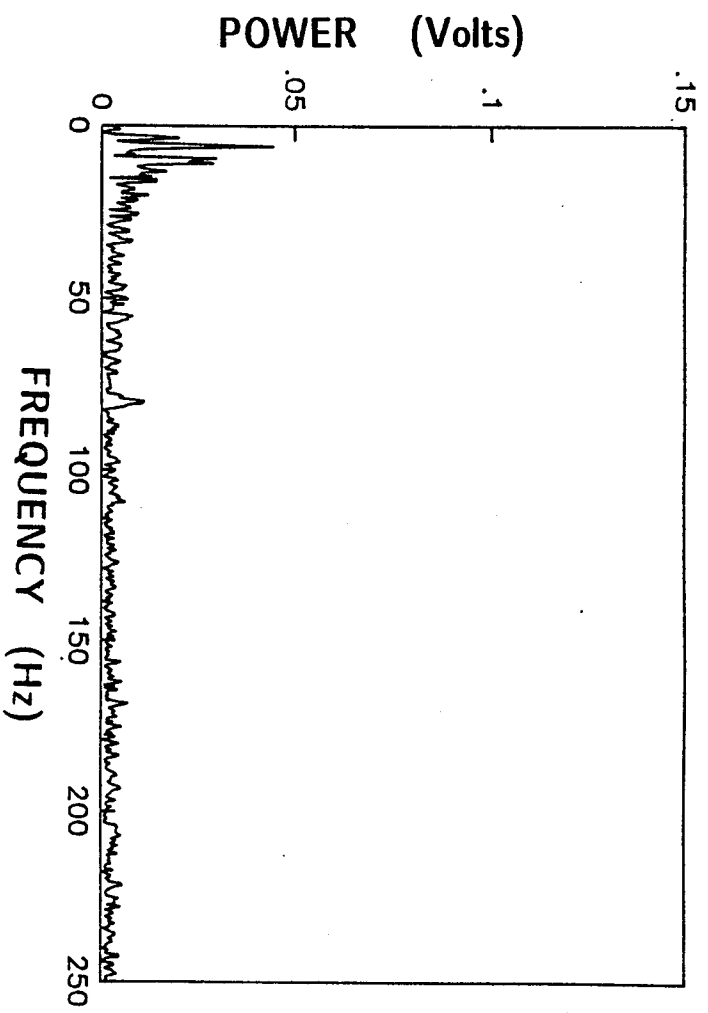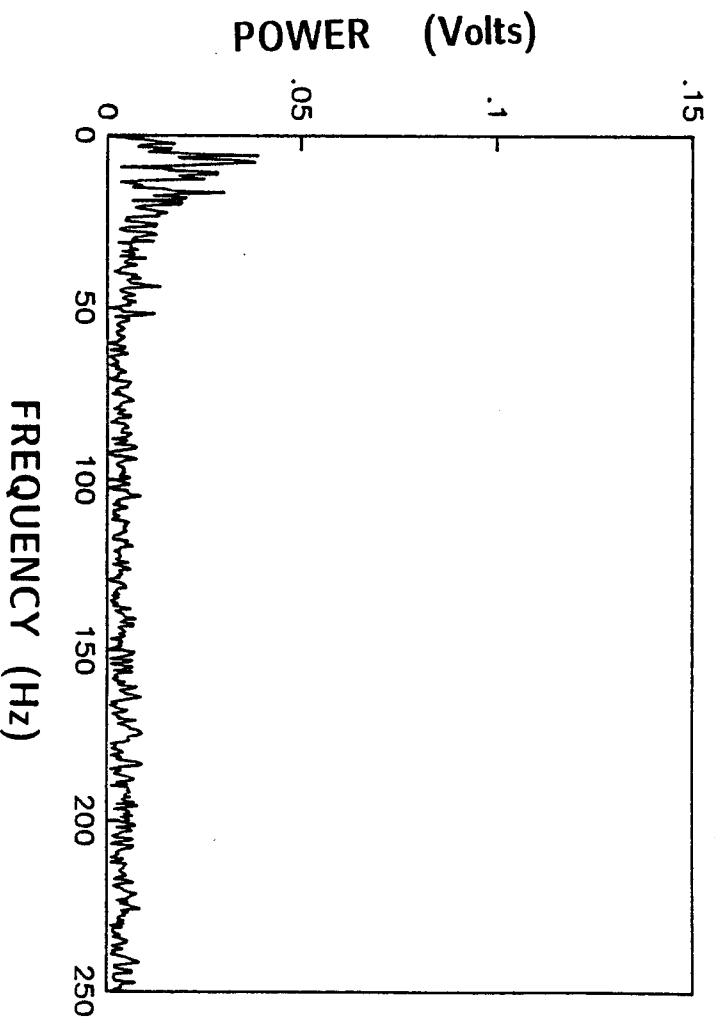
51f. Y = -9 mm.

Figure 51 continued

-112-
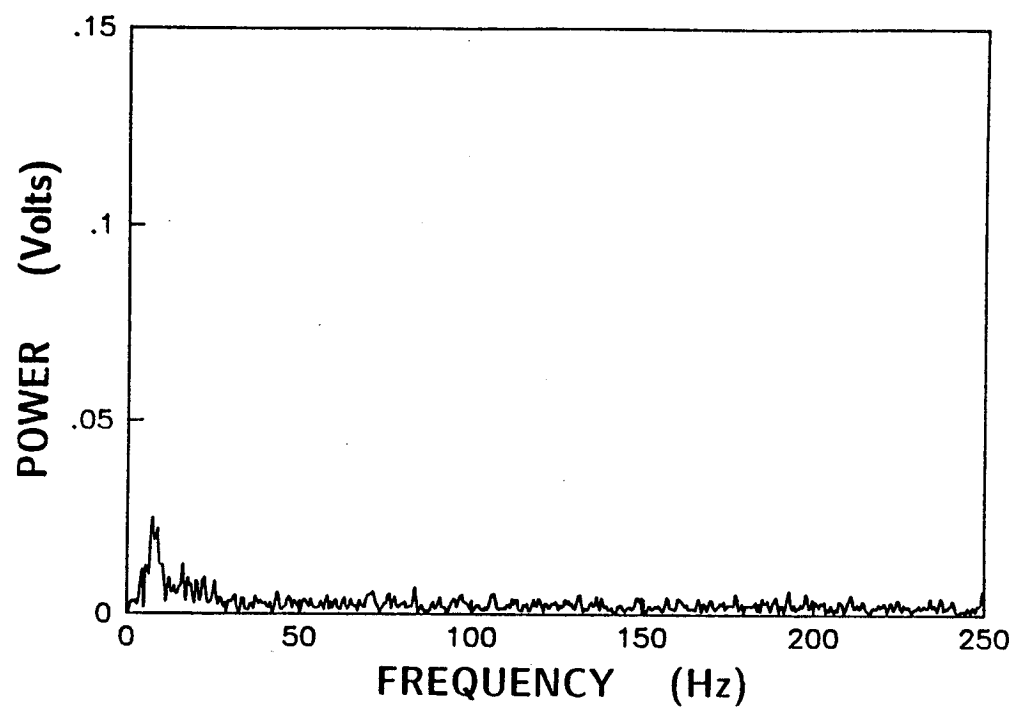
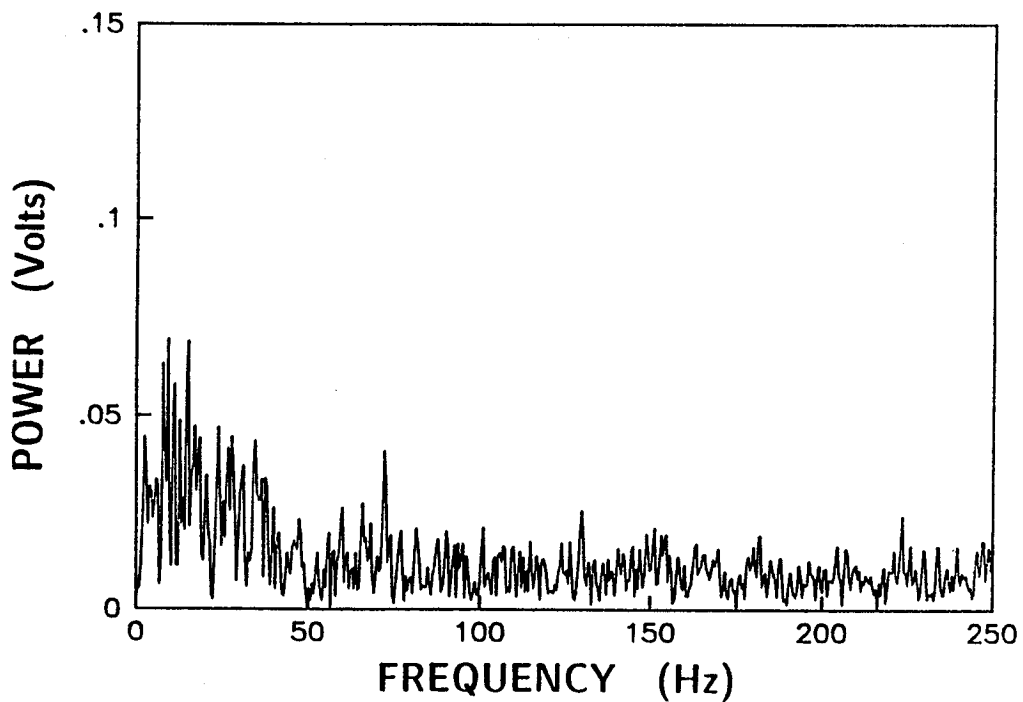51g. Y = +11 mm.
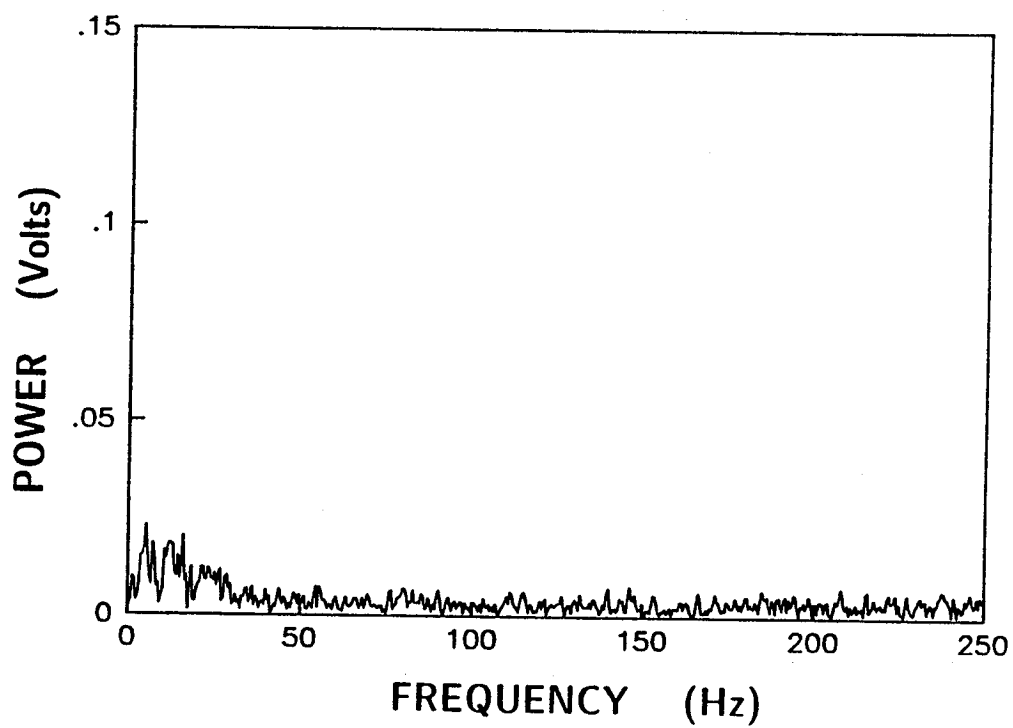
51h. Y = -11 mm.

Figure 51 continued
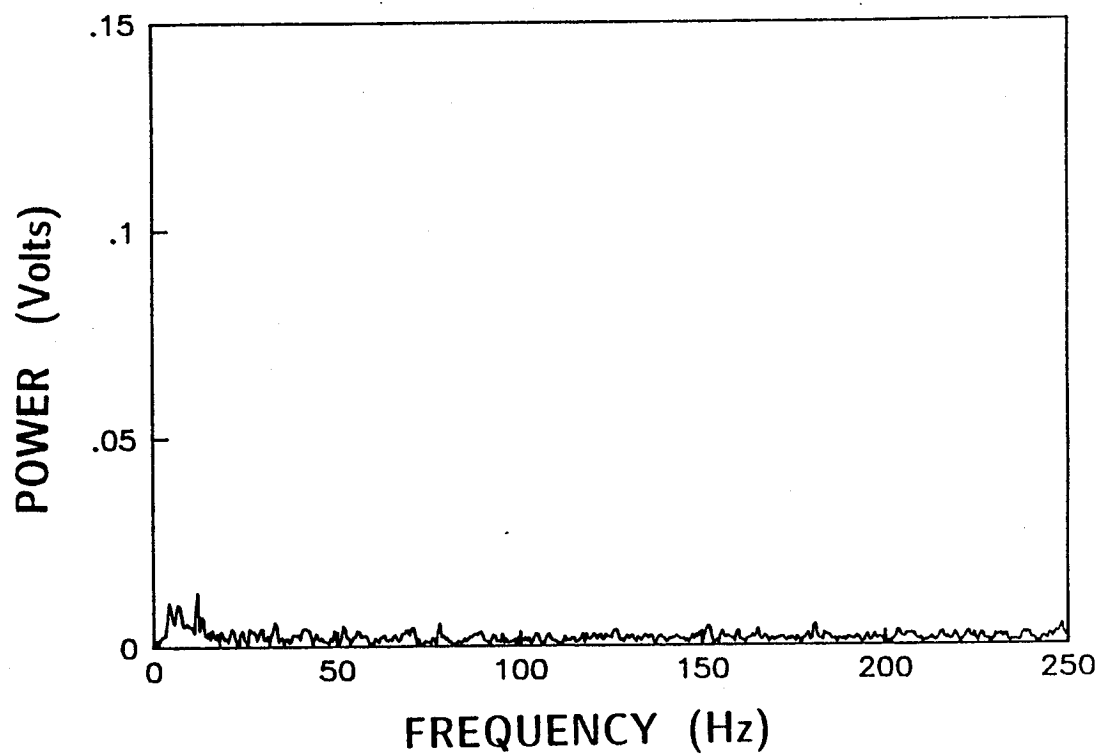
Figure 52. Frequency spectrum with probe located 20 mm above the vortex centerline. $U_\infty = 13.7$ m/s, $M_f = 79$ Hz, $\triangle P = 1.33$ torr (176 Pa.), $Y = +20$ mm, $X = 4.27$ m.
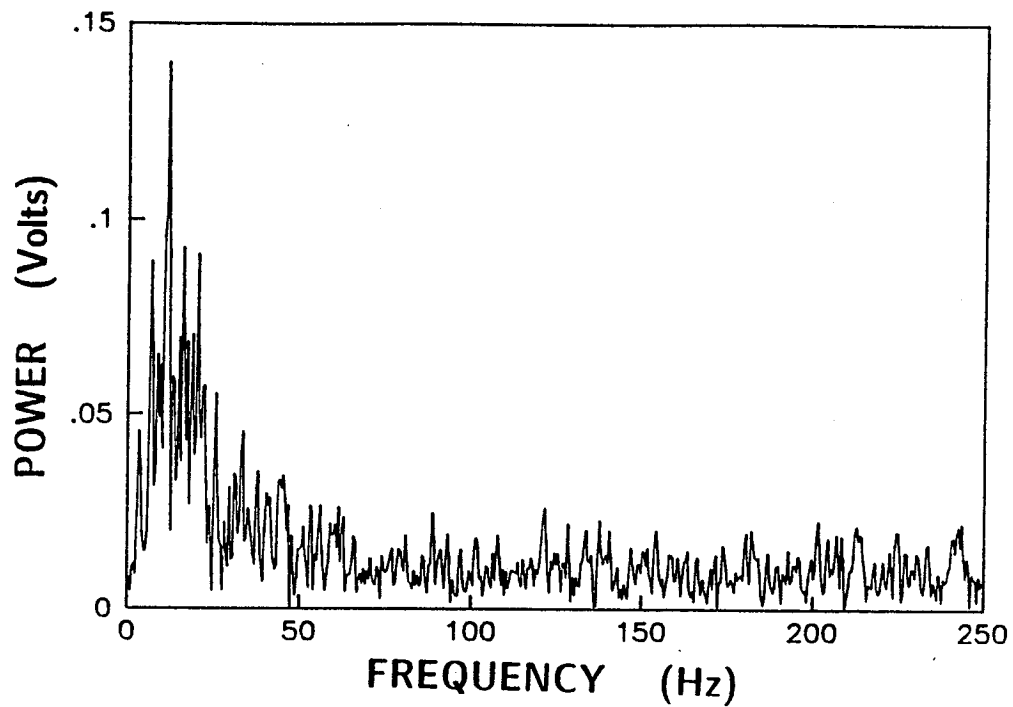
53a. $U_\infty = 20.7$ m/s, perturbation generator secured.

53b. $U_\infty = 20.7$ m/s, $M_f = 82.5$ Hz (counter-rotating), $\triangle P = 248$ Pa
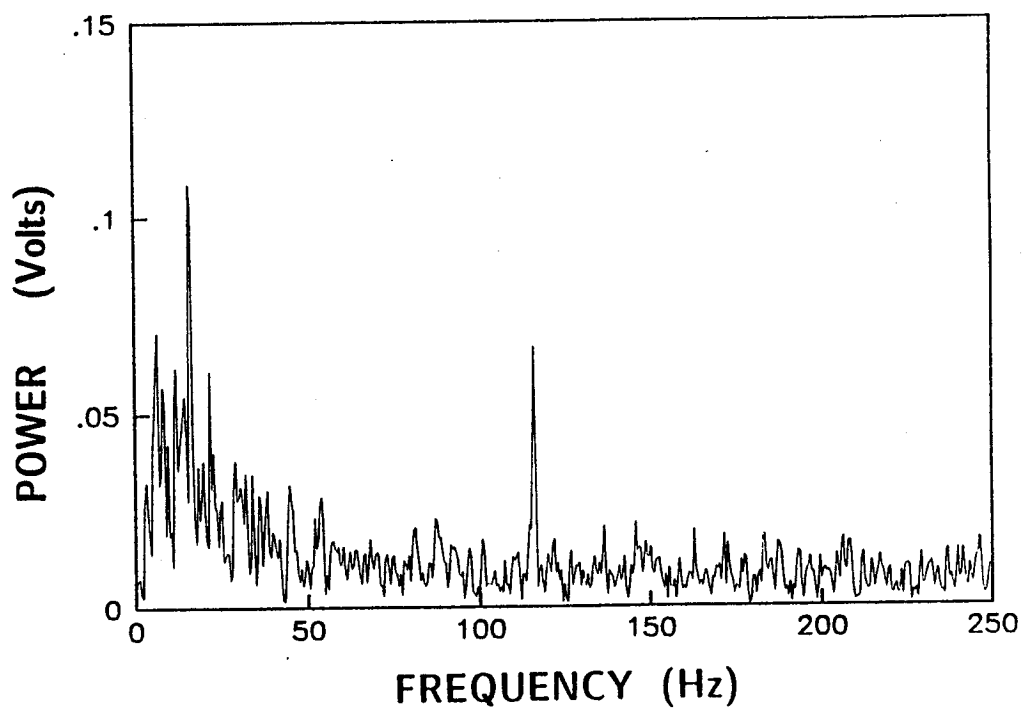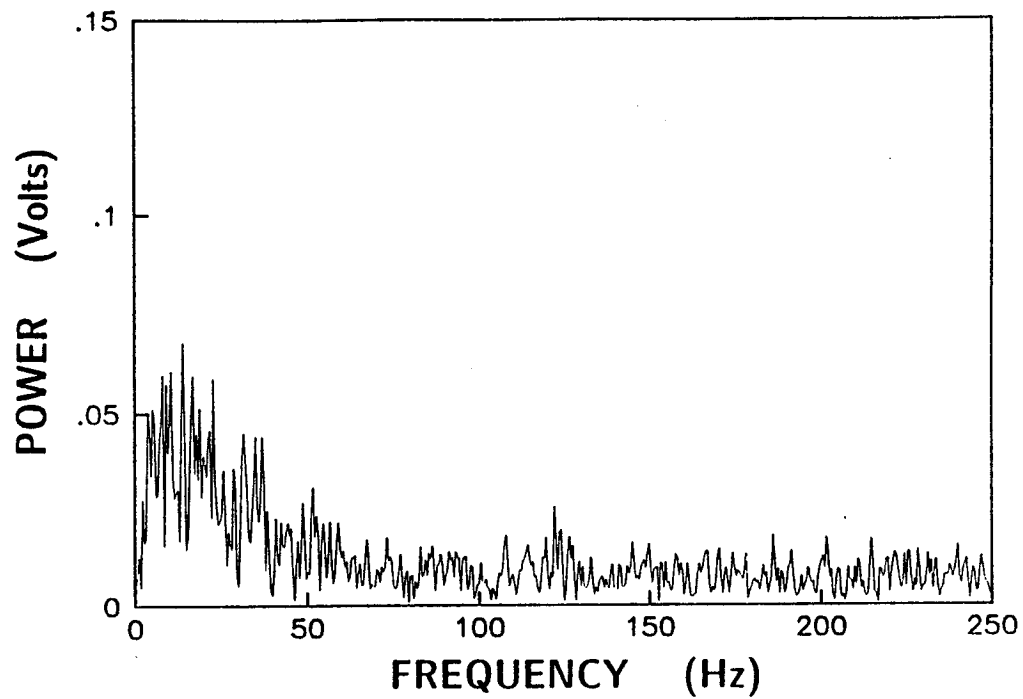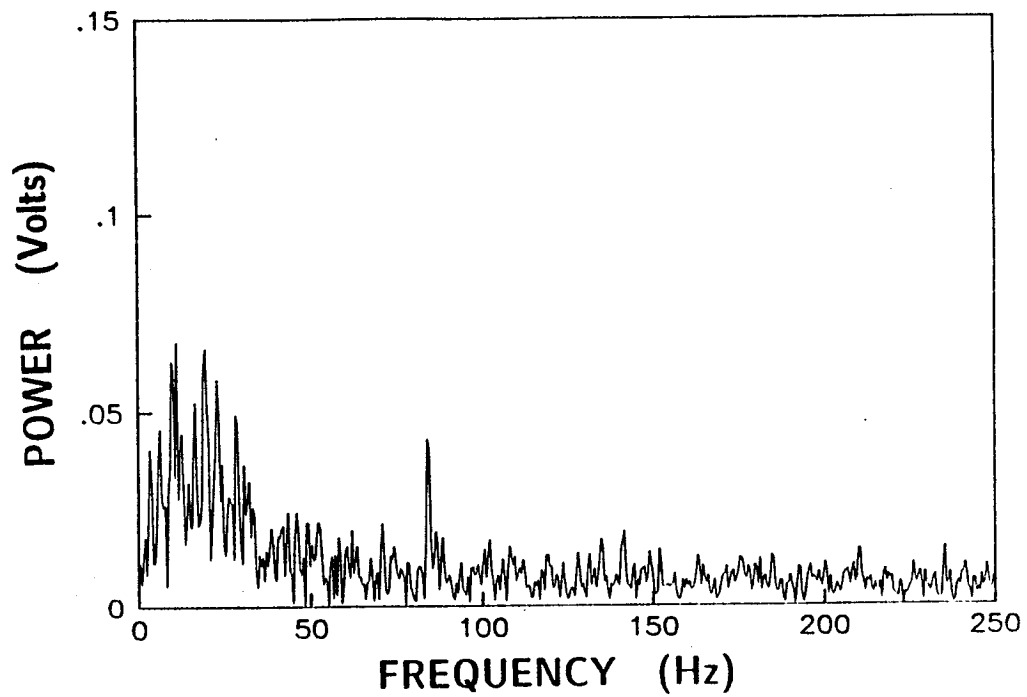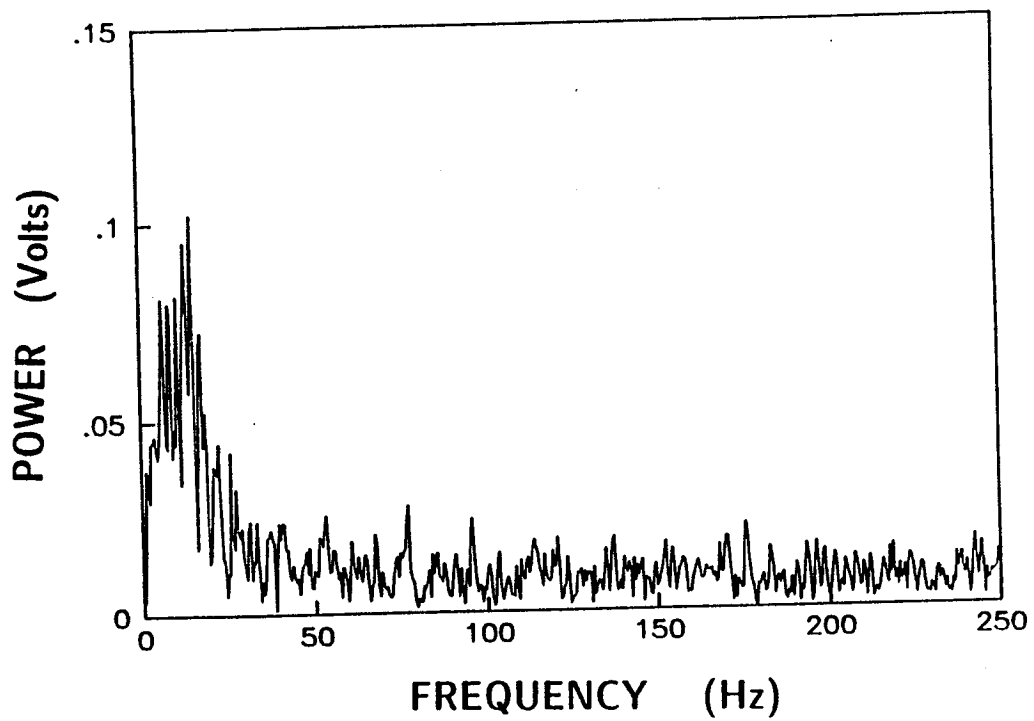
Figure 53.   Frequency spectra at $U_\infty = 21$ m/s.

53c. U_∞= 20.7 m/s, M_f = 122 Hz, (counter-rotating), $\triangle P$= 202 Pa

53d. U_∞= 20.7 m/s, M_f = 116 Hz (co-rotating), $\triangle P$= 206 Pa

Figure 53 continued

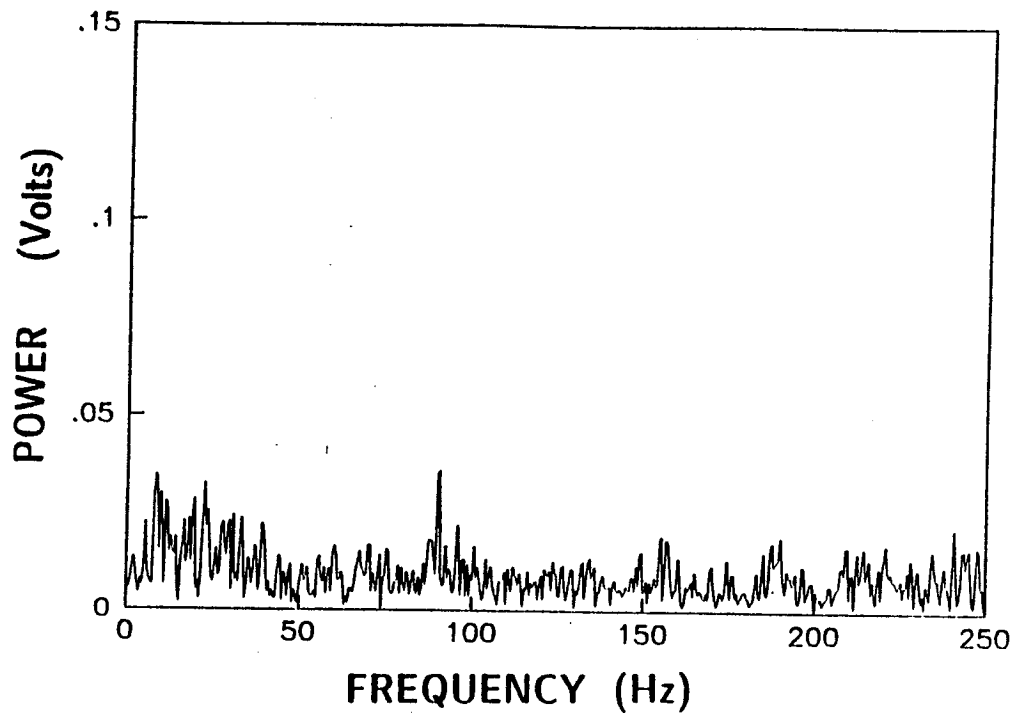53e. U_∞= 20.5 m/s, M_f = 84 Hz, (counter-rotating), $\triangle P$= 166 Pa

53f. U_∞= 20.7 m/s, M_f = 77 Hz, (counter-rotating), $\triangle P$= 367 Pa
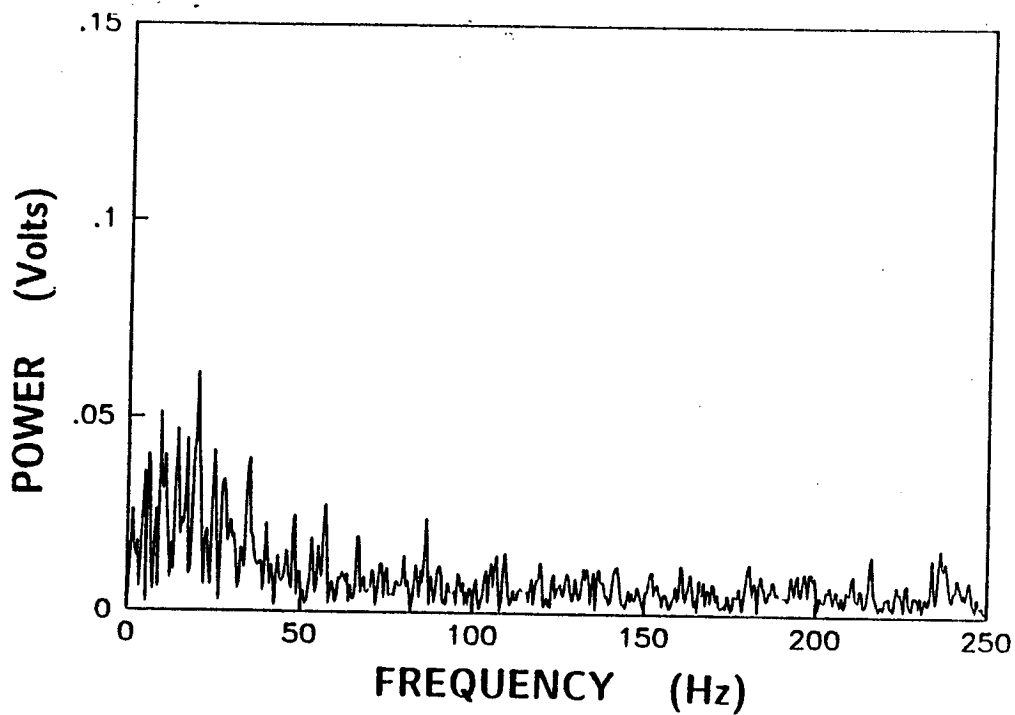
Figure 53 continued

53d.) which is not present in the corresponding counter-rotating case (Figure 53c.). The vortex core was also traversed to compare spectral amplitudes as a function of position in the core. Again, the fundamental or control frequency of the perturbation generator was seen in the center of the vortex core but not outside of the core. The amplitude of the spectral peaks corresponding to the fundamental frequency decreased as the probe was moved away from the core centerline. The spectra are shown in Figure 54.

The frequency spectra plots (Figures 53 and 54) showed evidence of possible voltage spikes corresponding to Strouhal Numbers of approximately 0.2 (135 Hz for 20.7 m/s). The amplitude of the spikes was not as evident as they were in spectra taken in the 4 inch pipe facility, but the probe is much further downstream. Also, the Strouhal measurements in the 4 inch pipe facility were conducted using a centerbody with a diameter of 30.5 mm (1.2 inches). Strouhal measurements in the 2'x3' wind tunnel however, used Stead's centerbody which is 25.4 mm (1 inch) in diameter. The motor housing was used in order to step up the centerbody diameter to that of the perturbation generator (30.5 mm). Instead of having a constant diameter centerbody, two different diameters characterized the centerbody flow. A diameter of 30.5 mm was used in calculations of Strouhal numbers for flow in the 2' x 3' wind tunnel.

Selected spectra with interesting Strouhal number spectral peaks are shown in Figure 55. These spectra were taken after the hot-wire was recalibrated for a maximum wind tunnel velocity of 42 m/s and with the perturbation generator secured. Spectra taken with the perturbation generator operating are shown in Figure 56. Free stream velocity was 42 m/s.
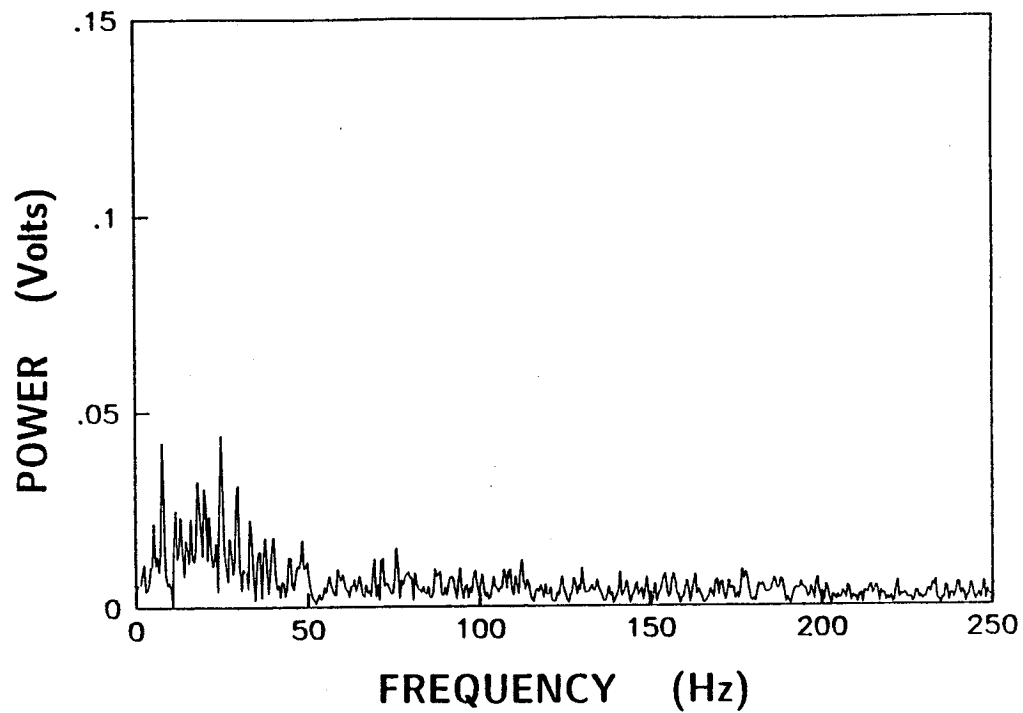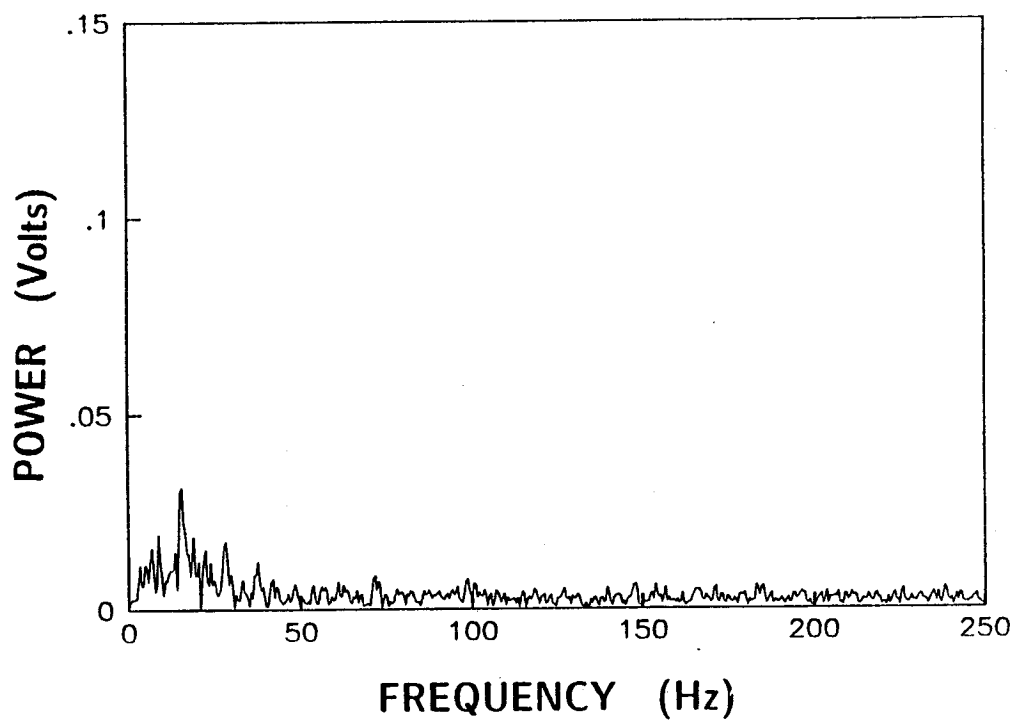
54a. Y = 0 mm (centerline)

54b. Y = - 4 mm

Figure 54. Influence of probe location on spectra, U_∞= 20.5 m/s, M_f = 90 Hz (counter-rotating). ΔP= 160 Pa, X = 4.27 m.

54c. Y = -8 mm

54d. Y = -14 mm

Figure 54 continued

55a. $U_\infty = 42$ m/s, perturbation generator secured.

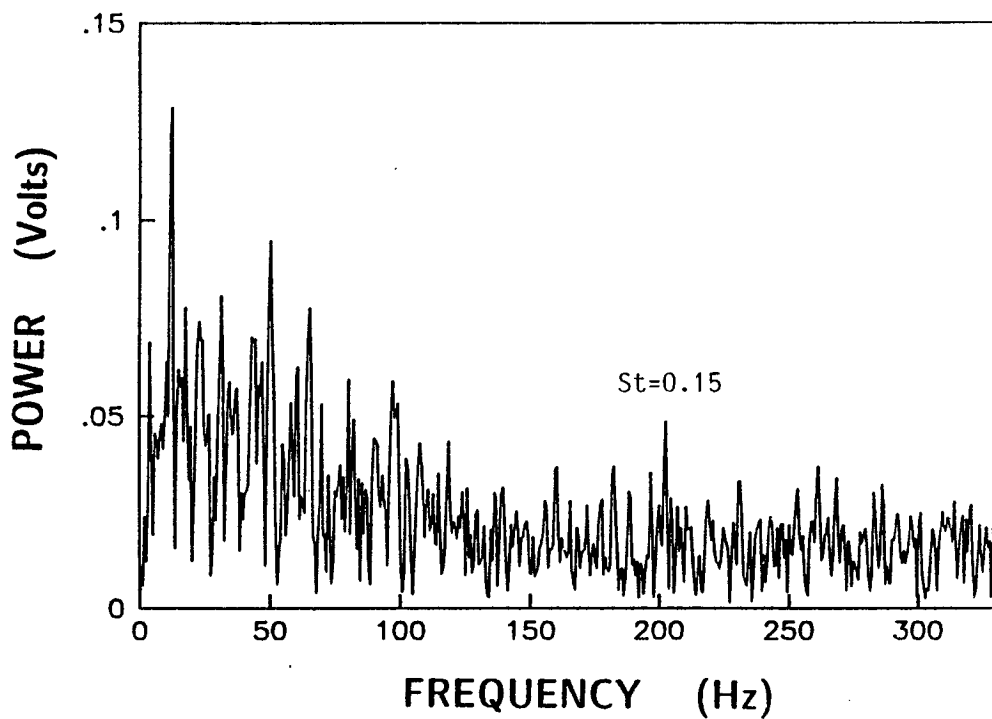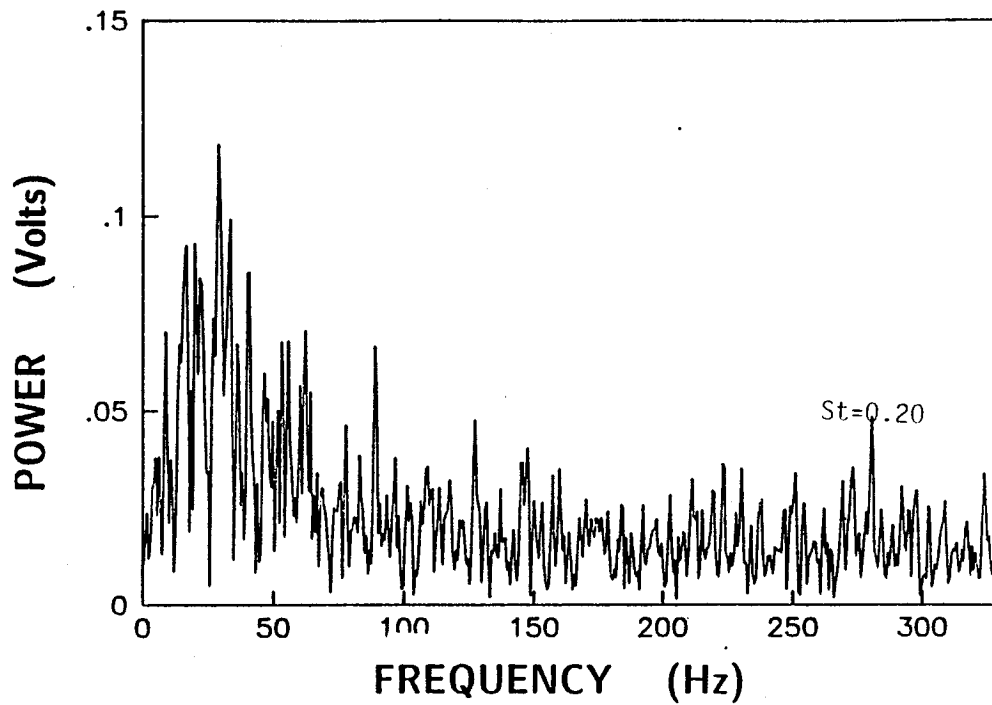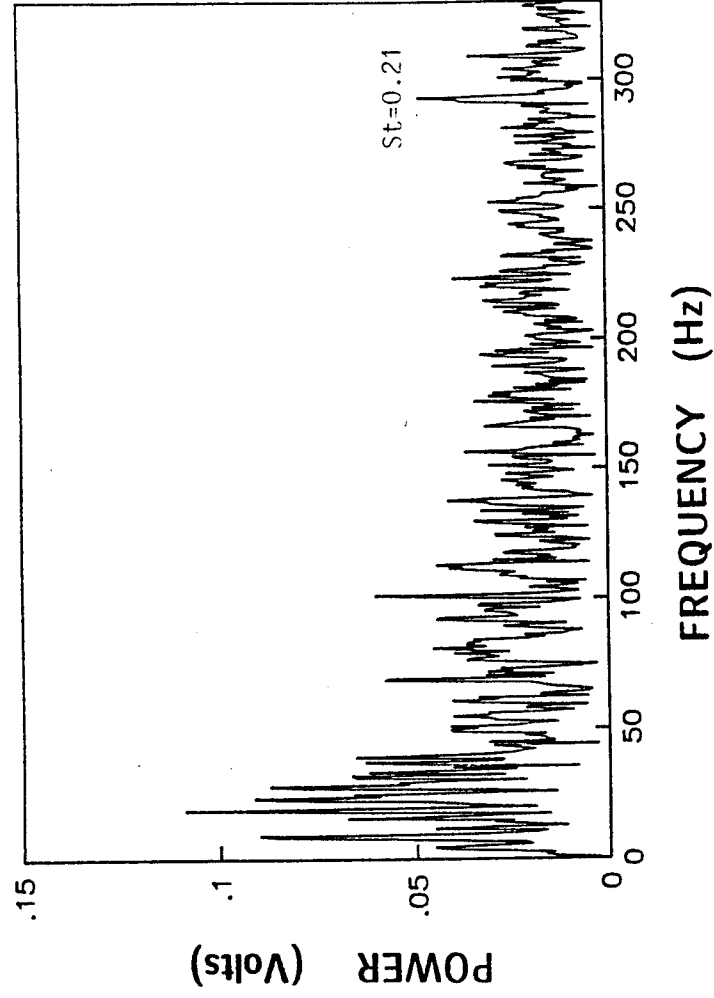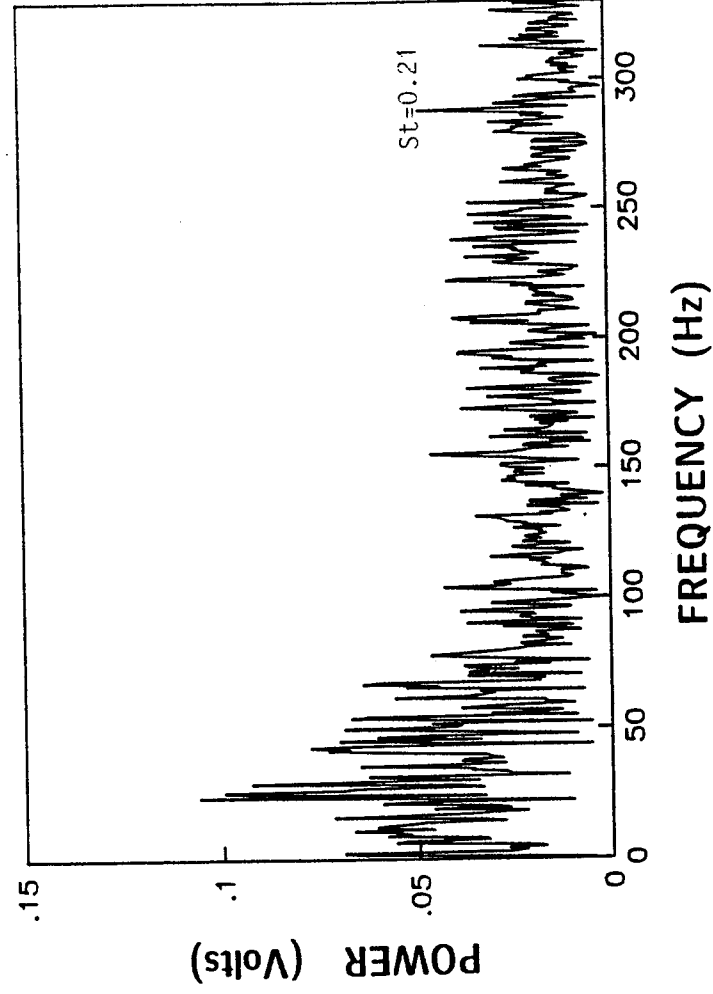55b. $U_\infty = 42$ m/s, perturbation generator secured.

Figure 55. Spectral measurements with perturbation generator secured

55c. $U_\infty = 42$ m/s, perturbation generator secured.

55d. $U_\infty = 42$ m/s, perturbation generator secured

These spectra were all taken while the model was turning with a counter-rotational direction of spin. At higher differential pressures (greater than 450 Pa), a spectral spike was noted at the control frequency (Figure 56). Spectra taken when plenum pressure was less than 450 Pa, exhibited a trough at the perturbation frequency (Figure 57). Troughs were not noted at the lower free stream velocities. Also noted were large spectral peaks in the higher frequencies and the respective Strouhal number is labeled.

Evidence of amplification or decay was examined. As stated previously, simultaneous measurements were not attempted. Representative sets of spectra at the downstream locations were taken and operating conditions repeated after the probe was moved upstream. The upstream location was not immediately behind the perturbation generator, in order to stay out of the vortex roll up region. Instead, an intermediate location was chosen. The downstream distance was 4.27 m (42 airfoil chord lengths) and the intermediate distance was 1.73 m (17 airfoil chord lengths) behind the perturbation generator. Comparisons between spectra measured at the intermediate and downstream locations are shown in Figure 58 for a free stream velocity of 14 m/s. Both measurements were for a counter-rotating spin direction. The amplitudes between the intermediate and downstream locations are given in Table 1. It is noted that in a perturbation frequency range of 80 Hz to 100 Hz, the amplitude appeared to increase downstream. All other frequencies showed amplitudes which appeared to decrease with distance. It is also noted that the downstream RMS levels were less than those at the midstream position.
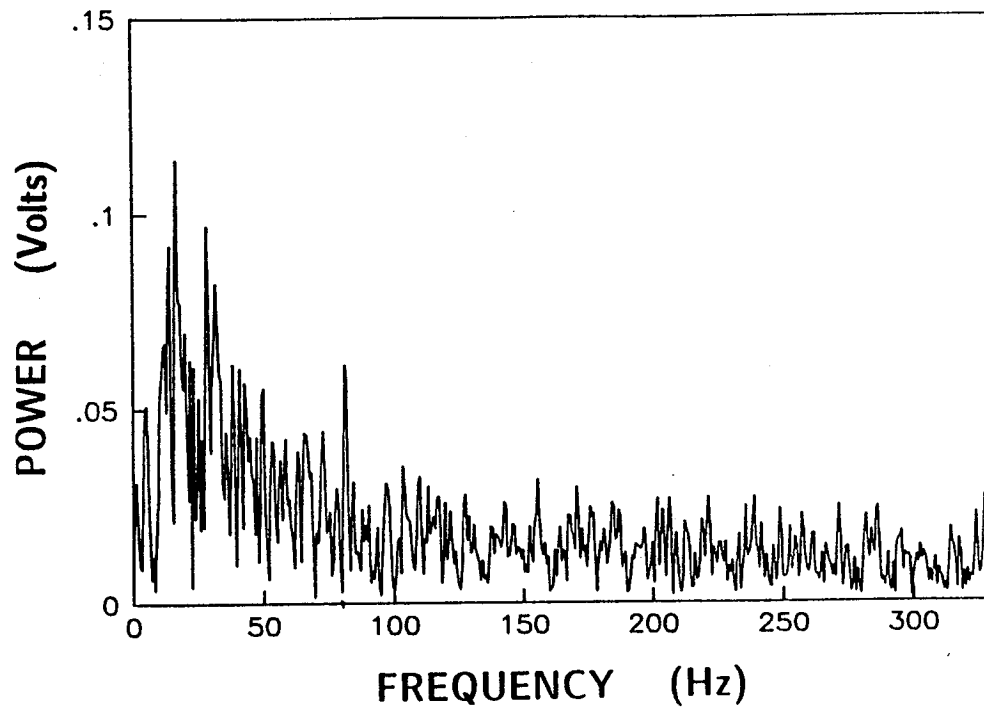
56a. $U_\infty = 42$ m/s, $M_f = 81$ Hz (counter-rotating), $\triangle P = 501$ Pa
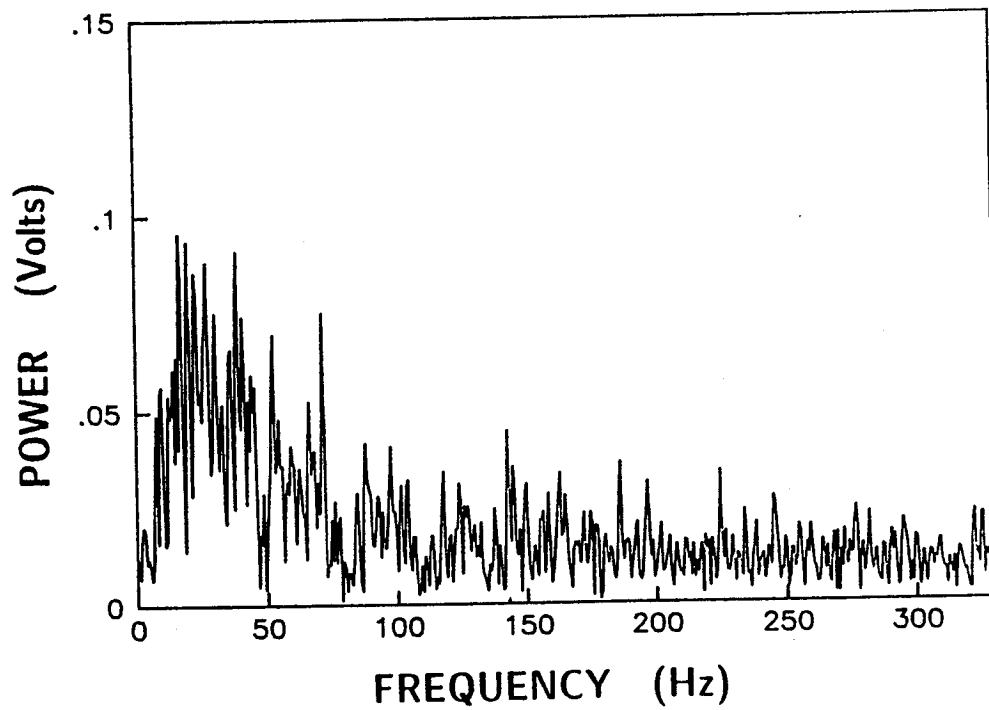
56b. $U_\infty = 42$ m/s, $M_f = 144$ Hz, $\triangle P = 726$ Pa.

Figure 56. Frequency spectra which exhibited a large spectral spike at the perturbation frequency.
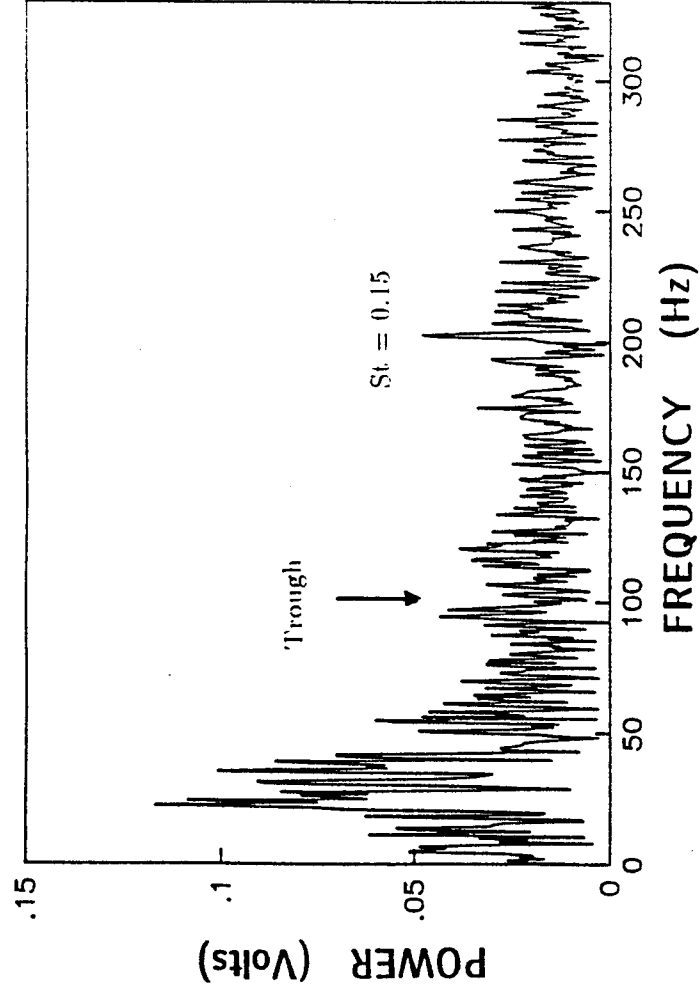
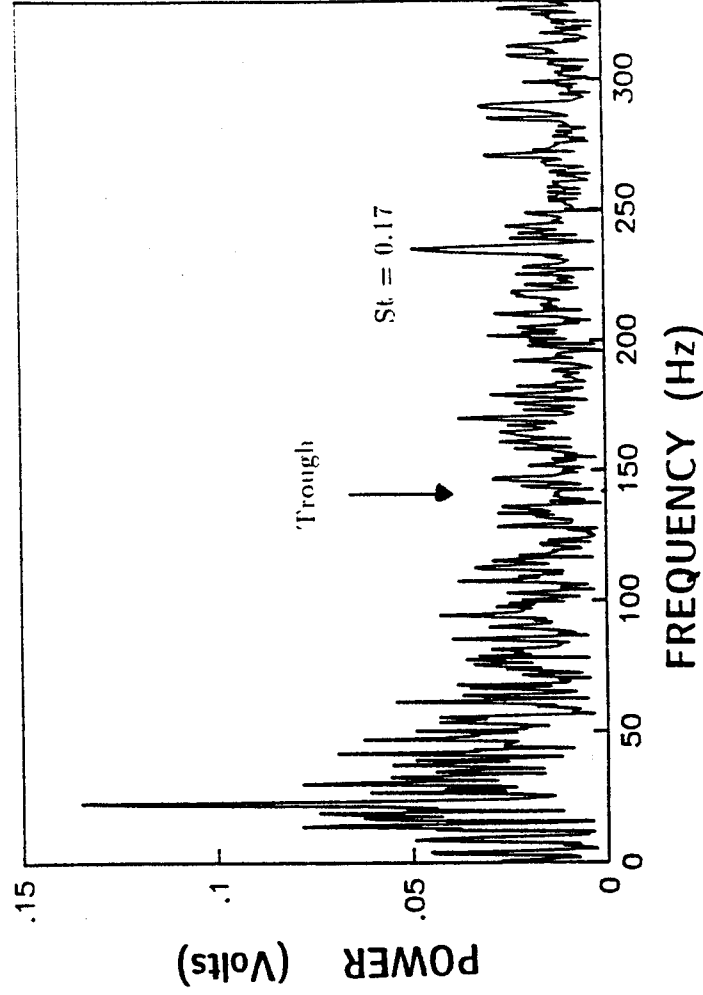57a. $U_\infty = 42$ m/s, $M_r = 100$ Hz (counter-rotating), $\Delta P = 396$ Pa

57b. $U_\infty = 42$ m/s, $M_r = 144$ Hz (counter-rotating), $\Delta P = 422$ Pa

Figure 57. Frequency spectra which exhibited a trough at the perturbation frequency.
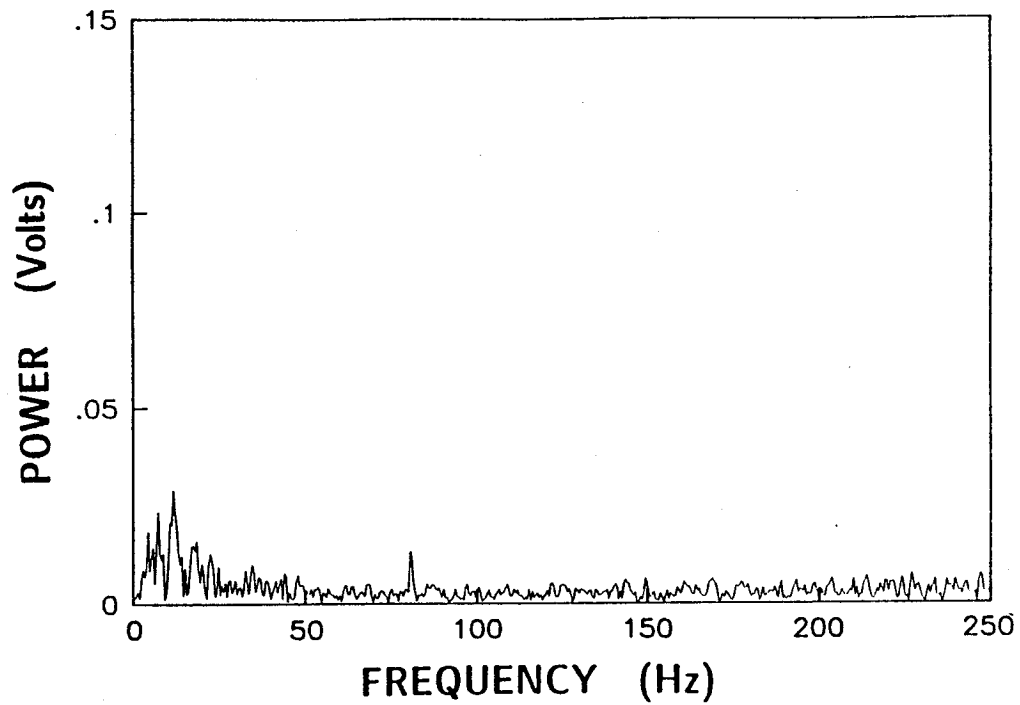
58a. X = 1.73 m, U_∞= 13.7 m/s, M_f = 80 Hz (counter-rotating), $\triangle P$= 236 Pa.
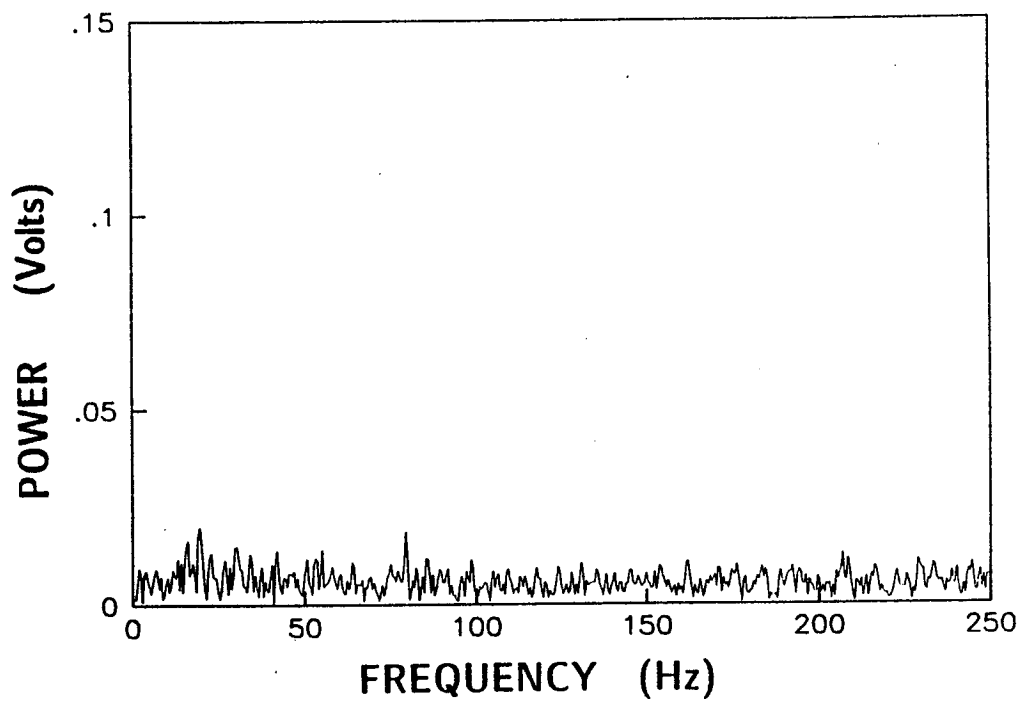
58b. X = 4.27 m, U_∞= 13.8 m/s, M_f = 80.5 Hz (counter-rotating), $\triangle P$= 249 Pa.

Figure 58. Frequency spectra for upstream and downstream probe locations with a freestream velocity of 13.7 m/s.

58c. X = 1.73 m, U_{∞} = 13.7 m/s, M_f = 99 Hz (counter rotating), ΔP = 176 Pa.

58d. X = 4.27 m, U_{∞} = 13.7 m/s, M_f = 98.6 Hz (counter rotating), ΔP = 178 Pa.

Figure 58 continued

Table 1. Upstream and Downstream Amplitudes for $U_\infty = 14$ m/s

Counter-rotating

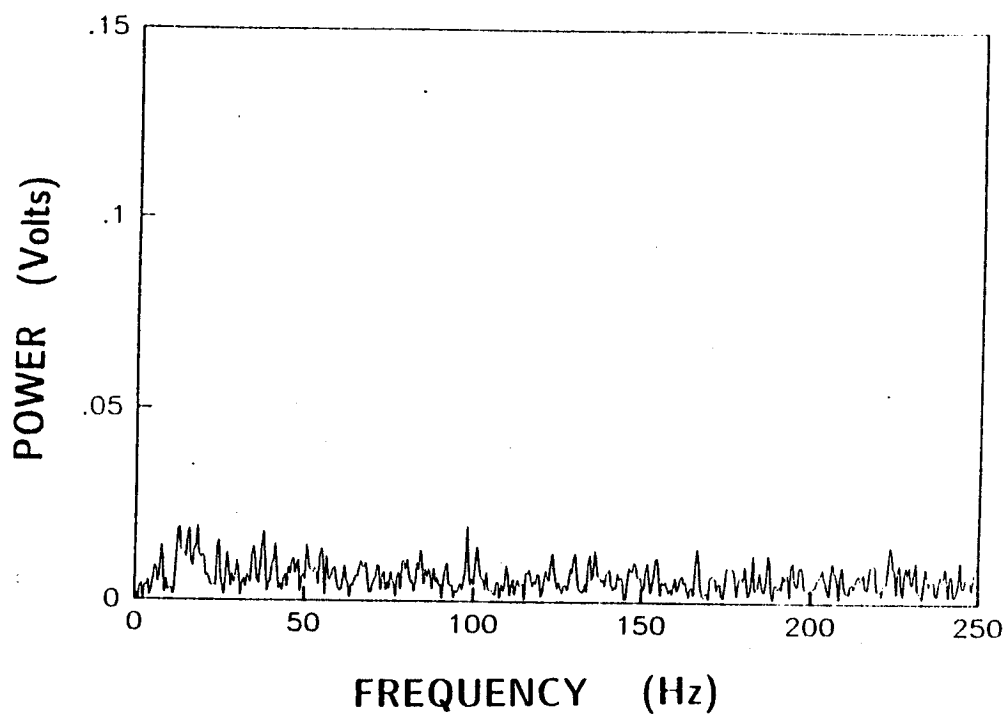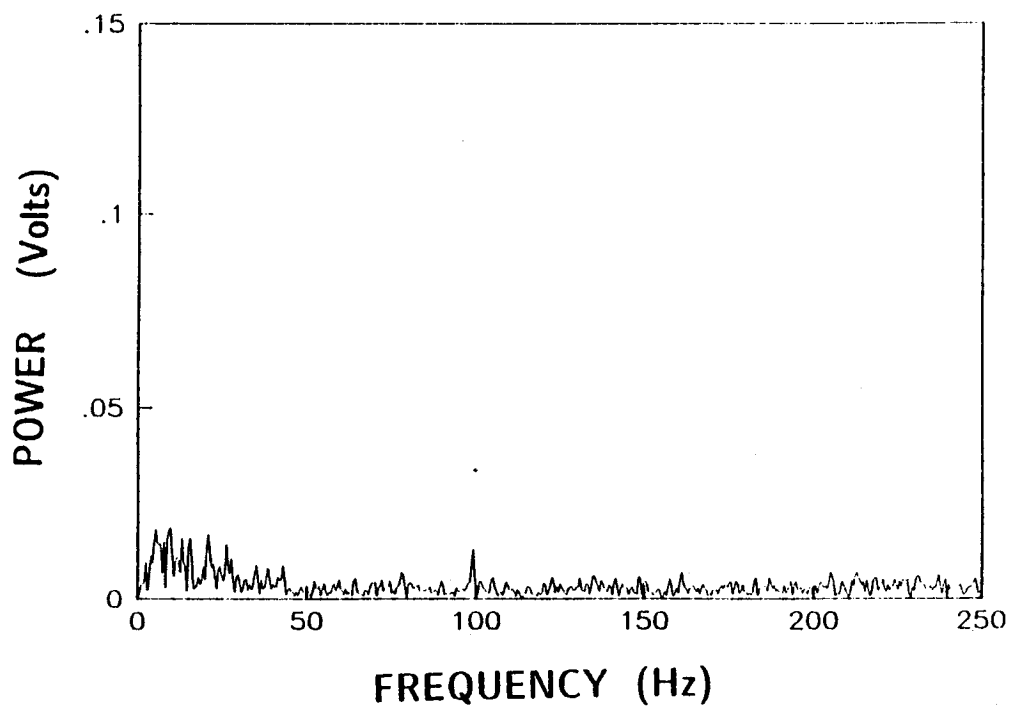| Midstream Location x = 2.73 m			Downstream Location x = 4.27 m		
Frequency (hz)	ΔP (Pa)	Amplitude (mv)	Frequency (hz)	ΔP (Pa)	Amplitude (mv)
60.0	310	11.6	61.5	302	12.7 *
62.0	298	13.3	63.9	302	12.9
72.2	320	9.5	69.8	302	12.4 *
73.2	293	4.0	70.8	302	11.4 *
79.6	311	13.5	80.5	320	16.7 *
79.6	308	14.4	80.6	320	15.6 *
79.5	412	18.7	80.5	436	13.1
79.8	322	13.1	80.1	299	17.3 *
85.4	309	11.0	83.0	302	14.5 *
89.8	307	11.0	89.0	297	15.8 *
92.7	202	12.2	92.7	295	11.8
98.6	310	15.0	98.6	310	10.8
98.6	308	19.0	98.9	310	13.1
102	296	16.0	102	302	8.1
102	309	11.5	101	302	7.2
102	294	19.0	101	299	13.4
115	307	15.4	118	297	12.6
142	322	12.0	139	318	10.4
145	450	12.4	143	450	10.2
145	310	22.5	149	303	9.3

* - Indicates amplification downstream

The counter-rotating perturbation spectra for intermediate and downstream locations are shown in Figure 59 for a free stream velocity of 21 m/s. The increased RMS levels at the intermediate location are more evident. The spectral peaks are much sharper in the downstream data due to lower background "noise" levels. Spectral amplitude comparisons for 21 m/s are given in Table 2. Again, in the perturbation frequency range of 80 to 100 Hz the amplitude of the spectral peak appears to increase downstream.

The last set of tests were to determine the effects of spin direction. Comparisons of the spectral data between the co-rotating and counter-rotating perturbations (while other parameters are held constant) are shown in Figure 60 for the intermediate location. It is evident that larger amplitudes are exhibited for the co-rotational measurements.

Energy levels in the spectra were determined around the frequencies produced by the perturbation generator. This was done by integrating the voltage levels for frequency bandwidths of ± 2.0, ± 1.0, and ± 0.5 Hz, centered around the perturbation generator frequency. The integrated frequency voltage product, E_f, was divided by the total integrated voltage for the spectrum, E_t. This E_f/E_t term is a measure of energy content and was plotted versus the perturbation frequencies to analyze the effects of frequency on the perturbation generator signal. Figure 61 shows the three frequency bandwidths (± 2.0, ± 1.0, ± 0.5 Hz) plotted for the probe at the upstream location, with $U_\infty = 42$ m/s, and a counter-rotating perturbation. It shows an increase in energy from 80 Hz to 100 Hz, followed by a gradual decrease as frequency continues to increase.
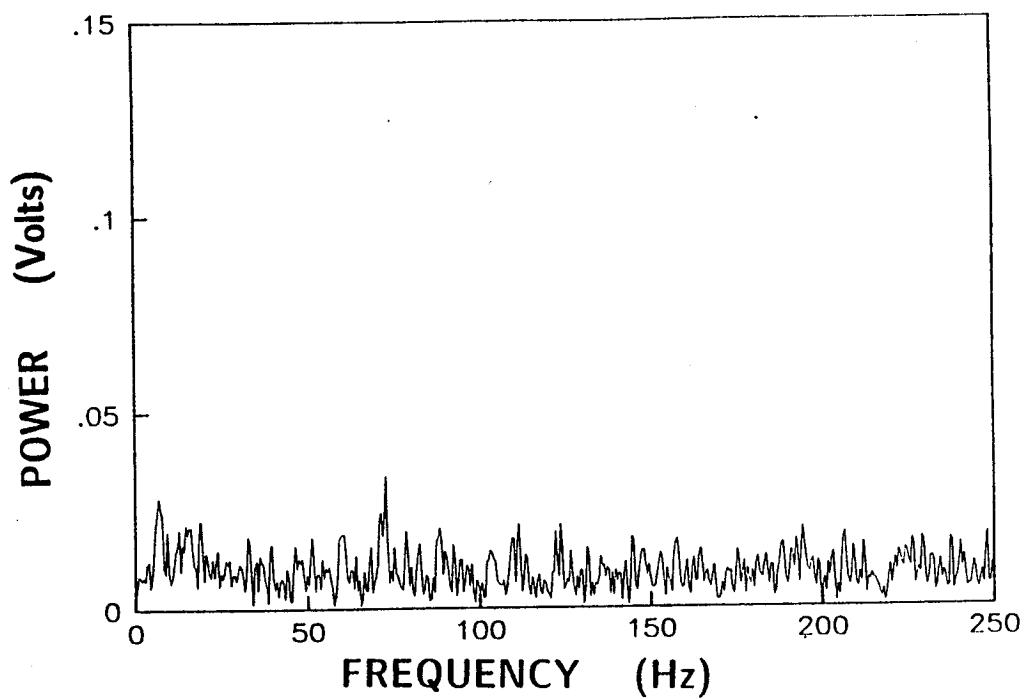
59a. X = 1.73 m, U_{∞}= 20.7 m/s, M_f = 73 Hz (counter-rotating)
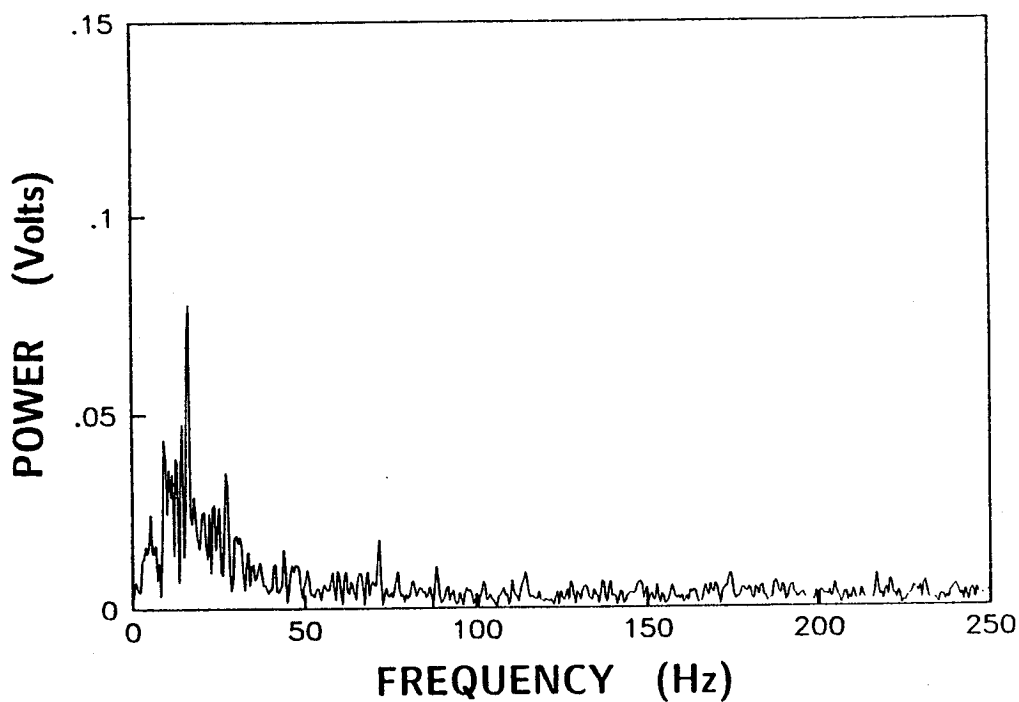
59b. X = 4.27 m, U_{∞}= 20.7 m/s, M_f = 72.3 Hz (counter-rotating)

Figure 59. Frequency spectra for upstream and downstream probe locations with a freestream velocity of 20.7 m/s.

59c. X = 1.73 m, U_{∞} = 20.7 m/s, M_f = 115 Hz (counter-rotating)
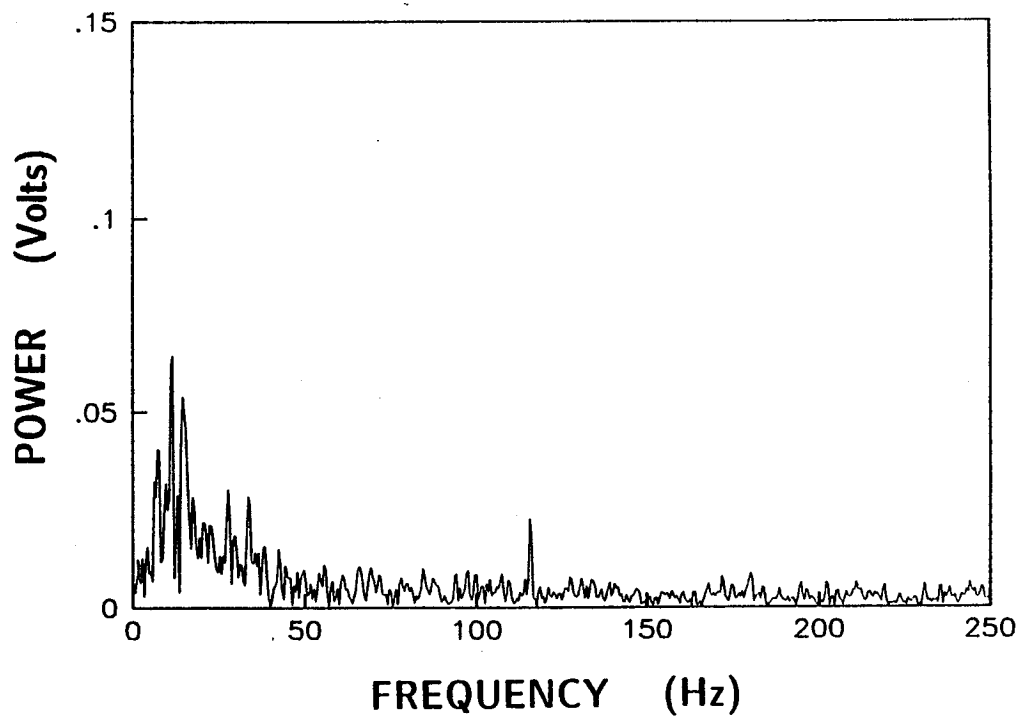
59d. X = 4.27 m, U_{∞} = 20.7 m/s, M_f = 116 Hz (counter-rotating)

Figure 59 continued

59e. X = 1.73 m, U$_\infty$= 20.7 m/s, M$_f$ = 98 Hz (counter-rotating)

59f. X = 4.27 m, U$_\infty$= 20.7 m/s, M$_f$ = 101 Hz (counter-rotating)

Figure 59 continued

59g. X = 1.73 m, U_∞ = 20.7 m/s, M_f = 113 Hz (counter-rotating)
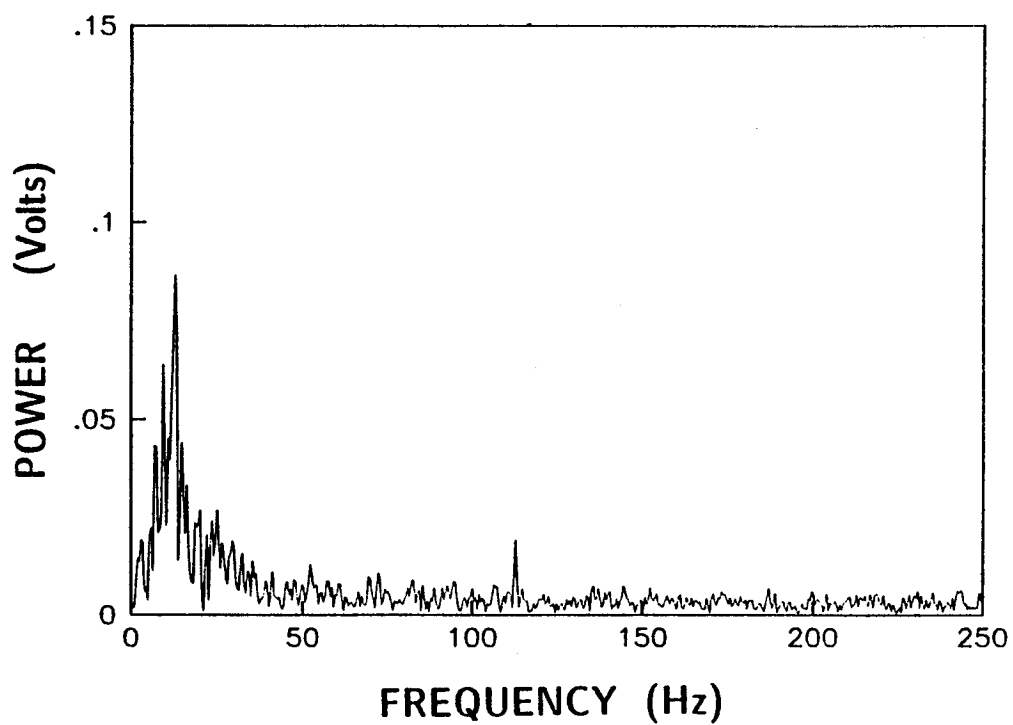
59h. X = 4.27 m, U_∞ = 20.7 m/s, M_f = 112 Hz (counter-rotating)
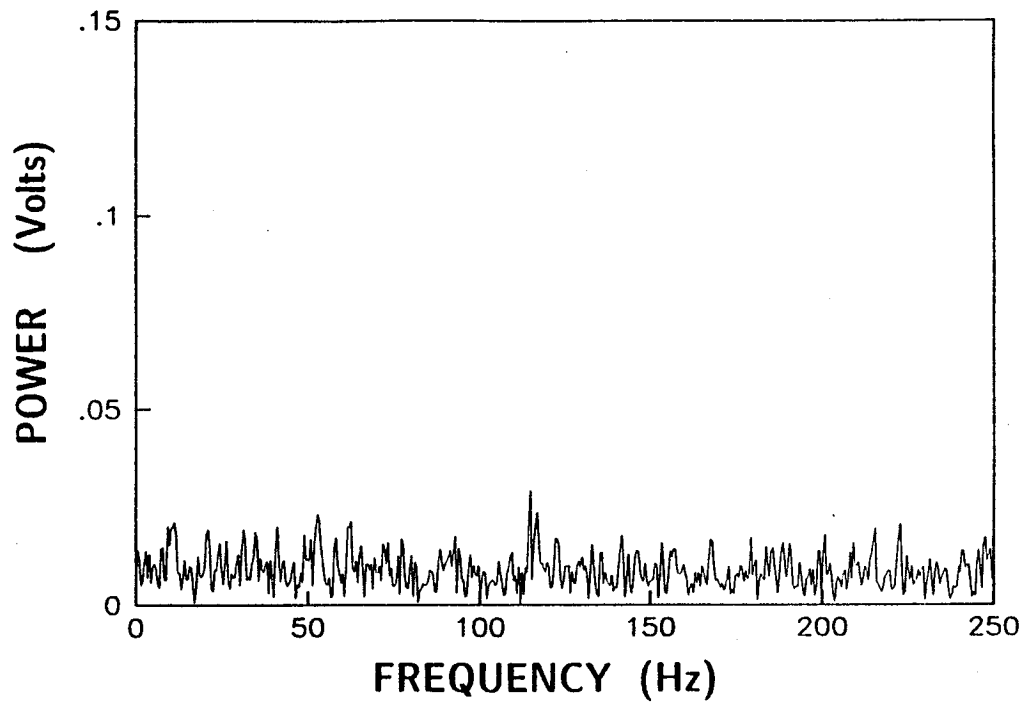
Figure 59 continued

-133-
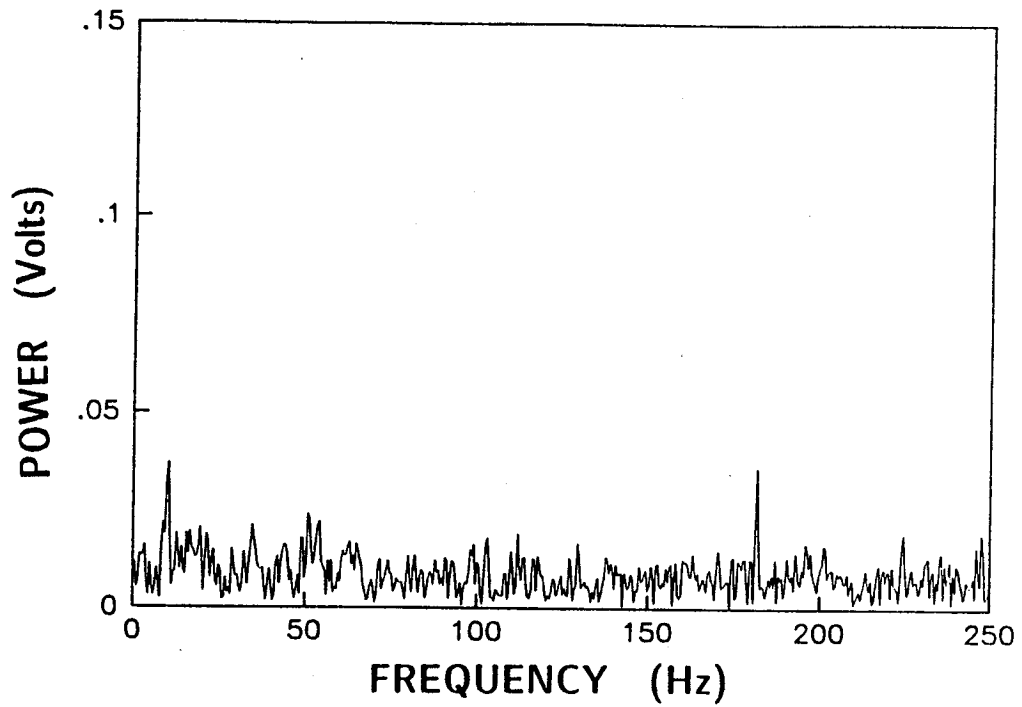
59i. X = 1.73 m, U_∞ = 20.7 m/s, M_f = 181 Hz (counter-rotating)
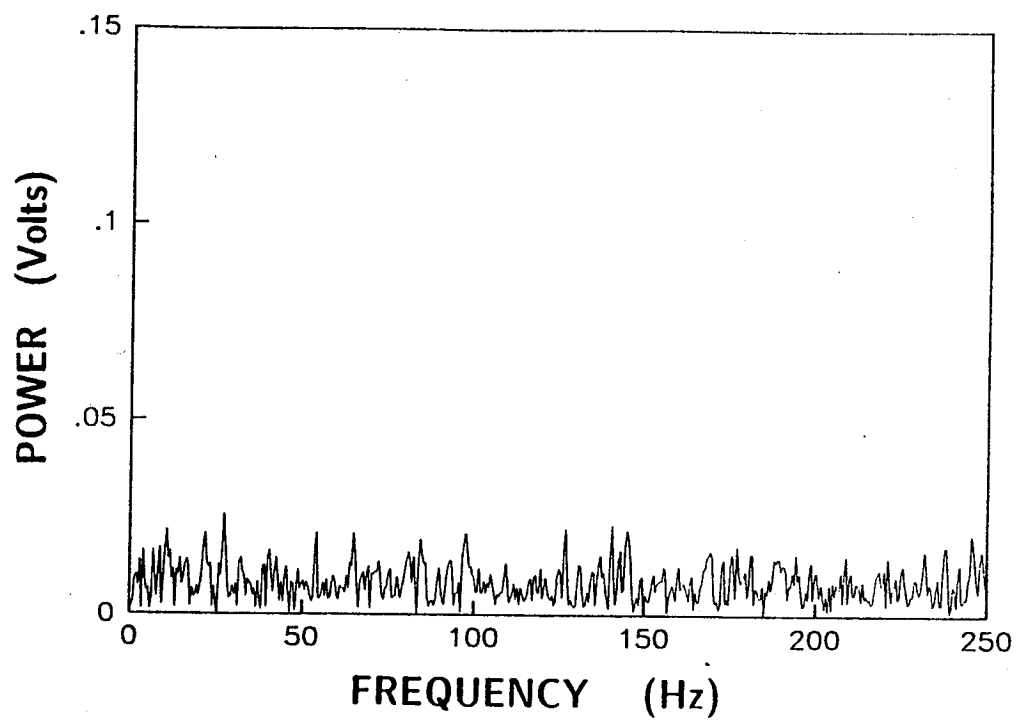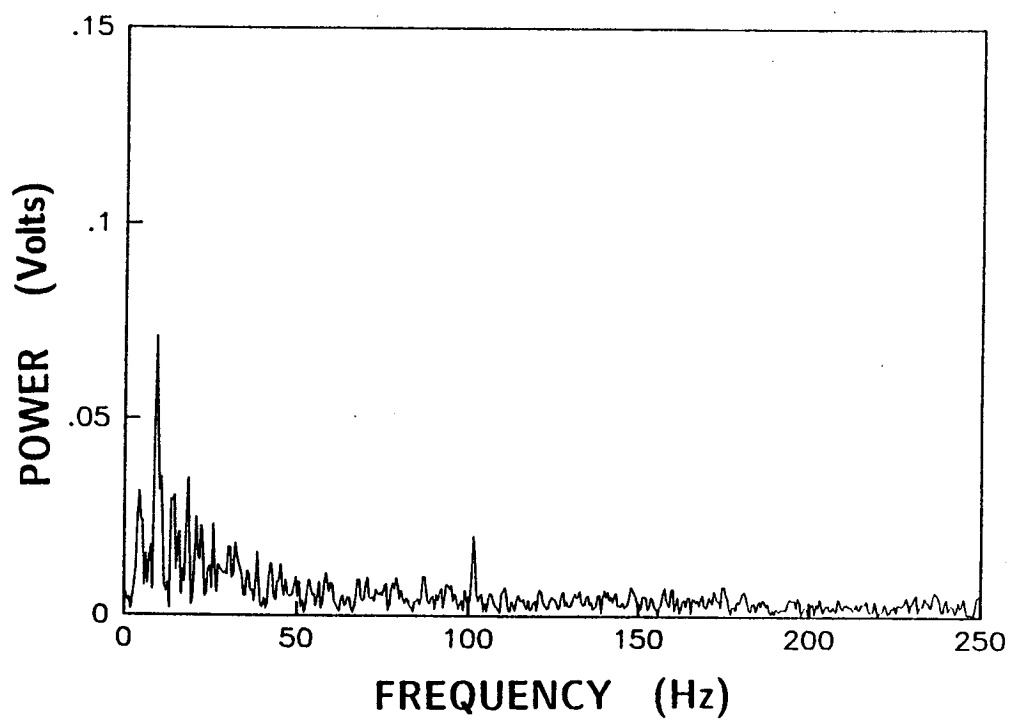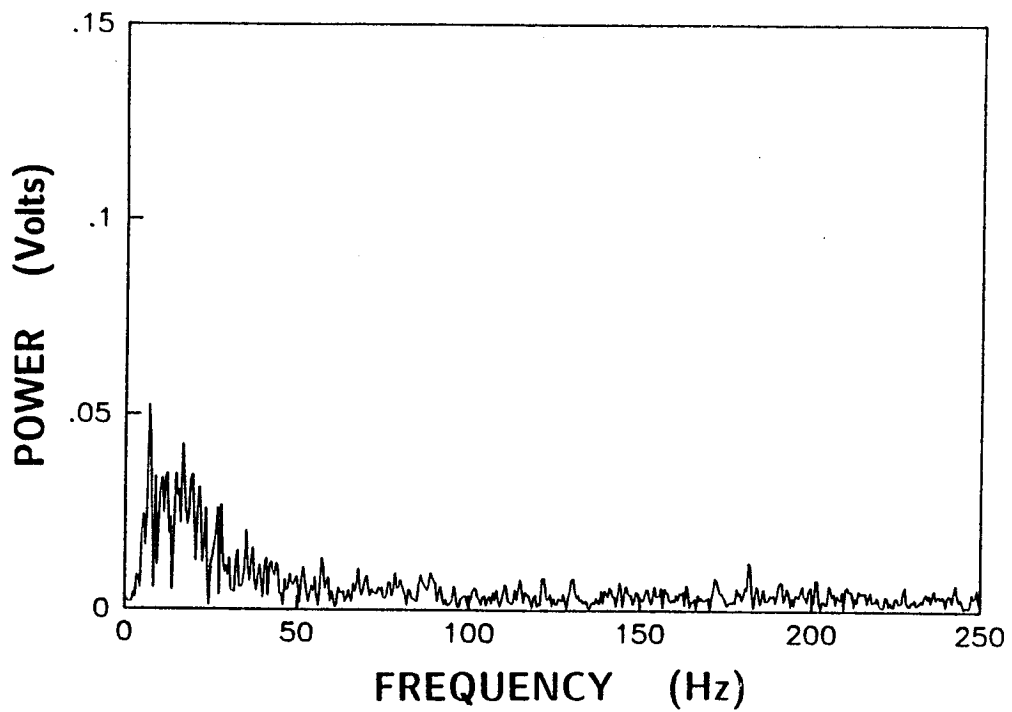

59j. X = 4.27 m, U_∞ = 20.7 m/s, M_f = 182 Hz (counter-rotating)

Figure 59 continued

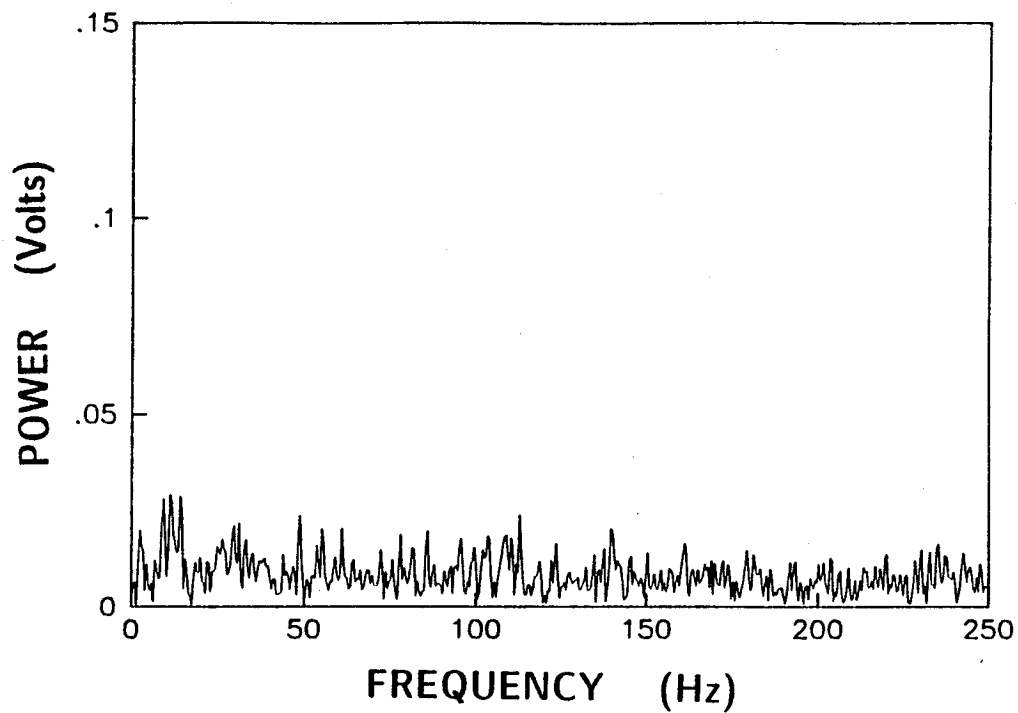Table 2. Upstream and Downstream Amplitudes for $U_\infty = 21$ m/s

Counter-rotating

Midstream Location x = 2.73 m			Downstream Location x = 4.27 m		
Frequency (hz)	$\triangle$ P (Pa)	Amplitude (mv)	Frequency (hz)	$\triangle$ P (Pa)	Amplitude (mv)
69.3	473	14.6	70.6	469	16.1 *
72.7	425	33.4	71.7	420	17.7
73.2	593	25.9	71.2	601	15.4
73.2	594	21.6	71.7	610	15.8
74.2	471	25.0	67.9	468	19.5
85.9	448	20.8	84.0	441	21.3 *
97.7	422	20.7	101	422	20.4
106	466	28.6	112	462	19.0
113	483	23.7	113	451	11.0
115	357	29.1	116	374	21.3
181	471	26.2	182	460	12.4

* - Indicates amplification downstream
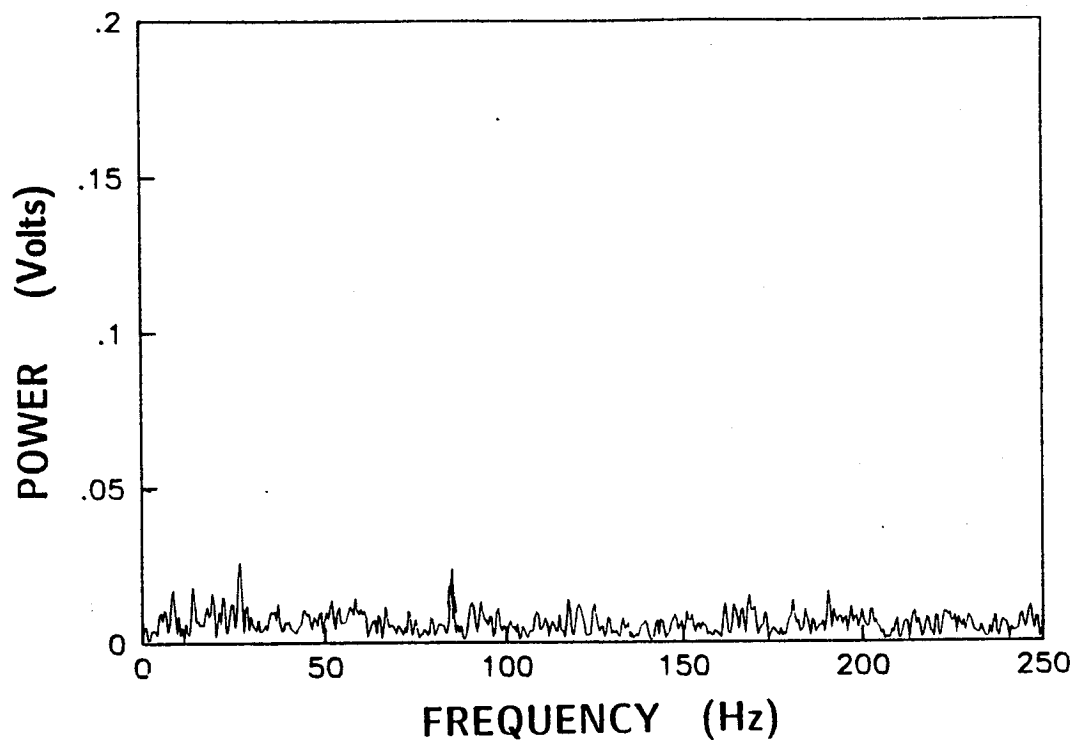
60a. Co-rotating, $U_\infty = 13.7$ m/s, $M_f = 85$ Hz, $\Delta P = 203$ Pa
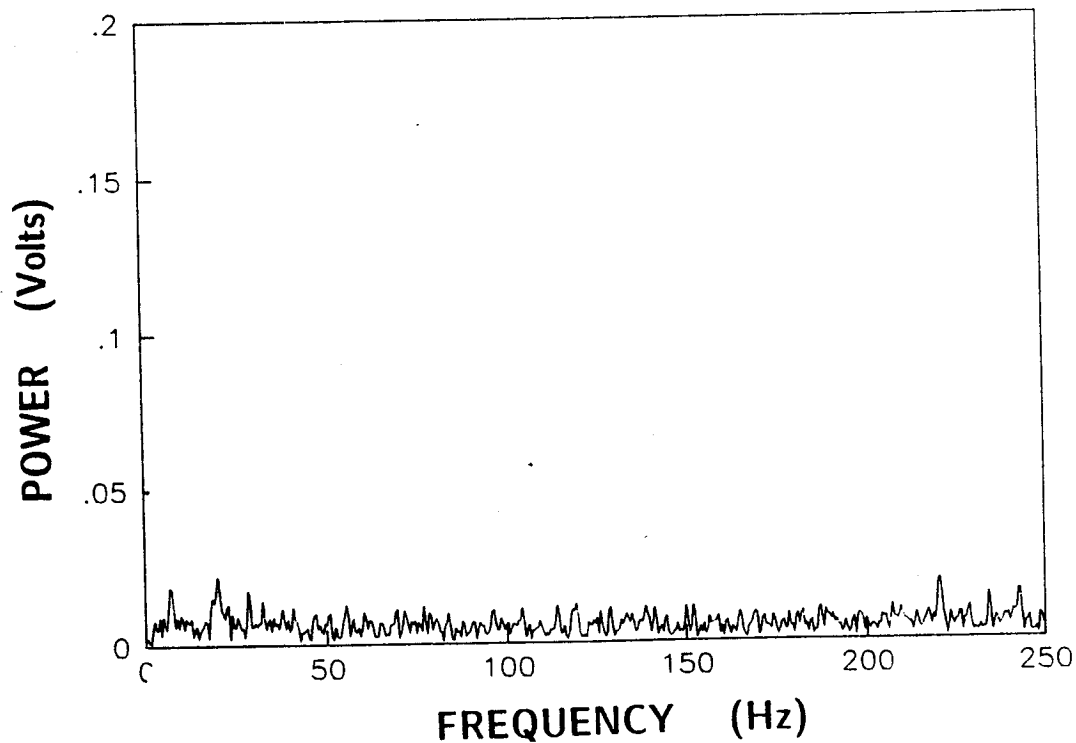
60b. Counter-rotating, $U_\infty = 13.7$ m/s, $M_f = 86$ Hz, $\Delta P = 177$ Pa

Figure 60. Comparison of co-rotating and counter-rotating perturbations, $X = 1.73$ m(upstream).

60c. Co-rotating, $U_\infty = 13.7$ m/s, $\dot{M}_f = 95$ Hz, $\triangle P = 207$ Pa.

60d. Counter-rotating, $U_\infty = 13.7$ m/s, $M_f = 95$ Hz, $\triangle P = 209$ Pa.
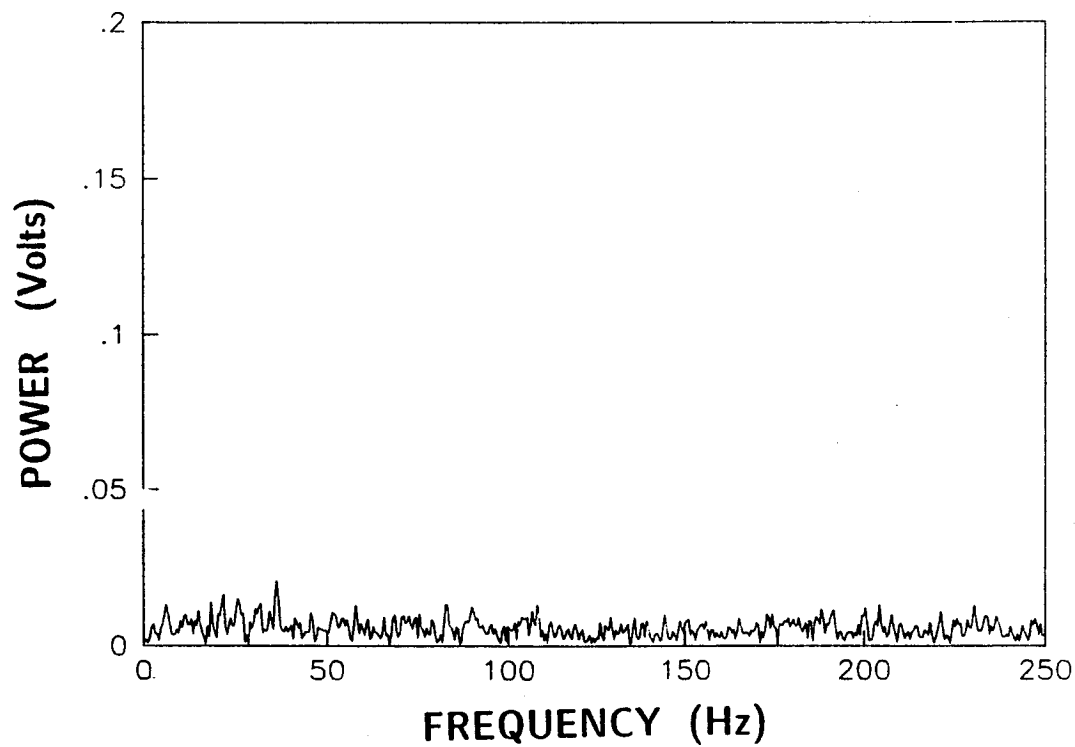
Figure 60 continued

60e. Co-rotating, $U_\infty = 42$ m/s, $M_f = 119$ Hz, $\triangle P = 396$ Pa.

60f. Counter-rotating, $U_\infty = 42$ m/s, $M_f = 118$ Hz, $\triangle P = 370$ Pa.

Figure 60 continued

-138-

60g. Co-rotating, $U_\infty = 42$ m/s, $M_f = 171$ Hz, $\triangle P = 430$ Pa.

60h. Counter-rotating, $U_\infty = 42$ m/s, $M_f = 164$ Hz, $\triangle P = 400$ Pa

Figure 60 continued
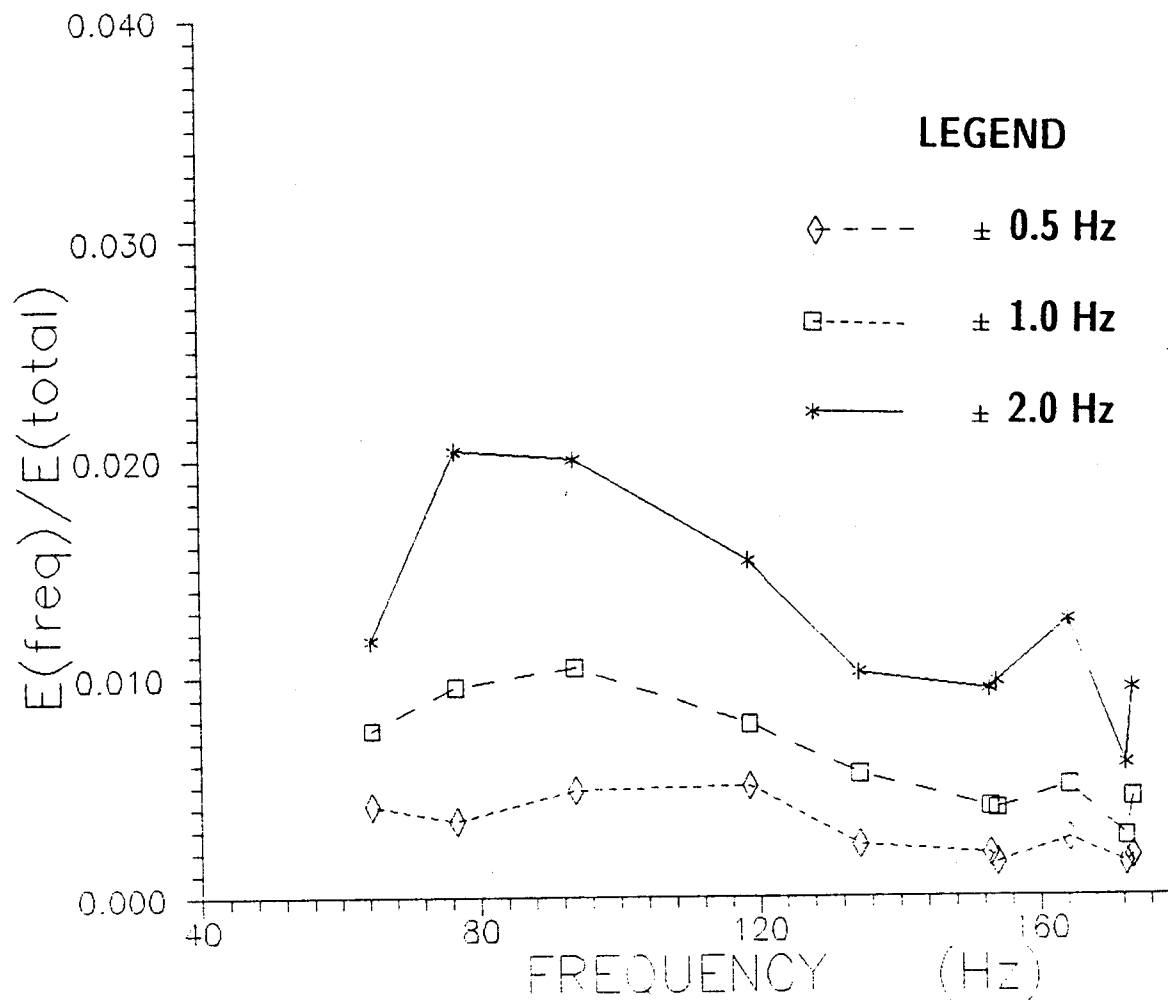
Figure 61. Energy vs Frequency , U_∞ = 42 m/s, X = 1.73 m, frequency bandwidths ± 0.5, ± 1.0, ± 2.0 Hz

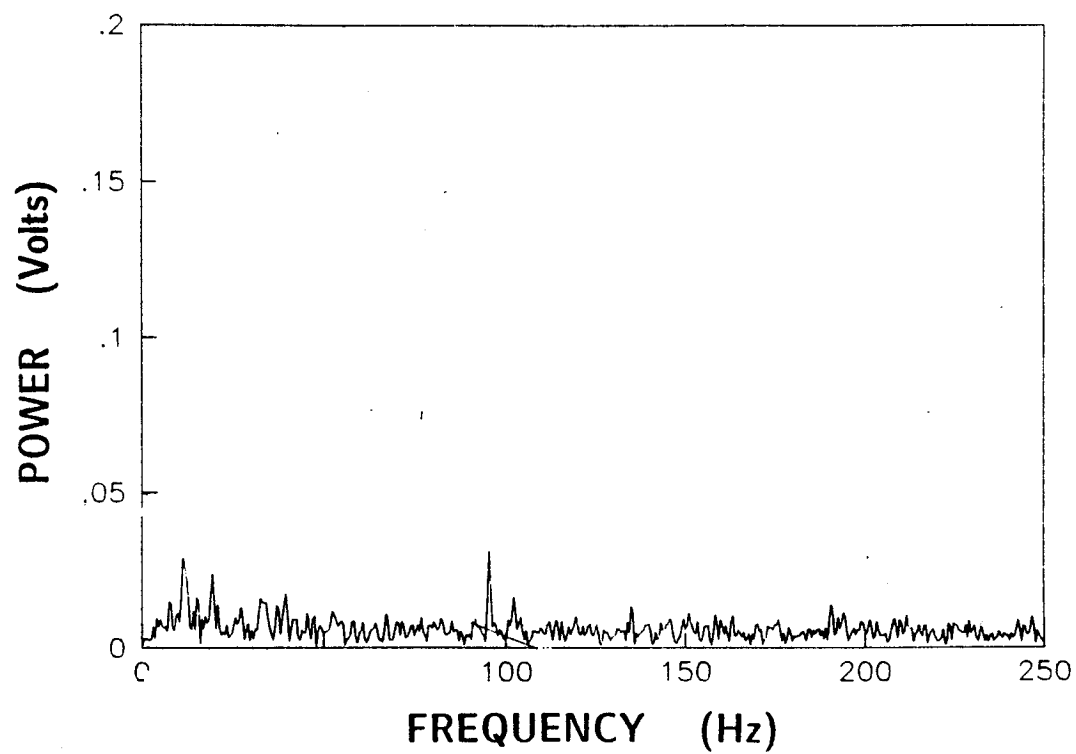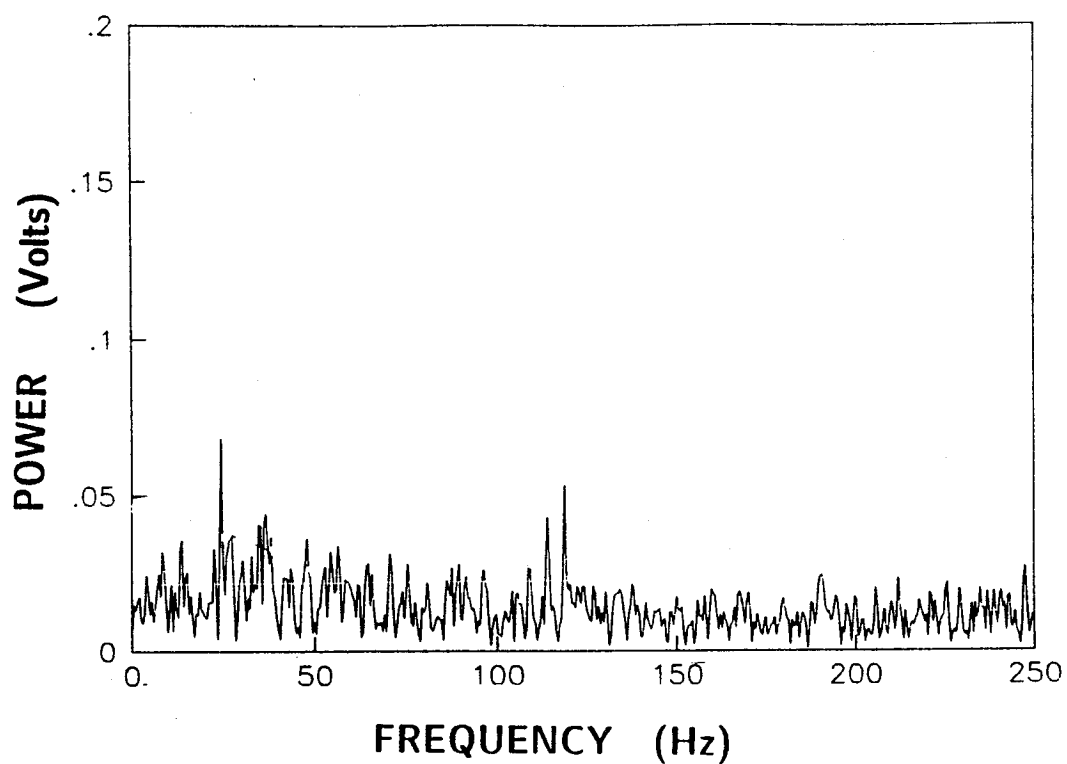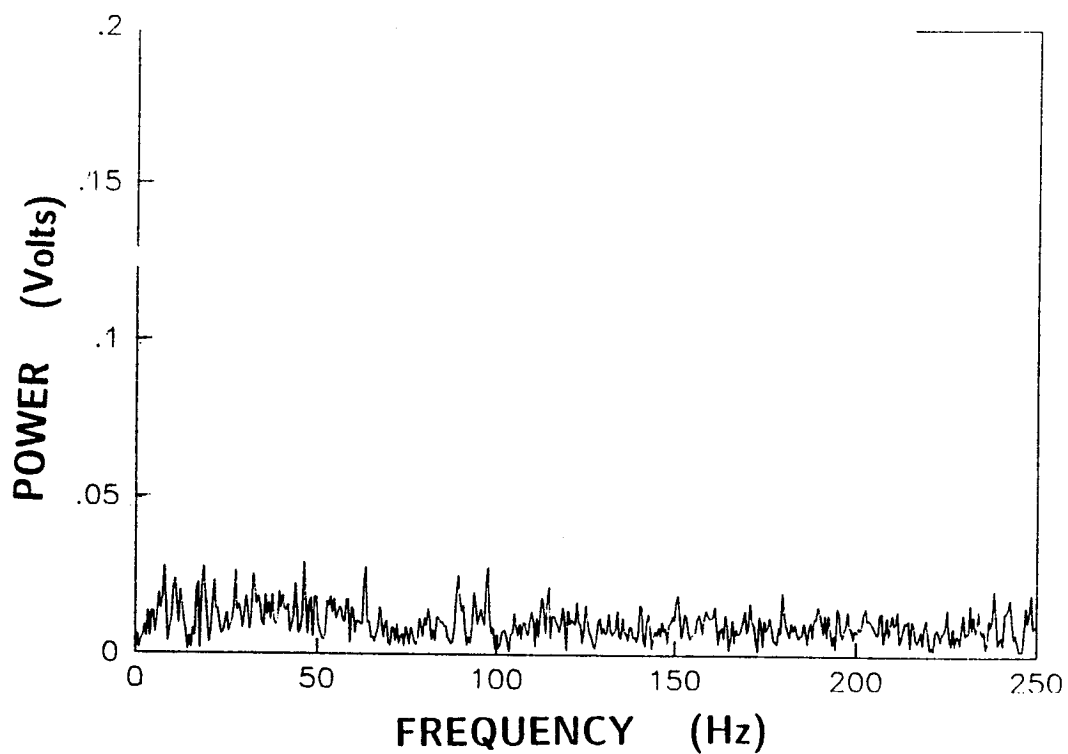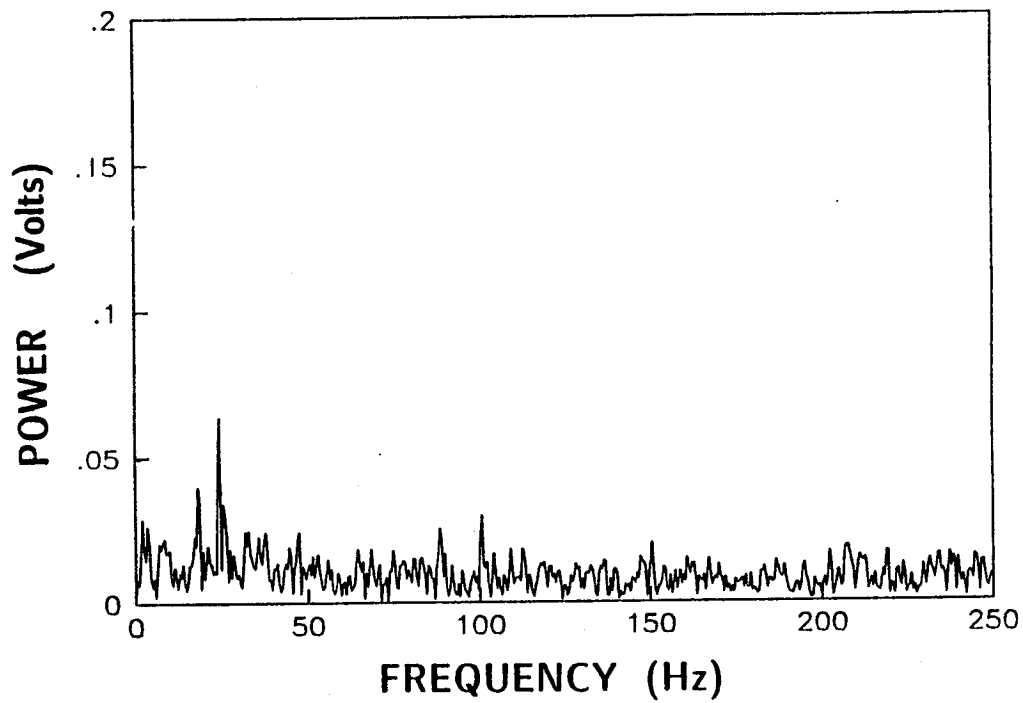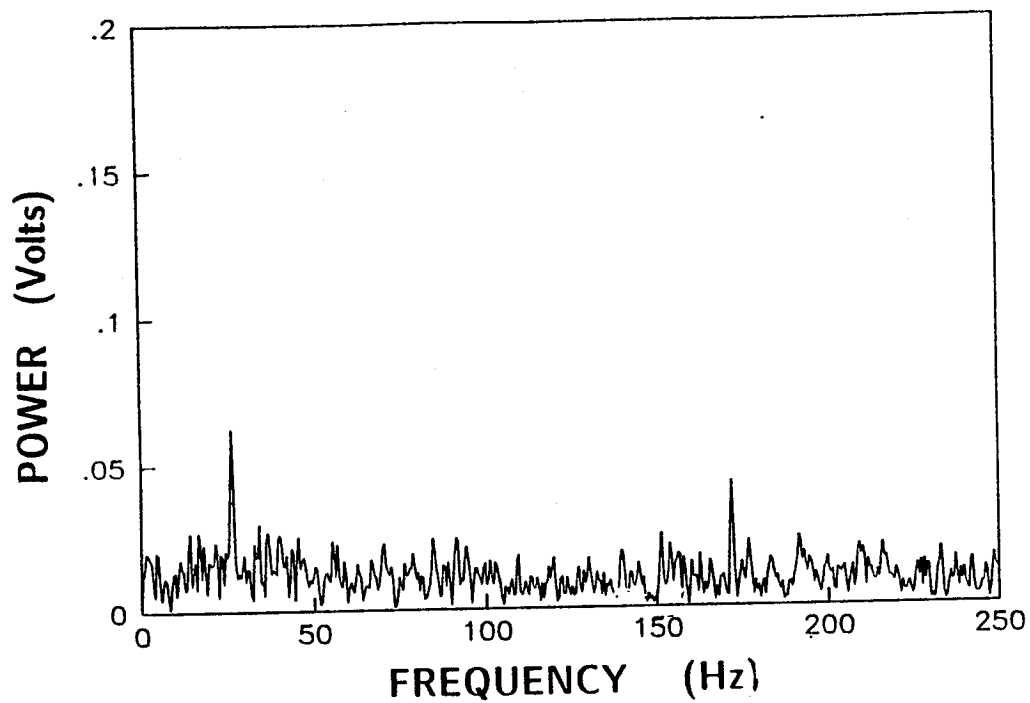Figure 62 compared the co-rotating perturbations with the counter-rotating perturbations at the upstream probe position with $U_\infty = 42$ m/s. Energy levels for the co-rotating perturbations are lower than the counter-rotating levels at low frequencies, but they exceed the counter-rotating energy levels above 100 Hz.

Similar plots were developed for 14 m/s flow velocities. Figure 63 compares the co-rotating and counter-rotating perturbations in the ± 0.5 frequency bandwidth. It also plots the unperturbed energy levels for similar conditions. Figure 63a gives a comparison at the intermediate location and Figure 63b is for the downstream location. At the intermediate location, energy levels separate between 60 and 120 Hz, with the co-rotation energy levels greater than the counter-rotation levels. Downstream energy levels are about the same order of magnitude, except the co-rotating levels are less than the counter-rotating levels. Again, an exception downstream is the increase in counter-rotating energy level in the 80 to 100 Hz frequency range while the co-rotating levels dropped.

.The upstream energy levels have been compared to the downstream energy levels in Figure 64 for the counter-rotating perturbations with a nominal free stream velocity of 14 m/s. Interestingly, the two curves mirrored each other with the downstream curve generally lying above the upstream curve for frequencies of approximately 70 to 120 Hz (especially in the ± 0.5 Hz bandwidth). Both had a sharp increase in the 80 to 100 Hz frequency range. However, the co-rotating perturbation case was quite different as seen in Figure 65. The upstream energy levels were significantly higher than the downstream energy levels. The downstream levels also decreased in the 80 to 100 Hz frequency range while the upstream

LEGEND

◊ − − Counter-rotating
☐ − − − − Co-rotating

E_{freq} / E_{total}

62a. ± 0.5 Hz frequency bandwidth

62b. ± 1.0 Hz frequency bandwidth

62c. ± 2.0 Hz frequency bandwidth.
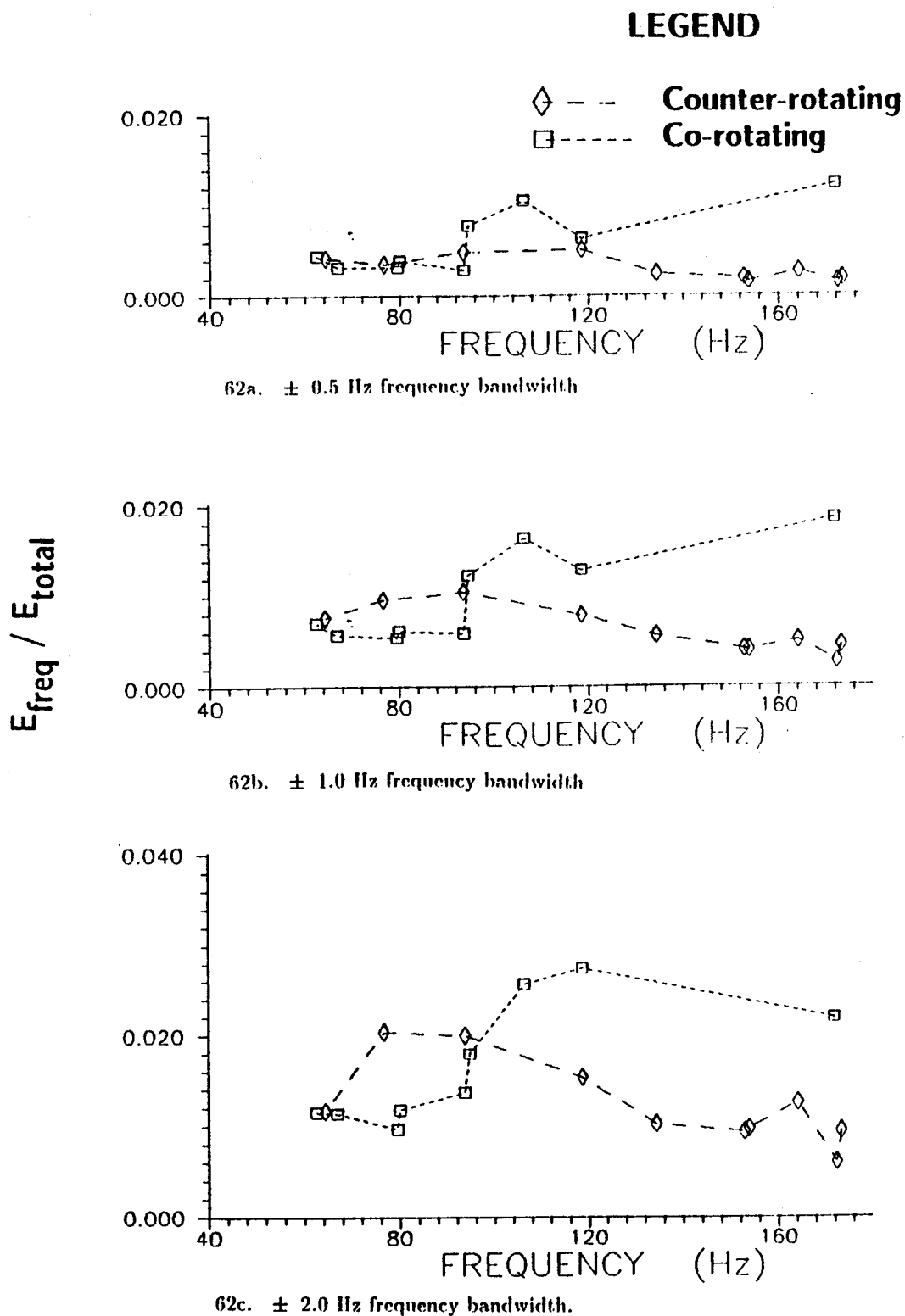
Figure 62. Comparison of co-rotating and counter-rotating perturbations energy levels vs frequency, $U_\infty = 42$ m/s, $X = 1.73$ m, frequency bandwidths ± 0.5, ± 1.0, ± 2.0 Hz

-142-

LEGEND

◇ – –   **Counter-rotating**
◻ - - - -   **Co-rotating**
✳ ——   **Unperturbed**

63a. X = 1.73 m

63b. X = 4.27 m
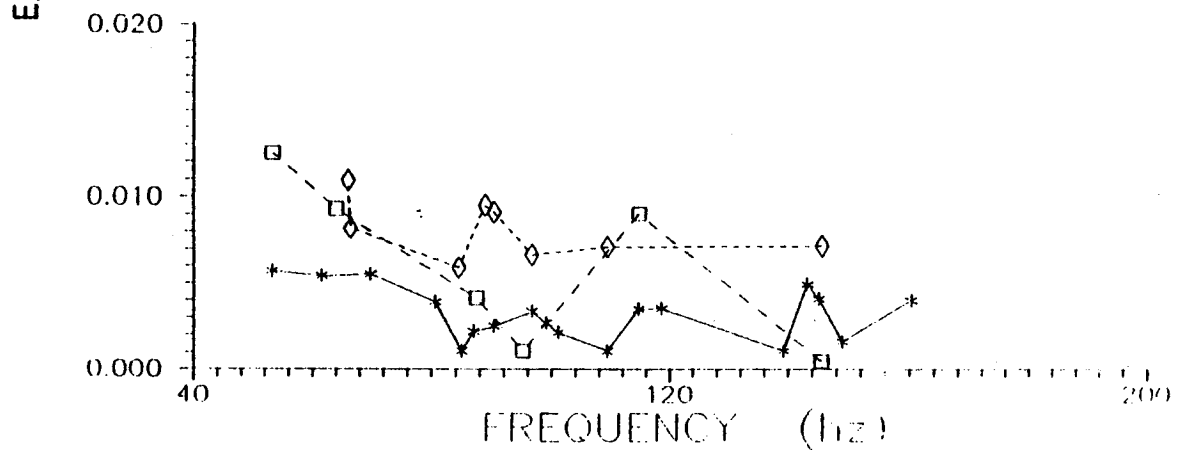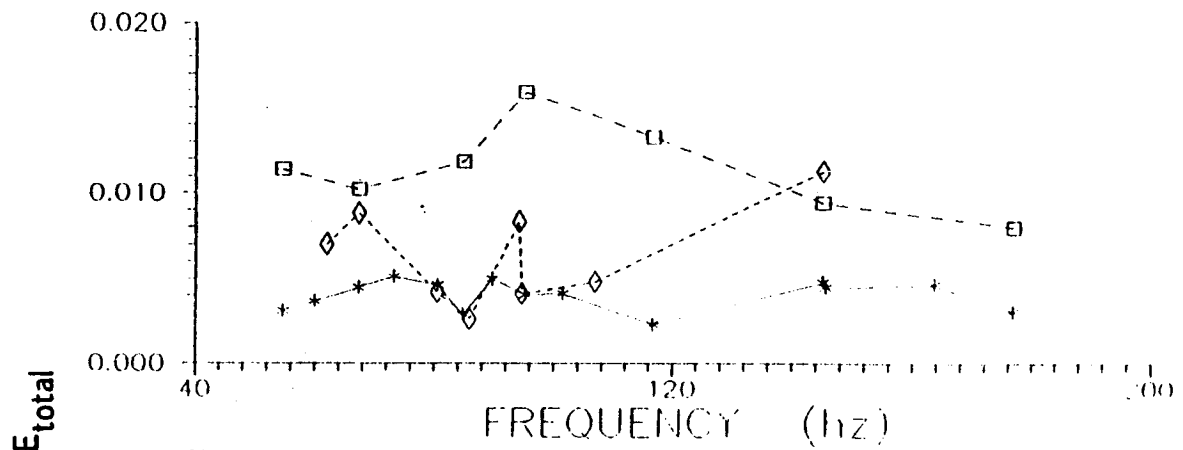
Figure 63.   Comparison of co-rotating and counter rotating perturbation energy levels vs frequency at the upstream and downstream probe locations, U_∞ = 14 m/s, frequency bandwidth ± 0.5 Hz.

LEGEND

⊡---- **X = 4.27 m (Downstream)**
◇ -- **X = 1.73 m (Upstream)**
*—— **Unperturbed**
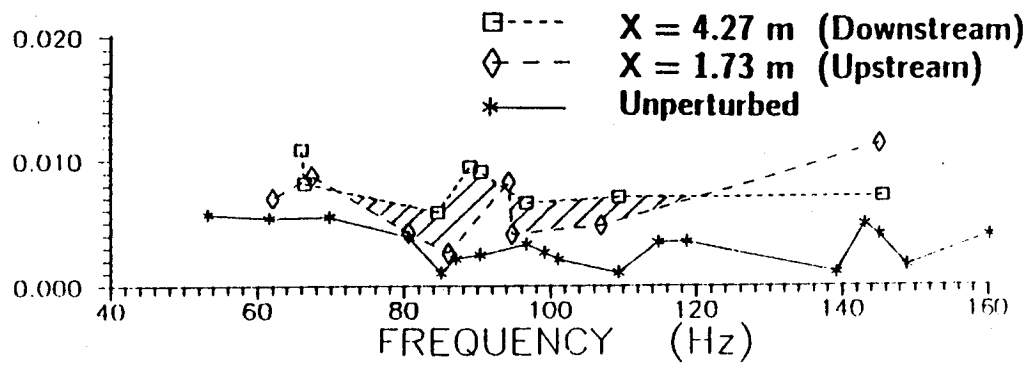
64a. Frequency bandwidth ± 0.5 Hz
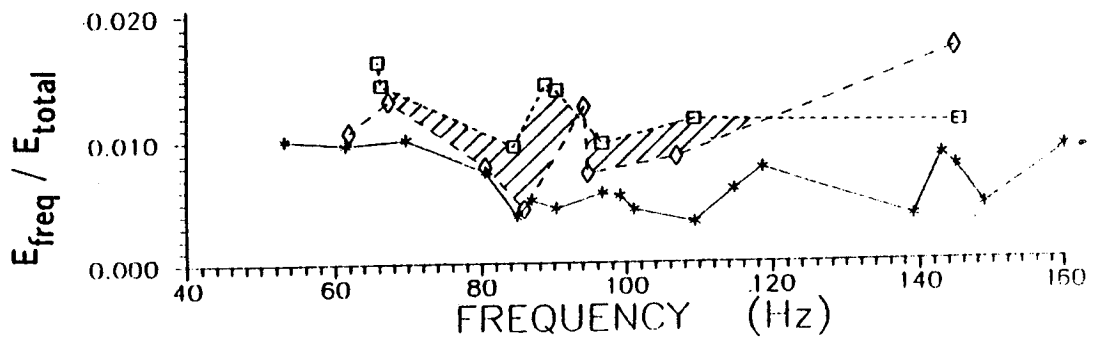
64b. Frequency bandwidth ± 1.0 Hz
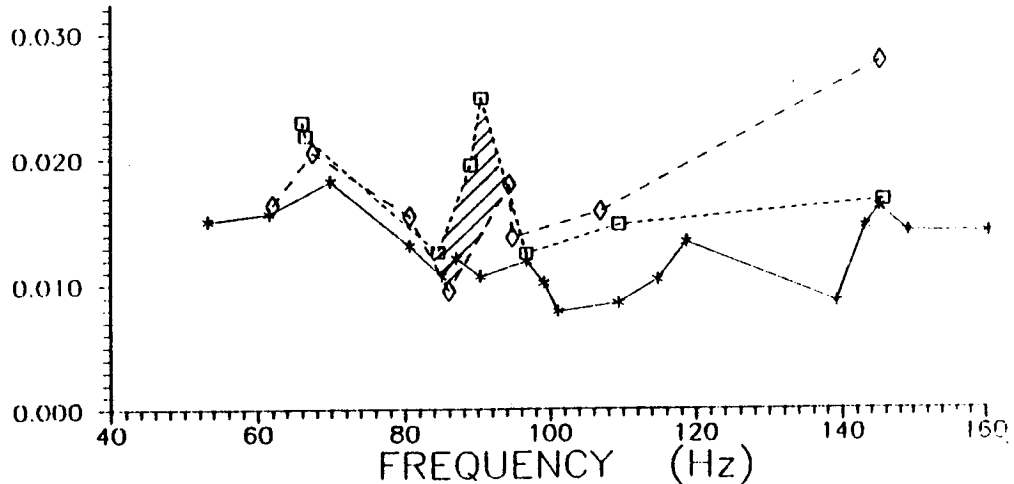
64c. Frequency bandwidth ± 2.0 Hz

Figure 64. Comparison of energy levels between upstream and downstream for counter-rotating perturbations, $U_\infty = 14$ m/s, frequency bandwidths ± 0.5, ± 1.0, ± 2.0 Hz. Cross-hatched zones indicate possible amplification

LEGEND

☐---- X = 4.27 m (Downstream)
◇-- X = 1.73 m (Upstream)
*—— Unperturbed

65a. Frequency bandwidth ± 0.5 Hz

E_{freq} / E_{total}
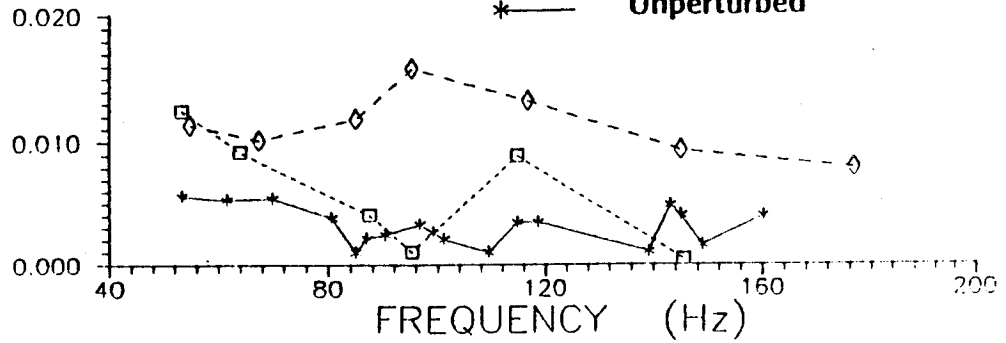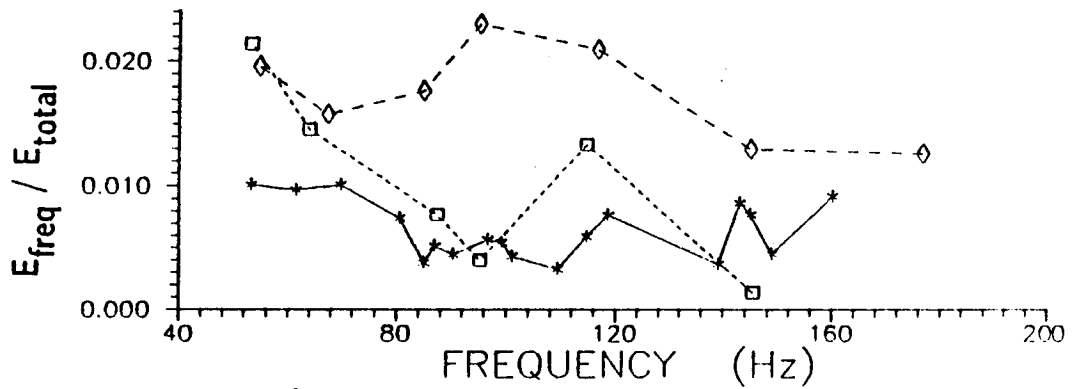
FREQUENCY (Hz)

65b. Frequency bandwidth ± 1.0 Hz
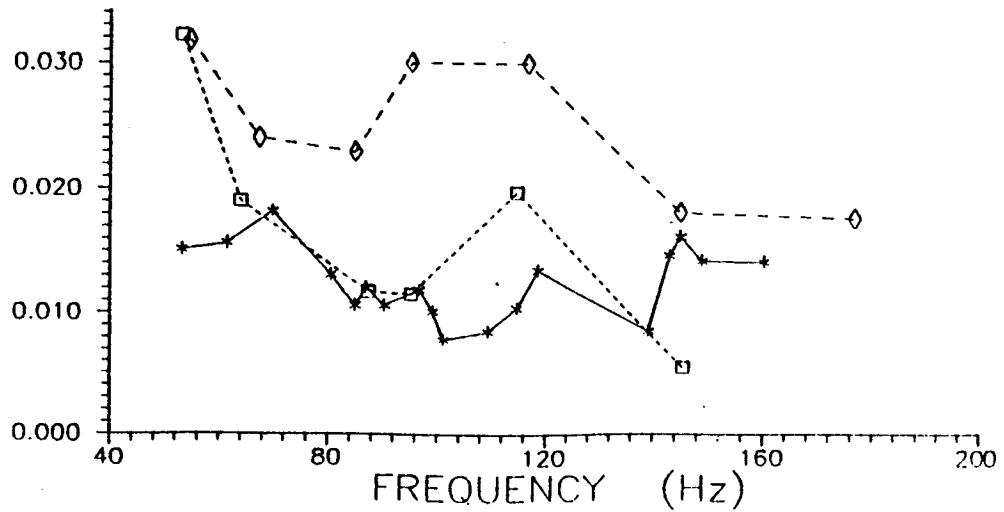
FREQUENCY (Hz)

65c. Frequency bandwidth ± 2.0 Hz

Figure 65. Comparison of energy levels between upstream and downstream for co-rotating perturbations, U_∞ = 14 m/s, frequency bandwidth ± 0.5, ± 1.0, ± 2.0 Hz

energy levels increased in this frequency range. Hence, even though the co-rotational spectral peaks displayed greater amplitudes than the counter-rotational spectral peaks, they decayed downstream, while the counter-rotational perturbation appeared to be amplified as they convected downstream.

5. CONCLUSIONS:

A perturbation generator has been designed and built which can introduce a controlled, circumferential velocity fluctuation into an axial vortex flow. The perturbation varies periodically and circumferentially over a range of frequencies and injected flow rates. Evaluation of the generator behavior has indicated that many other uncontrolled perturbations are produced, ranging from what appear to be amplified Tollmien-Schlichting waves produced in the boundary layer on the generator body through coupled wake-perturbation flow fluctuations which mask the simple sinusoidal oscillation signal, produced in the absence of a cross flow.

Energy spectra from hot-wire velocity measurements support the conclusion that a perturbation can be produced which has a controlled fundamental frequency. However, without using more than one hot-wire, it is not possible to determine definitively whether or not helical perturbations were produced.

Wind tunnel experiments showed that the injected perturbation was convected downstream in the vortex core. Differences were seen between counter-rotating and co-

rotating perturbations which corresponded to n = ±1 perturbations, as reported in reference 10. The differences were relative amplitudes of the spectral perturbation signal. The perturbation spectral amplitudes also were affected by the frequency of the perturbation generator, and the perturbation signals displayed differences between upstream and downstream behavior.

Future testing should include injecting the perturbation forward of the airfoil as well as changing the pitch angle of the airfoils to analyze the effects of changing the vortex. Testing with two hot-wires is also necessary since simultaneous hot-wire measurements are needed to determine phase information and whether the perturbation signal is actually amplified or decaying as it travels downstream. Future testing needs to produce a parametric map of instability frequencies and flow conditions to establish vortex control regimes. More measurements need to be made to differentiate the co-rotating and counter-rotating perturbations. With simultaneous measurements, there would be no question as to the validity of comparing the amplitudes between the upstream and downstream locations. Since it has been shown that a cyclic signal can be injected into the vortex, and survive the vortex roll-up, numerous studies of the effects of perturbations on a vortex can be conducted.

In addition, the cause of troughs at high free stream velocities with the counter-rotation perturbation needs to be studied. It is possible that some type of instability has occurred rapidly enough to produce non-linear effects over the axial sampling distance.

References

1. Raleigh, J. W. S.: "On the Dynamics of Revolving Fluids," Pro. Royal Society of London, Series A, Vol. 93, 1916, pp. 148-154.

2. Howard, L. N.; and Gupta, A. S.: "On the Hydrodynamic and Hydromagnetic Stability of Swirling Flows," Journal of Fluid Mechanics, Vol. 14, 1962, pp. 463 - 476.

3. Squire, H.B.: "Analysis of the Vortex Breakdown Phenomenon; Part I" Aero. Dept., Imperial College, London, Report 102, 1960.

4. Benjamin, T.B.: "Theory of the vortex breakdown phenomenon", Journal of Fluid Mechanics, Vol. 14, 1962, pp. 593 - 629.

5. Leibovich, S.: "Wave Motion and Vortex Breakdown", AIAA No. 69-645, 1969

6. Leibovich, S.: "Vortex Stability and Breakdown: Survey and Extension", AIAA Journal., Vol. 22, No. 9, 1984, pp. 1192 - 1206.

7. Sarpkaya, T.: "On Stationary and Traveling Vortex Breakdown", Journal of Fluid Mechanics, Vol. 45, part 3, 1971, pp. 545-559.

8. Sarpkaya, T.: "Effect of Adverse Pressure Gradient on Vortex Breakdown", AIAA Journal, Vol. 12, May, 1974, pp. 602 - 607.

9. Batchelor, G. K.: "Axial flow in trailing line vortices", Journal of Fluid Mechanics, Vol. 20, 1964, pp. 645-658.

10. Lessen, M.; Singh, P. J.; and Paillet, F.: "The stability of a trailing line vortex. Part 1. Inviscid theory", Journal of Fluid Mechanics, Vol.63, 1974, pp. 753-763.

11. Khorrami, M. R.; Malik, M. R.; and Ash, R. L.: "Application of Spectral Collocation Techniques to the Stability of Swirling Flows", Journal of Computational Physics, Vol. 81, 1989, pp. 206-229.

12. Khorrami, M. R.: "A Study of the Temporal Stability of Multiple Cell Vortices", Ph.D. Dissertation, Old Dominion University, May, 1989. Also, NASA CR 4261, November, 1989.

13. Schubauer, G. B.; and Skramstad, H. K.: "Laminar Boundary Layer Oscillations and Stability of Laminar Flow," National Bureau of Standards Research Paper 1772, 1943, Also, NACA Report 909, 1947.

14. Tollmien, W.: "Uber die Entstehung der Turbulence, "English Translation in NACA TM 609, 1931.

15. Schlichting, H.: Boundary Layer Theory, Seventh Edition, McGraw Hill, New York, 1979, pp. 476 -481.

16. Singh, P. I.; and Uberoi, M. S.: "Experiments on Vortex Stability," The Physics Fluids, Vol. 19, No. 12, December, 1976, pp. 1858-1863.

17. Ash, R. L.; and Stead, D. J.: "Influence of Free Stream Turbulence on a Trailing Line Vortex," Proc. Third International Conference of Fluid Mechanics, Cairo, Egypt, Vol. 1, 1990, pp. 345-358.

18. Bandyopadhyay, P. R.; and Weinstein, L. M.: "A Simplified Oil-Film Skin-Friction Meter," Proceedings of the AIAA/ASME/SIAM/APS 1st National Fluid Dynamics Congress, Part 3, Cincinnati, Ohio, 1988, pp. 1487-1499.

19. Bandyopadhyay, P. R.: "Resonant Flow in Small Cavities Submerged in a Boundary Layer," Proc. Royal Society of London, Series A, Vol. 420, 1988, pp. 219-245.

20. Stead, D. J.: Master's Thesis, Mechanical Engineering and Mechanics Department, Old Dominion University, To appear.

21. Mc Ginley, C. B.: "Three-Dimensional Mean Flow Experimental Study of Vortex Unwinding, Master's Thesis, The George Washington University, May,1987.

Appendix A:

Measurements of the velocity exiting the slit between the nominal 1" brass pipe (22.2 mm ID), and a mating flat washer were taken to determine the variation of maximum air velocity with gap width. The gap was set to zero and then opened using a micrometer. P_{pipe} is a measure of the pressure (torr) in the brass pipe and P_{dyn} is a measure of the total pressure (torr) at the exit of the gap. The static pressure was atmospheric pressure and the velocity was calculated using:

$$\frac{\triangle P}{\rho} = \frac{V^2}{2} \qquad (A.1)$$

or using standard atmospheric values, velocity was calculated using:

$$V = (222.2 \times \triangle P)^{1/2} \qquad (A.2)$$

where the velocity units were m/s and $\triangle P$ was $P_{pipe} - P_{dyn}$ measured in torr. The gap distance was measured in millimeters and was the difference between the micrometer reading for the opening and the micrometer reading with no opening. Data from the tests are shown in Tables A.1 through A.4. The data are plotted in Figure A1.

Table A.1

Gap Calibration for $\Delta P = 80$ Torr (185 kPa)

Micrometer (mm)	Gap Width (mm)	P (pipe) (torr)	P (dynamic) (torr)	Velocity (m/s)
-1.31	0.00	77.3	39.9	94.2
-1.30	0.01	79.3	43.3	98.1
-1.28	0.03	79.5	44.9	99.9
-1.23	0.08	79.8	47.2	102.4
-1.13	0.18	79.8	48.2	103.4
-0.93	0.28	79.3	50.2	105.6
-0.83	0.38	79.1	51.3	106.9
-0.51	0.80	79.5	52.3	107.9
-0.31	1.00	79.4	52.4	107.9
+0.15	1.46	78.6	52.3	107.8

Pressures are too high for the analysis desired or needed. Velocities desired are to be much less.

Table A.2

Gap Calibration for $\Delta P = 1$ Torr (232 Pa)

Micrometer (mm)	Gap Width (mm)	P (pipe) (torr)	P (dynamic) (torr)	Velocity (m/s)
-1.28	0.00	1.00	0.13	5.37
-1.27	0.01	1.04	0.13	5.37
-1.26	0.02	1.05	0.13	5.37
-1.23	0.05	1.00	0.20	6.63
-1.20	0.08	1.02	0.29	7.97
-1.18	0.10	1.00	0.32	8.43
-1.08	0.20	1.03	0.56	11.14
-0.78	0.50	1.02	0.67	12.19
-0.28	1.00	1.02	0.68	12.25
+0.72	2.00	1.00	0.70	12.40
+0.72	2.00	0.99	0.69	12.30
-0.28	1.00	1.03	0.68	12.25
-0.78	0.50	1.01	0.65	12.02
-1.08	0.20	1.01	0.50	10.52
-1.18	0.10	1.01	0.27	7.79
-1.23	0.05	1.01	0.08	4.08
-1.26	0.02	1.00	0.09	4.37
-1.27	0.01	1.02	0.10	4.64
-1.28	0.00	0.99	0.09	4.57

Table A.3

Gap Calibration for $\Delta P = 5$ Torr (1160 Pa)

Micrometer (mm)	Gap Width (mm)	P (pipe) (torr)	P (dynamic) (torr)	Velocity (m/s)
-1.26	0.00	4.96	1.60	18.9
-1.25	0.01	5.00	1.62	19.0
-1.24	0.02	5.02	1.57	18.7
-1.21	0.05	4.99	2.06	21.4
-1.16	0.10	5.00	2.65	24.3
-1.06	0.20	5.00	3.19	26.6
-0.76	0.50	5.01	3.24	26.8
-0.26	1.00	5.01	3.29	27.0
+0.74	2.00	5.00	3.38	27.4
+0.74	2.00	5.00	3.39	27.4
-0.26	1.00	5.01	3.27	27.0
-0.76	0.50	5.01	3.18	26.6
-1.06	0.20	4.98	3.16	26.5
-1.16	0.10	4.98	2.74	24.7
-1.21	0.05	5.00	2.19	22.1
-1.24	0.02	4.98	1.59	18.8
-1.25	0.01	5.01	1.54	18.5
-1.26	0.00	5.01	1.64	19.1

Table A.4

Gap Calibration for $\Delta P = 10$ Torr (2320 Pa)

| Micrometer (mm)	Gap Width (mm)	P (pipe) (torr)	P (dynamic) (torr)	Velocity (m/s)
-1.25	0.00	10.04	3.90	26.2
-1.24	0.01	10.06	3.04	26.0
-1.23	0.02	10.01	3.04	26.0
-1.20	0.05	10.02	3.41	27.5
-1.15	0.10	10.02	5.11	33.7
-1.05	0.20	10.03	6.09	36.8
-0.75	0.50	10.04	6.11	36.8
-0.25	1.00	10.07	6.61	38.3
+0.75	2.00	10.02	6.84	39.0
+0.75	2.00	10.03	6.85	39.0
-0.25	1.00	9.97	6.50	38.0
-0.75	0.50	10.00	6.09	36.8
-1.05	0.20	9.97	6.01	36.5
-1.15	0.10	10.04	5.20	34.0
-1.20	0.05	10.01	3.28	27.0
-1.23	0.02	10.03	3.07	26.1
-1.24	0.01	10.03	3.26	26.9
-1.25	0.00	10.03	3.22	26.4
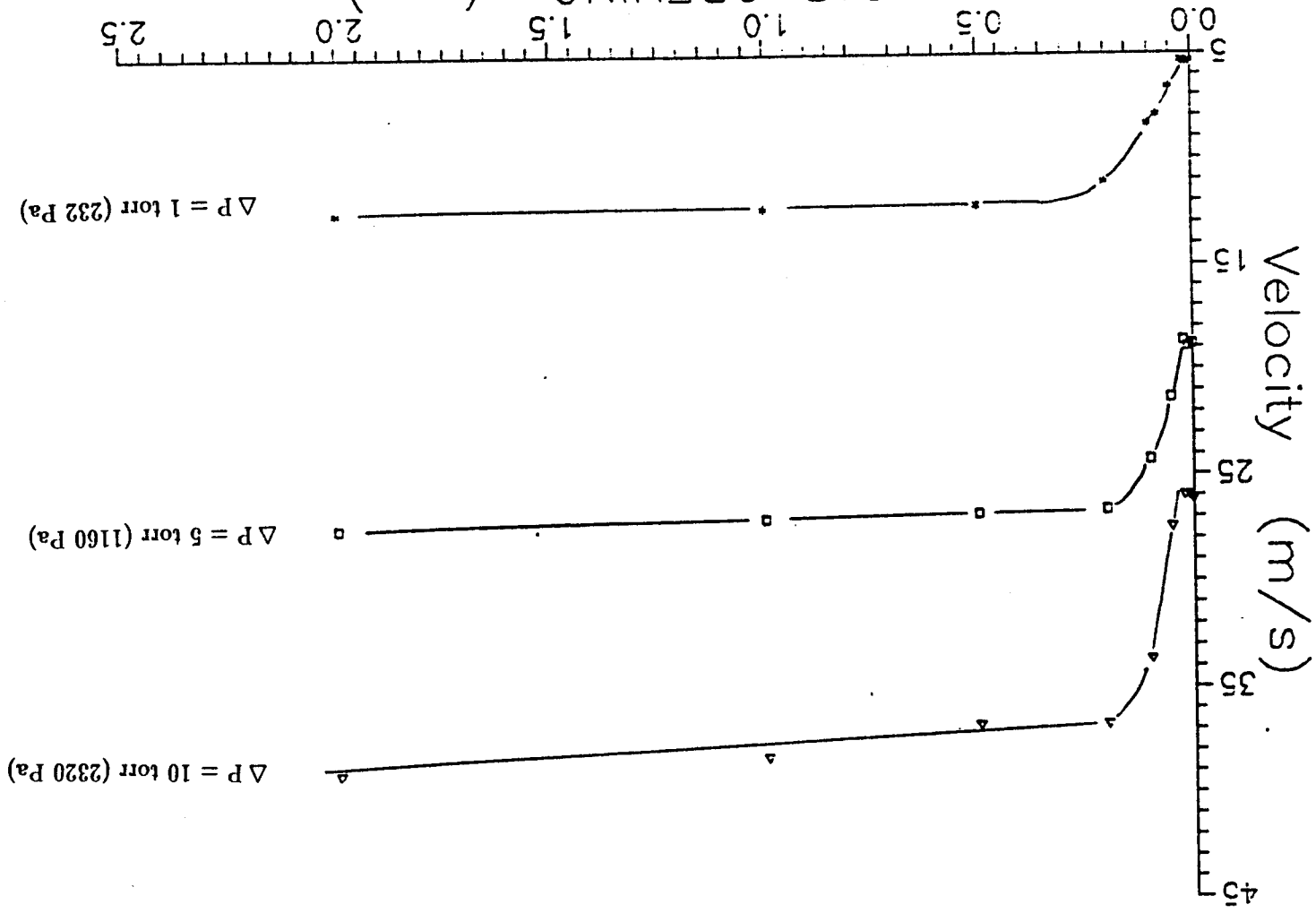
Figure A.1. Velocity for gap opening for differential pressures of 1, 5, and 10 torr for the development of viscous control.